



**HAL**  
open science

# III-nitrides on silicon : a platform for integrated photonics from the ultraviolet to the near-infrared

Farsane Tabataba-Vakili

► **To cite this version:**

Farsane Tabataba-Vakili. III-nitrides on silicon : a platform for integrated photonics from the ultraviolet to the near-infrared. Optics [physics.optics]. Université Paris-Saclay, 2020. English. NNT : 2020UPAST014 . tel-02968449

**HAL Id: tel-02968449**

**<https://theses.hal.science/tel-02968449>**

Submitted on 15 Oct 2020

**HAL** is a multi-disciplinary open access archive for the deposit and dissemination of scientific research documents, whether they are published or not. The documents may come from teaching and research institutions in France or abroad, or from public or private research centers.

L'archive ouverte pluridisciplinaire **HAL**, est destinée au dépôt et à la diffusion de documents scientifiques de niveau recherche, publiés ou non, émanant des établissements d'enseignement et de recherche français ou étrangers, des laboratoires publics ou privés.

# III-nitrides on silicon: a platform for integrated photonics from the ultraviolet to the near-infrared

**Thèse de doctorat de l'Université Paris-Saclay**

École doctorale n°575 : electrical, optical, bio : physics and engineering (EOBE)  
Spécialité de doctorat : Physique  
Unité de recherche : Université Paris-Saclay, CNRS, Centre de Nanosciences et de  
Nanotechnologies, 91120, Palaiseau, France  
Réfèrent : Faculté des sciences d'Orsay

**Thèse présentée et soutenue à Palaiseau, le 24/09/2020, par**

**Farsane TABATABA-VAKILI**

## Composition du Jury

**Maria TCHERNYCHEVA**

DR, CNRS, C2N

Présidente du jury

**Alfredo DE ROSSI**

Ingénieur HdR, TRT

Rapporteur & Examineur

**Nicolas GRANDJEAN**

Professeur, EPFL

Rapporteur & Examineur

**Yannick DUMEIGE**

MC, HdR, Institut Foton

Examineur

**Michael KNEISSL**

Professeur, TU Berlin

Examineur

**Philippe BOUCAUD**

DR, CNRS, CRHEA

Directeur de thèse

**Bruno GAYRAL**

Ingénieur HdR, CEA, IRIG

Co-Encadrant





Thèse effectuée au sein du **Centre de Nanosciences et de Nanotechnologies**  
de l'Université Paris-Saclay  
10 boulevard Thomas GOBERT  
91120 PALAISEAU cedex  
FRANCE

Ce travail a bénéficié d'une aide de l'Etat gérée par l'Agence Nationale de la Recherche  
au titre du programme Investissements d'Avenir portant la référence  
ANR-11-LABX-0014 : Labex GANEX



*To Damir, Fachreddin, Jutta, and Nureddin for their love and support.*



# Acknowledgements

Before I start thanking all the amazing people who have made this journey possible and enjoyable, I want to point out some of the major obstacles I encountered over the past 4 years.

The day I visited then IEF in May 2016 to give a seminar talk was marked by a truck falling on the tracks of the RER B. Maybe I should have taken this as a bad omen. But my future advisor came to my rescue by car, picking me up in Les Bacconnets where the RER had stranded, making a great first impression.

After my visit and before I started my thesis, IEF, which had in the meantime changed its name to C2N-Orsay, was flooded by the Yvette and the cleanroom was shut down for something like 3 months. To my luck, I had spent those 3 months on vacation not even aware of the problem!

The first year of my PhD went rather smoothly with just a few standard hiccups (there is no experimental PhD without major technical problems!), like several machines being down for several months at a time, an expired bottle of e-beam resist that took 8 months to replace. The usual.

The next major issue was the ever-impending lab move, whose impact on my life I initially could not fathom. Scheduled originally for fall of 2017 it was delayed by a year. Unfortunately, in the months prior to the cleanroom closure it was a sweltering 37°C in the fume hoods due to a broken AC. (This is the reason why the sample in chapter 3 doesn't have any gratings!)

My advisor had moved to the south of France to become the new director of CRHEA at the beginning of 2018. We discussed regularly by Skype and email, so this was fine for me, even though I certainly missed having him around, and in retrospect maybe I should have moved as well at that point.

In September 2018, C2N moved into the beautiful new building in Palaiseau. Clearly, even in the best case, moving a cleanroom takes a lot of time, and a serious disruption to our experimental work was inevitable. Unfortunately, in our case, there were some quite serious issues that are still being dealt with two years later. Tough luck for the PhD students and postdocs... I spent fall of 2018 at conferences and workshops, and visiting collaborators in Hong Kong for 3 weeks. (Fall weather in Hong Kong is amazing.)

By the beginning of 2019, it became clear that the cleanroom would be down for a long time, and I used this opportunity to discover France. I started working more at our collaborators' labs in Grenoble (CEA-IRIG and Institut Néel) and Valbonne (CRHEA). We also extended my contract

by a year to try to make up for the time lost by the lab move. I certainly did the "tour de France" during my PhD, while travelling pretty much every week for more than a year. I can highly recommend the beaches and scuba diving on the Côte d'Azur and the skiing around Grenoble!

By February 2020, I had finally succeeded to fabricate three good samples, after a year without any new results. I managed to measure one of them with our collaborators in Montpellier, and it turned into a beautiful paper. The other two samples are still awaiting characterization at our collaborators' lab in Nice.

And then Covid-19 happened. This was pretty much the universe telling me it was time to stop doing experiments and to finish writing my thesis. The confinement was in some ways actually quite convenient for writing, little distraction even on the weekends and my advisor had more time available to discuss with me. Many PhD students go into self-isolation while writing their thesis... In my case, half the world went into self-isolation while I was writing my thesis. Weird... Unfortunately, the pandemic did not stop when my thesis was finished...

#### **Moving on to the acknowledgements:**

My biggest thanks goes to my advisor **Philippe Boucaud**. Philippe you have been really amazing. I have learned so much from you. You've been a mentor, a role model, and a friend. In spite of all the things that happened over the past 4 years, I cannot think of anywhere I would have rather been than doing my thesis with you on III-nitride integrated photonics. You have helped me grow as a scientist and as an individual. Your advice has allowed me to figure out what I want to do with my life, be a CNRS researcher like you. Often you believed in me more than I did in myself, which has been extremely motivating. I cannot think of a better word to describe you than the German term "Doktorvater" (PhD advisor, literally PhD father). I really hope that we will stay in touch and that we will work together again in the future. Looking forward to our next beer!

Next, I want to thank my co-supervisor **Bruno Gayral**. While initially, I was only supposed to come to Grenoble every once in a while for some spectroscopy, I ended up spending a lot of time there during 2019 to do processing, and ultimately very little spectroscopy. While this is not at all your domain, you helped where you could, especially with getting access to equipment and negotiating with people in charge. This was very valuable. I've also enjoyed discussing with you, especially on our road-trip Grenoble-CRHEA.

I want to thank **Nicolas Grandjean** and **Alfredo de Rossi** for careful reading of my manuscript, writing thorough and positive reviews, and asking interesting and important questions at my defense. I also want to thank the other members of the jury, **Maria Tchernycheva**, **Michael Kneissl**, and **Yannick Dumeige** for taking the time to read my manuscript, participate in my defense, and asking interesting questions.

My gratitude goes to **Benjamin Damilano** for being a great colleague. You are the kind of guy who is always willing to help, usually the first (and sometimes the only one) to respond to an email sent to several people. Also you are really fun at Karaoke!

I want to acknowledge **Fabrice Semond** without whom I would not be here, since it was him

who I contacted about a PhD position and who forwarded my email to Philippe and Bruno. I also thank you for fruitful and enjoyable discussions and a successful collaboration in the framework of Milagan.

My thanks also goes to the QD group at C2N for the time we spent together before the lab move and also after, even though these encounters were a bit more rare. Thank you **Sébastien Sauvage**, **Moustafa El Kurdi**, **Xavier Checoury**, and **Emilie Saket** for many interesting discussions over lunch. I thank Xavier also for his help with FDTD simulations. I also thank my former colleagues **Petru Borta**, **Anas Elbaz**, **Leornard Monniello**, **Mohammed Chaibi**, and **Riazul Arefin** for making life at C2N more enjoyable, I miss you guys. A special thanks also goes to **Iannis Roland** with whom I only had a 2 month overlap, but who has taught me a lot and who has helped make the beginning of my thesis very smooth.

I am grateful to our remaining epitaxy team: **Blandine Alloing**, **Stéphanie Rennesson**, and **Eric Frayssinet** for a plethora of samples and for many friendly discussions.

**Jean-Yves Duboz**, I thank you for making GANEX a great success, and for always being there to tease me or to provide support.

I thank our collaborators at L2C in Montpellier **Thierry Guillet**, **Christelle Brimont**, and **Laetitia Doyennette** for a fruitful collaboration and especially for hosting me for two stays at their lab, allowing me to use their spectroscopy setup.

Over the last two years, the colleagues at CRHEA and at IRIG-Pheliqs (previously INAC) have been extremely welcoming. I was an outsider who was only there part-time, but they allowed me to join their community. I will be forever grateful. I especially want to thank my many PhD and postdoc friends: **Maria Spies**, **Nathaniel Feldberg**, **Philipp John**, **Victor Fan Arcara**, **Colin Paillet**, **Renato Juliano Martins**, **Reda Elwaradi**, **Rajath Sawant**, **Max Meunier**, **Sandeep Yadav Golla**, **Akhil Ajay**, **Roy Dagher**, **Kilian Baril**, **Marion Gruart**, **Alexandre Concordel**, **Akanksha Kapoor**, **Madalina Siladie**, **Saptarshi Kotal**, **Vincent Grenier**, **Ioanna Dimkou**, **Camille Barbier**, **Anjali Harikumar**, **Romain Fons**, **Guilherme Torelly**, **Masoud Kheyri**, **Anthony Gourdin**, **Mario Ferraro**, **Valeria Bonito Olivia**, **Gauthier Brière**, **Congying You**, **Remy Vermeersch**, **Sergi Cuesta**, **Saransh Gosain**, **Jane Chen**, **Samuel Mata**, and **Thi Huong Ngo**. Maria and Nathaniel, you guys are amazing, I love you. You've made my stays in Grenoble, especially during 2019, very enjoyable with a lot of game nights, dinners, bars. Victor, you've been the worst office mate, haha, but you're a great friend, even if you kind of disappeared there during the end of your thesis and we haven't even managed to meet up in Grenoble since... Philipp: HOPSTORE!! CAP D'ANTIBES!! It was great to have another German around who shared my enthusiasm for beer and for Cap d'Antibes. I really appreciated being able to have secret conversations with you in German. Colin, for a while I thought that you were purposefully avoiding me by always being in Grenoble when I was in Antibes and vice versa, but we've had many good times, and I especially appreciated that you came to Paris for my defense. Reda, you only showed up at the very end of my thesis, but you have been a good friend over these final months, and I really appreciated that you came to Paris for my defense. Renato, my friend, your

Caipirinhas are just world class, can't wait to drink another one. It's always been fun to hang out with you, even though you are never ever on time. Max, my little friend, I've been teasing you too much for how young you are, but you've been making fun of me too, so it's ok. Sandeep, my friend, my friend, my friend...definitely enjoyed hanging out at La Gravette. Raj, Raj, Raj, Raj, Raj why aren't you writing? We should have had more board game nights, my friend. I can't write a sentence about each and every one of you guys, but please know how much I've appreciated our time together (however brief in some cases). I've loved all the adventures with the Open Space and Bon Application gang, as well as the H2 kids, you guys really rock, even though I was quite disappointed that most of you did not come to my defense. Thanks for everything guys, hope to keep in touch. Don't hesitate to visit me in Munich.

At CRHEA I am also very thankful to **Sébastien Chenot** and **Virgine Brändli** from the CRHEATEC team for their support with processing. I thank **Jesus Zuniga-Perez** for many fun discussions and for picking me up by car whenever the buses were on strike. I thank **Patrice Genevet** for many discussions, especially about my future. I also thank **Philippe Vennéguès**, **Mathieu Leroux**, **Julien Brault**, **Yvon Cordier**, **Jean-Michel Chauveau**, **Stéphane Vezean**, **Maud Nemoz**, **Aimeric Courville**, **Eric Drezet**, **Patrick Chalbet**, and **Anne-Marie Cornuet** for many friendly discussions over coffee or lunch or wine. I thank **Samira Khadir** for fun discussions, especially on the bus! I also particularly thank Jesus, Patrice, Jean-Yves, Fabrice, Benjamin, and Blandine for a very annoying and thus very useful mock defense.

At IRIG-Pheliqs I also thank **Eva Monroy**, **Joel Bleuse**, **Bruno Daudin**, and **Christophe Durand** for many friendly interactions. At PTA I thank **Thierry Chevolleau** and **Thomas Charvolin** for providing me with etch recipes and being available to discuss when needed. I thank **Delphine Constantin** for PECVD depositions and **Irène Pheng** for saw dicing. At Institut Néel I thank **Thierry Crozes** and **Gilles Nogues** for providing me access to the NB5 and being available for discussions. I thank **Bruno Fernandez** for doing BOE for me, since I wasn't allowed to. I also thank **Guy Fullet** for many friendly discussions.

At C2N I thank the cleanroom team for their help back in Orsay. I thank **David Bouville** for saw dicing and mask writing. I thank **Jean-René Coudeville** and **Abdelhanin Aassime** for their help with the NB4. I thank **Nathalie Isaac** for her help with ICP. I thank the C2N administration, especially **Bernadette Laborde** and **Natacha Civaton** for dealing with my countless "ordres de mission". I also thank **Adrien Vincent** for this beautiful Latex template. I thank the young colleagues from other groups I had the pleasure to meet and become friends with, especially **François Joint**, **Pierre-Baptiste Vigneron**, **Laurent Bouley**, **Claire Abadie**, and **Chris Bennett** (who was also my flatmate for two years).

I thank the CNRS and GANEX for providing funds to extend my thesis due to the lab move.

I am grateful to our collaborators in Hong Kong for hosting me for three weeks. I especially thank **Anthony Choi**, **Li Kwai Hei**, and **Gordon Fu**.

A thanks in advance goes to our collaborators at Inphyni for the measurements they will do on the samples discussed in chapter 6.

My gratitude goes to the wonderful people from the **Bourse L'Oréal-UNESCO** for women in science for awarding me with one of 30 scholarships in 2018. The prize money was very useful and it was a great opportunity to meet other young women in science with whom I am still in contact regularly, especially **Stéphanie Challita**, thank you.

I thank all the amazing people of the III-nitrides community that make every conference a pleasure to attend. I was very sad that the 2020 conferences got cancelled. I really loved this community.

Many thanks go to my friends from my studies in Berlin: **Kilian Kluge, Constanze and Markus Hantschmann, Kilian Kuhla, Janina Lebendig-Kuhla, Felix Kramer, Jan-Philip Schröder, Alex Schimpf, Benedikt Hartung, Wassilij Kopylov, Jan Totz, Max Bucher, Christoph Reich, Jens Rass, Tim Wernicke**, and **Konrad Bellmann** for making my BSc and MSc a very good experience. It was great to learn with you and from you and enjoy our time together at parties, bars, etc. I will never forget our weekend homework and study sessions at the university with Kilian, Kilian, Conny, JP, Felix, etc.

I am deeply grateful to **Michael Kneissl** for his support over the past seven years, since I did my BSc thesis in his group. I especially thank you for giving me the opportunity to do an internship and my MSc thesis at PARC, and for writing letters of recommendation for me whenever I asked you. It was great to also have you in my thesis jury. I also thank **Thomas Wunderer** and **Nobel Johnson** from PARC for making my time in California a very rich experience. Certainly my life would have taken a different path if I hadn't gone to California.

Endless thanks goes to my boyfriend, **Damir Vodenicarevic** for his infinite support over the past four years. You have been my rock. Even when I was travelling non-stop, you never stopped being by my side. I also thank you for your help with Python and equations. You've made math fun again! I love you so much my Cherry.

I thank my brother, **Fachreddin Tabataba-Vakili** who is probably the reason why I am a physicist today. It was a pleasure growing up with you and our friendship is very important to me. It is too bad that we haven't lived on the same continent in the past 6 years, can't wait for you to come back to Europe. I also want to thank my sister-in-law **Alice Schwarze** for being a good friend for all my adult life and also a strong influence on me choosing physics over say engineering in my BSc!

I am very grateful to my parents **Jutta** and **Nureddin Tabataba-Vakili** without whom I would not be here or anywhere. Thank you for always supporting me and believing in me unconditionally. Education was always the most important thing for you. You made me feel like doing a PhD was the only and natural next step after an MSc.

Finally, I want to thank my childhood friends **Joanna O'Neill, Tatiana Bühler, Jasmin Herrmann**, and **Leslie Barbour** for their friendship and support over the last 17-odd years.



# Contents

<b>Acknowledgements</b>	<b>vii</b>
<b>Contents</b>	<b>xiii</b>
<b>List of Figures</b>	<b>xvii</b>
<b>List of Tables</b>	<b>xxiii</b>
<b>List of Abbreviations</b>	<b>xxv</b>
<b>Introduction</b>	<b>1</b>
<b>1 Photonic devices using III-nitrides on silicon</b>	<b>7</b>
1.1 III-nitride semiconductors . . . . .	7
1.1.1 Crystal structure and polarization fields . . . . .	8
1.1.2 Band structure . . . . .	10
1.1.3 Refractive index . . . . .	13
1.1.4 Defect luminescence in GaN and AlN . . . . .	14
1.1.5 Choice of substrate . . . . .	14
1.1.6 III-nitride growth on silicon . . . . .	15
1.2 Photonic devices . . . . .	17
1.2.1 Slab waveguide . . . . .	17
1.2.2 Ridge waveguide . . . . .	22
1.2.3 Microdisk cavity . . . . .	26
1.2.4 Coupling between a microdisk and a bus waveguide . . . . .	34
1.2.5 Semiconductor laser . . . . .	38
1.2.6 2D photonic crystal slab . . . . .	40
1.2.7 Grating coupler . . . . .	46
1.2.8 FDTD method . . . . .	48
1.3 Fabrication of III-nitride on silicon photonic devices . . . . .	51
1.3.1 Mask files . . . . .	53
1.3.2 E-beam lithography . . . . .	54

1.3.3	Etch recipes . . . . .	55
1.3.4	Fabrication of III-nitride microdisks . . . . .	55
1.3.5	Fabrication of suspended III-nitride microdisk photonic circuits . . . . .	57
1.3.6	Fabrication of passive photonic circuits bonded on SiO <sub>2</sub> . . . . .	63
1.3.7	Fabrication of III-nitride PhC slabs . . . . .	64
1.4	Optical spectroscopy setups . . . . .	66
1.4.1	μ-PL setups . . . . .	66
1.5	Conclusion . . . . .	67
<b>2</b>	<b>III-nitride on silicon microdisk lasers</b>	<b>69</b>
2.1	Introduction and state of the art . . . . .	69
2.1.1	Lasing under pulsed optical pumping . . . . .	69
2.1.2	Lasing under continuous-wave optical pumping . . . . .	71
2.2	Before this thesis . . . . .	73
2.3	Results and discussion . . . . .	75
2.3.1	Sample description . . . . .	75
2.3.2	Optical confinement . . . . .	79
2.3.3	Band structure simulations . . . . .	80
2.3.4	Fabrication of microdisks . . . . .	82
2.3.5	Quality factor . . . . .	83
2.3.6	Pulsed optically pumped lasing . . . . .	84
2.3.7	Calculation of the threshold power . . . . .	85
2.3.8	Pump laser . . . . .	89
2.3.9	Growth method . . . . .	91
2.3.10	Dislocation density . . . . .	91
2.3.11	Chemical treatment . . . . .	92
2.3.12	Blue vs. UVA . . . . .	95
2.3.13	Lasing threshold vs. PL . . . . .	96
2.3.14	Lasing threshold vs. mode overlap . . . . .	96
2.3.15	Sample on bulk GaN . . . . .	97
2.4	Conclusion and Outlook . . . . .	98
<b>3</b>	<b>III-nitride on silicon microlaser photonic circuits in the blue</b>	<b>101</b>
3.1	Introduction and state of the art . . . . .	101
3.1.1	Monolithic integration . . . . .	101
3.1.2	Heterogeneous integration . . . . .	103
3.1.3	Critical coupling in III-nitride photonic circuits . . . . .	104
3.2	Design of photonic circuits on D559 and D677 . . . . .	104
3.3	Fabrication of photonic circuits on D559 and D677 . . . . .	109

3.4	Results and discussion . . . . .	112
3.4.1	CW spectroscopy of sample D559 . . . . .	112
3.4.2	Critical coupling in the spontaneous emission regime . . . . .	116
3.4.3	Observation of pulsed lasing in a III-nitride photonic circuit . . . . .	118
3.4.4	Dependence of lasing threshold and output signal on Q factor and coupling distance . . . . .	119
3.4.5	Proximity effect . . . . .	125
3.5	Conclusion and perspectives . . . . .	127
<b>4</b>	<b>Integrated microlaser photonic circuits and 2D photonic crystal slabs in the ultraviolet</b>	<b>129</b>
4.1	Introduction and state of the art . . . . .	129
4.1.1	UV photonic circuits . . . . .	130
4.1.2	III-nitride photonic crystal slab cavities . . . . .	132
4.2	Microdisk laser photonic circuits . . . . .	132
4.2.1	Design and fabrication . . . . .	132
4.2.2	Results and discussion . . . . .	135
4.3	2D photonic crystal slab cavities . . . . .	141
4.4	Conclusion and outlook . . . . .	146
<b>5</b>	<b>Electrical injection in III-nitride microdisks and microrings on silicon</b>	<b>149</b>
5.1	Introduction and state of the art . . . . .	149
5.2	Microdisk under electrical injection . . . . .	152
5.2.1	Fabrication of microdisks under electrical injection . . . . .	152
5.2.2	EL results obtained from sample C404 . . . . .	153
5.2.3	Current path through defects in undoped buffer layers . . . . .	155
5.3	Microrings under electrical injection . . . . .	156
5.3.1	Fabrication of electrically injected microrings . . . . .	156
5.3.2	Results and discussion . . . . .	159
5.4	White LED . . . . .	162
5.5	Conclusion and outlook . . . . .	163
<b>6</b>	<b>III-nitride photonic circuits in the near-infrared</b>	<b>167</b>
6.1	Introduction and state of the art . . . . .	167
6.2	Design and fabrication of passive photonic circuits on SiO <sub>2</sub> . . . . .	169
6.2.1	Choice of wavelength . . . . .	170
6.2.2	Design of microring to waveguide coupling on A2390 at 780 nm . . . . .	171
6.2.3	Design of microdisk to waveguide coupling on A2390 at 780 nm . . . . .	173
6.2.4	Design of grating couplers on A2390 at 780 nm . . . . .	174

---

6.2.5	Fabrication of microring and microdisk photonic circuits on A2390 at 780 nm . . . . .	175
6.3	Design and fabrication of passive photonic circuits suspended on Si(100) . . . . .	177
6.3.1	Design of microdisk to waveguide coupling on A2587 at 780 nm . . . . .	178
6.3.2	Design of grating couplers on A2587 at 780 nm . . . . .	179
6.3.3	Fabrication of suspended microdisk photonic circuits on A2587 at 780 nm . . . . .	179
6.4	Design of a microring photonic circuit on SiO <sub>2</sub> for degenerate parametric down-conversion and SHG . . . . .	182
6.4.1	Mask with two waveguides for parametric frequency conversion and SHG . . . . .	186
6.5	Conclusion and outlook . . . . .	187
	<b>Conclusions and future work</b>	<b>189</b>
	<b>List of Publications and Contributions</b>	<b>193</b>
	<b>Synthèse en Français</b>	<b>199</b>
	<b>Bibliography</b>	<b>209</b>

# List of Figures

1	State of the art of III-nitride photonic devices from the UVC to the NIR. . . . .	3
2	III-nitride photonic devices from the UVC to the NIR from our collaboration before this thesis. . . . .	4
1.1	Schematic of the wurtzite crystal structure. . . . .	8
1.2	Sketch of QWs with and without QCSE. . . . .	10
1.3	Schematic of different crystal planes and their calculated polarization. . . . .	10
1.4	Valence band splitting for AlN, GaN, and InN. . . . .	11
1.5	Band gap over lattice constant for III-nitrides. . . . .	12
1.6	EQE of LEDs visible and UV spectral ranges. . . . .	13
1.7	Refractive indices of AlN and GaN. . . . .	14
1.8	Sketch of tilt and twist in AlN grown on Si. . . . .	16
1.9	Sketch of a slab waveguide. . . . .	18
1.10	Calculations of $H_z$ field and TE and TM modes for slab waveguides. . . . .	22
1.11	Sketch of a rectangular ridge waveguide. . . . .	23
1.12	Calculations of $n_{eff}$ and mode profiles of TE and TM modes in ridge waveguides. . . . .	25
1.13	3D sketch of a microdisk laser. . . . .	27
1.14	Schematics of a microdisk resonator. . . . .	27
1.15	Plots of Eqs. 1.60 and 1.51 giving the wavelength and radial profile of WGMs. . . . .	31
1.16	FDTD simulations of the $H_z$ field of WGMs. . . . .	32
1.17	3D sketch of a photonic circuit. . . . .	34
1.18	Schematic of microdisk to waveguide coupling. . . . .	35
1.19	Calculated transmission curves of the three coupling regimes. . . . .	37
1.20	Schematics of bad and good phase matching. . . . .	37
1.21	Normalized photon number over pump power for different values of $\beta$ for a semiconductor laser. . . . .	40
1.22	Schematic of 1D, 2D, and 3D photonic crystals. . . . .	41
1.23	Sketch of the triangular lattice and reciprocal lattice of a PhC. . . . .	42
1.24	Sketch of a triangular air-hole slab PhC and its calculated band structure. . . . .	44
1.25	2D PhCs slabs with L1 and L3 cavity. . . . .	44
1.26	Sketches of L3 and H2 cavities. . . . .	45

1.27 Simple model describing the need for gentle confinement in a slab cavity. . . . .	46
1.28 Sketch of a grating coupler. . . . .	47
1.29 FDTD simulations of the $H_z$ field for two different coupling regions. . . . .	49
1.30 2D FDTD simulation of the $E_y$ field of a grating coupler. . . . .	51
1.31 Mask of a photonic circuit. . . . .	53
1.32 Mask of a photonic circuit with proximity effect correction. . . . .	54
1.33 Schematic of the fabrication process of a III-nitride microdisk. . . . .	56
1.34 SEM images of microdisks fabricated with different e-beam lithography and etch parameters. . . . .	57
1.35 SEM images of suspended waveguides held by nanotethers. . . . .	58
1.36 Process flow of an active microdisk coupled to a waveguide terminated by out-coupling gratings. . . . .	59
1.37 Reduced process flow of an active microdisk coupled to a waveguide with out-coupling gratings that are not fully etched. . . . .	60
1.38 SEM images of the microdisk to waveguide coupling region. . . . .	60
1.39 SEM image of a device with etch damage at the edges. . . . .	61
1.40 SEM images of successful and unsuccessful out-coupling gratings for the blue spectral range. . . . .	61
1.41 Process flow of a passive microdisk coupled to a waveguide terminated by out-coupling gratings. . . . .	62
1.42 Process flow of a passive microring coupled to a waveguide terminated by out-coupling gratings and bonded on $\text{SiO}_2$ . . . . .	64
1.43 Process flow of an active 2D PhC slab cavity. . . . .	65
1.44 SEM images of 2D PhC cavities. . . . .	65
1.45 $\mu$ -PL setup in Montpellier. . . . .	66
1.46 Scheme of the $\mu$ -PL setup in Grenoble. . . . .	67
2.1 Reports of pulsed optically pumped lasing in III-nitride microdisks. . . . .	70
2.2 Reports of optically pumped RT CW lasing in III-nitride microdisks. . . . .	72
2.3 III-nitride microdisk resonators and lasers from our collaboration from before 2017. . . . .	74
2.4 Sketches of the heterostructures of the investigated samples. . . . .	76
2.5 AFM images of some of the investigated samples. . . . .	77
2.6 High excitation power density pulsed PL spectra from the as-grown MBE and MOCVD samples. . . . .	79
2.7 Optical confinement of TE modes for samples D678 and C1081. . . . .	79
2.8 Calculated band structure and squared electron and hole wave functions for samples D559 and C1021D. . . . .	81
2.9 Side-view SEM images of microdisks. . . . .	82
2.10 Q factor over energy in literature. . . . .	83
2.11 Pulsed optically pumped lasing spectra of microdisks on C1081. . . . .	85

2.12	Analysis of the lasing spectra of C1081. . . . .	86
2.13	(a) Calculation of $n$ over $P$ for different values of $U\eta_{inj}$ using Eqs. 2.1 and 2.5, and indicating the values of $n_{tr}$ and $n_{th}$ . (b) Calculation of $P_{th}$ over $g\Gamma Q$ for different values of $U\eta_{inj}$ using Eqs. 2.1, 2.2, 2.3, and 2.5. . . . .	88
2.14	SEM images of the four pieces of C1021D after AZ400K treatment. . . . .	93
2.15	Schematic of a $3\mu\text{m}$ diameter disk with truncated edges and depicting the $H_z$ field of a first order radial mode. . . . .	93
2.16	SEM image of an $8\mu\text{m}$ diameter disk on a different piece of C1021D. . . . .	94
2.17	SEM images of $5\mu\text{m}$ diameter disks on C1080 with and without chemical treatment. . . . .	95
2.18	Lasing threshold as a function of underetch depth for sample C1080. . . . .	96
2.19	Lasing threshold as a function of relative peak PL intensity. . . . .	97
2.20	Lasing threshold as a function of overlap with the $\text{TE}_0$ mode. . . . .	97
3.1	Sketches of different monolithic integration schemes. . . . .	102
3.2	Critical coupling in passive photonic circuits in literature. . . . .	104
3.3	Sketch of the microdisk and waveguide coupling region. . . . .	105
3.4	FDTD simulations of critical coupling. . . . .	106
3.5	Simulation of the $H_z$ field of a $d = 3\mu\text{m}$ diameter disk for a first-order radial mode with azimuthal order $m = 48$ . . . . .	107
3.6	FDTD simulations of the $H_z$ field for devices with $d = 5\mu\text{m}$ diameter and different gap sizes. . . . .	107
3.7	Influence on the waveguide height on coupling. . . . .	108
3.8	FDTD simulations of the $E_y$ field of grating couplers with different periods. . . . .	109
3.9	Sketch of fabrication process of a microdisk and suspended waveguide. . . . .	109
3.10	SEM image of III-nitride photonic circuit fabricated on sample D559. . . . .	110
3.11	Optical microscope images of photonic circuits fabricated on sample D559. . . . .	110
3.12	SEM images of photonic circuits fabricated on sample D677. . . . .	111
3.13	Measurement of gap size. . . . .	112
3.14	Visualization of the spatial distribution of the emission for sample D559. . . . .	113
3.15	Comparison of simulation and measurement for a $3\mu\text{m}$ diameter disk fabricated on sample D559. . . . .	114
3.16	PL spectra measured at the grating coupler for devices with different parameters on sample D559. . . . .	115
3.17	Critical coupling of $5\mu\text{m}$ diameter disks on sample D677. . . . .	117
3.18	Comparison of simulated and experimental spectra for devices on D677. . . . .	118
3.19	Pulsed optically pumped lasing spectra of photonic circuits on sample D559. . . . .	119
3.20	Pulsed optically pumped lasing spectra at the critical coupling gap size for devices on sample D677. . . . .	120
3.21	Pulsed optically pumped lasing spectra for devices with 30 and 55 nm gaps on sample D677. . . . .	121

3.22 Spectra around threshold for a device on sample D677. . . . .	122
3.23 Analysis of lasing threshold as a function of gap and $Q_{load}$ . . . . .	123
3.24 Out-coupled signal over $Q_C$ for devices on D677. . . . .	124
3.25 Maximum output $Q_C$ as a function of $P_{pump}$ . . . . .	125
3.26 Wavelength shift as a function of gap size. . . . .	126
3.27 Simulated mode shift over disk diameter. . . . .	126
3.28 Pulsed optically pumped lasing spectra for different waveguide angles. . . . .	127
4.1 State of the art of UV photonic circuits. . . . .	130
4.2 State of the art of III-nitride PhCs in the blue/UV. . . . .	131
4.3 Heterostructure and FDTD transmission simulations of photonic circuits on sample C1159D. . . . .	133
4.4 2D FDTD simulations of the $E_y$ field of fully etched grating couplers on sample C1159D. . . . .	133
4.5 Optical microscope and SEM images of photonic circuits fabricated on sample C1159D. . . . .	134
4.6 Low-excitation power density CW and pulsed spectra below and above threshold measured at the out-coupling grating of devices on C1159D. . . . .	136
4.7 FDTD simulation of $H_z^2$ of 3 $\mu$ m disk on sample C1159D. . . . .	137
4.8 Band diagram and electron and hole wave functions of the QWs of sample C1159D. . . . .	138
4.9 2D CCD maps of the device with 50 nm gap at different pump powers. . . . .	139
4.10 Energy dependent pulsed optical pumping spectra of devices on C1159D with 50 and 90 nm gap measured above the disk and the grating. . . . .	140
4.11 Integrated peak intensity over pulse energy for different modes for the 90 nm gap and threshold over gap size. . . . .	141
4.12 Sketch of the heterostructure of sample A2083 and SEM images of fabricated 2D PhC slabs. . . . .	142
4.13 $\mu$ -PL spectra of H2 cavities on sample A2083. . . . .	142
4.14 Spectra, Q factor and FDTD mode profile of L3 cavities on sample A2083. . . . .	143
4.15 Measured and calculated Q factors for different cavities over wavelength. . . . .	144
4.16 Spectroscopic ellipsometry measurement and model for different angles. . . . .	145
5.1 III-nitride microdisk lasers in literature. . . . .	151
5.2 Schematic of the process flow of a III-nitride on Si microdisk under electrical injection. . . . .	152
5.3 Schematic of the full device and a zoom-in into the microdisk and microbridge, showing the bridge holder layer. . . . .	153
5.4 Heterostructure of C404 and SEM images of microdisks. . . . .	154
5.5 EL of sample C404. . . . .	154

5.6	Top-view and side-view of test devices with a p-contact and without and with a mesa. . . . .	155
5.7	Process flow of microrings for electrical injection. . . . .	157
5.8	Heterostructure of and SEM images of devices fabricated on C522. . . . .	158
5.9	Simulated modal confinement and band structure of C522. . . . .	159
5.10	JV curves of a microring and a lateral LED on C522. . . . .	160
5.11	EL of microrings on sample C522. . . . .	161
5.12	White microring-LEDs on C522. . . . .	162
5.13	Microring under electrical injection with bus waveguide side coupling. . . . .	163
5.14	Heterostructure and optical confinement of C1162D. . . . .	165
6.1	Transparency ranges of different materials that can be used for photonic circuits. . . . .	168
6.2	State of the art of non-linear optics in the NIR using AlN on sapphire. . . . .	169
6.3	Sketches of the structure of samples A2390 before and after bonding and substrate removal. . . . .	170
6.4	Images of a sample after bonding and substrate removal. . . . .	170
6.5	Transverse profiles of the $ H_z $ field of the $TE_{00}$ mode for waveguides on sample A2390 at $\lambda = 1550\text{ nm}$ and $\lambda = 780\text{ nm}$ . . . . .	171
6.6	3D FDTD simulations around 1550 nm of an 8 $\mu\text{m}$ diameter disk coupled to a straight waveguide with a waveguide width of 500 nm and a gap of 200 nm for different III-nitride thicknesses on $\text{SiO}_2$ . . . . .	172
6.7	VarFDTD transmission simulations of 20 $\mu\text{m}$ diameter microrings with 800 nm ring width, 420 nm waveguide width, and a 90° angle of the waveguide around the ring for gaps of 120 nm and 170 nm for sample A2390. . . . .	172
6.8	3D FDTD simulations of 8 $\mu\text{m}$ diameter disks with 370 nm waveguide width, and $\theta = 90^\circ$ for gaps of 140 nm to 180 nm for sample A2390. . . . .	174
6.9	2D FDTD simulations of the $E_y$ field of a waveguide with grating coupler for sample A2390 at 780 nm with different grating periods. . . . .	175
6.10	Optical microscope and SEM images of passive microring photonic circuits fabricated on A2390. . . . .	176
6.11	Optical microscope and SEM images of passive microdisk photonic circuits fabricated on A2390. . . . .	176
6.12	Heterostructure and AFM image of A2587. . . . .	177
6.13	Calculation of the $ H_z $ field of the $TE_0$ mode in 1 dimension (slab waveguide) for 1550 nm and 780 nm for A2587 suspended in air. . . . .	178
6.14	FDTD simulations of 8 $\mu\text{m}$ diameter disks with 390 nm waveguide width, and straight waveguides for gaps of 140 nm to 180 nm for sample A2587. . . . .	179
6.15	2D FDTD simulations of the $E_y$ field of a waveguide with grating coupler for sample A2587 at 780 nm with different grating periods. . . . .	180
6.16	SEM images of suspended passive photonic circuits fabricated on A2587. . . . .	181

---

6.17 SEM images of partially and fully broken nanotethers on sample A2587. . . . .	181
6.18 SEM images of microdisk with a partially fallen waveguide and a fallen grating coupler. . . . .	181
6.19 Structure of sample A2610 and effective refractive index over microring width and wavelength. . . . .	183
6.20 CAD layout of the varFDTD simulation . . . . .	184
6.21 VarFDTD transmission spectra of a 20 $\mu$ m diameter ring with $WR = 1050$ nm and $WG = 900$ nm and different gaps for sample A2610 around $\lambda = 1560$ nm. . . . .	184
6.22 VarFDTD transmission spectra of a 20 $\mu$ m diameter ring with $WR = 1050$ nm, $WG = 300$ nm, $\theta = 90^\circ$ , and gaps of 170 nm to 210 nm for sample A2610 around $\lambda = 780$ nm.	185
6.23 Phase-matching as a function of ring width for A2610. . . . .	186
6.24 Mask for a microring for parametric frequency conversion. . . . .	187

# List of Tables

1.1	Summary of the lattice constants and spontaneous and piezoelectric polarization of GaN, AlN, and InN. . . . .	9
1.2	$\Delta_{so}$ and $\Delta_{cr}$ for wurtzite AlN, GaN, and InN. . . . .	12
1.3	Parameters of the Sellmeier equation for AlN and GaN. . . . .	14
1.4	Material parameters of hetero- and homoepitaxial substrates. . . . .	15
1.5	Parameters of two 2D waveguides. . . . .	26
1.6	Parameters for a grating coupler at $\lambda = 780$ nm for sample A2587, giving the angles for different periods. . . . .	48
2.1	Summary of various parameters of the samples studied. . . . .	76
2.2	Summary of thickness, number of QWs, and overlap of the TE <sub>0</sub> , TE <sub>1</sub> , and TE <sub>2</sub> modes with the QWs. . . . .	80
2.3	Summary of transition energies and oscillator strengths of D559 and C1021D. . . . .	81
2.4	Q factors of some of our samples and compared to literature. . . . .	83
2.5	Summary of pulsed optically pumped lasing of the investigated samples. . . . .	84
2.6	Summary of parameters to determine the penetration depth and the threshold carrier density. . . . .	90
2.7	Summary of the AZ400K treatment with sample number, piece number, chemical treatment time, and threshold peak power density. . . . .	95
6.1	Coupling parameters of first-order radial modes of microrings and microdisks on samples A2390 and A2587. . . . .	173



# List of Abbreviations

- **AFM:** atomic force microscopy
- **AlGaN:** aluminum gallium nitride
- **AlN:** aluminum nitride
- **BOE:** buffered oxide etchant
- **CCD:** charge coupled device
- **CW:** continuous-wave
- **EL:** electroluminescence
- **FDTD:** finite-difference time-domain
- **FSR:** free spectral range
- **FWHM:** full width at half maximum
- **ICP:** inductively coupled plasma
- **InAlN:** indium aluminum nitride
- **InGaN:** indium gallium nitride
- **InN:** indium nitride
- **LED:** light emitting diode
- **MBE:** molecular beam epitaxy
- **MOCVD:** metal organic chemical vapor deposition
- **NIR:** near-infrared
- **OPO:** optical parametric oscillator
- **PECVD:** plasma-enhanced chemical vapor deposition

- **PhC**: photonic crystal
- **PL**: photoluminescence
- **Q factor**: quality factor
- **QCSE**: quantum confined Stark effect
- **QD**: quantum dot
- **QW**: quantum well
- **RIE**: reactive ion etching
- **RT**: room temperature
- **SAG**: selective area growth
- **SEM**: scanning electron microscope
- **SHG**: second-harmonic generation
- **Si**: silicon
- **TDD**: threading dislocation density
- **TE**: transverse electric
- **TM**: transverse magnetic
- **UV**: ultraviolet
- **VIS**: visible
- **WGM**: whispering-gallery mode

# Introduction

**T**HREE DECADES have passed since the seminal work by Isamu Akasaki, Hiroshi Amano, and Shuji Nakamura on the growth and p-doping of gallium nitride (GaN) [1–5], which has led to efficient blue and white light emitting diodes (LEDs) and a revolution in solid-state lighting. Their work was awarded with the Nobel prize in physics in 2014.

The III-nitride material system is extremely versatile. It provides active emitters from the deep-ultraviolet (UV) to the visible (VIS) spectral range due to its widely tunable direct band gap. III-nitrides can be n- and p-doped, which allows for electrical injection and opens up electronic and optoelectronic applications. Blue, green, and white LEDs for general lighting and displays are commercially available. Blue laser diodes are used in blu-ray disc readers. Efficient III-nitride transistors are also commercially available and are being used, for example, in automotive, IT, and consumer applications.

Over the past 15 years, the domain of III-nitride micro- and nanocavity photonics has become a field of significant interest [6], opening up a wide variety of potential applications [7]. Aluminum nitride (AlN) and GaN are transparent from the near-infrared (NIR) to the UV, which enables low-loss optical waveguiding, a prerequisite for photonic circuits [8–10]. III-nitrides have a large exciton binding energy, which allows for on-chip single photon emission at room-temperature (RT) [11], opening up the domain of quantum optics. Quantum sensing [12, 13] and the optical manipulation of ion-trapped qubits in the UV [14] can also be envisioned. On-chip applications in the field of non-linear optics are equally feasible due to rather large second and third order non-linearities. The emission of entangled photon pairs in the NIR through parametric down-conversion [15], frequency combs [16, 17], and optical parametric oscillators (OPOs) [18, 19] have already been demonstrated. Visible-light communication, light fidelity (Li-Fi) communication, and telecommunication using photonic integrated circuits are also possible [20, 21]. Additionally, III-nitrides are bio-compatible, which enables lab-on-chip bio-photonics and bio-sensing applications [22–24].

This thesis seeks to demonstrate the viability of the III-nitride on silicon platform for next generation photonic integrated circuits operating in the UV to NIR spectral range with active and passive components under optical pumping or electrical injection. We aim to combine active microlasers with passive photonic circuits and to expand the passive photonic circuits to novel platforms, i.e. III-nitrides bonded on SiO<sub>2</sub>. Furthermore, we aim to inject our active

devices electrically, working towards electrically injected microlaser photonic circuits.

More conventional integrated photonics platforms include silica suspended on silicon ( $\text{SiO}_2/\text{Si}$ ), silicon on insulator (SOI), lithium niobate on insulator (LNOI), and indium phosphide (InP) [25]. These platforms have some disadvantages as compared to III-nitrides.  $\text{SiO}_2/\text{Si}$ , SOI, and LNOI are lacking (efficient) integrated active laser emitters. InP has native lasers but is limited to the NIR spectral range [26]. In the NIR, SOI and InP have the disadvantage of two-photon absorption [27, 28] due to their small band gaps, which is not observed in III-nitrides. III-nitride photonic circuits have the additional advantage of possible co-integration with III-nitride electronics, thus offering a complete toolbox for designers. III-nitrides on Si also offer a path for the integration with standard complementary metal oxide semiconductor (CMOS) platforms.

High crystal quality III-nitride layers can be grown epitaxially by molecular beam epitaxy (MBE) or metal organic chemical vapor deposition (MOCVD) on various substrates, including bulk AlN and GaN as well as sapphire, silicon carbide (SiC), and Si. For photonic cavities and photonic circuits, heteroepitaxy on a foreign substrate with small refractive index or with large etch selectivity is needed to confine light in the vertical direction. The material can also be bonded to a carrier wafer, such as  $\text{SiO}_2$  on Si, for subsequent substrate removal. This works particularly well for sapphire and Si substrates using laser lift-off and dry etching, respectively. AlN can also be sputter-deposited on insulator for use in passive devices [8, 29]. In order to fabricate active devices, the material needs to be grown epitaxially to allow for the monolithic integration of quantum wells (QWs) or quantum dots (QDs), which confine charge carriers in one or three dimensions, allowing for efficient light emission.

Active III-nitride micro- and nano-resonators and lasers have been reported in the UV-VIS spectral range by various groups [30–37]. Figs. 1 (a) and (b) show an active microdisk resonator with quality (Q) factor of  $1 \times 10^4$ , achieved through passivation in oxygen in Grandjean's group at EPFL [36], showing the importance of controlling optically active surface states to achieve high-Q microcavities. Passive photonic circuits have been demonstrated in the NIR around  $\lambda = 1.55 \mu\text{m}$  using microrings coupled to waveguides [18, 29, 38, 39]. Fig. 1 (c) shows a scanning electron microscope (SEM) image of microrings and (d) a transmission measurement showing a loaded Q factor of  $6 \times 10^5$  from Tang's group at Yale [18]. Photonic circuits in the UV-VIS spectral range with Q factors up to  $4 \times 10^5$  have also been demonstrated recently [9, 10, 29, 40–42]. Fig. 1 (e)-(g) show a microring coupled to a waveguide and transmission spectra in the UVA and blue spectral range showing loaded Q factors of  $1 \times 10^5$  from Tang's group [42]. Furthermore, electrically injected lasing in the blue and UVA has been demonstrated in thick sandwich-type microdisks with thresholds of  $I_{th} = 9 \text{ kA} \cdot \text{cm}^{-2}$  in Yang's group at the Chinese Academy of Sciences [43–45].

In our collaboration, which consists of researchers from four French research labs (C2N, CRHEA, IRIG, L2C), we focus on the III-nitride on Si platform. One advantage of this platform is the very high etch selectivity of Si as compared to III-nitrides, which provides a large refractive index contrast to air. Before this thesis, our collaboration worked on individual micro- and

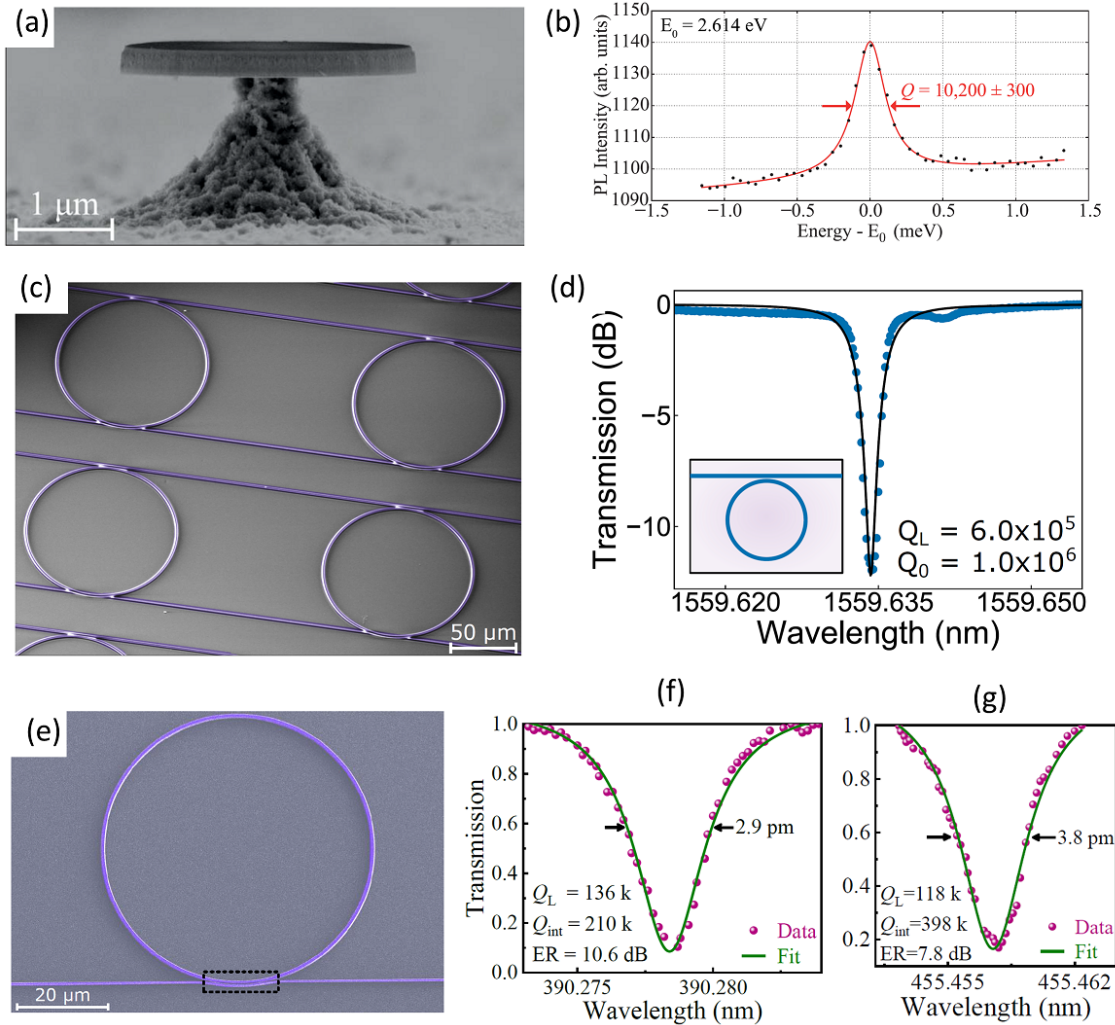


Figure 1: State of the art of III-nitride photonic devices from the UVC to the NIR. (a) SEM image and (b) PL spectrum showing  $Q = 1 \times 10^4$  of a microdisk in the blue (reproduced from Ref. [36]). (c) SEM image and (d) transmission spectrum of a microring photonic circuit in the NIR showing loaded Q factors of  $6 \times 10^5$ , reproduced from Ref. [18]. (e) false-color SEM image and transmission spectral in (f) the UVA and in (g) the blue spectral range showing loaded Q factors of  $1 \times 10^5$  (reproduced from Ref. [42]).

nano-resonators and lasers in the UV-VIS spectral range [46–50], as well as passive photonic circuits in the NIR [51, 52], where they also demonstrated non-linear effects like second and third harmonic generation (SHG and THG) [53–55]. In Fig. 2 (a) we show photoluminescence (PL) spectra of microdisk lasers from the UVC to the green spectral range [50]. Figs. 2 (b) and (c) show a microdisk coupled to a waveguide and transmission spectra with  $Q = 8 \times 10^4$  [52]. The previous theses from our collaboration have dealt with the growth and study of QD containing photonic cavities grown by MBE (S. Sergent 2010) [56], the optical study of III-nitride microcavities, including microdisk resonators and lasers and photonic crystal waveguides (D. Sam-Giao 2012 and J. Selles 2015) [57, 58], and the design, fabrication, and spectroscopy of III-

nitride photonic circuits in the NIR, including SHG and THG (Y. Zeng 2017) [59]. This thesis is based on the prior work of our collaboration.

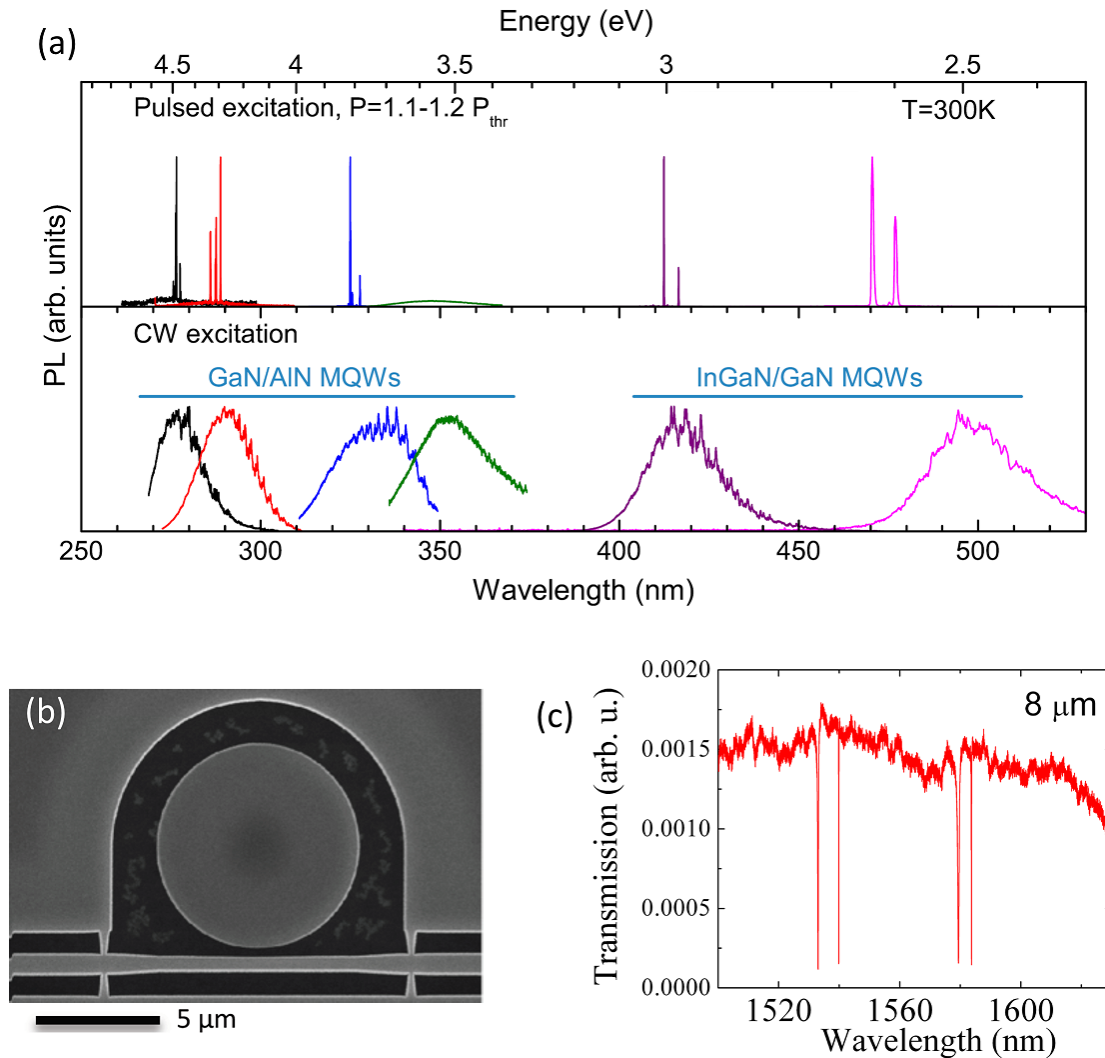


Figure 2: III-nitride photonic devices from the UVC to the NIR from our collaboration before this thesis. (a) Microdisk lasers from the UVC to green spectral range (reproduced from Ref. [50]). (b) SEM image and (c) transmission spectrum of a microdisk photonic circuit in the NIR showing  $Q = 8 \times 10^4$  (reproduced from Ref. [52]).

In this thesis, we design, fabricate, and characterize active and passive photonic cavities operating in the UVA, blue, and NIR spectral ranges using thin epilayers of III-nitrides on Si. We assemble the different building blocks necessary for more complex integrated photonic circuits in this young and versatile photonic platform. We start with individual microdisk lasers in the blue and UVA and then integrate them monolithically into photonic circuits, first in the blue than in the UVA. In the UVA, we also investigate 2D photonic crystal (PhC) slab cavities. We then study the electrical injection in thin microdisks and microrings with the goal of achieving microlaser photonic circuits operating under electrical injection. Finally, we study passive

devices with a focus on III-nitrides bonded on SiO<sub>2</sub> in the NIR spectral range. All our devices operate at room temperature (RT). This work provides a foundation for more advanced integrated photonic circuits using III-nitrides on Si and on SiO<sub>2</sub> to achieve active photonic circuits under electrical injection, as well as non-linear effects in the NIR, such as OPOs or frequency combs.

In chapter 1, we discuss the III-nitride on silicon material and the different types of photonic devices that make up our integrated photonic circuits. We start by giving the relevant basic material properties of III-nitrides. Then we discuss the choice of substrate, the growth and its challenges. We discuss the slab and ridge waveguide, the microdisk resonator, the evanescent coupling between a microdisk and a bus waveguide, the microlaser, the PhC cavity, and the grating coupler. Subsequently, we elaborate on the cleanroom fabrication processes, including their challenges. Lastly, we give an overview of the different spectroscopic setups used to characterize our devices in the different wavelength ranges.

Chapter 2 discusses experimental results obtained on individual microdisk lasers grown by MBE and MOCVD. We report on low threshold peak power densities of  $18 \text{ kW} \cdot \text{cm}^{-2}$  or pulse energies of  $0.07 \text{ mJ} \cdot \text{cm}^{-2}$  under pulsed optical pumping conditions. We also calculate the threshold using a rate equation model which is in good agreement with the experimental result. We study the influence of various parameters including the growth method, the dislocation density, the mode overlap with the QWs, and a chemical treatment on the lasing threshold.

In chapter 3, we discuss active microdisk photonic circuits in the blue spectral range. We demonstrate for the first time lasing in the blue in a microdisk evanescently coupled to a bus waveguide with extraction of the emission at an out-coupling grating. Furthermore, we demonstrate critical coupling in such an active microdisk photonic circuit for very small gaps of  $g = 45 \text{ nm}$  and narrow waveguides ( $w = 170 \text{ nm}$ ) and study the threshold dependence on the gap and the loaded Q factor, as well as the output signal as a function of coupling. This is the shortest wavelength demonstration of critical coupling.

Chapter 4 discusses active microdisk photonic circuits as well as active 2D PhC slabs in the UVA. We demonstrate for the first time a UV microlaser monolithically integrated into a photonic circuit. We achieve low thresholds of  $35 \text{ kW/cm}^2$  or  $0.14 \text{ mJ/cm}^2$  at  $\lambda = 379 \text{ nm}$  and Q factors of 3500 under continuous-wave (CW) excitation. For the PhCs, we observe  $Q = 1085$  at  $\lambda = 337 \text{ nm}$  and we propose an explanation for the reduction in Q factor with decreasing wavelength related to the residual absorption in AlN grown on Si.

In chapter 5, we investigate electrical injection in active microdisks and microrings in the blue spectral range. We observe electroluminescence (EL) but no lasing. We discuss two different injection schemes, as well as the challenges imposed by thin heterostructures and an insulating buffer layer. Our electrical injection scheme is compatible with integrated photonic circuits. We obtain an output power density of  $440 \text{ mW} \cdot \text{cm}^{-2}$  at  $I = 20 \text{ mA}$  from such microrings with diameters of 30 to 50  $\mu\text{m}$ .

In chapter 6, we discuss passive photonic circuits in the NIR in III-nitrides grown on silicon

and bonded to SiO<sub>2</sub> or suspended in air operating at 780 nm. We design and fabricate microring and microdisk photonic circuits with large theoretical Q factors. These devices have not been characterized optically as of June 2020 due to the Covid-19 pandemic. Furthermore, we investigate the design of a double-resonant microring for phase-matched degenerate parametric down conversion and SHG operating around 780 and 1560 nm, as this is a prerequisite for OPO.

Finally, we give a summary and discuss the perspectives of future work.

This thesis was funded by GaNeX, a French excellence cluster on III-nitrides led by J.-Y. Duboz. The work was performed in the framework of the Agence National de la Recherche (ANR) project Milagan (2018-2021), as well as some preliminary work for the beginning of Opoint (2020-2024). Milagan deals with the electrical injection in blue III-nitride microdisk lasers on silicon. The goal of Opoint is the realization of OPOs using III-nitride microring photonic circuits on SiO<sub>2</sub>. These two very different topics exemplify the versatility of III-nitrides very well. These projects are a collaboration between C2N in Palaiseau, CRHEA in Valbonne, CEA-IRIG in Grenoble, L2C in Montpellier, Inphyni in Nice, and the University of Hong Kong. I spent time at each of these labs and was very closely involved in all steps apart from the growth and the material characterization.

All samples were grown at CRHEA by B. Damilano, F. Semon, S. Rennesson, B. Alloing, and E. Frayssinet. Characterization of the as-grown samples, including atomic force microscopy (AFM) and high excitation power density PL were also performed at CRHEA by B. Damilano, B. Alloing, A. Courville, and S. Rennesson. All processing was performed by myself at C2N, IRIG, Institut Néel, and CRHEA. The blue-UV spectroscopy on fabricated devices was performed at IRIG and L2C, in large parts by myself and in close interaction with B. Gayral, L. Doyennette, C. Brimont, and T. Guillet. The finite-difference time-domain (FDTD) simulations and device design were performed by myself, and were based on prior designs by I. Roland and X. Checoury. P. Boucaud closely supervised the entire project and gave valuable input at every step. In the following chapters, I will clearly point out all data not directly obtained by myself.

# Chapter 1

## Photonic devices using III-nitrides on silicon

**I**N THIS CHAPTER, we introduce the domain of III-nitride on silicon photonics by discussing the material system and the device theory and fabrication. This chapter covers:

- An introduction to the III-nitride material system, its most relevant material properties, and its growth on silicon.
- A theoretical description of the photonic devices used in this thesis, including slab and ridge waveguide, microdisk cavity, microdisk to waveguide coupling, semiconductor laser, 2D photonic crystal slab, and grating coupler.
- The fabrication of mushroom-type microdisks, active and passive photonic circuits, and 2D photonic crystal slabs in III-nitrides on silicon.
- The optical spectroscopy setups used to characterize these devices.

### 1.1 III-nitride semiconductors

The III-nitride material system includes the binary semiconductors gallium nitride (GaN), aluminum nitride (AlN), indium nitride (InN) and their ternary and quaternary alloys. III-nitrides exhibit a direct band gap which can be engineered from 0.7 eV (InN) [60] to 6.02 eV (AlN) [61], making them good candidates for light emitters and lasers in the visible and ultra-violet (UV) spectral range. Furthermore, AlN and GaN are mostly transparent from the infra-red (IR) to the UV spectral range, which opens up the possibility for low-loss and high quality passive photonic components, such as resonators, waveguides, or grating couplers.

### 1.1.1 Crystal structure and polarization fields

The stable crystal structure of III-nitrides is the wurtzite structure with six-fold symmetry (Fig. 1.1), which consists of two close-packed hexagonal sublattices of III-nitride atoms (gray spheres) and nitrogen atoms (red spheres), respectively. The two lattices are shifted along the [0001] or  $c$ -direction by  $u \cdot c$ . Each atom forms a tetrahedron with its nearest neighbors of the other element.

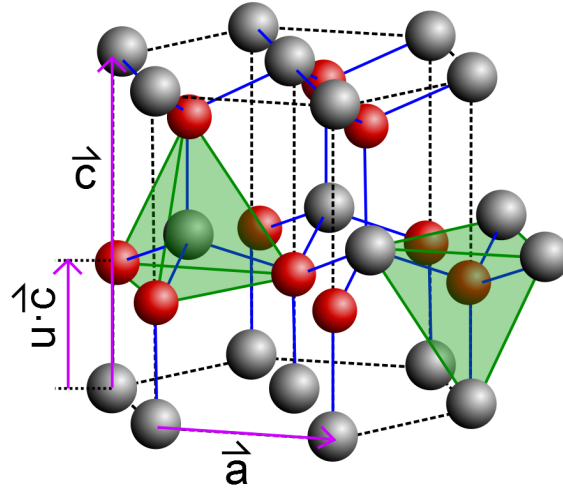


Figure 1.1: A schematic of the wurtzite crystal structure of III-nitrides. Gray spheres represent the group III atoms and red spheres represent the nitrogen atoms. Reproduced from Ref. [62].

The wurtzite structure is non-centrosymmetric, which means that the [0001] and [000-1] directions are not the same. This results in a difference in bond length along the  $c$ -axis as compared to the other three bonds, which shifts the charge distribution and creates a polarization field that is known as spontaneous polarization  $\mathbf{P}_{sp}$  or pyroelectric polarization, as it changes with temperature. The spontaneous polarization coefficients for GaN, AlN, and InN are given in Table 1.1. In the case of GaN, the [0001] direction is called Ga-polar and the [000-1] direction N-polar. The two polarizations behave differently in respect to growth, surface roughness, defect density, and even chemical etching. All our structures are grown Ga-polar. Some structures are bonded to a carrier wafer with subsequent substrate removal. Their surface is then N-polar.

Strain in the heterostructure causes an additional deformation of the bond lengths and consequently a change in the polarization. The resulting additional polarization field is called the piezoelectric polarization  $\mathbf{P}_{pz}$  and is based on the same phenomenon as the spontaneous polarization.  $\mathbf{P}_{pz}$  is related to the strain tensor  $\epsilon$  by [63]

$$P_{pz,i} = \sum_j e_{ij} \epsilon_j, \quad (1.1)$$

where the  $e_{ij}$  are components of the piezoelectric tensor.

The polarization along the [0001] axis is given by

$$P_{pz,3} = e_{33}\epsilon_3 + e_{31}(\epsilon_1 + \epsilon_2), \quad (1.2)$$

with  $\epsilon_3 = (c - c_0)/c_0$  and  $\epsilon_1 = \epsilon_2 = (a - a_0)/a_0$  where  $c_0, a_0$  are the relaxed and  $c, a$  the strained lattice constants. Table 1.1 summarizes the unstrained lattice constants and piezoelectric coefficients of GaN, AlN, and InN.

	GaN	AlN	InN
$a_0$ (Å)	3.189	3.112	3.533
$c_0$ (Å)	5.185	4.982	5.693
$P_{sp}$ (C·m <sup>-2</sup> )	-0.029	-0.081	-0.032
$e_{31}$ (C·m <sup>-2</sup> )	-0.49	-0.60	-0.57
$e_{33}$ (C·m <sup>-2</sup> )	0.73	1.46	0.97

Table 1.1: Summary of the lattice constants and spontaneous and piezoelectric polarization of GaN, AlN, and InN [63].

The total polarization field is  $\mathbf{P}_{tot} = \mathbf{P}_{sp} + \mathbf{P}_{pz}$ . In heterostructures consisting of layers of different materials, the difference in polarization fields causes dipole charges to build up at the interfaces, creating an internal electric field, which causes the energy bands to bend.

To allow for efficient light emission, very thin layers (quantum wells (QWs)) or small islands (quantum dots (QDs)) of a material of smaller band gap (e.g. InGaN) can be inserted into the heterostructure (e.g. GaN), confining carriers in one or three dimensions, respectively [64]. This carrier confinement increases the radiative recombination probability significantly. In this work, we investigate heterostructures with InGaN/GaN and GaN/AlN QWs emitting in the blue to UVA spectral range.

In the case of QWs, the polarization fields cause the quantum confined Stark effect (QCSE). The band bending spatially separates the electron and hole wavefunctions in the QW, which reduces the radiative recombination probability and causes a reduction of the transition energy (red-shift). Sketches of QWs without and with QCSE are depicted in Fig. 1.2, where we can see that the red-shift roughly varies as  $E \cdot d$ , where  $E$  is the electric field and  $d$  the QW thickness. By growing very thin QWs, we can reduce the effect of the QCSE. At high optical excitation power densities, the internal electric field is screened by free carriers and the emission blue shifts.

A crystal can be grown in other directions than the polar c-direction. Non-polar and semi-polar planes have no or a reduced polarization field, which can significantly increase QW efficiency. Some of these planes are indicated in Fig. 1.3 (a), indicating their angle of rotation  $\theta$  in respect to the c-plane. Fig. 1.3 (b) shows the calculated total polarization difference for the interface of an  $\text{In}_x\text{Ga}_{1-x}\text{N}/\text{GaN}$  QW for different In compositions  $x$  and as a function of  $\theta$ . For these  $\text{In}_x\text{Ga}_{1-x}\text{N}/\text{GaN}$  QWs the polarization difference is zero for  $\theta$  around  $50^\circ$  (a semi-polar orientation that depends on the composition) and  $90^\circ$  (non-polar). However, it is much more difficult to grow semi- or non-polar planes and substrates are very small and not readily

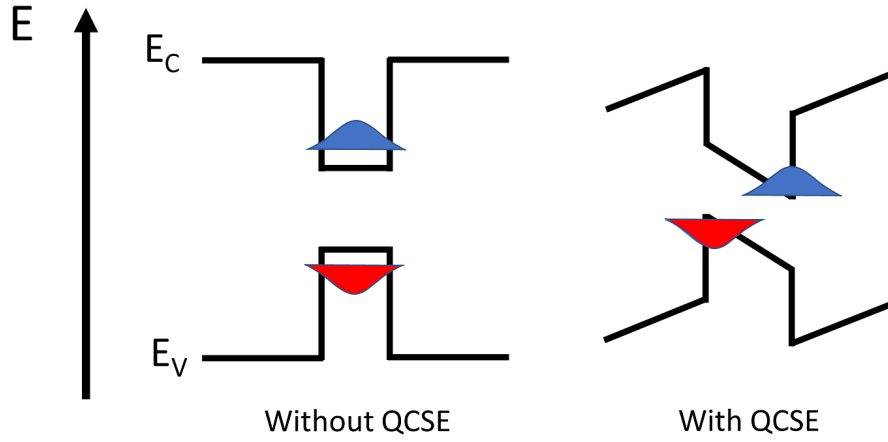


Figure 1.2: Sketch of a QW without (left) and with (right) QCSE. (The potential drop indicated in the schematic is not real).

available.

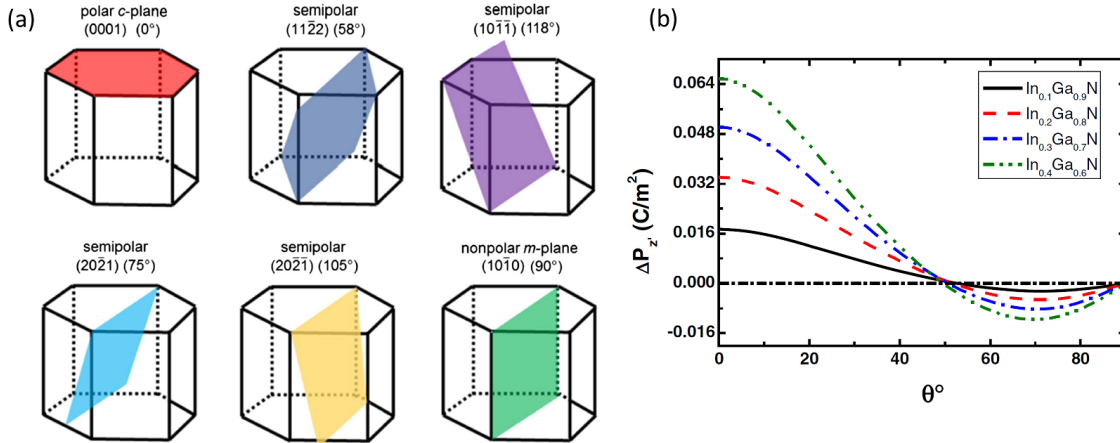


Figure 1.3: (a) Schematic of polar, semi-polar, and non-polar planes in III-nitrides with their rotation from c-plane  $\theta$ , reproduced from Ref. [65]. (b) Calculated total polarization difference at the interface of an  $\text{In}_x\text{Ga}_{1-x}\text{N}/\text{GaN}$  QW as a function of the angle of rotation from c-plane  $\theta$  for different In compositions  $x$ , reproduced from Refs. [66, 67].

### 1.1.2 Band structure

For III-nitrides, the top-most valence band at the  $\Gamma$  point of the first Brillouin zone is split into three, because the degeneracy is lifted due to the spin-orbit interaction  $\Delta_{so}$  and the non-cubic crystal-field splitting  $\Delta_{cr}$ . Fig. 1.4 shows the valence band splitting for AlN, GaN, and InN taking spin-orbit and crystal-field splitting into account for zinc blend and wurtzite structures and Table 1.2 gives values of  $\Delta_{so}$  and  $\Delta_{cr}$  [68]. For AlN  $\Delta_{cr}$  is negative and large, resulting

in the  $\Gamma_{7+}$  band being the top-most valence band (see Fig. 1.4 (a)). For GaN and InN  $\Delta_{cr}$  is positive and the  $\Gamma_9$  band is the top-most valence band (see Figs. 1.4 (b) and (c)). The transitions between the conduction band and the different valence bands have different polarizations. For the  $\Gamma_9$  band the light is  $\sigma$ - or  $xy$ -polarized, while for the  $\Gamma_{7+}$  and  $\Gamma_{7-}$  bands the light is  $\pi$ - ( $z$ ) and  $\sigma$  ( $xy$ ) polarized. In GaN, the top valence band is  $\Gamma_9$  and the emission is polarized along  $xy$  (transverse electric (TE)). In AlN, the top valence band is  $\Gamma_{7+}$  and the emission is mostly polarized along  $z$  (transverse magnetic (TM)). In bulk AlGaIn, the  $\Gamma_{7+}$ - $\Gamma_9$  cross-over induces a polarization switch for an Al content estimated to about 15-40%, depending on authors. In AlGaIn QWs, the situation is more complex, and depends on the strain state. The polarization changes from TE to TM occurs in the UVC spectral range [69]. In this work, we use InGaIn/GaN and GaN/AlN QWs that emit TE-polarized light. This is important to note because it means that we need to design the active photonic circuits for TE-polarization.

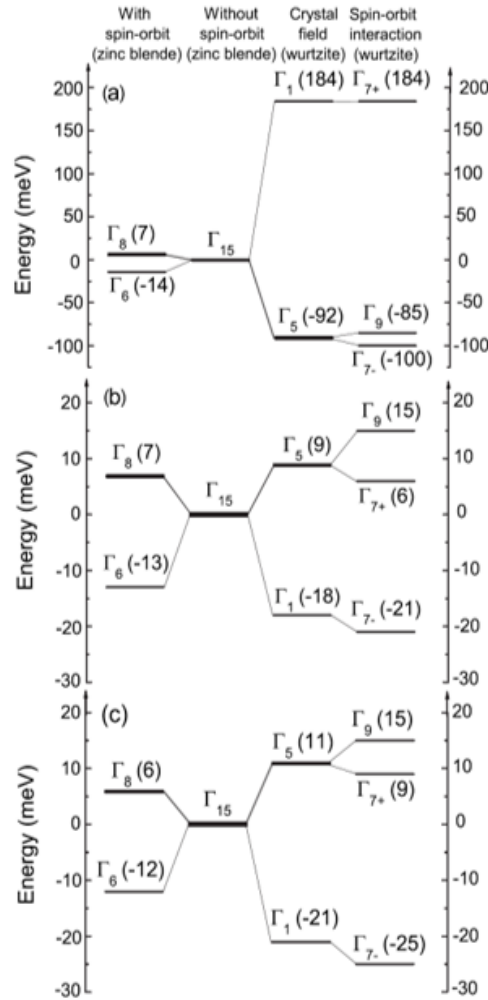


Figure 1.4: Valence band splitting for (a) AlN, (b) GaN, and (c) InN zinc-blend and wurtzite crystal structure due to spin-orbit and crystal-field splitting. Reproduced from Ref. [70].

Fig. 1.5 shows the band gap over the in-plane lattice constant  $a$  for AlN, GaN, and InN. The

	AlN	GaN	InN
$\Delta_{so}$ [meV]	19	17	5
$\Delta_{cr}$ [meV]	-169	10	40

Table 1.2:  $\Delta_{so}$  and  $\Delta_{cr}$  for wurtzite AlN, GaN, and InN, taken from Ref. [68].

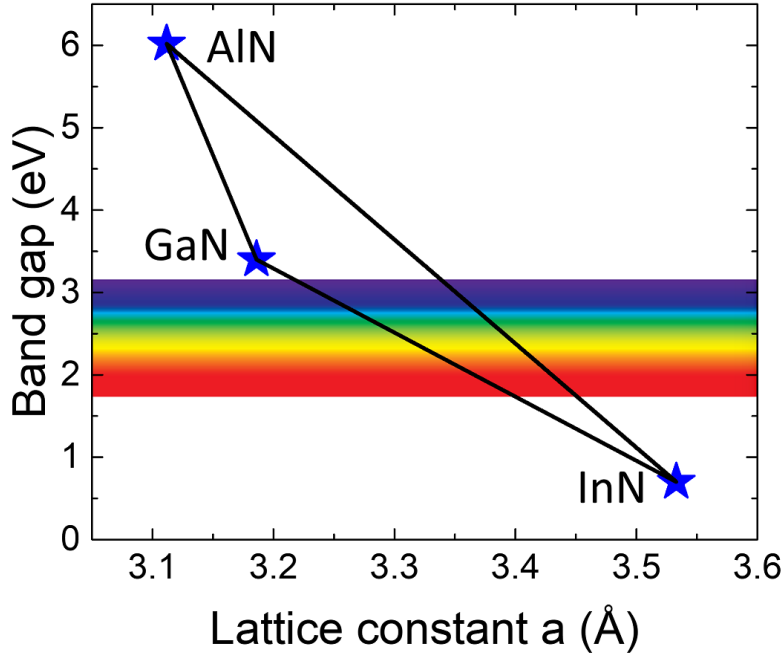


Figure 1.5: Band gap over lattice constant  $a$  for AlN, GaN, and InN. The straight lines represent the possible ternary alloys. We are neglecting the bowing parameters. The visible spectral range is indicated.

ternary alloys are indicated by the straight lines, neglecting the band gap bowing parameters. Visible light emitters can theoretically be attained with InGaN and InAlN, as indicated by the rainbow in Fig. 1.5. InAlN is very difficult to grow due to the large difference in growth temperature between InN and AlN. Very efficient blue LEDs and laser diodes have been realized based on InGaN/GaN QWs. However, for longer wavelengths the efficiency drops significantly and we observe the so-called "green gap". Fig. 1.6 (a) shows the external quantum efficiency (EQE) of III-nitride and phosphide LEDs in the visible spectral range. For III-nitrides, the EQE decreases with increasing wavelength, achieving only about 40% in the green and only a few percent in the red spectral range. This efficiency droop is not fully understood yet, but may be related to point and extended defects related to the growth of InGaN, as well as a larger Auger-like effect as compared to GaN, and piezoelectric polarization [71–73]. UV emitters can be obtained with low In-content InGaN/GaN, GaN/AlN, or  $\text{Al}_x\text{Ga}_{1-x}\text{N}/\text{Al}_y\text{Ga}_{1-y}\text{N}$  with  $y > x$  QWs. Fig. 1.6 (b) shows the EQE for UV LEDs, which decreases with decreasing wavelengths. This decrease is due to the less developed AlGaN material, including difficulties in doping of high Al-content

AlGaN.

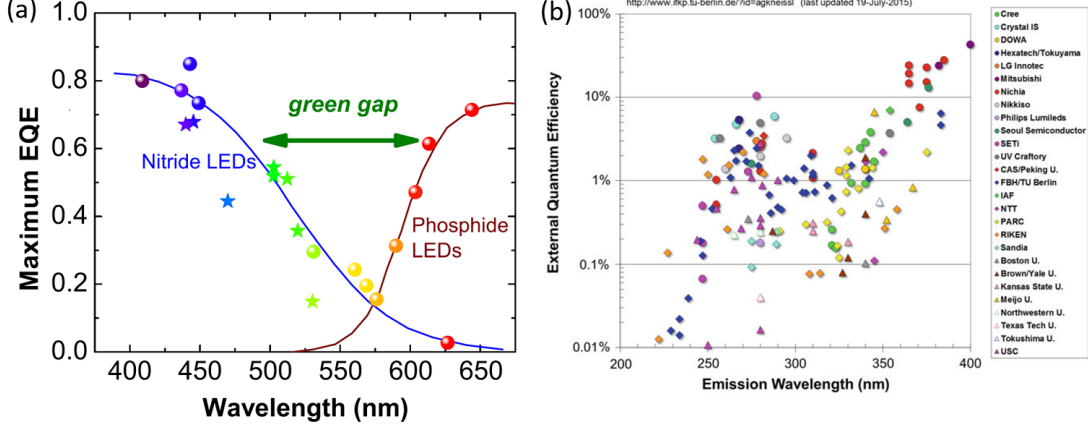


Figure 1.6: (a) EQE of III-nitride and phosphide commercial LEDs showing the "green gap". Reproduced from Ref. [74]. (b) EQE of UV LEDs, reproduced from Ref. [75].

### 1.1.3 Refractive index

III-nitrides show a uniaxial birefringence, which means that the refractive index depends on the propagation direction. A c-plane crystal has ordinary refractive index ( $n_o$ ) in the layer plane ( $n_x = n_y = n_o$ ) and extraordinary refractive index ( $n_e$ ) out-of-plane ( $n_z = n_e$ ). For propagation in  $z$ , there is no birefringence, while for propagation in the layer plane (i.e.  $x$ ) there is a birefringence between the polarization in  $z$  and the in-plane polarization (i.e.  $y$ ). In this thesis, the propagation direction is usually in-plane and we consequently have birefringence.

The chromatic dispersion of the refractive indices can be determined using planar waveguides and the prism coupling method [76, 77]. The experimental data can be fitted by Sellmeier equations of the form:

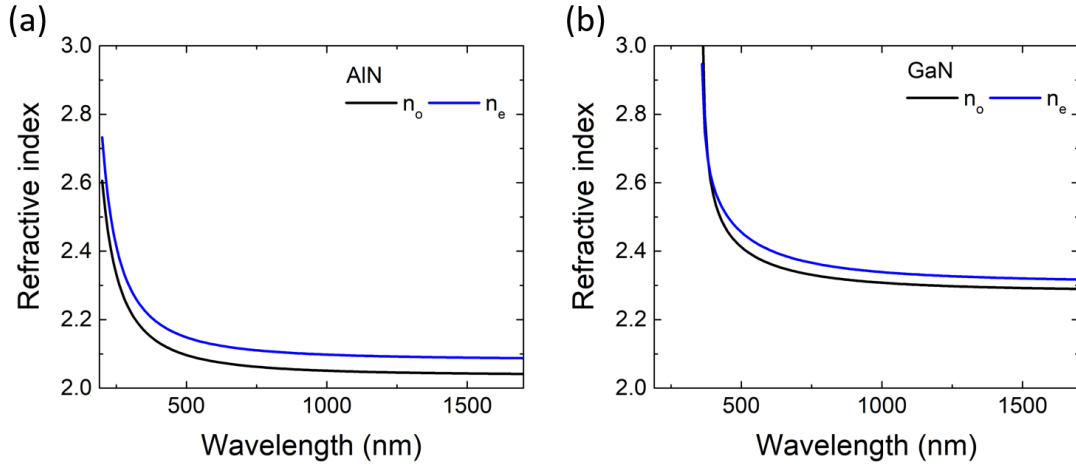
$$n_o(\lambda) = \sqrt{1 + \frac{A_o \lambda^2}{\lambda^2 - \lambda_{o,1}^2} + \frac{B_o \lambda^2}{\lambda^2 - \lambda_{o,2}^2}}, \quad (1.3)$$

$$n_e(\lambda) = \sqrt{1 + \frac{A_e \lambda^2}{\lambda^2 - \lambda_{e,1}^2} + \frac{B_e \lambda^2}{\lambda^2 - \lambda_{e,2}^2}}, \quad (1.4)$$

where  $A_o$ ,  $A_e$ ,  $B_o$ ,  $B_e$ ,  $\lambda_{o,1}$ ,  $\lambda_{e,1}$ ,  $\lambda_{o,2}$ , and  $\lambda_{e,2}$  are constants determined by the fit, which are given in Table 1.3 for AlN [76] and GaN [77]. The measurements for the refractive indices of GaN were performed on samples grown at CRHEA on sapphire [77]. The dispersion curves are depicted in Fig. 1.7. These values are used throughout this thesis for the simulations and device design.

	$A_o$	$A_e$	$B_o$	$B_e$	$\lambda_{o,1}$ [ $\mu\text{m}$ ]	$\lambda_{e,1}$ [ $\mu\text{m}$ ]	$\lambda_{o,2}$ [ $\mu\text{m}$ ]	$\lambda_{e,2}$ [ $\mu\text{m}$ ]
AlN	3.148	0.139	0	0	0.135	0.139	0	0
GaN	0.213	0.118	3.988	4.201	0.350	0.350	0.153	0.177

Table 1.3: Parameters of the Sellmeier equation for AlN [76] and GaN [77].

Figure 1.7: Refractive indices  $n_o$  and  $n_e$  of AlN and GaN [76, 77].

### 1.1.4 Defect luminescence in GaN and AlN

III-nitrides are not perfectly transparent at all energies below their band gaps. Point defects in III-nitrides, such as vacancies and impurities can cause unwanted luminescence or absorption bands. GaN films show a yellow luminescence band centered around 2.2 - 2.3 eV (540-564 nm) and AlN films show a 1 eV broad UV luminescence band centered at 3.2 eV (390 nm) [78–81]. Furthermore, impurities can cause donor-acceptor or conduction-band-acceptor complexes for energies slightly below the band gap that can result in undesired absorption and losses in III-nitride waveguides.

### 1.1.5 Choice of substrate

In epitaxy, the growing material adopts the in-plane lattice constant  $a$  of the substrate, resulting in tensile or compressive strain in the structure in the case of hetero-epitaxy. However, for a lattice mismatch larger than 1 or 2%, dislocations are created at the interface and the material adopts its intrinsic lattice constant with residual strain. The choice of substrate is thus very important.

Possible substrates for III-nitrides are bulk AlN and GaN, sapphire ( $\text{Al}_2\text{O}_3$ ), silicon carbide (SiC), and silicon. Growing III-nitrides homo-epitaxially on bulk substrates can yield very high material quality and is essential for some applications, such as UV laser diodes. However, the

cost of these bulk substrates is still very high and their dimensions still rather small (1-2 inches), and especially in the case of AlN, impurities in the substrate can cause unwanted absorption in the deep-UV spectral range [82]. To reduce the cost and thus make III-nitrides more accessible for real-world consumer applications, hetero-epitaxy on sapphire, SiC, or silicon is widely used. The material parameters of hetero- and homo-epitaxial substrates are summarized in Table 1.4.

	Si (111)	Al <sub>2</sub> O <sub>3</sub>	SiC	AlN	GaN
<i>a</i> lattice constant [Å]	3.840	4.765	3.073	3.113	3.188
<i>c</i> lattice constant [Å]	3.136	12.982	15.117	4.982	5.185
Lattice mismatch with AlN [%]	-19	-13.3	1.3	0	2.2
Lattice mismatch with GaN [%]	-17.1	-16.1	3.5	2.2	0
Thermal expansion coefficient at RT [ $10^{-6} \text{ K}^{-1}$ ]	2.6	7.5	4.2	4.2	5.6
Thermal mismatch with AlN [%]	62	-44	0	0	-33
Thermal mismatch with GaN [%]	116	-25	33	33	0

Table 1.4: Material parameters of hetero- and homoepitaxial substrates, taken from Ref. [83]. The lattice mismatch to sapphire takes a 30° rotation into account.

In this work, our substrate of choice is silicon (111). This choice can be motivated by the low cost and ready availability of large substrates (up to 12 inches). It allows for the potential monolithic integration of III-nitrides into the well-established silicon photonics platform, extending it to the visible and UV spectral range. Furthermore, it is possible to highly selectively underetch silicon, which allows for thin suspended photonic circuits. Such suspension is much more challenging with other substrates due to significantly lower etch selectivity.

### 1.1.6 III-nitride growth on silicon

III-nitride thin films can be grown epitaxially by molecular beam epitaxy (MBE) and metal organic chemical vapor deposition (MOCVD).

MBE requires ultra-high vacuum and uses solid sources for the group III elements that are heated until they sublime, forming a beam of atoms that is directed towards the substrate. A gas or plasma source can be used as the nitrogen source. The group III elements react with nitrogen on the surface of the heated substrate to form epitaxial III-nitride films. All samples investigated in this thesis that were grown by MBE use ammonia (NH<sub>3</sub>) as the nitrogen source.

MOCVD uses metal organic sources for the group III elements, namely trimethyl aluminum (TMAl), trimethyl gallium (TMGa), and trimethyl indium (TMIn) and NH<sub>3</sub> as the nitrogen source. The metal organics are stored in liquid form and are diluted in a carrier gas, H<sub>2</sub> or N<sub>2</sub>. The substrate is heated and the metal organics and NH<sub>3</sub> enter the reactor through a shower-head system and are thermally decomposed on the substrate surface where they react to form epitaxial films of III-nitrides.

Review articles about III-nitride growth can be found in Neumayer and Ekerdt [84] and Ambacher [85]. Samples grown by either MBE or MOCVD or a hybrid combination of both meth-

ods are investigated in this thesis. When growing GaN on Si, an AlN buffer layer is required, as Ga atoms react very strongly with Si causing meltback etching. Achieving a high material quality with thin layers on silicon is challenging. The biggest challenges are the large lattice and thermal mismatch (see Table 1.4) and the meltback etching.

### 1.1.6.1 Lattice mismatch

The lattice mismatch of AlN on Si (111) is  $-19\%$ , which is comparable to AlN on sapphire (see Table 1.4). This mismatch results in a high density of misfit dislocations at the AlN/Si interface. Small AlN nuclei are formed with a high twist and tilt to each other. When these nuclei coalesce, grain boundaries are created. The relative tilt and twist of these grains is illustrated schematically in Fig. 1.8.

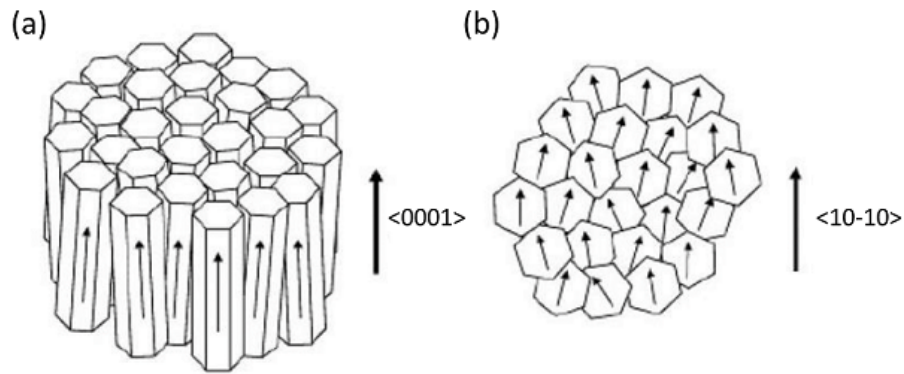


Figure 1.8: Sketch of (a) the tilt and (b) the twist of AlN grains grown on Si, reproduced from Ref. [56].

Threading dislocations are formed at the grain boundaries. The threading dislocation densities (TDD) in thin layers of III-nitrides on silicon is usually in the order of  $10^9$  to  $10^{10} \text{ cm}^{-2}$  [86, 87].

Using a 3D growth mode during the buffer layer growth could reduce the TDD, however, it implies growth of thicker layers as the 3D islands need to coalesce.

### 1.1.6.2 Thermal mismatch

The large difference in thermal expansion coefficient of 116% between GaN and silicon results in tensile strain upon cool-down of the grown sample from around  $1000^\circ\text{C}$  to RT. This can result in cracking of the grown layers. Buffer layer strain engineering can be employed to mitigate the stress and prevent cracking. One such technique is to use thin AlN interlayers when growing GaN.

Growth on mesa patterned templates can also be used to reduce the tensile stress in the GaN layers [88, 89], however, this approach is difficult to implement for larger photonic circuits.

Our colleagues at CRHEA use either MOCVD or MBE to grow the AlN buffer layer on silicon.

When growing by MOCVD, a minimum thickness of around 200 nm of AlN is required for a good material quality [90]. By MBE thinner layers (i.e. 40 nm) can be realized [91, 92]. For some devices, e.g. vertical mono-mode waveguides or microdisks, it is important to have a very thin layer, in which case MBE is the growth method of choice.

## 1.2 Photonic devices

In this section, we will discuss theoretically the photonic devices that constitute our photonic integrated circuits. The most important component of a photonic circuit is the optical cavity or resonator. A resonator is an arrangement of reflectors that allows light to circulate on a closed path. A simple example is the Fabry-Perot cavity, which consists of two flat opposing mirrors. When the optical path length of one round-trip is an integer multiple of a wavelength, the light experiences constructive interference and forms a standing wave within the cavity. These standing waves are the cavity modes. The other wavelengths are suppressed by destructive interference. A cavity has multiple modes and their spacing or free spectral range (FSR) depends on the resonator's size.

There is an interest in forming small footprint cavities with low optical losses that confine light strongly. There are various types of these micro- and nanocavities, such as planar microcavities, micropillars, microrings, microspheres, microdisks, and photonic crystal (PhC) slabs. They can use the reflection at a single interface or dielectric multi-layer stacks as reflectors. An overview of the different types of microcavities can be found in Ref. [93]. In this thesis, we investigate mushroom-type microdisk and 2D PhC slab cavities. We can classify microcavities by the type of modes they support, i.e. Fabry-Perot resonator or whispering-gallery mode (WGM) resonator. A WGM resonator confines light through total internal reflection at a circular perimeter, such as in a sphere, disk, or ring. It is named after the acoustic phenomenon first observed by Lord Rayleigh in Saint Paul's cathedral in London in 1910 [94]. Micro- and nanoresonators have the advantage of large  $Q/V_m$ , where  $V_m$  is the mode volume, making them very useful components for on-chip integrated photonics.

To form a laser, we need an optical cavity, a gain medium, and a pump. The gain medium in our case are III-nitride QWs, and the pump can be a laser or injected current. The optical gain of one round-trip needs to outweigh the losses, in order to reach the lasing threshold. The lasing modes will be one or several of the microresonator modes overlapping with the QW emission spectrum. A review article about different types of WGM microlasers can be found in He et al. [95].

### 1.2.1 Slab waveguide

The out-of-plane confinement for both microdisks and PhC slabs is given by the refractive index contrast to the surrounding material (i.e. air or SiO<sub>2</sub>). To describe these cavities, we will

thus first study the out-of-plane confinement by looking at an infinite slab waveguide, which is represented in Fig. 1.9. The refractive indices of the slab and the surrounding material are  $n_1$  and  $n_2$ , respectively. When the slab thickness  $d$  is in the order of the wavelength in the material, the wave sees an effective index  $n_{eff}$ , as it is partially in the waveguide and partially in the surrounding material. We will determine  $n_{eff}$  in this section. We follow a standard textbook approach that can be found, for example, in Ref. [96]. We assume that we have uncoupled orthogonal modes, TE and TM, which is the case for symmetrical structures.

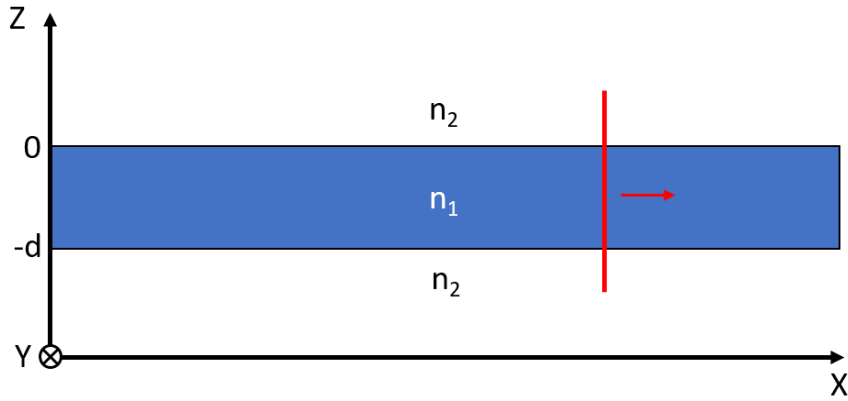


Figure 1.9: Sketch of a slab waveguide.

We start from Maxwell's equations in a medium in absence of free charge and currents:

$$\nabla \cdot \mathbf{D} = 0, \quad (1.5)$$

$$\nabla \cdot \mathbf{B} = 0, \quad (1.6)$$

$$\nabla \times \mathbf{E} = -\frac{\partial \mathbf{B}}{\partial t}, \quad (1.7)$$

$$\nabla \times \mathbf{H} = \frac{\partial \mathbf{D}}{\partial t}, \quad (1.8)$$

with electric field  $\mathbf{E}$ , magnetic field  $\mathbf{B}$ , displacement field  $\mathbf{D}$ , and magnetizing field  $\mathbf{H}$ . The relationship between  $\mathbf{D}$  and  $\mathbf{E}$  fields as well as  $\mathbf{B}$  and  $\mathbf{H}$  fields are given by:

$$\mathbf{D} = \epsilon_0 \epsilon_r \mathbf{E}, \quad (1.9)$$

$$\mathbf{B} = \mu_0 \mu_r \mathbf{H}, \quad (1.10)$$

where  $\mu_0$  and  $\epsilon_0$  are the vacuum permeability and permittivity with  $\mu_0 \epsilon_0 = 1/c^2$ , with  $c$  the speed of light in vacuum, and  $\mu_r$  and  $\epsilon_r$  are the relative permeability and permittivity with  $\mu_r \epsilon_r = n^2$ , where  $n$  is the refractive index. For dielectric materials  $\mu_r = 1$ .

We apply  $\nabla \times$  on Eq. 1.7, and by using the vector identity  $\nabla \times (\nabla \times \mathbf{E}) = \nabla(\nabla \cdot \mathbf{E}) - \Delta \mathbf{E}$  and inserting Eqs. 1.5 and 1.8 we obtain the wave equation

$$\Delta \mathbf{E} - \frac{n^2}{c^2} \frac{\partial^2 \mathbf{E}}{\partial t^2} = 0. \quad (1.11)$$

We assume that the E-field is of the form  $\mathbf{E}(\mathbf{r}, t) = \text{Re}(\mathbf{E}(\mathbf{r})e^{i\omega t})$  with angular frequency  $\omega$  and time-independent amplitude  $\mathbf{E}(\mathbf{r})$ .

For a general wave function  $u(\mathbf{r}, t) = F(\mathbf{r})T(t)$ , we can use the separation of variables approach to get

$$\frac{\Delta F}{n^2 F} = \frac{1}{c^2 T} \frac{\partial^2 T}{\partial t^2} = k^2, \quad (1.12)$$

with the vacuum dispersion relation  $k = \omega/c$ , where  $k$  is the wave vector. This gives us two independent equations:

$$\Delta F + k^2 n^2 F = 0, \quad (1.13)$$

$$\frac{\partial^2 T}{\partial t^2} + \omega^2 T = 0, \quad (1.14)$$

where Eq. 1.13 is the time-independent Helmholtz equation and Eq. 1.14 is a second-order ordinary differential equation in time with solution

$$T(t) = S e^{i\omega t}, \quad (1.15)$$

with constant  $S$ .

In the slab waveguide, the wave propagates along the x-axis and we can write:  $\mathbf{E}(\mathbf{r}) = \mathbf{E}(y, z)e^{-i\beta x}$ , where  $\beta$  is the propagation constant. Thus, we can rewrite Eq. 1.13 as

$$\left( \frac{\partial^2}{\partial y^2} + \frac{\partial^2}{\partial z^2} \right) \mathbf{E}(y, z) + (k^2 n^2 - \beta^2) \mathbf{E}(y, z) = 0. \quad (1.16)$$

We suppose that the wave is constant in the y-direction, so that  $\partial/\partial y = 0$ .

We differentiate between two perpendicular polarizations of light: TE and TM. For TE modes the E-field is perpendicular to the propagation direction (here  $x$ ) and only the components  $H_x$ ,  $E_y$ , and  $H_z$  are non-zero. For TM modes the H-field is perpendicular to the propagation direction and the components  $E_x$ ,  $H_y$ , and  $E_z$  are non-zero.

We will look at TE modes, since the light emitted by InGaN/GaN and GaN/AlN QWs is TE polarized.

We write the Helmholtz equation for  $E_y(z)$  for the three areas:

$$\begin{aligned}
\frac{\partial^2 E_y(z)}{\partial z^2} + (k^2 n_2^2 - \beta^2) E_y(z) &= 0, \text{ for } x > 0, \\
\frac{\partial^2 E_y(z)}{\partial z^2} + (k^2 n_1^2 - \beta^2) E_y(z) &= 0, \text{ for } -d < x < 0, \\
\frac{\partial^2 E_y(z)}{\partial z^2} + (k^2 n_2^2 - \beta^2) E_y(z) &= 0, \text{ for } x < -d.
\end{aligned} \tag{1.17}$$

For each material  $n_i$ ,  $i = 1, 2$ , we need to distinguish between two cases:

- $k^2 n_i^2 \geq \beta^2$  with  $E_y(z) = C_1 \sin(\zeta z) + C_2 \cos(\zeta z)$  and
- $k^2 n_i^2 < \beta^2$  with  $E_y(z) = C_3 e^{\zeta z} + C_4 e^{-\zeta z}$ ,

where  $\zeta = \{\alpha, \kappa\}$  with  $\alpha^2 = k^2 n_1^2 - \beta^2$  and  $\kappa^2 = k^2 n_2^2 - \beta^2$  and the  $C_i$  are constants.

The case  $k^2 n_1^2, k^2 n_2^2 \geq \beta^2$  describes leaky modes and  $k^2 n_1^2, k^2 n_2^2 < \beta^2$  describes a divergent or unphysical case. And with  $n_1 > n_2$  it follows that the case of guided modes is given for:  $kn_1 > \beta > kn_2$ .

We thus get for the three regions:

$$E_y(z) = A e^{-\kappa z}, \quad \text{for } x > 0, \tag{1.18}$$

$$E_y(z) = B \cos(\alpha z) + C \sin(\alpha z), \quad \text{for } -d < x < 0, \tag{1.19}$$

$$E_y(z) = D e^{\kappa(z+d)}, \quad \text{for } x < -d, \tag{1.20}$$

with constants  $A, B, C, D$ .

These equations need to fulfil the boundary conditions that  $E_y$  and  $E_y'$  are continuous at both  $x = 0$  and  $x = -d$ . We obtain at  $x = 0$ :

$$\begin{aligned}
A &= B, \\
-\kappa A &= \alpha C,
\end{aligned} \tag{1.21}$$

and at  $x = -d$ :

$$\begin{aligned}
A \cos(\alpha d) - A \frac{\kappa}{\alpha} \sin(\alpha d) &= D, \\
\left( \frac{\alpha}{\kappa} - \frac{\kappa}{\alpha} \right) \sin(\alpha d) &= 2 \cos(\alpha d),
\end{aligned} \tag{1.22}$$

And we thus get:

$$\begin{aligned}
\tan(\alpha d) &= \frac{2\kappa\alpha}{\alpha^2 - \kappa^2}, \\
\beta^2 + \alpha^2 &= k^2 n_1^2, \\
\beta^2 - \kappa^2 &= k^2 n_2^2, \\
k &= \frac{\omega}{c}.
\end{aligned} \tag{1.23}$$

The constants  $\alpha$  and  $\kappa$  describe the oscillation and attenuation of the field, respectively. The Eqs. 1.23 give us the conditions for the discrete solutions of the propagation constant  $\beta$  for a given thickness  $d$  and frequency  $\omega$ . The solutions can be obtained using a 1D mode solver software (OMS) [97]. The effective refractive index  $n_{eff}$  is related to  $\beta$  via

$$n_{eff} = \frac{\beta}{k} = \beta \frac{\lambda}{2\pi}. \tag{1.24}$$

We will discuss two examples: samples D559 and A2587. Sample D559 consists of 100 nm AlN and 410 nm GaN (containing 10 InGaN QWs that we will ignore here for simplicity) and sample A2587 consists of 330 nm AlN. Figs 1.10 (a) and (b) show the calculated  $H_z$  field for the lowest order TE modes for samples D559 and A2587 at  $\lambda = 420$  nm and  $\lambda = 780$  nm, respectively. The calculated  $n_{eff}$  for the lowest order TE and TM modes for both samples are plotted over the wavelength in Figs. 1.10 (c) and (d). For structures similar to samples D559 and A2587, we have plotted  $n_{eff}$  over the slab height for  $\lambda = 420$  nm and  $\lambda = 780$  nm, respectively, in Figs. 1.10 (e) and (f). We can see that for sample D559, where the thickness of 510 nm is large compared to the wavelength in the material,  $n_{eff}$  for the TE<sub>0</sub> mode is only slightly less than the bulk refractive index. However, in the case of sample A2587, a large part of the TE<sub>0</sub> mode sees air and the  $n_{eff}$  is lower. We can see that when reducing the thickness of the sample, the  $n_{eff}$  of the modes decrease. For a slab of thickness  $d = \lambda/(2n_{eff})$ , only the fundamental modes are guided and the waveguide is called mono-mode, which is the case in Fig. 1.10 (f) for  $h < 220$  nm.

The choice of the thickness of a sample depends on several factors. There are growth constraints that forbid us from having arbitrarily thick or thin layers. If the epitaxial layer is too thick, the tensile stress in the sample will create cracks. For very thin layers, the material quality is not very good, as the region near the Si substrate is highly defective. When we include InGaN QWs in the layer stack, a few hundred nm of GaN/AlN buffer layer are required to obtain a good material quality. Within these limits, we need to ensure that the layer is not too thin to allow most of the TE<sub>0</sub> mode to be confined in the slab, in order to have not too high losses. Especially for longer wavelengths, i.e. 780 nm or 1550 nm, we need to ensure that the sample thickness is sufficient.

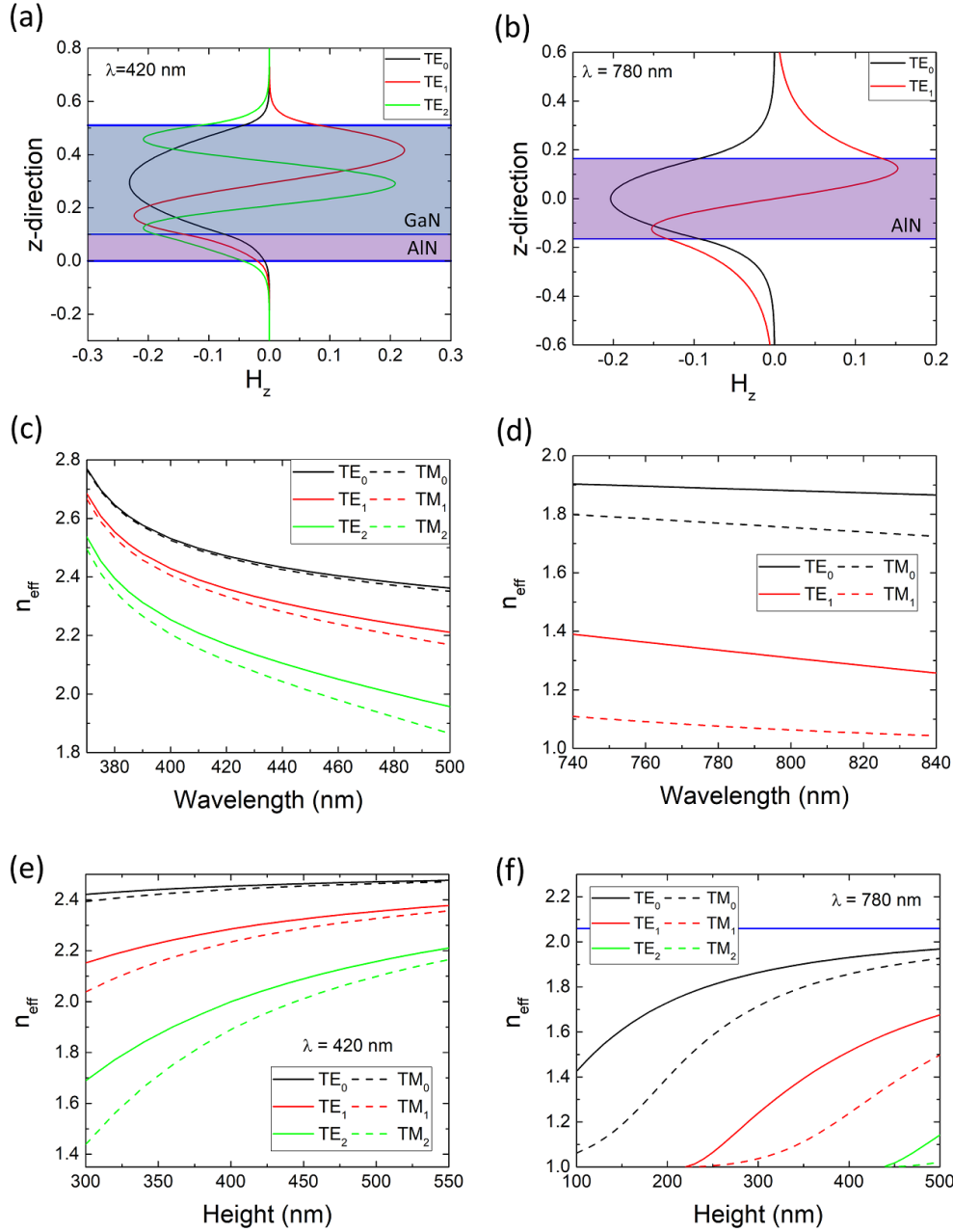


Figure 1.10: Calculations of the  $H_z$  field of TE modes for (a) sample D559 at  $\lambda = 420$  nm, and (b) for sample A2587 at  $\lambda = 780$  nm. Calculations of  $n_{eff}$  for TE and TM modes for (c) sample D559 in the blue and (d) sample A2587 in the NIR. Calculations of  $n_{eff}$  over the slab height at (e)  $\lambda = 420$  nm for a structure similar to sample D559 and (f)  $\lambda = 780$  nm for a structure similar to sample A2587. The bulk refractive index of AlN is indicated in (f).

## 1.2.2 Ridge waveguide

Before we discuss microresonators, we will briefly discuss the rectangular ridge waveguide. The problem is very similar to the slab waveguide, only that now we have confinement in two

dimensions, which makes the description a lot more complicated due to the field singularities in the corners. An approximate analytical solution can be found by looking only at the areas directly above/below and to the left/right of the waveguide and disregarding the fields in the corners. In this work, we use ridge waveguides to evanescently couple to microdisks, as we will discuss later. Here, we will discuss the simplest case of a waveguide with perfect confinement, where the E-field and the first derivative of the H-field are zero at the boundaries.

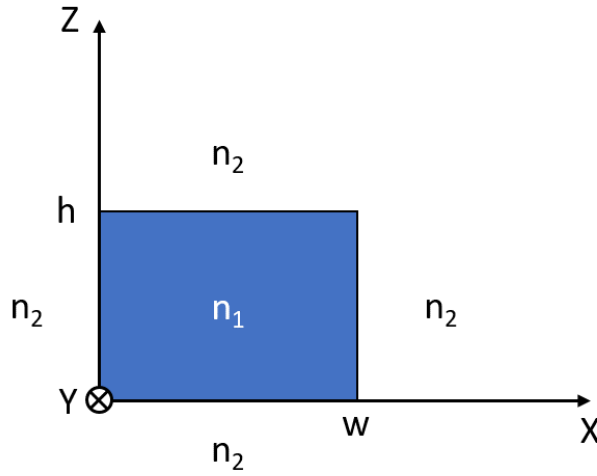


Figure 1.11: Sketch of a rectangular ridge waveguide with height  $h$  and width  $w$ . The refractive index of the waveguide is  $n_1$  and of the surrounding  $n_2$  with  $n_1 > n_2$ .

Fig. 1.11 shows a sketch of the  $x$ - $z$  cross-section of a rectangular ridge waveguide with height  $h$  and width  $w$ . The refractive index of the waveguide is  $n_1$  and of the surrounding (usually air)  $n_2$  with  $n_1 > n_2$ . The wave propagates in the  $y$ -direction and is confined in the  $x$  and  $z$  directions. For TE modes, the  $E_y$  component is zero, while for TM modes the  $H_y$  component is zero. We will look at TE modes and give the Helmholtz equation for  $H_y$ :

$$\Delta H_y(x, y, z) + k^2 H_y(x, y, z) = 0. \quad (1.25)$$

We assume that  $H_y$  is separable into  $H_y(x, y, z) = F(x)G(y)K(z)$  and insert this into Eq. 1.25. We divide by  $FGK$  and rearrange both sides to obtain

$$\frac{1}{F} \frac{\partial^2 F}{\partial x^2} + \frac{1}{K} \frac{\partial^2 K}{\partial z^2} + k^2 = -\frac{1}{G} \frac{\partial^2 G}{\partial y^2}, \quad (1.26)$$

where the left side is independent of  $y$  and the right side is independent of  $x, z$ . Thus, both sides are equal to a constant,  $\beta^2$ .

For  $G$ , we obtain

$$\frac{\partial^2 G}{\partial y^2} + \beta^2 G = 0, \quad (1.27)$$

with solutions

$$G(y) = g_0 e^{-i\beta y} + g_1 e^{i\beta y}. \quad (1.28)$$

We are only interested in waves travelling in the positive  $y$ -direction, which is given by the first term in Eq. 1.28.

We take the left side of Eq. 1.26 and separate it into a part that depends only on  $x$  and a part that depends only on  $z$ . We obtain

$$\frac{1}{F} \frac{\partial^2 F}{\partial x^2} + k^2 - \beta^2 = -\frac{1}{K} \frac{\partial^2 K}{\partial z^2}. \quad (1.29)$$

For  $K$ , we obtain

$$\frac{\partial^2 K}{\partial z^2} + k_z^2 K = 0, \quad (1.30)$$

which has the solution

$$K(z) = \alpha_0 \cos(k_z z) + \alpha_1 \sin(k_z z), \quad (1.31)$$

that needs to fulfil the boundary conditions  $K'(0) = K'(h) = 0$ . Consequently,  $\alpha_1 = 0$  and  $k_z = q\pi/h$ , where  $q = \{1, 2, 3, \dots\}$ .

Finally, we obtain the following equation for  $F$ :

$$\frac{1}{F} \frac{\partial^2 F}{\partial x^2} + k^2 - \beta^2 - \left(\frac{q\pi}{h}\right)^2 = 0, \quad (1.32)$$

and we define  $k_x^2 = k^2 - \beta^2 - (q\pi/h)^2$ .

The solution is

$$F(x) = f_0 \cos(k_x x) + f_1 \sin(k_x x), \quad (1.33)$$

with boundary conditions  $F'(0) = F'(w) = 0$ , which gives us  $f_1 = 0$  and  $k_x = p\pi/w$  with  $p = \{1, 2, 3, \dots\}$

Thus, we obtain

$$H_y(x, y, z) = H_{p,q} \cos\left(\frac{p\pi x}{w}\right) \cos\left(\frac{q\pi z}{h}\right) e^{-i\beta y}, \quad (1.34)$$

with  $H_{p,q} = f_0 g_0 \alpha_0$  a constant and  $\beta^2 = k^2 - (p\pi/w)^2 - (q\pi/h)^2$ , where  $k = k_0 n_1$ .

A mode of order  $p - 1$ ,  $q - 1$  has  $p$  maxima along the  $x$ -direction and  $q$  maxima along the  $z$ -direction. We give two calculation examples whose parameters are summarized in Table 1.5. For  $\lambda = 420 \text{ nm}$ ,  $n_1 = 2.4$ ,  $w = 170 \text{ nm}$ , and  $h = 410 \text{ nm}$  and  $p = q = 1$ , we get  $\beta = 30 \mu\text{m}^{-1}$

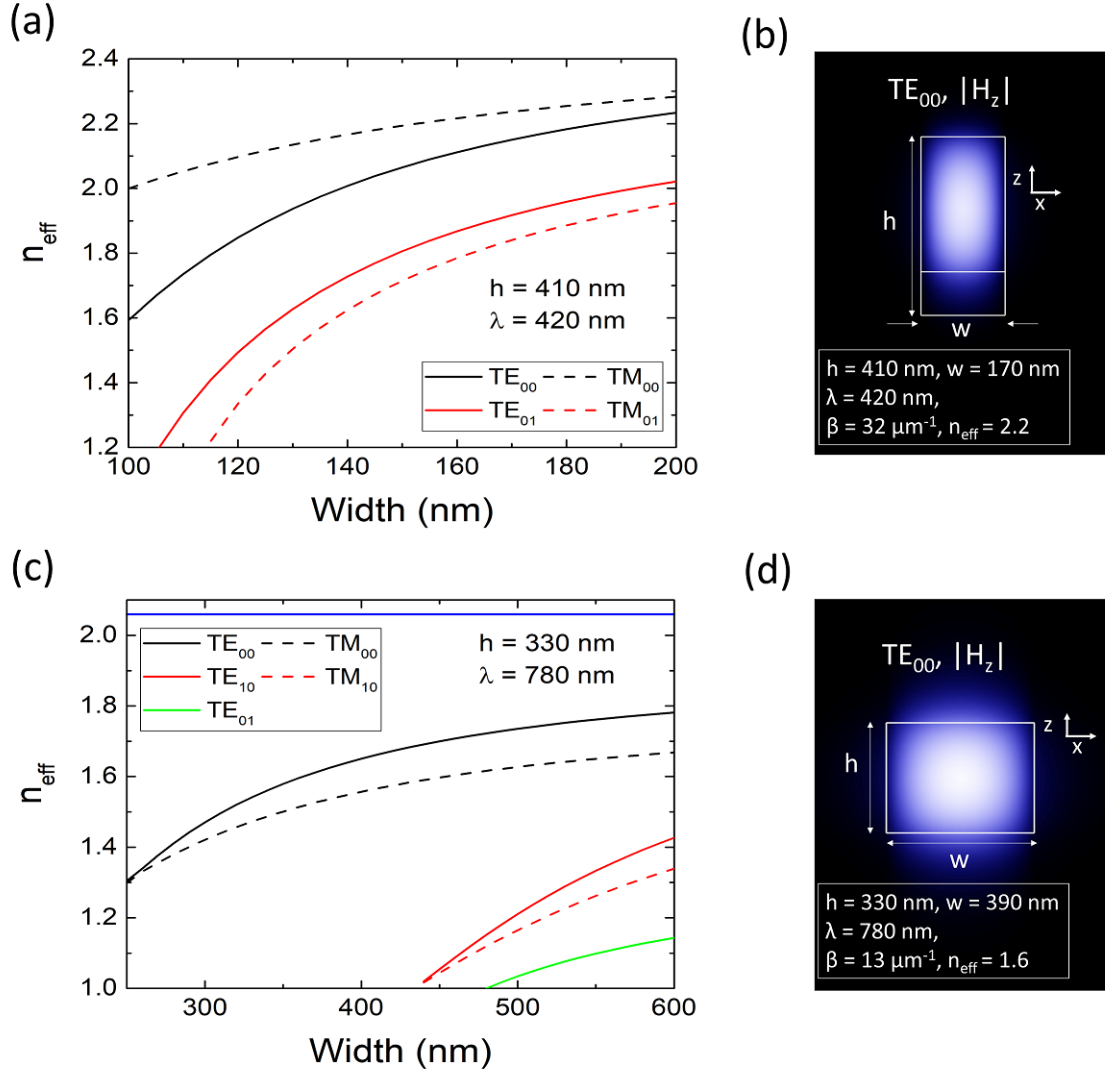


Figure 1.12: Ridge waveguides: (a)  $n_{eff}$  over the waveguide width for sample DD59 at 420 nm, (b) transverse profile of the  $|H_z|$  field of the  $TE_{00}$  mode for sample D559 with a waveguide width of  $w = 170$  nm, (c)  $n_{eff}$  over the waveguide width for sample A2587 at 780 nm, (d) transverse profile of the  $|H_z|$  field of the  $TE_{00}$  mode for sample A2587 with a waveguide width of  $w = 390$  nm.

and  $n_{eff} = 2$ . For  $\lambda = 780$  nm,  $n_1 = 2.1$ ,  $w = 390$  nm, and  $h = 330$  nm and  $p = q = 1$ , we get  $\beta = 11 \mu\text{m}^{-1}$  and  $n_{eff} = 1.4$ . We will compare these values with more rigorous simulations that take evanescent fields into account.

We use a 2D mode solver (EIMS) [98] using a variational effective index approximation to solve for  $\beta$ , which is explained in Ref. [99]. First, taking only the vertical confinement into account,  $n_{eff}$  is determined like for the slab waveguide. Then the lateral confinement is taken into account to determine  $\beta$  for the 2D waveguide. In Fig. 1.12 (a) and (c), we depict  $n_{eff}$  over the waveguide width for the lowest order TE and TM modes for samples D559 and A2587 at  $\lambda =$

420 nm and 780 nm, respectively. In Fig. 1.12 (b), we depict the transverse  $|H_z|$  field of the TE<sub>00</sub> modes of a waveguide with  $h = 410$  nm and  $w = 170$  nm at  $\lambda = 420$  nm with  $\beta = 32 \mu\text{m}^{-1}$  and  $n_{eff} = 2.2$ . Fig. 1.12 (d) shows the TE<sub>00</sub> mode of a waveguide with  $h = 330$  nm and  $w = 390$  nm at  $\lambda = 780$  nm with  $\beta = 13 \mu\text{m}^{-1}$  and  $n_{eff} = 1.6$ . In Table 1.5, we compare the analytically obtained results with the 2D mode solver. The results for both are fairly similar. The 2D mode solver gives more accurate results, but is also approximate. When investigating the coupling between a microdisk and a waveguide, we rely on the finite-difference time-domain (FDTD) method, which is the most accurate simulation method we have available. We will discuss FDTD in section 1.2.8.

h (nm)	w (nm)	$\lambda$ (nm)	$\beta$ ( $\mu\text{m}^{-1}$ ) analytical	$\beta$ ( $\mu\text{m}^{-1}$ ) 2D mode solver	$n_{eff}$ analytical	$n_{eff}$ 2D mode solver
410	170	420	30	32	2	2.2
330	390	780	11	13	1.4	1.6

Table 1.5: Parameters of two 2D waveguides with height, width, wavelength, propagation constant and  $n_{eff}$  using the analytical formulas and the 2D mode solver.

### 1.2.3 Microdisk cavity

After having determined the out-of-plane confinement and  $n_{eff}$ , we can now investigate the in-plane confinement of the microdisk cavity. We will start with a geometric approach, which gives a good approximation of the WGM positions and the FSR. Then, we solve the Helmholtz equation in cylindrical coordinates, in order to more rigorously determine the radial and azimuthal mode orders. We describe the different components that make up the Q factor.

#### 1.2.3.1 Geometrical description

A microdisk is a cylindrically-shaped microresonator that utilizes total internal reflection to confine light in-plane at its periphery. It can be placed either on a non-absorbing substrate of lower refractive index or suspended on a pedestal, in which case it is called mushroom-type. Fig. 1.13 shows a 3D illustration of a mushroom-type III-nitride microdisk laser with a Si pedestal. A WGM profile is overlaid on the disk surface and the QWs can be seen at the edge of the disk. Fig. 1.14 schematically illustrates the design of a mushroom-type microdisk resonator of radius  $a$ , height  $h$ , and effective refractive index  $n_{eff}$ .

The in-plane light confinement is illustrated by the red line in Fig. 1.14 (a). Out-of-plane optical confinement is achieved through the refractive index contrast to the surrounding material (i.e. air) with refractive index  $n_0$ .

A standing wave at the periphery of the resonator is obtained when one round-trip (slightly smaller than the circumference of the disk) is a multiple of the wavelength in the material:

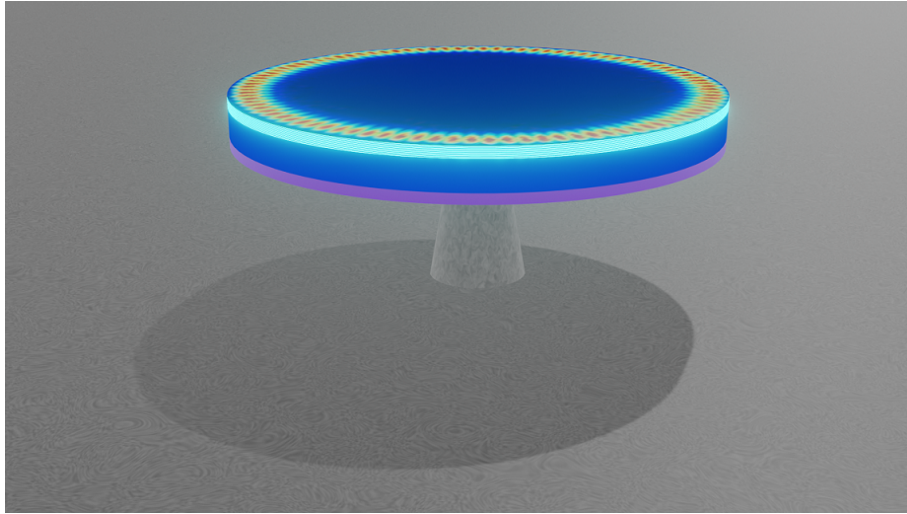


Figure 1.13: 3D sketch of a microdisk laser.

$$2\pi a_{eff} = \frac{m\lambda}{n_{eff}}, \quad (1.35)$$

where  $a_{eff}$  is the effective radius of the optical mode,  $m \in \mathbb{N}$  is called the azimuthal number of the optical mode, and  $\lambda$  is the vacuum wavelength at the resonance. We need to consider the effective radius  $a_{eff}$ , since the center of the mode will not be directly at the edge of the disk but a bit further inside. For these wavelengths constructive interference is obtained, while all other wavelengths are suppressed. These are the WGMs.

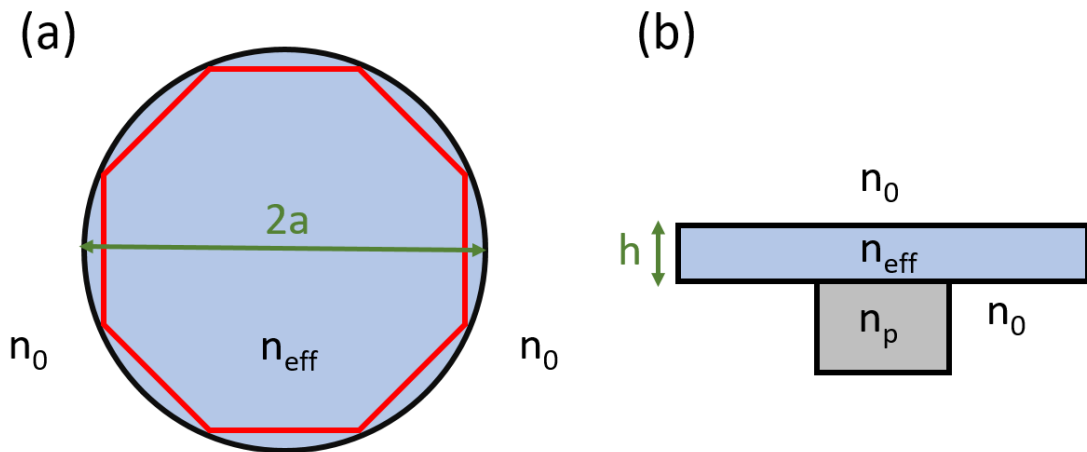


Figure 1.14: Schematics of a microdisk resonator. (a) Top-view with refractive index  $n_{eff}$  of the microdisk and  $n_0$  of the surrounding material (i.e. air). The ray-optics path of total internal reflection is illustrated in red. (b) Side-view of the microdisk and pedestal with refractive index  $n_p$

For a resonator, the FSR, the distance between two adjacent modes is given by [100]

$$FSR = -\frac{2\pi}{L} \left( \frac{\partial\beta}{\partial\lambda} \right)^{-1}, \quad (1.36)$$

where  $L$  is the round-trip length inside the cavity, which for a microdisk is given by  $L = 2\pi a$ , and  $\beta = kn_{eff} = 2\pi n_{eff}/\lambda$  is the propagation constant.

We get

$$\frac{\partial\beta}{\partial\lambda} = 2\pi \frac{\partial}{\partial\lambda} \left( \frac{n_{eff}}{\lambda} \right) = -\frac{2\pi}{\lambda^2} \left( n_{eff} - \lambda \frac{\partial n_{eff}}{\partial\lambda} \right) = -\frac{2\pi}{\lambda^2} n_g, \quad (1.37)$$

with  $n_g$  the group index given by

$$n_g = n_{eff} - \lambda \frac{\partial n_{eff}}{\partial\lambda}. \quad (1.38)$$

We thus obtain

$$FSR = \frac{\lambda^2}{Ln_g} = \frac{\lambda^2}{2\pi a_{eff} n_g}, \quad (1.39)$$

where  $\lambda$  is close to the wavelengths of the two modes of interest.

Since  $n_{eff}$  varies strongly in the blue spectral range (see Fig. 1.10 (c)), we cannot make the approximation  $n_g \approx n_{eff}$ . The FSR is inversely proportional to the round-trip length, which means that it increases with decreasing microdisk radius.

We give a calculation example. For a microdisk with  $a = 1.5\mu\text{m}$ ,  $n_g = 3.46$  (sample D559) at  $\lambda = 424\text{nm}$ , Eq. 1.35 gives us  $m = 55$  and Eq. 1.39 gives us  $FSR = 5.5\text{nm}$ , if we assume  $a_{eff} = a$ . This is already a pretty good approximation. Taking  $a_{eff} = 1.4\mu\text{m}$ , we get  $m = 51$  and  $FSR = 5.9\text{nm}$ , which matches rather well with the calculation and simulation examples of the same sample in Figs. 1.15 and 1.16.

### 1.2.3.2 Analytical description of WGMs

We follow the description in Refs. [58, 101–103]. In order to describe the WGMs analytically, we need to make two assumptions. Firstly, that the TE and TM modes are uncoupled, like in the case of the slab waveguide. Due to the cylindrical symmetry of the microdisk, we will use cylindrical coordinates. The non-zero components of the E- and H-fields are  $(E_r, E_\theta, H_z)$  for TE modes and  $(H_r, H_\theta, E_z)$  for TM modes. Secondly, we assume that the microdisk is a homogeneous medium with effective refractive index  $n_{eff}$  that allows us separate the fields in  $r$ ,  $\theta$ , and  $z$ . We can thus write the field component  $F_z$ , where  $F \in \{E, H\}$  as

$$F_z(r, \theta, z) = R(r)\Theta(\theta)Z(z). \quad (1.40)$$

We start from Eq. 1.13 and rewrite the Laplace operator in cylindrical coordinates  $(r, \theta, z)$ :

$$\Delta = \frac{\partial^2}{\partial r^2} + \frac{1}{r} \frac{\partial}{\partial r} + \frac{1}{r^2} \frac{\partial^2}{\partial \theta^2} + \frac{\partial^2}{\partial z^2}. \quad (1.41)$$

Then, we rewrite the Helmholtz equation as

$$\frac{\partial^2 R\Theta Z}{\partial r^2} + \frac{1}{r} \frac{\partial R\Theta Z}{\partial r} + \frac{1}{r^2} \frac{\partial^2 R\Theta Z}{\partial \theta^2} + \frac{\partial^2 R\Theta Z}{\partial z^2} + \frac{\omega^2}{c^2} n^2 R\Theta Z = 0. \quad (1.42)$$

We divide Eq. 1.42 by  $R\Theta Z$  and rearrange the terms to isolate  $\theta$ :

$$\frac{1}{\Theta} \frac{\partial^2 \Theta}{\partial \theta^2} = -r^2 \frac{1}{R} \frac{\partial^2 R}{\partial r^2} - r \frac{1}{R} \frac{\partial R}{\partial r} - r^2 \frac{1}{Z} \frac{\partial^2 Z}{\partial z^2} - r^2 \frac{\omega^2}{c^2} n^2 \quad (1.43)$$

Now the left and right sides of Eq. 1.43 are independent and equal to a constant, which we choose to be  $-m^2$ .

Thus, we obtain for  $\theta$ :

$$\frac{\partial^2 \Theta}{\partial \theta^2} + m^2 \Theta = 0, \quad (1.44)$$

which has the solution

$$\Theta(\theta) = P e^{im\theta}, \quad (1.45)$$

where  $P$  is a constant.

We continue by separating the right side of Eq. 1.43 and obtain

$$\frac{1}{Z} \frac{\partial^2 Z}{\partial z^2} + \frac{\omega^2}{c^2} n^2 = -\frac{1}{R} \frac{\partial^2 R}{\partial r^2} - \frac{1}{rR} \frac{\partial R}{\partial r} + \frac{m^2}{r^2}, \quad (1.46)$$

where both sides are again independent and equal to a constant,  $\beta^2$ . The equation we obtain for  $Z$  is

$$\frac{\partial^2 Z}{\partial z^2} + \left( \frac{\omega^2}{c^2} n^2 - \beta^2 \right) Z = 0, \quad (1.47)$$

with  $\beta = \omega n_{eff}/c$ . We compare Eq. 1.47 with Eq. 1.17 for the slab waveguide and conclude that they are the same, as we have assumed previously.

Finally, we are left with the following equation for  $R$ :

$$\frac{\partial^2 R}{\partial r^2} + \frac{1}{r} \frac{\partial R}{\partial r} + \left( \frac{\omega^2}{c^2} n_{eff}^2 - \frac{m^2}{r^2} \right) R = 0. \quad (1.48)$$

We multiply Eq. 1.48 by  $r^2$  and make a change of variables. We define  $x := \omega n_{eff} r/c$ . Consequently,  $R(r) = R(\frac{c}{\omega n_{eff}} x) =: K(x)$ . We rewrite Eq. 1.48 as

$$x^2 \frac{\partial^2 K(x)}{\partial x^2} + x \frac{\partial K(x)}{\partial x} + (x^2 - m^2) K(x) = 0. \quad (1.49)$$

Eq. 1.49 is Bessel's differential equation and the solutions are known to be [104]

$$K(x) = A J_m(x) + B Y_m(x), \quad (1.50)$$

where  $J_m$  and  $Y_m$  are the Bessel functions of first and second kind and order  $m$ , and  $A, B$  are constants.

Inside the disk, the  $Y_m$  are an unphysical solution because they diverge at  $r = 0$  at the center of the disk. Thus, we get for  $R(r)$

$$R(r) = AJ_m\left(\frac{\omega}{c}n_{eff}r\right), \quad \text{for } r \leq a, \quad (1.51)$$

$$R(r) = CH_m^{(1)}\left(\frac{\omega}{c}r\right), \quad \text{for } r > a, \quad (1.52)$$

where  $C$  is a constant and  $H_m^{(1)}$  are the Henkel functions of first kind and order  $m$ , which are given by

$$H_m^{(1)}(x) = J_m(x) + iY_m(x). \quad (1.53)$$

The tangential fields are continuous at the boundary  $r = a$ . For TE modes,  $H_z$  and  $E_\Theta$  are continuous, while for TM modes it is  $E_z$  and  $H_\Theta$ .

From Maxwell's source-free curl equations (Eqs. 1.8 and 1.7), we determine the remaining components of the E and H-fields.

For TE modes, we get

$$E_\Theta = \frac{i}{\epsilon_0\epsilon_r\omega} \frac{\partial H_z}{\partial r}, \quad (1.54)$$

$$E_r = \frac{m}{\epsilon_0\epsilon_r r\omega} H_z. \quad (1.55)$$

For TM modes, we get

$$H_\Theta = \frac{-i}{\mu_0\omega} \frac{\partial E_z}{\partial r}, \quad (1.56)$$

$$H_r = -\frac{m}{\mu_0 r\omega} E_z. \quad (1.57)$$

The boundary conditions become

$$AJ_m\left(\frac{\omega}{c}n_{eff}a\right) = CH_m^{(1)}\left(\frac{\omega}{c}a\right), \quad (1.58)$$

$$\frac{\omega}{c}NAJ'_m\left(\frac{\omega}{c}n_{eff}a\right) = \frac{\omega}{c}CH_m^{(1)'}\left(\frac{\omega}{c}a\right), \quad (1.59)$$

where  $J'_m$  and  $H_m^{(1)'}$  are the first derivatives, and  $N = \frac{1}{n_{eff}}$  for TE modes and  $N = n_{eff}$  for TM modes. We divide 1.59 by 1.58 and get

$$N \frac{J'_m\left(\frac{\omega}{c} n_{eff} a\right)}{J_m\left(\frac{\omega}{c} n_{eff} a\right)} - \frac{H'_m^{(1)}\left(\frac{\omega}{c} a\right)}{H_m^{(1)}\left(\frac{\omega}{c} a\right)} = 0, \quad (1.60)$$

Eq. 1.60 is a transcendental equation that can only be solved numerically. For a given  $m$  it gives us the complex WGM eigenfrequencies  $\omega$ , which can be labelled with the radial number  $n$ .

Using Python, we wrote a script to plot the left side of Eq. 1.60 for a given  $m$ ,  $n_{eff}$ , and  $a$ . When this function is zero, we have solutions to Eq. 1.60. The lowest energy (longest wavelength) solution has  $n = 1$ , the second one has  $n = 2$ , etc. Fig. 1.15 shows this for  $m = 48$ ,  $n_{eff} = 2.465$ ,  $a = 1.5 \mu\text{m}$  and TE polarization. The  $n = 1$  mode is at  $\lambda = 423.8 \text{ nm}$  and the  $n = 2$  mode is at  $\lambda = 384.5 \text{ nm}$ . Plotting Eq. 1.60 for  $m = 47$  and  $m = 49$  gives us a FSR for first-order radial modes of around 6.2 nm. These results are rather accurate and the remaining inaccuracy stems from the estimated  $n_{eff}$ . Fig. 1.15 (b) shows the radial field according to Eq. 1.51 for the mode with  $n = 1$ ,  $m = 48$  at  $\lambda = 423.8 \text{ nm}$ . The radial maximum of the mode is located at  $1.4 \mu\text{m}$ , which corresponds to the effective radius  $a_{eff}$  that we discussed in section 1.2.3.1.

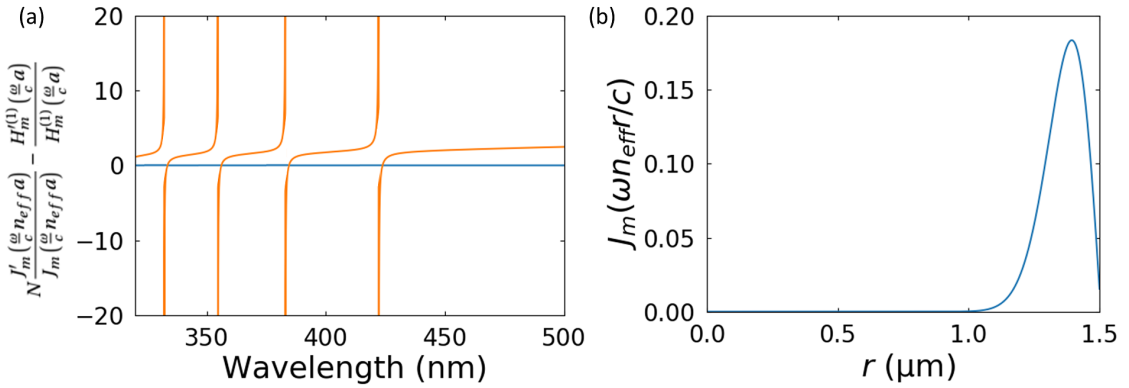


Figure 1.15: a) Plot of the left side of Eq. 1.60 for  $m = 48$ ,  $n_{eff} = 2.465$ ,  $a = 1.5 \mu\text{m}$  for TE polarization. (b) Radial field inside the disk according to Eq. 1.51 for  $\lambda = 423.8 \text{ nm}$ ,  $n = 1$ ,  $m = 48$ ,  $n_{eff} = 2.465$ , and  $a = 1.5 \mu\text{m}$ .

To summarize, we have three mode indices for the microdisk resonator:

- The vertical index  $l$  in the  $z$  coordinate that gives the number of TE and TM modes due to the out-of-plane confinement, like in the slab waveguide. The fields have  $l$  zeros in the  $z$ -direction. We are mainly interested in the modes with  $l = 0$ , even though higher order modes are usually possible.
- The azimuthal index  $m$  in the  $\theta$  coordinate that gives the number of maxima or minima in the fields along the circumference of the disk (or  $2m$  maxima in the squared field).
- The radial index  $n$  in the  $r$  coordinate that gives the number of maxima and minima in the fields along the radius of the disk. We are mainly interested in modes of order  $n = 1$ ,

where the field maximum is closest to the edge of the disk. These are the modes that couple more easily to a bus waveguide. Higher order modes are also present and we can observe them easily in individual microdisks.

Fig. 1.16 (a) and (b) show a cross-sectional top and side-view of the  $H_z$  field of a first-order radial ( $n = 1$ ) WGM for a  $3\mu\text{m}$  diameter disk with the heterostructure of sample D559 at  $\lambda = 429.5\text{ nm}$  with  $m = 48$  and  $l = 0$ . A second-order radial ( $n = 2$ ) mode is shown in Fig. 1.16 (c) and (d) at  $\lambda = 433\text{ nm}$  with  $m = 30$  and  $l = 3$ . These mode profiles were determined by FDTD simulations using MEEP [105], which we will discuss in more detail in section 1.2.8.

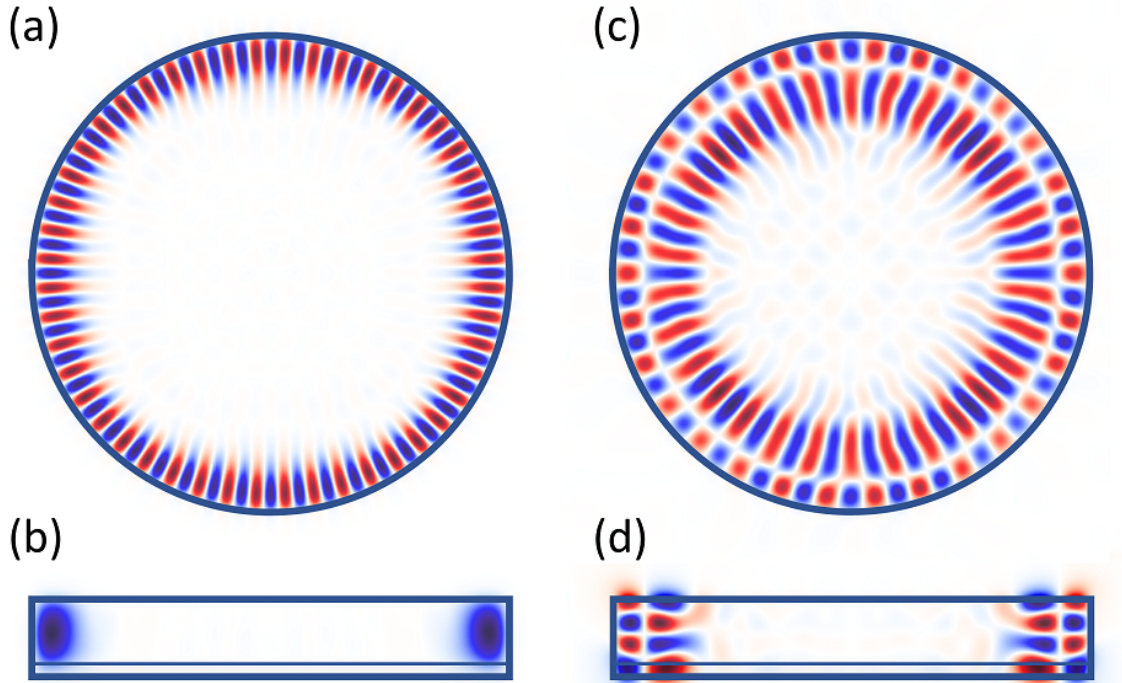


Figure 1.16: FDTD simulations of the  $H_z$  field of a  $3\mu\text{m}$  diameter disk (a) top-view and (b) side-view at  $\lambda = 429.5\text{ nm}$ , showing a first-order radial mode with  $m = 48$  and  $l = 0$  and (c) top-view and (d) side-view at  $\lambda = 433\text{ nm}$ , showing a second-order radial mode with  $m = 30$  and  $l = 3$ . The color scale goes from blue (negative) over white (0) to red (positive).

### 1.2.3.3 Discussion of the Q factor

An important figure of merit for microresonators is the quality factor or Q factor. Experimentally, the total or loaded Q factor of a resonance is given by

$$Q_{load} = \frac{\lambda}{\Delta\lambda}, \quad (1.61)$$

where  $\lambda$  is the resonance frequency and  $\Delta\lambda$  is the full width at half maximum (FWHM) of the resonance.

The Q factor describes how well energy is stored inside a cavity and is related to the losses of the cavity. The total energy decay rate  $1/\tau_{load}$  for a microresonator is given by

$$\frac{1}{\tau_{load}} = \sum_i \frac{1}{\tau_i} = \sum_i \frac{\omega_0}{Q_i}, \quad (1.62)$$

where  $\tau_{load}$  is the total cavity lifetime and  $\omega_0$  is the optical angular frequency. The  $Q_i$  describe the individual loss mechanisms.

We can divide  $Q_{load}$  into the following loss mechanisms:

$$\frac{1}{Q_{load}} = \frac{1}{Q_{th}} + \frac{1}{Q_{sc}} + \frac{1}{Q_{abs,bk}} + \frac{1}{Q_{abs,QW}} + \frac{1}{Q_{sa}} + \frac{1}{Q_C}. \quad (1.63)$$

$Q_{th}$  describes the theoretical radiative or bending losses due to tunnelling of light out of a perfect otherwise lossless resonator. This value is usually very high and does not limit the experimentally observed values of Q.

$Q_{sc}$  describes the surface and side-wall or Rayleigh scattering losses, which scale with  $\lambda^{-2}$  and can become significant at short wavelength [106]. It is thus important to reduce the side-wall roughness of the microdisk during the fabrication process and to grow smooth epilayers.

$Q_{abs,bk}$  describes the residual bulk absorption. It is given by

$$Q_{abs,bk} = \frac{2\pi n}{\alpha\lambda}, \quad (1.64)$$

where  $\alpha$  is the absorption coefficient, which in turn is given by

$$\alpha = \frac{4\pi k}{\lambda}, \quad (1.65)$$

with  $k$  the extinction coefficient. In the blue spectral range, the residual bulk absorption is probably negligible, while it can be significant in the UVA.

$Q_{abs,QW}$  describes the QW absorption, which becomes zero at transparency or negligible at the lower energy end of the QW emission spectrum. This value depends on the carrier density and thus on the excitation power. Consequently, measurements of active devices are not always easy to perform.

$Q_{sa}$  describes the surface absorption, which according to Refs. [6, 36] can have a substantial impact on experimental Q values. Rousseau et al. [36] state that for III-nitride microcavities in the visible spectral range, the optically active surface states need to be passivated with oxygen. We have not investigated this parameter, but have to keep in mind its potentially significant impact on  $Q_{load}$ .

$Q_C$  is the coupling Q factor, which describes the "by design" part of the coupling with the external environment. This coupling allows us to benefit from the emitted photons in a more

controlled way, if these losses dominate over the scattering losses. In the next section, we will discuss coupling to a bus waveguide.

### 1.2.4 Coupling between a microdisk and a bus waveguide

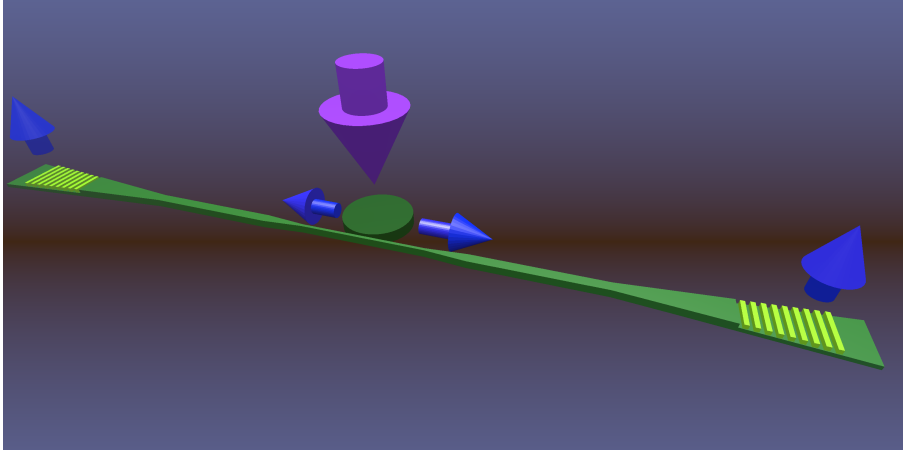


Figure 1.17: 3D sketch of a photonic circuit consisting of a microdisk laser coupled to a waveguide terminated by out-coupling gratings. The purple arrow indicates the pump and the blue arrows indicate the light emitted by the disk and coupled out at the gratings.

In this section, we will describe the evanescent coupling between a microdisk and a bus waveguide. A 3D sketch of a photonic circuit consisting of a microdisk coupled to a waveguide terminated by out-coupling gratings is depicted in Fig. 1.17. One of the key issues for such a system is the efficient energy transfer between the resonator and waveguide, which is achieved in the so-called critical coupling regime when the rate of energy decay from the cavity to the waveguide equals the intrinsic rate of energy decay from the uncoupled microresonator. All the energy can be transferred from the microresonator to the waveguide (or vice versa), by analogy with impedance matching in microwave devices.

We take the simplest case of a passive transparent microdisk, into which light is injected by a bus waveguide. We assume that the WGMs of the disk are not strongly affected by the presence of the waveguide.

The loaded Q factor given in Eq. 1.63 can be rewritten as

$$\frac{1}{Q_{load}} = \frac{1}{Q_{int}} + \frac{1}{Q_C}, \quad (1.66)$$

where  $Q_{int}$  describes all the losses intrinsic to the microdisk. From Eq. 1.63, we get

$$\frac{1}{Q_{int}} = \frac{1}{Q_{th}} + \frac{1}{Q_{abs,bk}} + \frac{1}{Q_{sc}} + \frac{1}{Q_{sa}}. \quad (1.67)$$

Fig. 1.18 shows a schematic of microdisk to waveguide coupling. A wave of amplitude  $s_+$

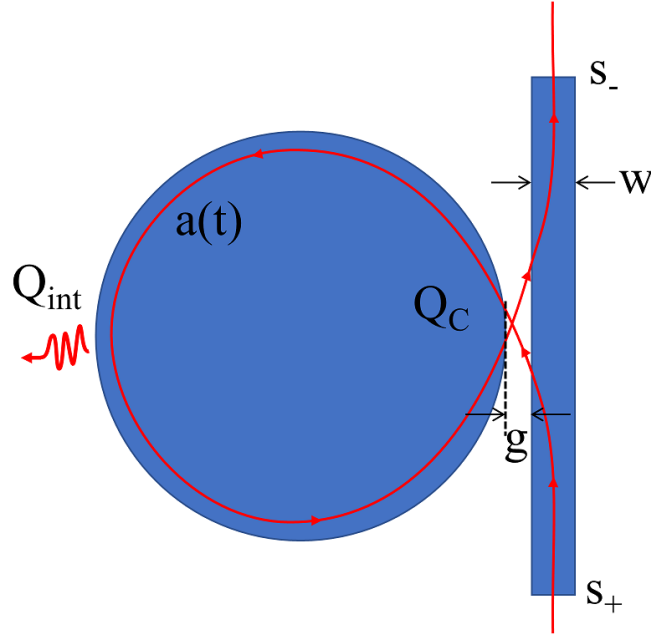


Figure 1.18: Schematic of microdisk to waveguide coupling indicating all relevant parameters.

is injected into the waveguide of width  $w$  and couples to the mode of amplitude  $a(t)$  of the resonator, which is placed at a distance  $g$  from the waveguide. The wave is coupled out of the disk and the amplitude  $s_-$  is transmitted through the other end of the waveguide.  $Q_{int}$  and  $Q_C$  are indicated. We can describe the coupling between a microdisk and a waveguide using coupled-mode theory (CMT) [103, 107]. The fundamental equations of a resonator coupled to one input port are given by [107]:

$$\frac{da}{dt} = i\omega_0 a - \left( \frac{1}{\tau_{int}} + \frac{1}{\tau_C} \right) a + \kappa s_+, \quad (1.68)$$

$$s_- = s_+ - \kappa a. \quad (1.69)$$

$\omega_0$  is the resonance frequency.  $\kappa$  is the coupling coefficient, which is given by  $\kappa = \sqrt{2/\tau_C}$ .  $1/\tau_{int}$  and  $1/\tau_C$  are the decay rates due to internal and external losses of the resonator, respectively. The lifetimes  $\tau$  are related to the Q factors by  $1/\tau_{int} = \omega_0/Q_{int}$  and  $1/\tau_C = \omega_0/Q_C$ .  $|a|^2$  is the energy and  $|s_+|^2$  is the power of the incident wave.

$s_+$  has an  $\exp(i\omega t)$  time-dependence and the solution to Eq. 1.68 is

$$a = \frac{\sqrt{\frac{2}{\tau_C}} s_+}{i(\omega - \omega_0) + \left( \frac{1}{\tau_{int}} + \frac{1}{\tau_C} \right)}. \quad (1.70)$$

We substitute Eq. 1.70 into Eq. 1.69 and obtain

$$s_- = s_+ \left( 1 - \frac{\frac{2}{\tau_C}}{i(\omega - \omega_0) + \left( \frac{1}{\tau_{int}} + \frac{1}{\tau_C} \right)} \right). \quad (1.71)$$

We find a common denominator for the term in parentheses in Eq. 1.71 and get for the transmission coefficient

$$\Gamma = \frac{s_-}{s_+} = \frac{\left( \frac{1}{\tau_{int}} - \frac{1}{\tau_C} \right) + i(\omega - \omega_0)}{\left( \frac{1}{\tau_{int}} + \frac{1}{\tau_C} \right) + i(\omega - \omega_0)}. \quad (1.72)$$

The transmission  $T$  follows as

$$T = |\Gamma|^2 = \Gamma \Gamma^* = \frac{\left( \frac{1}{\tau_{int}} - \frac{1}{\tau_C} \right)^2 + (\omega - \omega_0)^2}{\left( \frac{1}{\tau_{int}} + \frac{1}{\tau_C} \right)^2 + (\omega - \omega_0)^2}, \quad (1.73)$$

with  $\omega_0 = 2\pi c/\lambda_0$ .

On resonance  $\omega - \omega_0 = 0$  and we get

$$T_{on} = \left( \frac{1 - \frac{\tau_C}{\tau_{int}}}{1 + \frac{\tau_C}{\tau_{int}}} \right)^2 = \left( \frac{1 - \frac{Q_C}{Q_{int}}}{1 + \frac{Q_C}{Q_{int}}} \right)^2. \quad (1.74)$$

We need to distinguish between three coupling regimes, which can be identified by looking at the term  $Q_C/Q_{int}$ :

- $\frac{Q_C}{Q_{int}} > 1$  describes the under-coupled regime. Here the coupling is weak and  $Q_{int} > Q_{load} > 1/2 Q_{int}$  and  $1 > T_{on} > 0$ .
- $\frac{Q_C}{Q_{int}} = 1$  describes the regime of critical coupling. Here the coupling is optimal and the power loss into the resonator is equal to the waveguide input power. There is perfect destructive interference between the transmitted field and the microresonator's internal field coupled to the waveguide, thus leading to quenching of the transmission on resonance. We get  $Q_{load} = 1/2 Q_{int}$  and  $T_{on} = 0$ .
- $\frac{Q_C}{Q_{int}} < 1$  describes the over-coupled regime. Here the coupling losses are too large,  $Q_{load} < 1/2 Q_{int}$  and  $1 > T_{on} > 0$ .

In Fig. 1.19, we plot Eq. 1.73 for  $\lambda_0 = 420$  nm and  $Q_{int} = 5000$ . The red curve shows critical coupling with  $Q_C = 5000$ . Fig. 1.19 (a) shows the under-coupled regime with  $Q_C$  up to 50000 and Fig. 1.19 (b) shows the over-coupled regime with  $Q_C$  down to 500.

To achieve critical coupling, the phases of the WGM and the waveguide mode need to be aligned. This condition is called phase matching and is shown in Fig. 1.20. The modes are illustrated in red (positive) and blue (negative). Bad phase matching is depicted in Fig. 1.20 (a) where the mode profiles of disk and waveguide do not align. We can engineer the coupling parameters  $g$  and  $w$  to achieve good phase matching as shown in Fig 1.20 (b).  $g$  is the gap

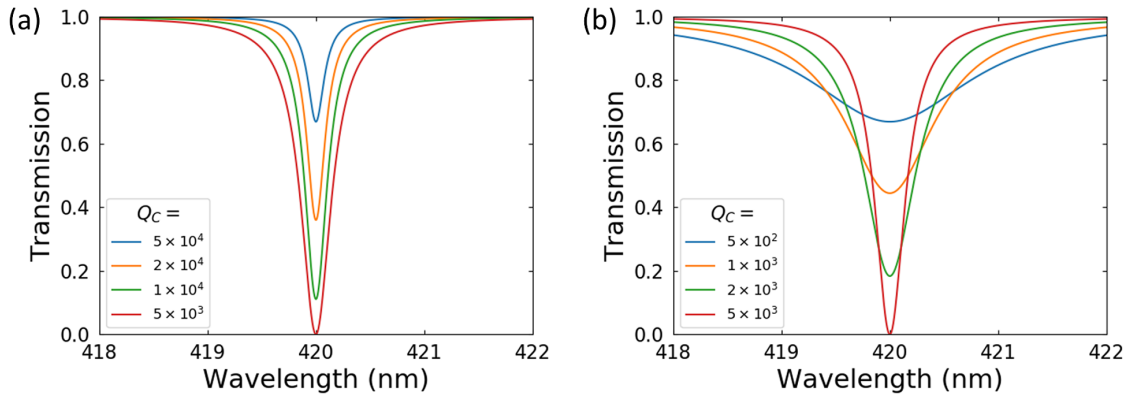


Figure 1.19: Transmission curves of the three coupling regimes for a mode at 420 nm with  $Q_{int} = 5000$ . The red curve in both graphs shows critical coupling with  $Q_C = 5000$ . (a) The under-coupled regime with  $Q_C$  up to 50000. (b) The over-coupled regime and  $Q_C$  down to 500.

between the disk and the waveguide and  $w$  is the waveguide width. By adjusting  $w$  we adjust the speed of light in the material, as the propagation constant  $\beta$  depends on the transverse profile of the waveguide.

With a straight waveguide at short wavelength, the gap must be very small in order to obtain efficient coupling. This poses huge fabrication challenges. By having the waveguide bend around the disk with an angle  $\theta$ , we can increase the coupling length, which allows to increase the gap size.

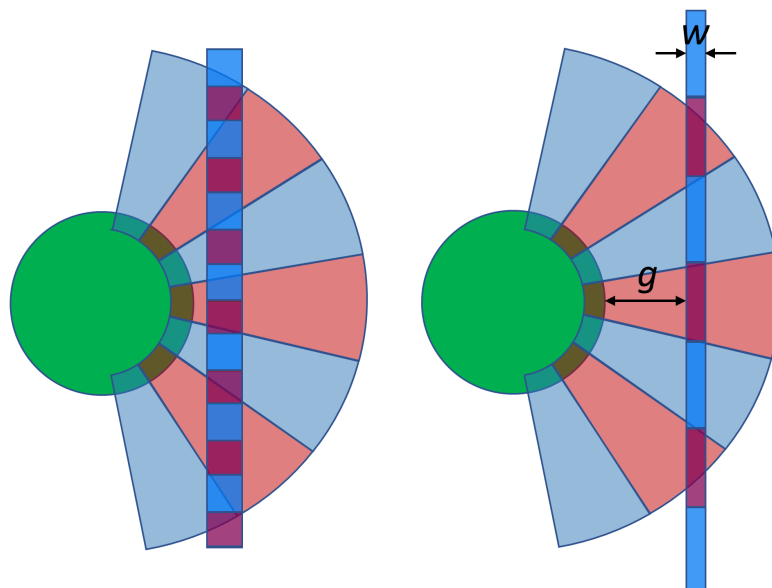


Figure 1.20: Schematic of (a) bad and (b) good phase matching between the modes of a micro-disk and a waveguide. The mode profiles are illustrated in red and blue.

While we only discussed the case of a passive microdisk in transmission, the coupling of an active microdisk to a waveguide behaves in a very similar way. While in this case we cannot look at the transmission to determine whether critical coupling is obtained, we can observe when  $Q_{load} = 1/2 Q_{int}$ . We further need to consider the QW absorption and we can rewrite Eq. 1.66 as

$$\frac{1}{Q_{load}} = \frac{1}{Q_{int}} + \frac{1}{Q_C(g)} + \frac{1}{Q_{abs,QW}(\lambda)}, \quad (1.75)$$

where  $Q_C(g)$  describes the gap-dependent coupling and  $Q_{abs,QW}(\lambda)$  describes the wavelength-dependent QW absorption.

To determine when critical coupling is attained in an active structure, it is thus important to investigate modes at the low-energy end of the spectrum, where absorption is negligible. Alternatively, we can investigate modes at transparency. For modes where  $Q_{abs,QW}$  is not negligible the coupling depends on the wavelength and the excitation power.

## 1.2.5 Semiconductor laser

In this section, we will discuss the laser rate equations for semiconductors taking spontaneous emission into account. We follow the book by Rosencher and Vinter [96] but with a correction in Eq. 1.77 (see for example Ref. [108]).

The coupling between the carrier density  $n$  and photon density  $s$  in the cavity is given by

$$\frac{dn}{dt} = P - \gamma_{tot}n - c'Gs(n - n_{tr}), \quad (1.76)$$

$$\frac{ds}{dt} = c'Gs(n - n_{tr})\Gamma - \gamma_Cs + \Gamma\beta\gamma_{spon}n. \quad (1.77)$$

The first term in Eq. 1.76 describes the electron-hole pairs created by the pump  $P$ . The second term describes the carriers lost through recombination processes excluding stimulated emission with  $\gamma_{tot}$  the total carrier recombination rate. The third term accounts for the carriers lost through stimulated emission and gained through absorption with  $c'$  the speed of light in the semiconductor,  $G$  the gain, and  $n_{tr}$  the transparency carrier density, that is the carrier density for which stimulated emission and absorption are equal. In Eq. 1.77, the first term describes the photons created through stimulated emission and those lost through absorption, with  $\Gamma$  the spatial overlap between the carriers and the cavity mode. The second term describes the cavity losses with  $\gamma_C$  the cavity loss rate. The third term describes the spontaneous emission with  $\beta$  the spontaneous emission factor, and  $\gamma_{spon}$  the spontaneous emission rate.

In the steady state,  $dn/dt = 0$  and  $ds/dt = 0$  and we can solve Eqs. 1.76 and 1.77 for  $P$  and  $s$  and we obtain

$$P = \gamma_{tot}n - c'G(n - n_{tr})s, \quad (1.78)$$

$$s = \frac{\Gamma\beta\gamma_{spon}n}{\gamma_C - c'G(n - n_{tr})\Gamma}. \quad (1.79)$$

The threshold carrier density  $n_{th}$  is reached when the denominator in Eq. 1.79 is 0, that is when the cavity losses are equal to the gain and we get

$$n_{th} = n_{tr} + \frac{\gamma_C}{c'\Gamma}. \quad (1.80)$$

We define two new variables:  $x := n/n_{tr}$  and  $\alpha := n_{th}/n_{tr} = 1 + \gamma_C/(\Gamma c'Gn_{tr})$ .

We can now rewrite Eq. 1.79 using Eq. 1.80 and  $x$  and  $\alpha$  as

$$s = \frac{\Gamma\beta\gamma_{spon}}{c'\Gamma} \frac{x}{\alpha - x}. \quad (1.81)$$

The pump power needed to reach transparency  $P_{tr}$  is obtained by setting  $n = n_{tr}$  in Eq. 1.78:

$$P_{tr} = \gamma_{tot}n_{tr}. \quad (1.82)$$

We divide Eq. 1.78 by  $P_{tr}$ , substitute  $s$  with Eq. 1.81, and use the definitions of  $x$  and  $\alpha$  and obtain

$$\frac{P}{P_{tr}} = x + \beta \frac{\gamma_{spon}}{\gamma_{tot}} \frac{x(x+1)}{\alpha - x}. \quad (1.83)$$

We now use Eq. 1.80 and  $\alpha$  to rewrite Eq. 1.81 as

$$s = \frac{\Gamma\beta\gamma_{spon}n_{tr}(\alpha - 1)}{\gamma_C} \frac{x}{\alpha - x}. \quad (1.84)$$

Eqs. 1.83 and 1.84 are parametric equations in  $x$ , which allows us to plot  $s(P)$ .

Alternatively, we can solve Eq. 1.83 for  $x$  and substitute it into Eq. 1.84.

We get

$$x = -\frac{-\sqrt{\alpha^2 + 2\alpha\left(2\frac{P}{P_{tr}}\beta\frac{\gamma_{spon}}{\gamma_{tot}} - \frac{P}{P_{tr}} + \beta\frac{\gamma_{spon}}{\gamma_{tot}}\right) + \left(\frac{P}{P_{tr}} + \beta\frac{\gamma_{spon}}{\gamma_{tot}}\right)^2} + \alpha + \frac{P}{P_{tr}} + \beta\frac{\gamma_{spon}}{\gamma_{tot}}}{2\left(\beta\frac{\gamma_{spon}}{\gamma_{tot}} - 1\right)}, \quad (1.85)$$

and consequently

$$s(P) = \frac{\Gamma \beta \gamma_{spon} n_{tr} (\alpha - 1)}{\gamma_C} \frac{-\sqrt{\alpha^2 + 2\alpha \left( 2 \frac{P}{P_{tr}} \beta \frac{\gamma_{spon}}{\gamma_{tot}} - \frac{P}{P_{tr}} + \beta \frac{\gamma_{spon}}{\gamma_{tot}} \right) + \left( \frac{P}{P_{tr}} + \beta \frac{\gamma_{spon}}{\gamma_{tot}} \right)^2} + \alpha + \frac{P}{P_{tr}} + \beta \frac{\gamma_{spon}}{\gamma_{tot}}}{2 \left( \beta \frac{\gamma_{spon}}{\gamma_{tot}} - 1 \right)} \cdot \quad (1.86)$$

$$\alpha + \frac{-\sqrt{\alpha^2 + 2\alpha \left( 2 \frac{P}{P_{tr}} \beta \frac{\gamma_{spon}}{\gamma_{tot}} - \frac{P}{P_{tr}} + \beta \frac{\gamma_{spon}}{\gamma_{tot}} \right) + \left( \frac{P}{P_{tr}} + \beta \frac{\gamma_{spon}}{\gamma_{tot}} \right)^2} + \alpha + \frac{P}{P_{tr}} + \beta \frac{\gamma_{spon}}{\gamma_{tot}}}{2 \left( \beta \frac{\gamma_{spon}}{\gamma_{tot}} - 1 \right)}$$

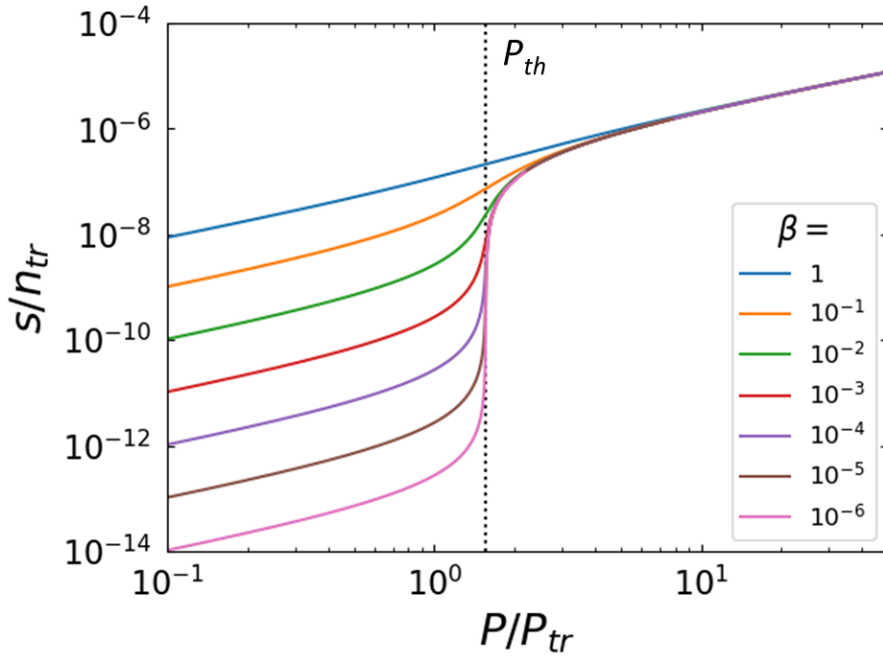


Figure 1.21: Intensity over pump power for different values of  $\beta$  for a semiconductor laser.  $P_{th}$  is indicated.

Fig. 1.21 shows a double-log plot of the normalized photon number over pump power for different values of  $\beta$  using  $\alpha = 1.56$ ,  $\gamma_C = 7.7 \times 10^{11} \text{ s}^{-1}$ ,  $\gamma_{tot} = 2.0 \times 10^8 \text{ s}^{-1}$ ,  $\gamma_{spon} = 4.7 \times 10^7 \text{ s}^{-1}$ , and  $\Gamma = 0.0044$ . The threshold is indicated by the vertical dashed line. It is located at the center of the S-shape where the slope is largest. For  $\beta < 1$ , we observe the characteristic S-shape showing the regimes of spontaneous emission, amplified spontaneous emission, and stimulated emission. For  $\beta = 1$  we have a "thresholdless" laser.

## 1.2.6 2D photonic crystal slab

Photonic crystals are optical structures in which the refractive index changes periodically in one, two, or three dimensions, which is illustrated schematically in Fig. 1.22. This periodicity creates a photonic band gap - a range of forbidden frequencies. This phenomenon is in analogy to the electronic band gap created in an atomic crystal. The periodicity of the refractive index change must be in the order of the wavelength in the material at the band gap. 1D pho-

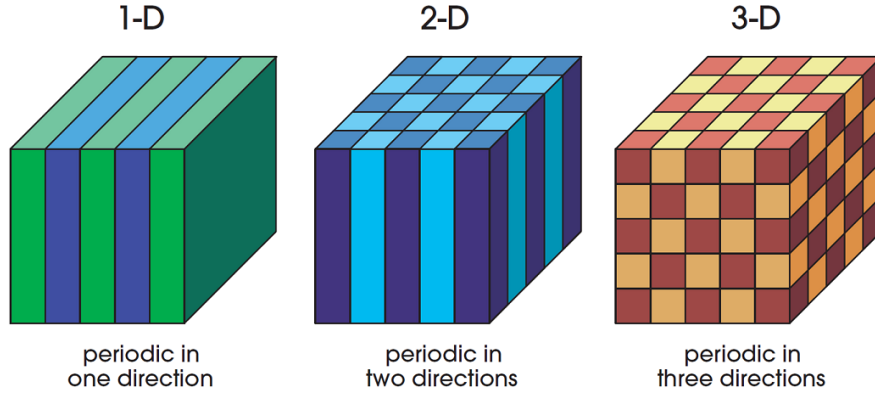


Figure 1.22: Schematic of 1D, 2D, and 3D PhCs. The different colors represent materials with different refractive indices. Reproduced from Ref. [109].

tonic band gaps were first observed by Lord Rayleigh in 1887, who studied periodic dielectric multi-layer stacks [110]. The well-known Bragg mirrors, which consist of  $\lambda/(4n)$  layers of two alternating dielectric materials with high and low refractive indices are 1D PhCs, for example. Wavelengths that are in the band gap of the Bragg mirror are reflected.

Another 100 years passed before the study of photonic crystals became popular thanks to two seminal papers by Yablonovitch [111] and John [112] in 1987. The first experimental realization of 3D photonic crystals followed quickly in 1991 by Yablonovitch et al. [113]. In 1996, Kraus et al. demonstrated 2D PhCs at optical wavelengths [114].

We will focus on 2D PhC slabs, which have a finite height  $h \approx \frac{\lambda}{2n_{eff}}$ . The out-of-plane confinement is given by the slab waveguide. First, we determine the photonic band diagram for a 2D photonic crystal by solving Maxwell's equations using Bloch's theorem for periodic dielectric media [115–117]. Then, we apply the total internal reflection of the slab, which gives us guided modes below the light line given by  $\omega = c \cdot |k_{\parallel}|$ , where  $k_{\parallel}$  is the in-plane wave-vector.

We follow the description in Ref. [115]. The relative dielectric constant  $\epsilon(\mathbf{r}_{\parallel})$  is periodic in the plane.  $\epsilon(\mathbf{r}_{\parallel} + \mathbf{a}_i) = \epsilon(\mathbf{r}_{\parallel})$ , with  $\mathbf{r}_{\parallel} = (x, y)$  and  $\mathbf{a}_i$  the elementary lattice vectors with  $i = 1, 2$ .

In the reciprocal lattice, the elementary vectors are  $\mathbf{b}_i$  with  $\mathbf{a}_i \cdot \mathbf{b}_j = 2\pi\delta_{ij}$ , where  $\delta_{ij}$  is the Kronecker delta. The reciprocal lattice vector  $\mathbf{G}_{\parallel}$  is given by  $\mathbf{G}_{\parallel} = l_1\mathbf{b}_1 + l_2\mathbf{b}_2$ , where  $l_i$  are arbitrary integers. Fig. 1.23 shows triangular real and reciprocal lattices, indicating the first Brillouin zone, the irreducible Brillouin zone, and the real and reciprocal lattice vectors.

We can expand  $1/\epsilon(\mathbf{r}_{\parallel})$  into a Fourier series:

$$\frac{1}{\epsilon(\mathbf{r}_{\parallel})} = \sum_{\mathbf{G}_{\parallel}} \kappa(\mathbf{G}_{\parallel}) e^{i\mathbf{G}_{\parallel} \cdot \mathbf{r}_{\parallel}}. \quad (1.87)$$

The electromagnetic waves travel in the x-y-plane and are uniform in z. Maxwell's curl equations (Eqs. 1.7 and 1.8) turn into

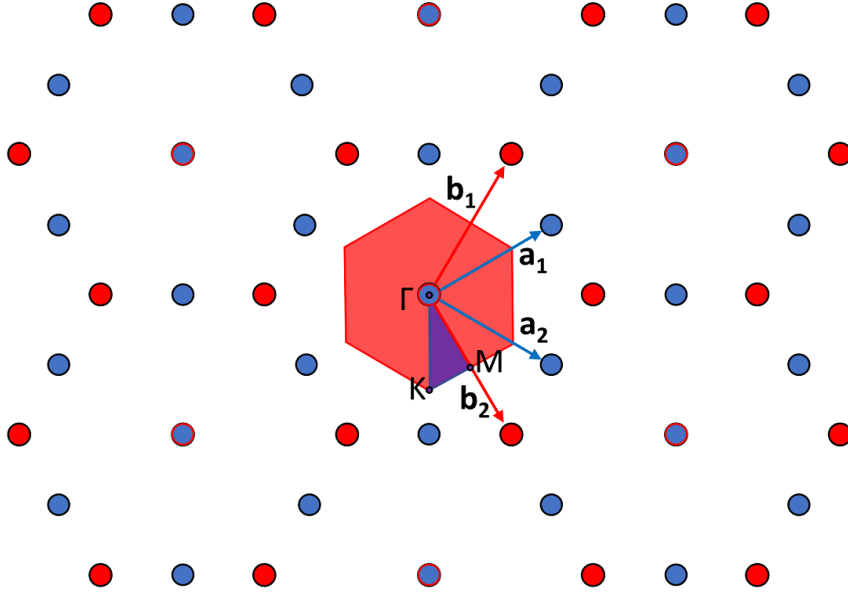


Figure 1.23: Sketch of the triangular lattice (blue circles) and reciprocal lattice (red circles). The first Brillouin zone is marked as a red hexagon. The elementary lattice vectors of the real lattice  $\mathbf{a}_1$ ,  $\mathbf{a}_2$  and of the reciprocal lattice  $\mathbf{b}_1$ ,  $\mathbf{b}_2$  are indicated. The  $\Gamma$ ,  $M$ , and  $K$  points of the irreducible Brillouin zone (purple triangle) are shown.

$$\frac{\partial}{\partial y} E_z(\mathbf{r}_{\parallel}, t) = -\mu_0 \frac{\partial}{\partial t} H_x(\mathbf{r}_{\parallel}, t), \quad (1.88)$$

$$\frac{\partial}{\partial x} E_z(\mathbf{r}_{\parallel}, t) = \mu_0 \frac{\partial}{\partial t} H_y(\mathbf{r}_{\parallel}, t), \quad (1.89)$$

$$\frac{\partial}{\partial x} E_y(\mathbf{r}_{\parallel}, t) - \frac{\partial}{\partial y} E_x(\mathbf{r}_{\parallel}, t) = -\mu_0 \frac{\partial}{\partial t} H_z(\mathbf{r}_{\parallel}, t), \quad (1.90)$$

$$\frac{\partial}{\partial y} H_z(\mathbf{r}_{\parallel}, t) = \epsilon_0 \epsilon(\mathbf{r}_{\parallel}) \frac{\partial}{\partial t} E_x(\mathbf{r}_{\parallel}, t), \quad (1.91)$$

$$\frac{\partial}{\partial x} H_z(\mathbf{r}_{\parallel}, t) = -\epsilon_0 \epsilon(\mathbf{r}_{\parallel}) \frac{\partial}{\partial t} E_y(\mathbf{r}_{\parallel}, t), \quad (1.92)$$

$$\frac{\partial}{\partial x} H_y(\mathbf{r}_{\parallel}, t) - \frac{\partial}{\partial y} H_x(\mathbf{r}_{\parallel}, t) = \epsilon_0 \epsilon(\mathbf{r}_{\parallel}) \frac{\partial}{\partial t} E_z(\mathbf{r}_{\parallel}, t). \quad (1.93)$$

From Eqs. 1.88, 1.89 and 1.93, we get the wave equation for  $E_z(\mathbf{r}_{\parallel}, t)$  and from Eqs. 1.90, 1.91, and 1.92, we get the wave equation for  $H_z(\mathbf{r}_{\parallel}, t)$ :

$$\frac{1}{\epsilon(\mathbf{r}_{\parallel})} \left( \frac{\partial^2}{\partial x^2} + \frac{\partial^2}{\partial y^2} \right) E_z(\mathbf{r}_{\parallel}, t) = \frac{1}{c^2} \frac{\partial^2}{\partial t^2} E_z(\mathbf{r}_{\parallel}, t), \quad (1.94)$$

$$\left( \frac{\partial}{\partial x} \frac{1}{\epsilon(\mathbf{r}_{\parallel})} \frac{\partial}{\partial x} + \frac{\partial}{\partial y} \frac{1}{\epsilon(\mathbf{r}_{\parallel})} \frac{\partial}{\partial y} \right) H_z(\mathbf{r}_{\parallel}, t) = \frac{1}{c^2} \frac{\partial^2}{\partial t^2} H_z(\mathbf{r}_{\parallel}, t). \quad (1.95)$$

We are looking for solutions of the form

$$E_z(\mathbf{r}_{\parallel}, t) = E_z(\mathbf{r}_{\parallel}) e^{-i\omega t}, \quad (1.96)$$

$$H_z(\mathbf{r}_{\parallel}, t) = H_z(\mathbf{r}_{\parallel}) e^{-i\omega t}, \quad (1.97)$$

with angular frequency  $\omega$ .

This gives us the following eigenvalue equations:

$$\mathcal{L}_E E_z(\mathbf{r}_{\parallel}) := -\frac{1}{\epsilon(\mathbf{r}_{\parallel})} \left( \frac{\partial^2}{\partial x^2} + \frac{\partial^2}{\partial y^2} \right) E_z(\mathbf{r}_{\parallel}) = \frac{\omega^2}{c^2} E_z(\mathbf{r}_{\parallel}), \quad (1.98)$$

$$\mathcal{L}_H H_z(\mathbf{r}_{\parallel}) := -\left( \frac{\partial}{\partial x} \frac{1}{\epsilon(\mathbf{r}_{\parallel})} \frac{\partial}{\partial x} + \frac{\partial}{\partial y} \frac{1}{\epsilon(\mathbf{r}_{\parallel})} \frac{\partial}{\partial y} \right) H_z(\mathbf{r}_{\parallel}) = \frac{\omega^2}{c^2} H_z(\mathbf{r}_{\parallel}), \quad (1.99)$$

with operators  $\mathcal{L}_E$  and  $\mathcal{L}_H$ .

Since  $\epsilon(\mathbf{r}_{\parallel})$  is periodic, we can apply Bloch's theorem and we can write  $E_z(\mathbf{r}_{\parallel})$  and  $H_z(\mathbf{r}_{\parallel})$  as

$$E_z(\mathbf{r}_{\parallel}) = E_{z,\mathbf{k}_{\parallel},n}(\mathbf{r}_{\parallel}) = u_{z,\mathbf{k}_{\parallel},n}(\mathbf{r}_{\parallel}) e^{i\mathbf{k}_{\parallel} \cdot \mathbf{r}_{\parallel}}, \quad (1.100)$$

$$H_z(\mathbf{r}_{\parallel}) = H_{z,\mathbf{k}_{\parallel},n}(\mathbf{r}_{\parallel}) = v_{z,\mathbf{k}_{\parallel},n}(\mathbf{r}_{\parallel}) e^{i\mathbf{k}_{\parallel} \cdot \mathbf{r}_{\parallel}}, \quad (1.101)$$

where  $n$  is the band index, and  $u_{z,\mathbf{k}_{\parallel},n}$  and  $v_{z,\mathbf{k}_{\parallel},n}$  are periodic vectorial functions with  $u_{z,\mathbf{k}_{\parallel},n}(\mathbf{r}_{\parallel} + \mathbf{a}_i) = u_{z,\mathbf{k}_{\parallel},n}(\mathbf{r}_{\parallel})$  and  $v_{z,\mathbf{k}_{\parallel},n}(\mathbf{r}_{\parallel} + \mathbf{a}_i) = v_{z,\mathbf{k}_{\parallel},n}(\mathbf{r}_{\parallel})$ .

We use the Fourier expansion due to the periodicity and obtain

$$E_{z,\mathbf{k}_{\parallel},n}(\mathbf{r}_{\parallel}) = \sum_{\mathbf{G}_{\parallel}} E_{z,\mathbf{k}_{\parallel},n}(\mathbf{G}_{\parallel}) e^{i(\mathbf{k}_{\parallel} + \mathbf{G}_{\parallel}) \cdot \mathbf{r}_{\parallel}}, \quad (1.102)$$

$$H_{z,\mathbf{k}_{\parallel},n}(\mathbf{r}_{\parallel}) = \sum_{\mathbf{G}_{\parallel}} H_{z,\mathbf{k}_{\parallel},n}(\mathbf{G}_{\parallel}) e^{i(\mathbf{k}_{\parallel} + \mathbf{G}_{\parallel}) \cdot \mathbf{r}_{\parallel}}. \quad (1.103)$$

We substitute Eqs. 1.87, 1.102, and 1.103 into Eqs. 1.98 and 1.99 and obtain

$$\sum_{\mathbf{G}'_{\parallel}} \kappa(\mathbf{G}_{\parallel} - \mathbf{G}'_{\parallel}) |\mathbf{k}_{\parallel} + \mathbf{G}'_{\parallel}|^2 E_{z,\mathbf{k}_{\parallel},n}(\mathbf{G}'_{\parallel}) = \frac{\omega_{E,\mathbf{k}_{\parallel},n}^2}{c^2} E_{z,\mathbf{k}_{\parallel},n}(\mathbf{G}_{\parallel}), \quad (1.104)$$

$$\sum_{\mathbf{G}'_{\parallel}} \kappa(\mathbf{G}_{\parallel} - \mathbf{G}'_{\parallel}) (\mathbf{k}_{\parallel} + \mathbf{G}_{\parallel}) \cdot (\mathbf{k}_{\parallel} + \mathbf{G}'_{\parallel}) H_{z,\mathbf{k}_{\parallel},n}(\mathbf{G}'_{\parallel}) = \frac{\omega_{H,\mathbf{k}_{\parallel},n}^2}{c^2} H_{z,\mathbf{k}_{\parallel},n}(\mathbf{G}_{\parallel}), \quad (1.105)$$

where Eq. 1.104 describes TM modes and Eq. 1.105 describes TE modes. These equations need to be solved numerically. We use a frequency domain eigensolver called MPB [118] to

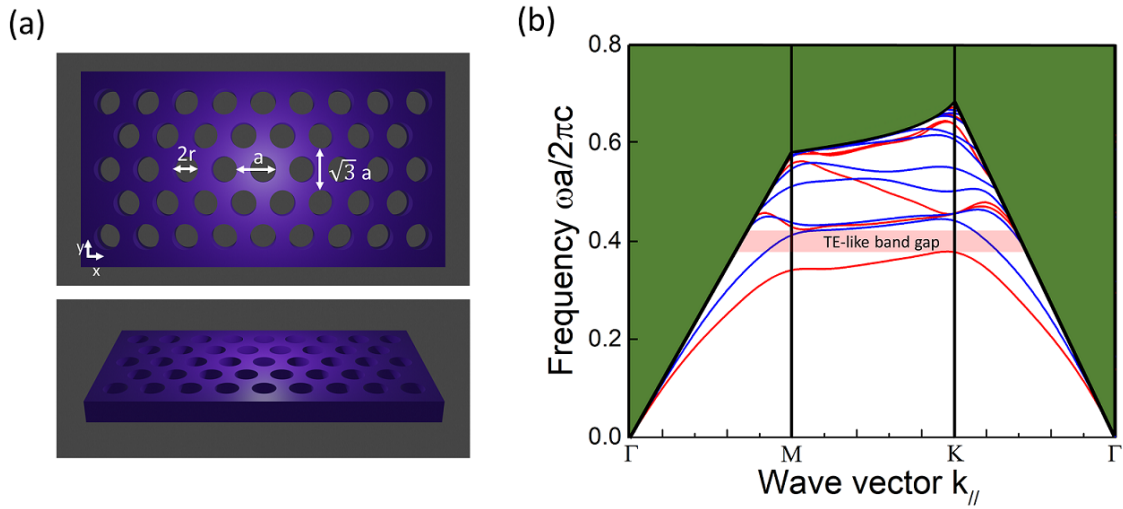


Figure 1.24: (a) Triangular air-hole slab PhC and (b) photonic band diagram of the PhC in (a) with TE-bands in red and TM-bands in blue, showing a TE-like gap and the light cone marked in green.

determine the photonic band diagram.

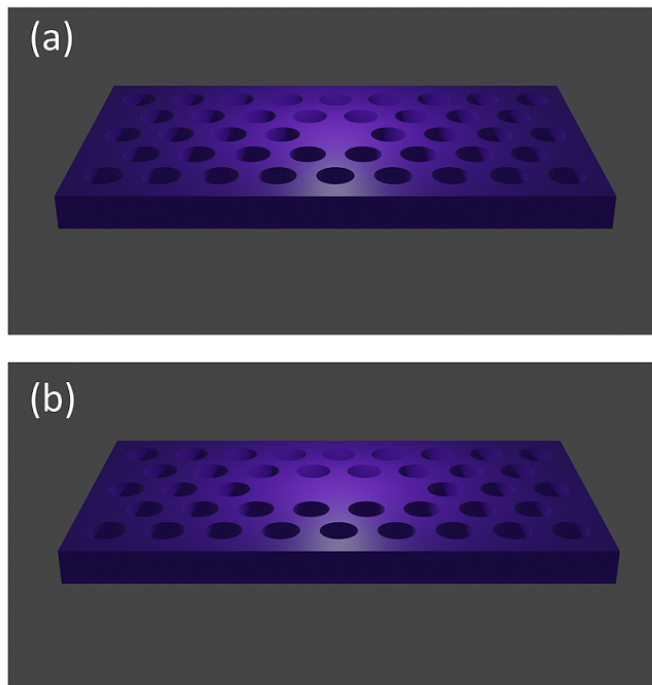


Figure 1.25: 2D PhCs slabs with (a) L1 and (b) L3 cavity.

There are two dominant designs for 2D PhCs, high-index rods in low-index material or low-index holes in high-index material. The rods have a TM band gap while the holes have a TE band gap, since the electric field needs to run along thin veins to create a band gap. We will

investigate triangular lattice air-hole slabs, as shown in Fig. 1.24 (a) with a period of  $a$  in  $x$ -direction, a period of  $\sqrt{3}a$  in  $y$ -direction, and a hole radius of  $r$ . A photonic band diagram is shown in Fig. 1.24 (b) for the PhC slab represented in Fig. 1.24 (a) for AlN with  $h = 80$  nm,  $a = 130$  nm, and  $r/a = 0.28$ . The red lines are TE-bands while the blue lines are TM-bands. This PhC has a TE-like band gap from 302 to 344 nm. The light cone given by the finite thickness is marked in green.

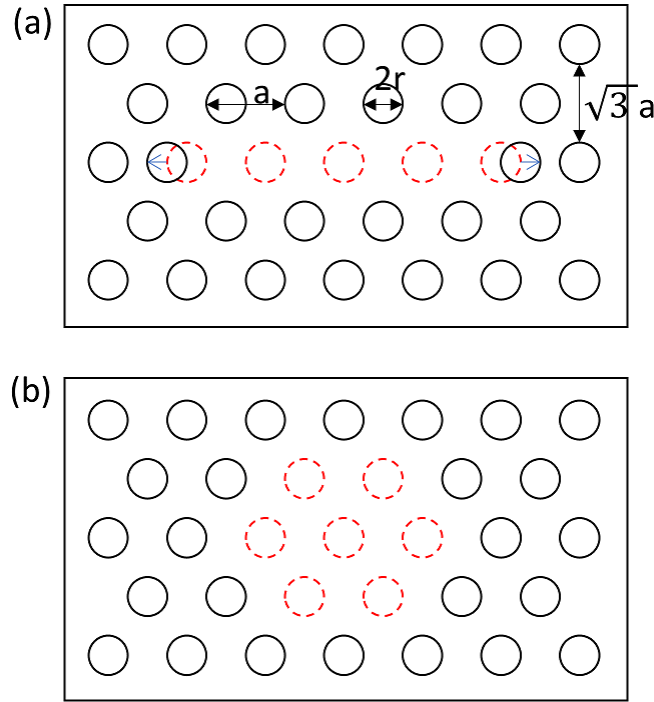


Figure 1.26: Sketches of (a) L3 and (b) H2 cavities.

Light can be confined inside a PhC by creating a defect in the lattice, i.e. by removing holes in the air-hole slab. Fig 1.25 shows two such PhC cavities with (a) one missing hole (L1 or H1 cavity) and (b) three missing holes in a line (L3 cavity). The L stands for line and the H for hexagon. In this thesis, we will study L3 and H2 cavities, which are schematically illustrated in Fig. 1.26. The L3 cavities correspond to the design introduced by Akahane et al. [119], i.e. of type 0, which means the two holes adjacent to the line defect are displaced by a value  $d/a$  [120]. The H2 cavity is a hexagon of missing holes with side-length 2. As Akahane et al. pointed out, light needs to be confined gently in order to be confined strongly [119]. Fig. 1.27 shows a simple model created by Akahane et al. [119]. They investigate a slab cavity with perfect mirrors in  $x$ -direction and total internal reflection in  $z$ -direction (Fig. 1.27 (a)). The corresponding electric field is shown in Fig. 1.27 (b) and its Fourier transform (FT) in Fig. 1.27 (c). The leaky  $k$ -vectors, which are outside of the light cone, are highlighted,  $k < 2\pi/\lambda$ . Fig. 1.27 (d) shows the electric field for more gentle  $x$ -confinement and its FT in Fig. 1.27 (e), which has fewer leaky components. For the 2D PhC slab, this means that by moving the holes adjacent to the defect,

the electric field is less abruptly confined and the leaky components are reduced, which results in a large Q factor.

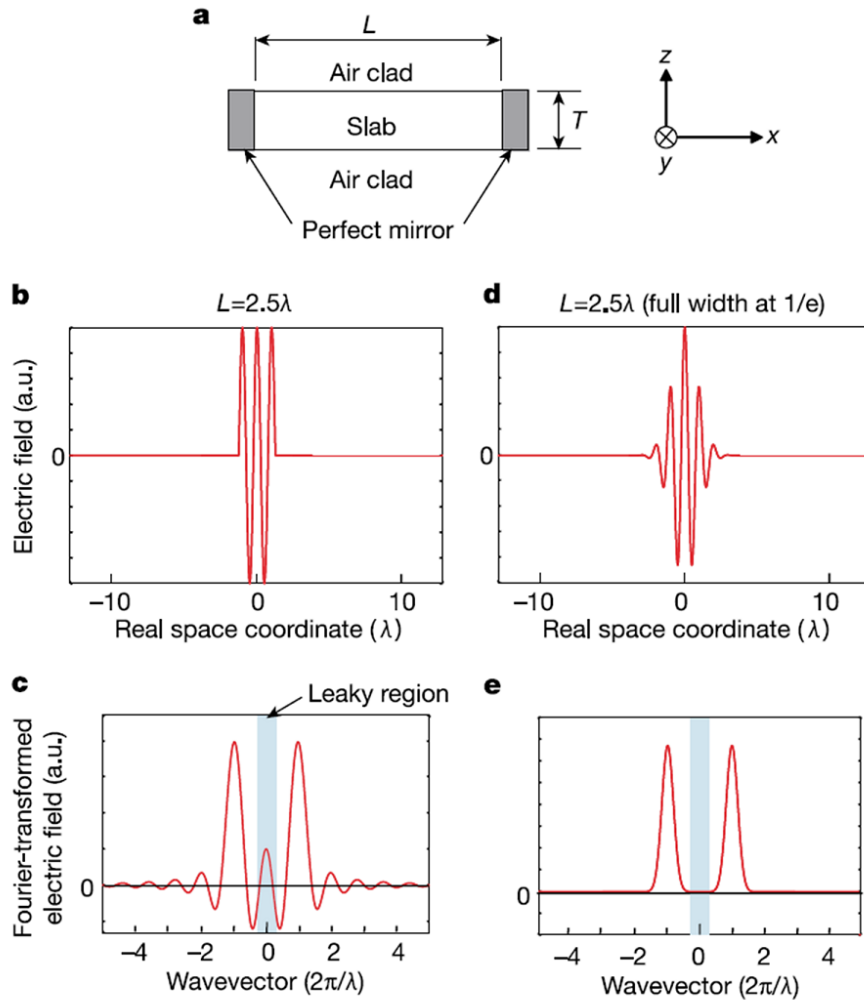


Figure 1.27: Simple model describing the need for gentle confinement in a slab cavity. (a) Slab with perfect mirrors, (b) E-field of the slab in (a), (c) FT of the E-field in (b), (d) E-field of a cavity with gentle confinement, (e) FT of the E-field in (d) with less components in the leaky region. Reproduced from Ref. [119].

### 1.2.7 Grating coupler

We use grating couplers to couple light out of and into waveguides in both active and passive devices. We can use a simple ray optics model to approximately determine the grating period required for a certain diffraction angle using the Bragg condition of constructive interference for a periodic one-dimensional structure.

Fig. 1.28 shows a sketch of two grating teeth. We require constructive interference between the two indicated light rays. This is given when the difference of their phases is an integer

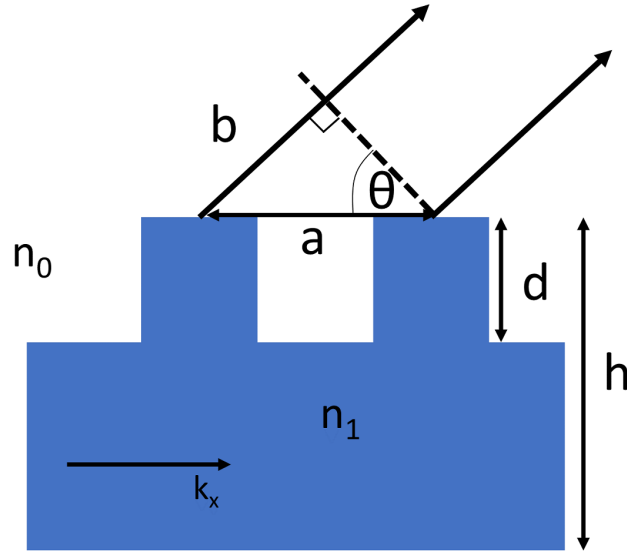


Figure 1.28: Sketch of a grating coupler.

multiple of  $2\pi$ .

$$k_x a - k_0 b = 2\pi m, \quad (1.106)$$

with grating period  $a$ , difference in path length  $b$ , angle of diffraction  $\theta$ , diffraction order  $m \in \mathbb{Z}$ ,  $\sin(\theta) = b/a$ , and  $k_x = 2\pi n_{eff}/\lambda$  and  $k_0 = 2\pi n_0/\lambda$  the wave numbers inside the waveguide and in the surrounding material (i.e. air).

This gives us the following equation for  $a$ :

$$a = \frac{m\lambda}{n_{eff} - n_0 \sin\theta}. \quad (1.107)$$

We can determine  $n_{eff}$  of the grating using the effective index of the slab waveguide  $n_{eff,1}$  (see section 1.2.1), the fill-factor (FF) of the grating, and the effective index of the etched part of the grating  $n_{eff,2}$ . We get

$$n_{eff} = n_{eff,1} FF + n_{eff,2}(1 - FF). \quad (1.108)$$

For a fully etched grating,  $n_{eff,2} = 1$ . For sample A2587 (330 nm AlN) with  $\lambda = 780$  nm and  $FF = 70\%$ , the effective index is  $n_{eff} = 1.6$  according to Eq. 1.108. Table 1.6 summarizes the parameters for this grating with different periods  $a$  and the resulting angles  $\theta$ . For example for  $a = 580$  nm, we get  $\theta = 15^\circ$ .

These equations work well for the simple case of a fully etched grating made of a single material. For more complicated layer stacks and not fully etched gratings, it is easier and more precise to use numerical simulations. We use FDTD, which we will discuss further in the fol-

lowing section for different devices.

$\lambda$ (nm)	FF (%)	$n_{eff,1}$	$n_{eff,2}$	$n_{eff}$	a (nm)	$\theta$ (°)
780	70	1.9	1	1.6	560	12
780	70	1.9	1	1.6	580	15
780	70	1.9	1	1.6	600	17

Table 1.6: Parameters for a grating coupler at  $\lambda = 780$  nm for sample A2587, giving the angles for different periods.

### 1.2.8 FDTD method

The finite-difference time-domain (FDTD) method is a numerical simulation method that solves the time-dependent Maxwell's equations by discretization of both space and time. This allows for the simulation of a large range of frequencies simultaneously. A leapfrog method is used, where in each spatial grid element the electric and magnetic field components are solved at different steps in time and different locations in space in an iterative manner. We refer to the book by Sullivan for more information about the FDTD method [121].

We mainly use MEEP [105], a free and open-source software package, for our simulations. Simulations can be performed in 1, 2, or 3 dimensions. For microdisks and microdisk to waveguide coupling, we use 3D simulations for maximum accuracy, while for grating couplers a 2D simulation is sufficient. In some cases, especially for large structures such as microrings, we use Lumerical MODE Solutions [122], a commercial software that employs 2D variational FDTD, which translates the 3D structure into a 2D structure with effective indices, which results in much shorter simulation times.

The spatial grid size needs to be sufficiently small to resolve the wavelength in the material. In MEEP, we typically use at least 8 grid elements per wavelength. Very fine grid sizes result in long simulation times. To precisely simulate the coupling between microdisks and waveguides in the blue, we use 16 grid elements per wavelength, which results in simulation times of up to 16 days.

#### 1.2.8.1 Simulating a microdisk

To simulate a microdisk in MEEP, first we define all our variables including the microdisk height  $h$  and radius  $r$ , the wavelength, and the dielectric constants  $\epsilon_o$  and  $\epsilon_e$  of AlN and GaN given by Eqs. 1.3 and 1.4 and Table 1.3 via  $\epsilon_i = n_i^2$ , where  $i = o, e$ . We define the cell in all three dimensions, making it a bit larger than the microdisk itself. Then, we define the center frequency and pulse width.

Next, we create the lattice and we create the microdisk within it by defining cylinders of the different materials (i.e. AlN and GaN) with their dielectric constants ( $\epsilon_x, \epsilon_y, \epsilon_z$ ). We can also make the microdisks absorbing to limit the Q factor to experimentally observed values.

We set the perfectly matched layers (PML), thin layers at the edge of the cell that absorb the electromagnetic waves in order to avoid reflection. We set the resolution to, for example, 8 grid elements per wavelength in the material.

Then, we set a Gaussian pulse source with the previously defined center frequency and pulse width. We choose the field component  $H_z$  because we are mainly interested in TE modes. We define the center and the size of the source. For the microdisk, we place the source at 10 nm from the edge as a line with the height of the disk.

Lastly, we define for how long the simulation runs. We usually take the run-time of the source plus  $2\pi\tau$ , where  $\tau$  is the decay time of the cavity mode. Meep uses natural units, so  $\tau = Q\lambda/(2\pi)$ . This allows to simulate accurately devices of quality factor  $Q$ . We output the  $H_z$  field at every 10th time-step.

The mode profiles shown in Fig. 1.16 have been obtained this way using a pulse width of 0.5 nm and  $Q = 5000$ .

### 1.2.8.2 Design of the coupling region

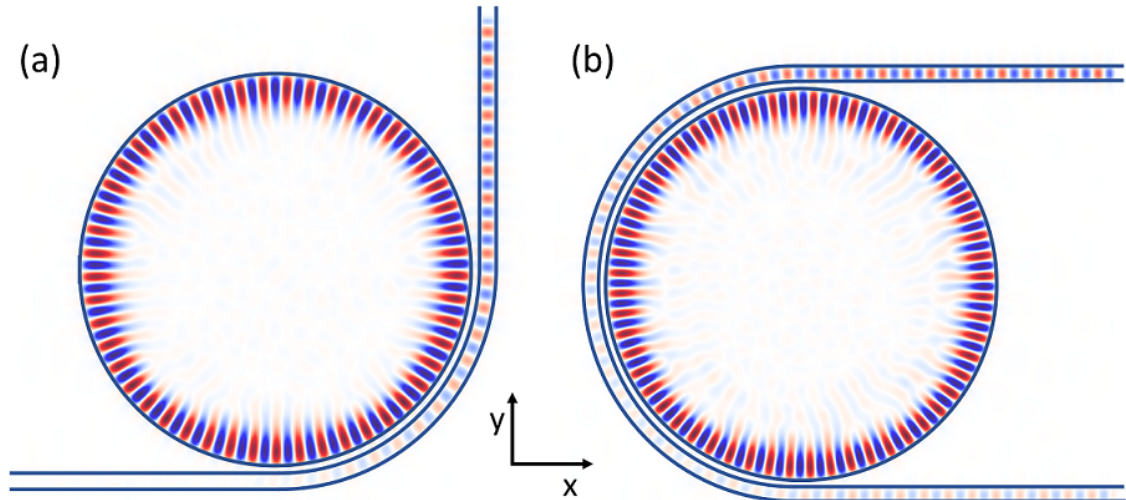


Figure 1.29: FDTD simulations of the  $H_z$  field for 3  $\mu\text{m}$  diameter disks with (a)  $A = 90^\circ$ ,  $g = 50$  nm, and  $w = 135$  nm at  $\lambda = 423$  nm and (b)  $A = 180^\circ$ ,  $g = 50$  nm, and  $w = 125$  nm at  $\lambda = 391$  nm.

To design the microdisk to waveguide coupling region, we start from the previously discussed microdisk and add a waveguide. We define its width  $w$ , its distance from the disk or gap  $g$ , and its height  $h_2$ . For a straight waveguide, we define a rectangular box. For a  $90^\circ$  or  $180^\circ$  bent waveguide, we first define AlN and GaN cylinders of radius  $r + g + w$  and then air cylinders of radius  $r + g$  to define the curved part of the waveguide. Then, we add rectangular boxes at the end of the curved part. For our active structures, the waveguide is thinner than the disk because we need to remove the QWs to avoid reabsorption. Fig. 1.29 shows two examples with  $90^\circ$

or  $180^\circ$  bent waveguide at  $\lambda = 423$  nm and  $\lambda = 391$  nm, respectively, showing first-order radial modes.

We place a Gaussian source of the same cross-section as the waveguide at one end of the waveguide (bottom left in Fig. 1.29 (a) and bottom right in Fig. 1.29 (b)). And we measure the flux going through the cross-section of the waveguide just after the source. We define a second flux region at the other end of the waveguide. The ratio of these two fluxes gives us the transmission as a function of wavelength, which will show the transmission dips at the WGMs.

With these simulations, we aim to find a combination of  $g$  and  $w$  that allows for critical coupling. We vary  $g$  and  $w$  until we find a minimum in the transmission for a given mode. We can verify the radial mode order by looking at the  $H_z$  profile. We choose  $g$  and  $w$  in such a way that the first order radial modes ( $n = 1$ ) couple preferentially.

We will discuss the sample and wavelength specific design of the coupling regions in the respective chapters.

### 1.2.8.3 Photonic crystal slab design

In the case of the photonic crystal (PhC) slab, we perform 3D simulations. We define a rectangular box of height  $h$  and with  $x$  and  $y$  dimensions larger than the simulation cell in order to emulate an infinite slab. Then, we define air-hole cylinders of radius  $r$  and height  $h$ , according to the triangular lattice described in section 1.2.6 with a period of  $a$ . In the center of the slab, we create the defect by omitting the corresponding air holes. The holes adjacent to the defect are displaced by  $d/a$ . We vary  $r/a$  and  $d/a$  to find high-Q modes in the band gap that overlap with the emission spectra of the QWs.

We place the Gaussian source in the center of the defect, where we also collect the  $H_z$  field, which we can later post-process with a Matlab script written by X. Chécoury to extract the spectrum and the Q factors of the modes.

Furthermore, using MPB [118], which computes definite-frequency eigenstates, we can determine the photonic band structure of our PhC slab as shown exemplary in section 1.2.6.

### 1.2.8.4 Grating coupler design

For the grating couplers, we use 2D simulations. The goal here is to identify the angle at which light is best extracted by the grating for a given grating period  $P$  and fill-factor  $FF$ . We simulate the  $E_y$  field (TE mode) in the  $x$ - $z$ -plane (see Fig. 1.30), where  $x$  is the propagation direction and  $z$  is the out-of-plane direction. We create rectangular boxes of AlN and GaN with their respective heights and with infinite width. The Gaussian pulse source is placed at one end of the waveguide (left side in Fig. 1.30). Fig. 1.30 shows an example of a waveguide with grating coupler with the structure of sample A2587 (330 nm AlN) and  $P = 580$  nm,  $FF = 70\%$ , and  $\lambda = 780$  nm. The grating is fully etched. The resulting angle of emission is  $15^\circ$ .

Depending on the wavelength range and experimental setup, different angles are targeted. For the NIR, it is very important to precisely know the angle of the grating in order to couple

light from a fiber into the grating or vice versa. We aim for an angle around  $15^\circ$ . In the blue/UV, where we use microscope objectives to collect the emission, the grating angle is not very relevant, however, large angles need to be avoided and we aim for around  $0^\circ$ .

In the framework of this thesis, we have not done any more advanced grating simulations or optimizations to try to improve the coupling efficiency, for example. This could be done in future work, especially for the NIR spectral range, as high coupling efficiency can help achieve non-linear optical effects like optical parametric oscillation.

We will discuss the device and sample specific simulations in more detail in the respective chapters.

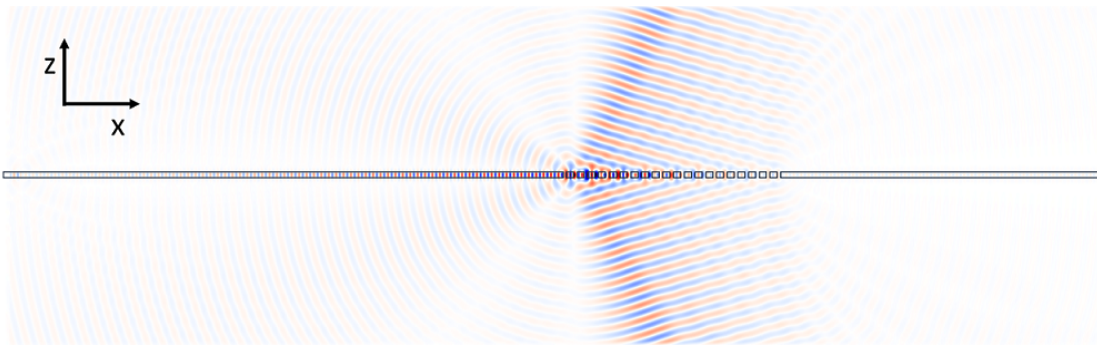


Figure 1.30: 2D FDTD simulation of  $E_y$  field of a grating coupler with  $P = 580\text{ nm}$ ,  $FF = 70\%$ , and  $\lambda = 780\text{ nm}$ . The angle of emission is  $15^\circ$ .

### 1.3 Fabrication of III-nitride on silicon photonic devices

In this section, we will discuss the processing of five types of devices: an active microdisk, an active microdisk coupled to a passive waveguide, two passive photonic circuits, one with a microdisk coupled to a waveguide and the other with a microring coupled to a waveguide, and a 2D PhC slab cavity. We will explain the process flows of these devices and highlight some of the challenges, giving fabrication examples. The sample specific details, can be found in the respective chapters. The processing of electrically injected devices will be treated separately in chapter 5.

After growth, all our 2 inch wafers are saw diced into samples of  $10 \times 11\text{ mm}$ . Our processes consist of four main components: the lithography, the etch mask, the etching, and the under-etching.

The most commonly used lithography technique for fabrication of micro- and nanoresonators is e-beam lithography due to its high resolution and precision. Conventional contact photolithography as used by research labs is limited to feature sizes in the  $500\text{ nm}$  range, while excimer laser lithography can provide minimum feature sizes down to  $50\text{ nm}$ . With e-beam lithography, features in the tens of nm range can be resolved. The drawback of e-beam lithography is its high cost and lack of scalability, making it not viable for industrial use. Another

technique that has been proposed is to use silica microspheres spin-coated in aqueous solution as a hard mask for inductively-coupled plasma (ICP) etching of III-nitride microdisks [32, 33, 123]. This approach is very cost effective, but does not allow for precision positioning nor multi-layer processes that require precision alignment. Manual pick-and-place has been used to make microdisks coupled to waveguides using silica microspheres and SiC nanowires [124], however, this method is very time-consuming.

Before discussing the etch mask, we need to choose our etch method, as this determines the requirements the mask needs to fulfil. III-nitrides are chemically very inert due to their very large bond energies. Conventional wet-etching methods are not very effective [125]. Thus, aggressive dry etching recipes need to be used to transfer patterns into the material. Different high-density plasma etch methods have been investigated, such as chemically assisted ion beam etching (CAIBE), electron-cyclotron-resonance reactive ion etching (ECR-RIE), and inductively-coupled plasma reactive ion etching (ICP-RIE) [126, 127]. Today, the probably most commonly used method is ICP etching using chlorine ( $\text{Cl}_2$ ) and boron trichloride ( $\text{BCl}_3$ ) gases. This technique allows for high etch rates up to several tens of  $\text{nm} \cdot \text{s}^{-1}$  and near-vertical sidewalls. However, dry etching can cause defects in the etched surface and post-process chemical treatments have been proposed to remove part of the etch damage [128].

In order to effectively transfer a pattern into III-nitrides, we must use a mask that can withstand the ICP etching with sufficient etch selectivity and without too much deformation, which becomes especially relevant as we deal with micro- and nanocavities and photonic circuits. Some photoresists are suitable, providing sufficient layer thickness [129]. However, more commonly, hard masks are used as an intermediary for dry etching. Thus, the resist is used to transfer the pattern into the hard mask, which in turn is used as an etch mask for dry etching. This is especially important when using e-beam lithography, where conventional resists tend to be thin and do not withstand dry etching well. Common hard masks for dry etching include plasma-enhanced chemical vapor deposited (PECVD)  $\text{SiO}_2$  or  $\text{SiN}$ , as well as e-beam evaporated Ni. The hard mask can either be dry etched using RIE or ICP, or it can be deposited after the resist patterning using a lift-off process. In the case of dry etching of the hard mask, a resist needs to be chosen that withstands the dry etching well. Many e-beam resists are not suitable for RIE etching of an  $\text{SiO}_2$  mask. Good candidates are UV8, UV5, and hardened ZEP resist, which are the ones that we use in this thesis. Another option that has gained recent popularity is to use a spin-on glass, hydrogen silsesquioxane (HSQ), for e-beam lithography, which can turn into an  $\text{SiO}_2$ -like material [6]. This allows to reduce the 2-step process to only one step, reducing the chance of etch-induced side-wall roughness and increasing the pattern precision. We are strongly considering to use HSQ in future work.

When fabricating photonic cavities on Si, the substrate needs to be underetched after transferring the pattern into the III-nitride layer, in order to have a high refractive index contrast and to avoid absorption in the substrate. Three main methods are used for this underetch: a wet-chemical etch using hydrofluoric acid (HF) and nitric acid ( $\text{HNO}_3$ ), a dry etch using sulphur

hexafluoride ( $\text{SF}_6$ ) gas, and a dry etch using pulsed xenon difluoride ( $\text{XeF}_2$ ) gas [6]. We use  $\text{XeF}_2$ , as it provides a very high etch selectivity between III-nitrides and Si.

As an alternative to underetching, we can transfer the III-nitride layer by wafer bonding on  $\text{SiO}_2/\text{Si}$  with subsequent substrate removal. We use this approach to fabricate microrings, as these cannot be underetched.

### 1.3.1 Mask files

We use the commercial software Tanner L-Edit [130] to write our mask files. In the case of photonic circuits, we use the coding environment to define our structures. Since we use positive e-beam resist, we have to define the areas around the device, where the writing occurs, the resist is opened, and the hard mask and III-nitride are etched. Each level of lithography needs to be defined in at least one separate mask layer. Multiple layers can be used to write with different doses during one level of lithography. Fig. 1.31 (a) shows the mask of a photonic circuit with four layers. Fig. 1.31 (b) shows level 1 (microdisks, waveguide, and grating couplers) consisting of three layers, the area near the disk, the waveguide away from the disk, and the grating couplers. These three layers will be written at the same time but with different doses. Fig. 1.31 (c) shows the second level (QW etch) that consists of a single layer.

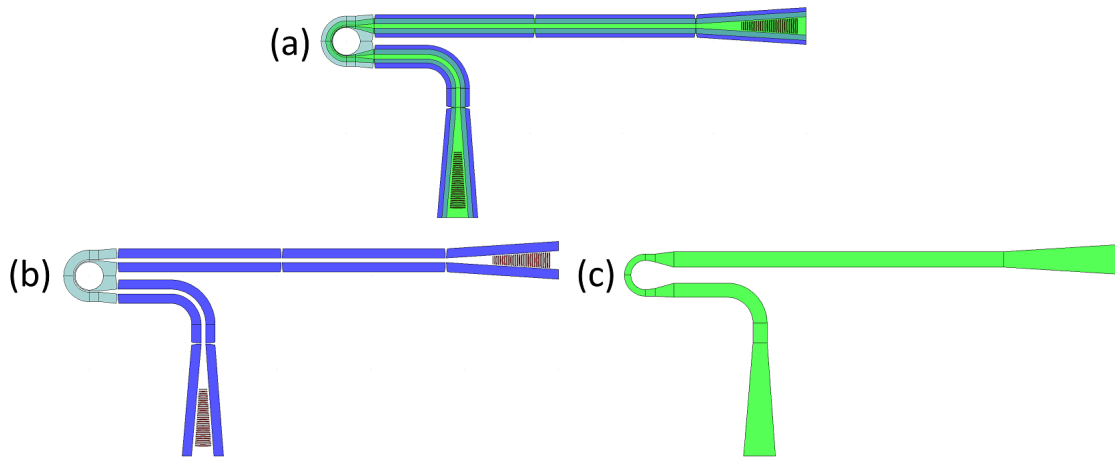


Figure 1.31: Mask of a photonic circuit. (a) All layers. (b) The first level consisting of three layers with different doses. (c) The second level consisting of one layer.

Within one layer, for very fine structures, we can use a proximity effect correction in nbPat, the software for pattern fracturing provided by NanoBeam Ltd. This allows us to identify the regions that require a higher dose and to separate them easily into a new layer. Fig. 1.32 shows the mask of the first level after proximity correction. We can see in the zoom-in in Fig. 1.32 (b) that the gap between the disk and the waveguide is now a separate layer, which requires a roughly 40% higher dose. The grating couplers also require a 20% higher dose.

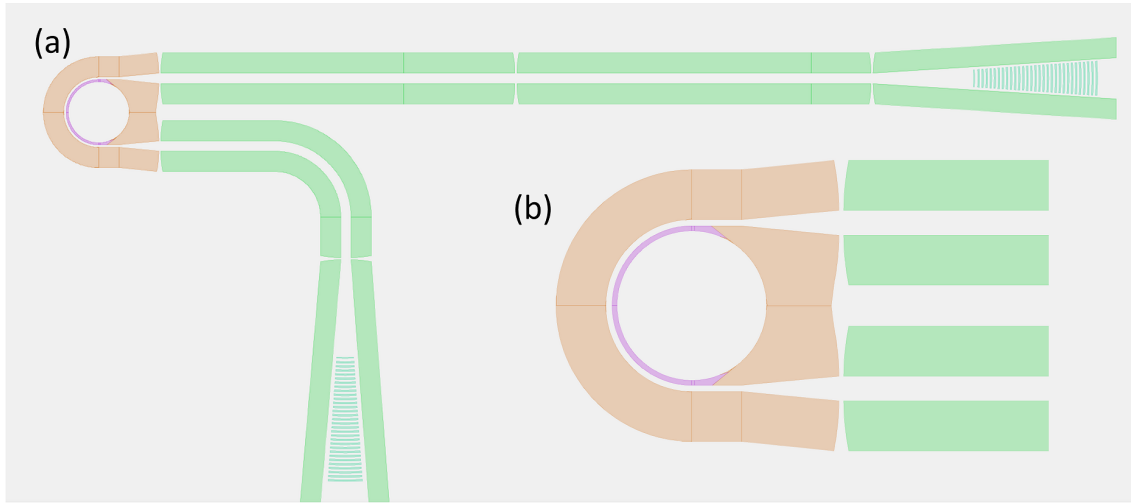


Figure 1.32: (a) Mask level 1 after proximity effect correction and (b) zoom-in into the area around the disk.

### 1.3.2 E-beam lithography

We use two different models of e-beam lithography machines from NanoBeam Ltd., the NB4 (in Orsay) and the NB5 (in Grenoble), both operating at a beam energy of 80 keV. When using the NB4, we employ UVIII and ZEP520A resist, and with the NB5 we use UV5 resist. UVIII and UV5 resists are UV sensitive positive resists that can also be used for e-beam lithography. They appear to be very similar, we have not noticed any significant difference. We use hexamethyldisilazane (HDMS), a primer to promote adhesion. The resist which is usually 500-600 nm thick after spin-coating for 60s at 4000 rpm can be diluted 1:1 with ethylene carbonate (EC) solvent to reduce the thickness by a factor 2 for increased resolution. The e-beam dose required to expose these resists for our samples is  $0.25$  to  $0.4 \text{ C} \cdot \text{m}^{-2}$ , depending on the thickness of the  $\text{SiO}_2$  and III-nitride layers. For the e-beam lithography, we use beam currents of 0.5 or 1 nA, which given the low dose and high writing speed of the NB, results in very short writing times of a few seconds to 30 min. UVIII and UV5 require a post-exposure bake to drive the photochemical effect. These resists withstand RIE of  $\text{SiO}_2$  without noticeable deformation.

We use ZEP520A resist for PhC cavities. It is a high resolution positive e-beam resist that has a thickness of around 350 nm when spin-coated at 4000 rpm for 60s. It can be diluted in anisol to reduce the thickness. We use HDMS to promote adhesion. The e-beam dose required for exposure is in the range of  $3$  to  $3.5 \text{ C} \cdot \text{m}^{-2}$  for our material. After development, the resist is hardened by e-beam irradiation with an SEM (dose  $65 \text{ C} \cdot \text{m}^{-2}$ ) for higher quality RIE of the  $\text{SiO}_2$  mask. Without this hardening step the holes with diameters of less than 100 nm become deformed during the RIE.

When aligning two or more layers, alignment marks are of paramount importance. For e-beam lithography, we use  $6 \times 8 \mu\text{m}^2$  rectangles made of 10 nm Ti and 80 nm Au. We fabricate the alignment marks using optical lithography and e-beam metal evaporation. The marks are

usually spaced by 500 $\mu\text{m}$  in both x- and y-directions. In order to have a good focus of the e-beam, we auto-focus on the alignment marks in small areas of 1.5 x 1.5 mm<sup>2</sup> around each pattern block.

For devices with only one level, we use a manual focus on scratches made at the edges of the sample using a diamond scribe. The manual focus on four scratches is generally good enough for devices in the NIR where larger gaps provide good coupling.

An important limitation with e-beam lithography is the stitching error (i.e. the misalignment) between write fields. The write fields are divided into mainfields and subfields, in which the beam is deflected by the slow and fast deflector magnets, respectively. With the NB, we usually choose mainfields of around 500 $\mu\text{m}$ . This gives the maximum dimension of a device as the stitching error between main fields is usually too large to assure the continuity of a waveguide, for example. The stitching error can be in the range of tens of nm for a well-aligned e-beam to hundreds of nm for bad alignment.

### 1.3.3 Etch recipes

#### 1.3.3.1 SiO<sub>2</sub> etching

We use both RIE and ICP to etch PECVD SiO<sub>2</sub>, depending on whether the etching is done in Orsay or in Grenoble. In Orsay, we use an RIE STS with 50 sccm of CHF<sub>3</sub> gas. The radio-frequency (RF) power is 325 W and the chamber pressure is 20 mT. The etch rate is 0.67 nm · s<sup>-1</sup>.

In Grenoble, we use an ICP Oxford with 25 sccm of CF<sub>4</sub> and 25 sccm of CH<sub>2</sub>F<sub>2</sub>. The RF power is 125 W and the ICP power is 600 W. The chamber pressure is 5 mT and the etch rate is 3.1 nm · s<sup>-1</sup>.

#### 1.3.3.2 III-nitride etching

For etching III-nitrides, we use two different ICP etch recipes. In Orsay, we use an ICP STS with 5 sccm of Ar, 25 sccm of Cl<sub>2</sub> and 10 sccm of BCl<sub>3</sub>. The RF power is 200 W and the ICP power is 400 W. The chamber pressure is 12 mT. The etch rate of AlN and GaN is 2 nm · s<sup>-1</sup>.

In Grenoble, we use the same ICP Oxford as for SiO<sub>2</sub> etching. We use 40 sccm of Cl<sub>2</sub> and 30 sccm of BCl<sub>3</sub>. The RF power is 115 W and the ICP power is 300 W. The chamber pressure is 7 mT and the etch rate is 3.3 nm · s<sup>-1</sup>.

### 1.3.4 Fabrication of III-nitride microdisks

A schematic of the process flow of a microdisk resonator is depicted in Fig. 1.33. First (Fig. 1.33 (a)), a PECVD SiO<sub>2</sub> hard mask is deposited. The thickness of this layer is typically a bit more than 1/3 of the III-nitride thickness due to the etch selectivity between SiO<sub>2</sub> and III-nitrides. HDMS and UVIII or UV5 resist are spin-coated onto the sample (Fig. 1.33 (b)). The resist is patterned with microdisks typically in the range of 1 to 20 $\mu\text{m}$  diameter using an 80 keV e-beam

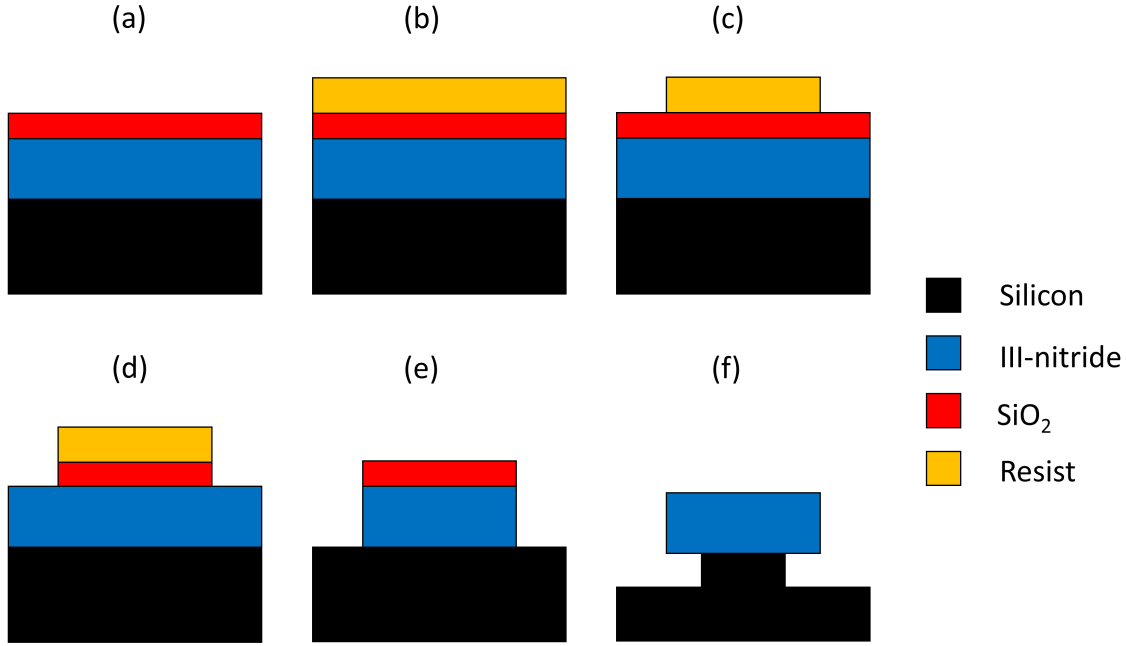


Figure 1.33: Schematic of the fabrication process of a III-nitride microdisk: (a) Deposition of PECVD  $\text{SiO}_2$ . (b) Spin-coating of e-beam resist. (c) Patterning of the resist by e-beam lithography. (d) Etching of the  $\text{SiO}_2$  by RIE. (e) Resist removal and etching of the III-nitride by ICP. (f)  $\text{SiO}_2$  removal and underetching of the silicon by  $\text{XeF}_2$ .

lithography system (Fig. 1.33 (c)). After development of the resist, the  $\text{SiO}_2$  layer is etched where the resist was opened by RIE using  $\text{CHF}_3$  or  $\text{CF}_4/\text{CH}_2\text{F}_2$  gas mixes (Fig. 1.33 (d)). The remaining resist is removed by  $\text{O}_2$  plasma, and the III-nitride layer is etched by ICP using  $\text{Cl}_2$  and  $\text{BCl}_3$  gases (Fig. 1.33 (e)). The remaining  $\text{SiO}_2$  mask is removed using buffered oxide etchant (BOE). The microdisks are subsequently underetched isotropically with  $\text{XeF}_2$  gas (Fig. 1.33 (f)).

Fig. 1.34 shows microdisks fabricated on different samples using different lithography and etch parameters. The microdisks shown in Figs. 1.34 (a) and (b) were fabricated in Orsay using UVIII resist, a 1 nA e-beam current, and the Orsay etch recipes for  $\text{SiO}_2$  and III-nitrides. The microdisks in Figs. 1.34 (c) and (d) were fabricated from the same wafer in Grenoble using UV5 resist, and the Grenoble etch recipes. We can clearly see that the side-walls of the microdisk in Fig. 1.34 (c) are much rougher (probably a few nm) than in Fig. 1.34 (d). The only nominal difference is the e-beam current, which was 1 nA in Fig. 1.34 (c) and 0.5 nA in Fig. 1.34 (d). This highlights the importance of the choice of e-beam current for smooth side-walls, as a lower current provides a smaller beam step-size. The step-size is given by

$$L = \sqrt{10^3 \frac{I_e}{D \cdot F}}, \quad (1.109)$$

with beam current  $I_e$ , dose  $D$ , and writing frequency  $F$ . For  $F = 60$  MHz and  $D = 0.3 \text{ C} \cdot \text{m}^{-2}$  we get  $L = 7.5$  nm for  $I_e = 1$  nA and  $L = 5.3$  nm for  $I_e = 0.5$  nA.

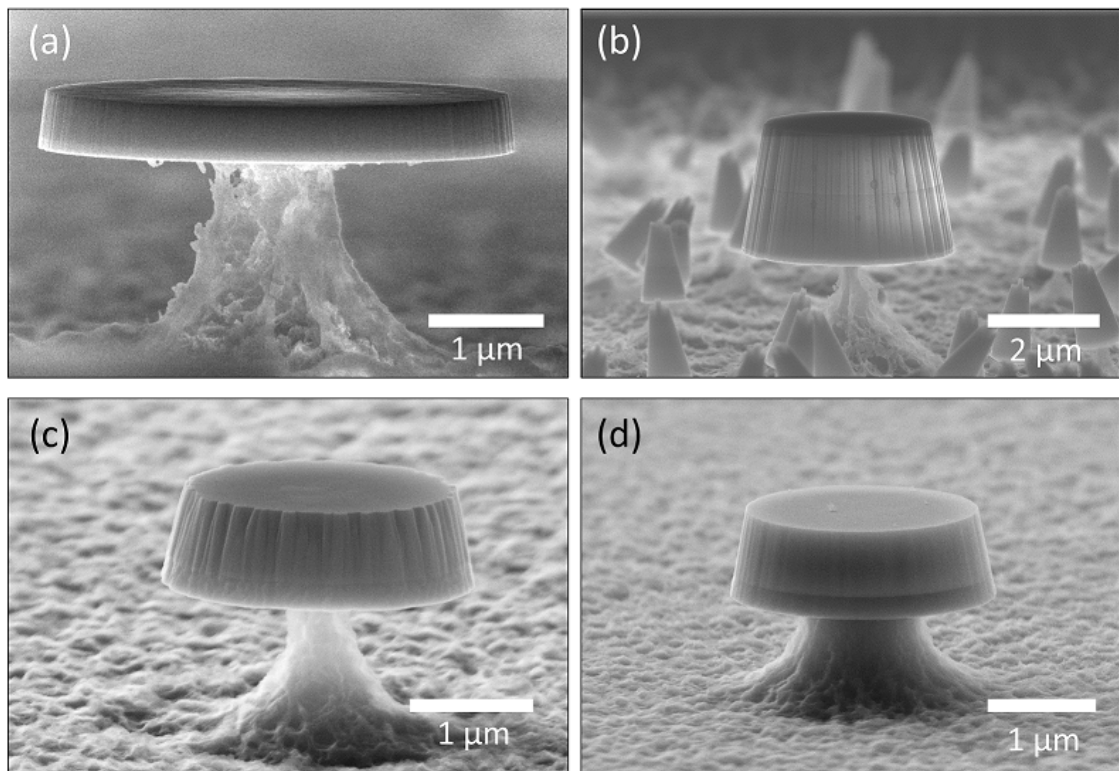


Figure 1.34: SEM images of microdisks fabricated with different e-beam lithography and etch parameters.<sup>1</sup>

A challenge in the fabrication of microdisks is the underetching using  $\text{XeF}_2$ , which is generally not very well controlled. The etch rate varies significantly, and once the sample is in air the native oxide forms again, making a subsequent etch even less controlled. When the microdisk's pedestal is fully etched away the disk falls and is lost.

### 1.3.5 Fabrication of suspended III-nitride microdisk photonic circuits

In order to suspend a waveguide, we need nanotethers to hold it in mid-air. We usually use variable width tethers with a width of 100 nm at the waveguide and 300 nm at the other side. Fig. 1.35 (a) shows a waveguide with mechanically stable tethers and (b) with broken tethers. The tethers broke in this case due to too much strain in the epilayer, which was released upon underetching of the Si.

#### 1.3.5.1 Active photonic circuits

We will discuss the process flows of a 2-level and a 3-level process for fabricating active microdisks coupled to passive waveguides terminated by out-coupling gratings.

<sup>1</sup>The image (b) was one of 20 winners in the 2019 "Preuve par l'image" competition of the CNRS with the title "Photonic forest".

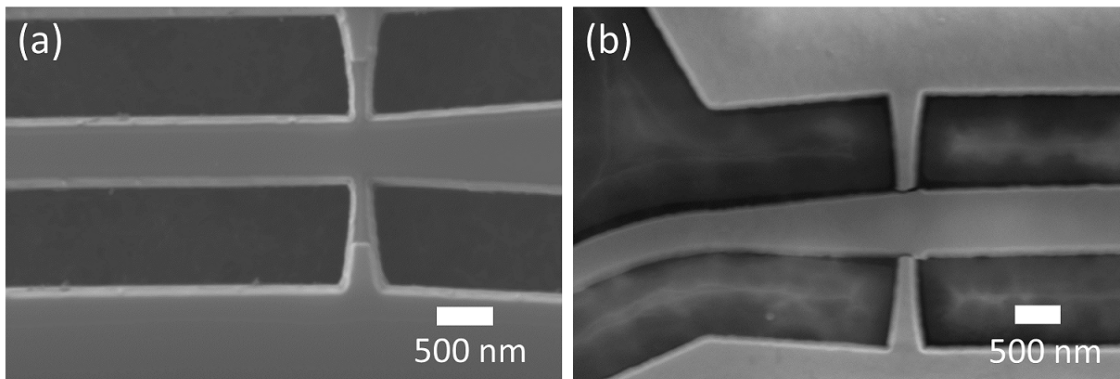


Figure 1.35: SEM images of suspended waveguides held by nanotethers. Waveguide with (a) mechanically stable tethers and (b) broken tethers.

There are several additional difficulties when fabricating active photonic circuits as compared to individual microdisks. Very small gap sizes of less than 100 nm between the disk and the waveguide need to be fabricated, as they are required in the blue/UV spectral range for efficient coupling. The waveguide needs to be bent around the disk to increase the coupling length, requiring precise control of the gap and waveguide width over several microns length. This requires high resolution e-beam lithography and RIE and ICP etching of  $\text{SiO}_2$  and III-nitrides with near-vertical side-walls. A second challenge is to remove the QWs from the waveguide to avoid reabsorption of the emission. This requires high alignment precision of two e-beam lithography steps and a good control of the etch rate of III-nitrides, as there is no etch-stop layer. The grating couplers pose an additional difficulty. This is where we have a difference between the 2-level and 3-level process. The first level consists of defining the microdisk and waveguide, while the second level consists of removing the QWs from the waveguide. We can either fabricate the grating couplers at the same time as the disk and waveguide, which results in them being etched all the way to the Si, or we can have them constitute a third layer, in which we can control the grating etch depth. The disadvantage of the 3-layer process is that every additional layer requires additional alignment and can result in additional problems during the fabrication. A potential issue with fabricating the gratings during the first level is that if the III-nitride layers are very thick the precision of the gratings will likely be reduced.

We present the 2-level approach in Fig. 1.36. First (Fig. 1.36 (a)), a PECVD  $\text{SiO}_2$  hard mask is deposited. Then (Fig. 1.36 (b)), UVIII or UV5 resist is spin-coated on the sample and (Fig. 1.36 (c)) the microdisk, waveguide and gratings are defined by e-beam lithography and the resist is developed. Next (Fig. 1.36 (d)), the  $\text{SiO}_2$  mask is etched by RIE or ICP and (Fig. 1.36 (e)) the III-nitride layer is etched by ICP to the Si substrate. Then (Fig. 1.36 (f)), the  $\text{SiO}_2$  mask is removed using BOE. For the second level, we essentially repeat steps (a) through (e). First (Fig. 1.36 (g)), we deposit a thinner  $\text{SiO}_2$  mask, since we will etch less III-nitride. Then (Fig. 1.36 (h)), we spin-coat the e-beam resist, and (Fig. 1.36 (i)) open up the area around the waveguide. We etch the  $\text{SiO}_2$  (Fig. 1.36 (j)) and etch away the QWs from the waveguide (Fig. 1.36 (k)) by knowing the

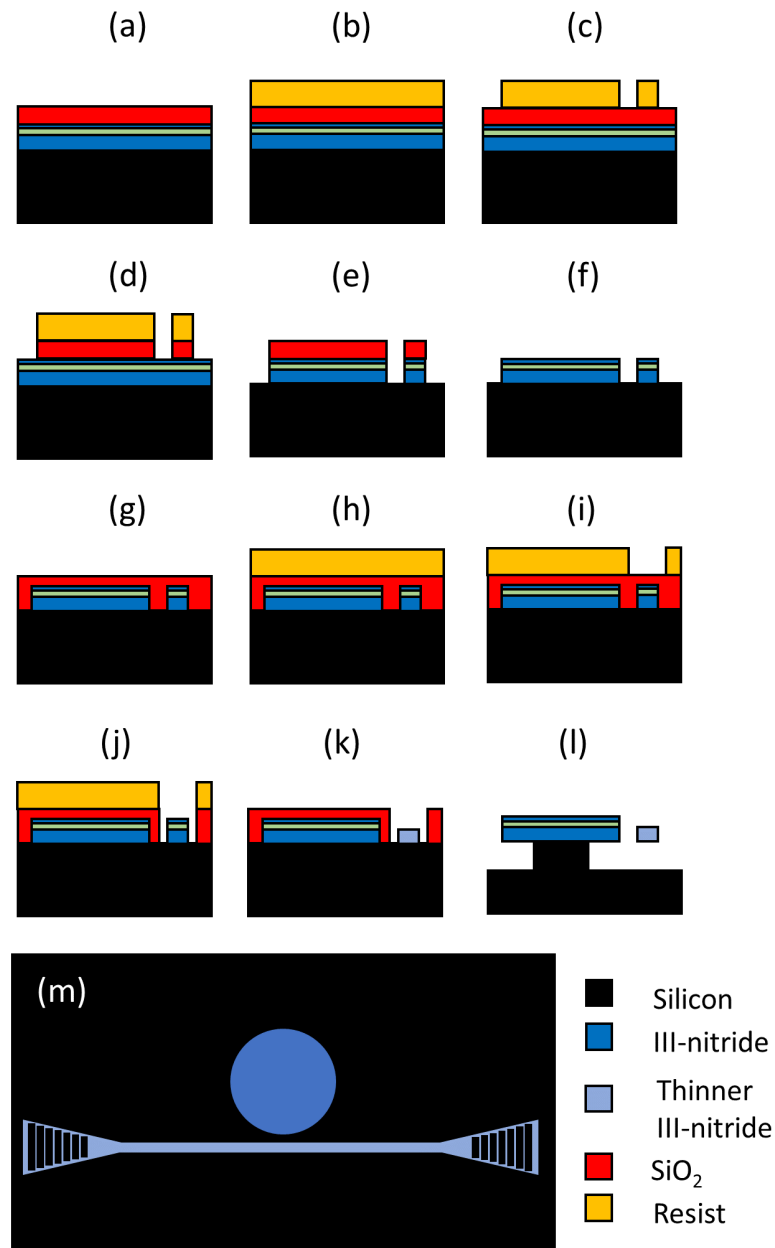


Figure 1.36: Process flow of an active microdisk coupled to a waveguide terminated by out-coupling gratings. (a) deposition of SiO<sub>2</sub> hard mask, (b) spin-coating of e-beam resist, (c) e-beam lithography, (d) RIE etching of SiO<sub>2</sub>, (e) ICP etching of III-nitride, (f) removal of SiO<sub>2</sub> mask by BOE, (g) deposition of SiO<sub>2</sub> hard mask, (h) spin-coating of e-beam resist, (i) e-beam lithography, (j) RIE etching of SiO<sub>2</sub> mask, (k) partial ICP etching of waveguide, (l) underetching of Si by XeF<sub>2</sub>, (m) top-view of the finished device.

etch rate. Finally (Fig. 1.36 (l)), we remove the SiO<sub>2</sub> and underetch the Si using XeF<sub>2</sub>. A sketch of the top-view of the finished device is shown in Fig. 1.36 (m).

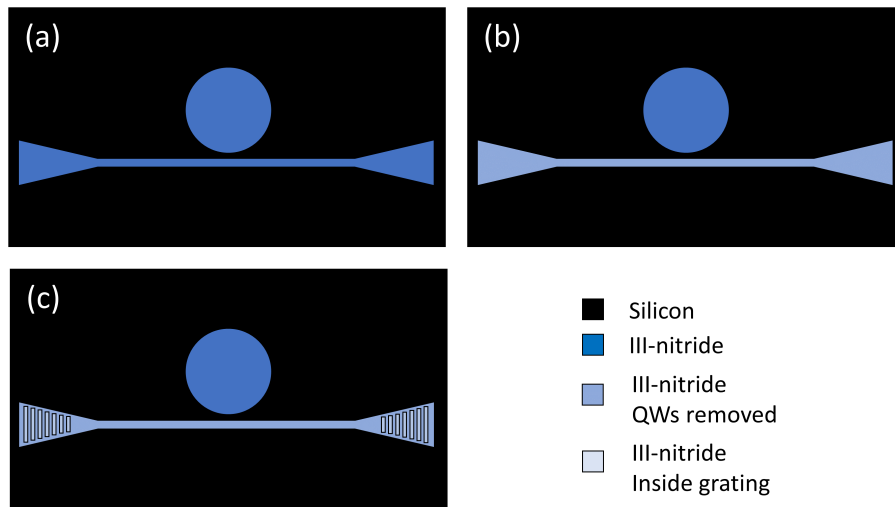


Figure 1.37: Reduced process flow of an active microdisk coupled to a waveguide with out-coupling gratings that are not fully etched. (a) first level: ICP etching of microdisk and waveguide down to Si, (b) second level: removal of QWs from waveguide by ICP etching, (c) third level: partial ICP etching of grating couplers.

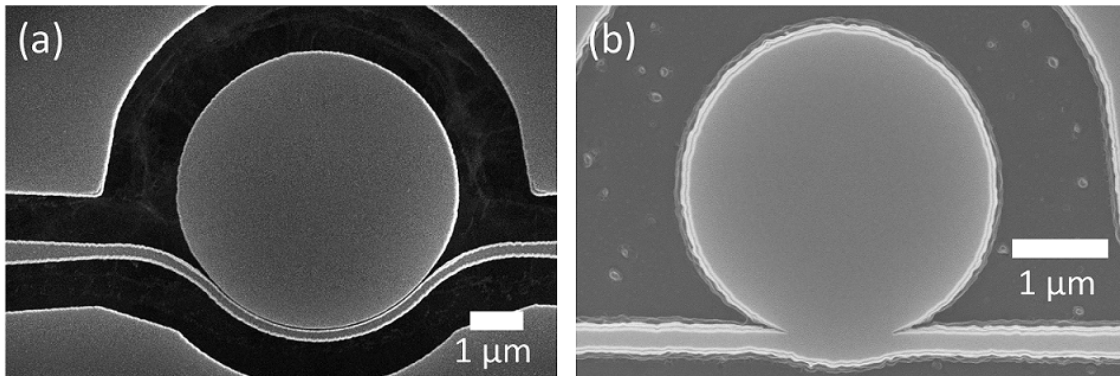


Figure 1.38: SEM images of the microdisk to waveguide coupling region. (a) Finished device with a small gap between disk and waveguide and (b) device after first level where the gap is not open.

A reduced process flow for the 3-level process is shown in Fig. 1.37. In the first level (Fig. 1.37 (a)), the microdisk and waveguide are defined and etched to the Si substrate. In the second level (Fig. 1.37 (b)), the QWs are etched away from the waveguide. And in the third level (Fig. 1.37 (c)), the grating couplers are etched partially into the III-nitride.

Fig. 1.38 shows SEM images of two examples of the microdisk to waveguide coupling region in active devices in the blue spectral range. Here, the gap needs to be around 50 nm for critical coupling. In Fig. 1.38 (a), the small gap is open, while in Fig. 1.38 (b) there is no gap. We have observed that when the e-beam current settings were not well calibrated, the small gaps would not be open. Another method to mitigate this problem is by using proximity correction in the mask file, as discussed in section 1.3.1. Essentially, this means that we can use a higher dose at

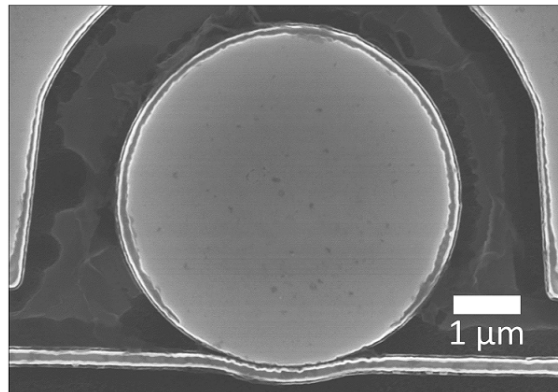


Figure 1.39: SEM images of a device where the previously etched disk was not well enough protected in the subsequent etch steps.

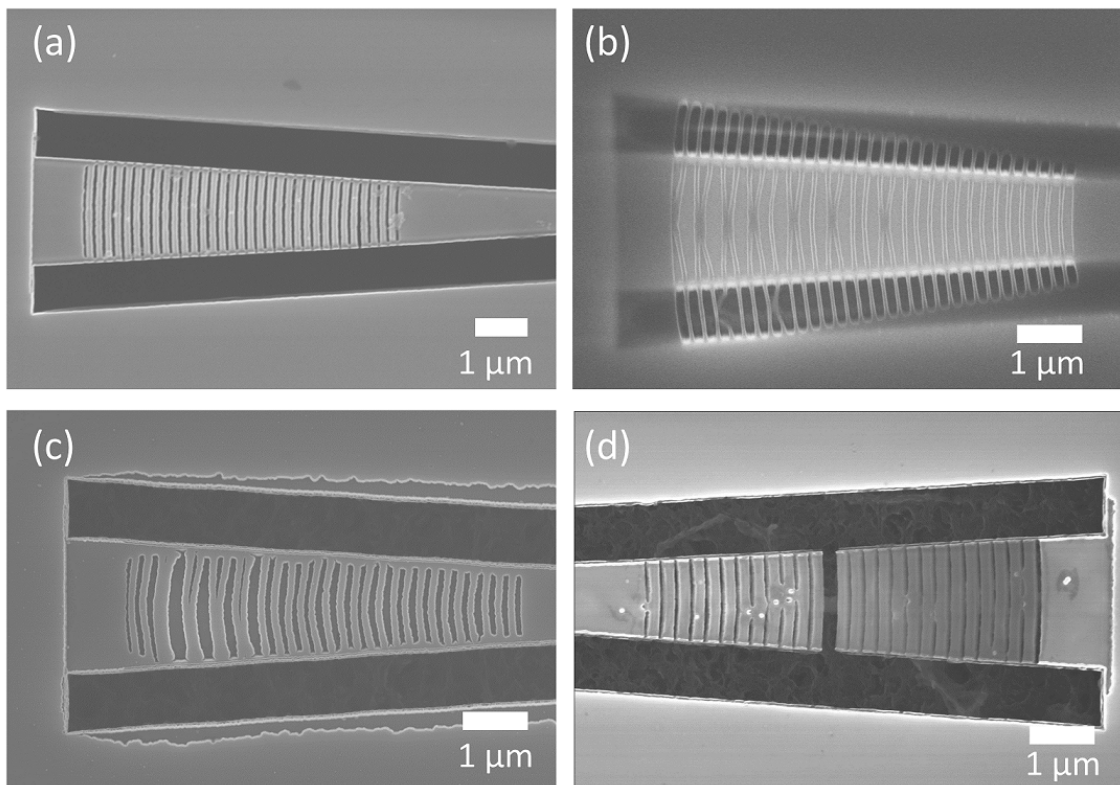


Figure 1.40: SEM images of out-coupling gratings for the blue spectral range. (a) Successfully fabricated grating on finished sample, (b) over-dosed grating lithography, (c) over-dosed grating on finished sample, (d) broken grating on finished sample.

the gap, which increases the chance of the gap being open.

We need to take care that the  $\text{SiO}_2$  hard mask used in the second or third level protects the borders of the already etched areas sufficiently well, since the layer thickness is non-uniform. In Fig. 1.39, we show a sample where this was not the case, and the edges of the microdisk have been attacked during the second ICP etch.

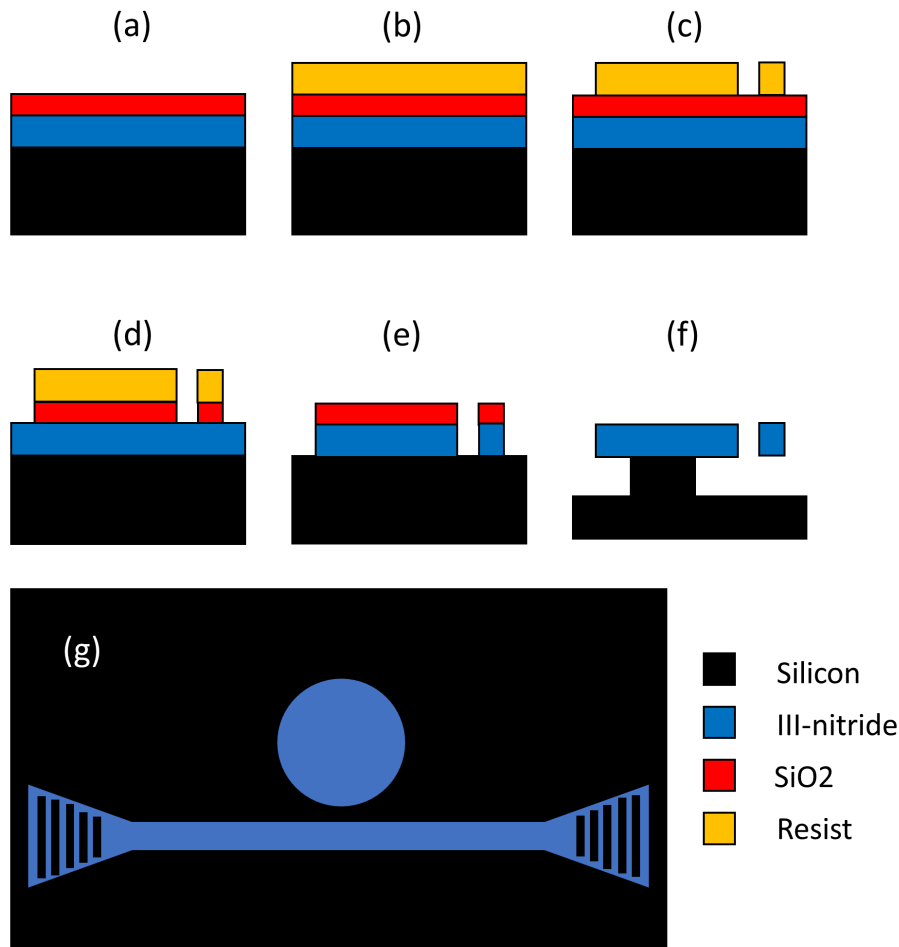


Figure 1.41: Process flow of a passive microdisk coupled to a waveguide terminated by out-coupling gratings. (a) deposition of  $\text{SiO}_2$  hard mask, (b) spin coating of e-beam resist, (c) e-beam lithography, (d) RIE etching of  $\text{SiO}_2$  mask, (e) ICP etching of III-nitride, (f)  $\text{XeF}_2$  underetching of Si, (g) top-view of finished device.

Another big challenge is the grating coupler. When it is fabricated as the third level, the lithography is very sensitive due to a change in height and focus as compared to the unetched area. In Fig. 1.40 (a), we show a successfully fabricated and suspended grating. In Fig. 1.40 (b), we show an over-dosed lithography, where some of the grating lines got loose and are sticking together. Fig. 1.40 (c) shows an underetched grating where the lithography was over-dosed. In addition, this sample also had the problem shown in Fig. 1.39, that the  $\text{SiO}_2$  did not sufficiently protect the previous layers. In Fig. 1.40 (d), we show a grating that broke during the underetching due to lack of mechanical stability.

### 1.3.5.2 Passive photonic circuits

In the case of passive photonic circuits, there is no need to selectively etch the waveguide. Thus, a one-level process can be employed. We use passive devices in the NIR, where process constraints are more relaxed, since large gaps and waveguide widths allow for efficient coupling even for straight waveguides. The gratings are also easier to fabricate as the grating period is larger for longer wavelengths. Fig. 1.41 shows the process flow. First (Fig. 1.41 (a)), an SiO<sub>2</sub> hard mask is deposited, followed by (Fig. 1.41 (b)) spin-coating of UVIII or UV5 resist. Next (Fig. 1.41 (c)), we write the pattern by e-beam lithography and develop the resist, and ((Fig. 1.41 (d)) we etch the SiO<sub>2</sub> mask by RIE or ICP. Then ((Fig. 1.41 (e)), we etch the III-nitride layer and ((Fig. 1.41 (f)) we underetch the Si using XeF<sub>2</sub>. A sketch of the top-view of the finished device is shown in Fig. 1.41 (g).

The main fabrication challenge that we have encountered for such devices is the lack of mechanical stability of nanotethers in AlN layers, due to large strain release upon underetching. Bonding such a sample to a carrier wafer and removing its substrate would mitigate this problem.

### 1.3.6 Fabrication of passive photonic circuits bonded on SiO<sub>2</sub>

A second type of passive device can be fabricated by bonding to an SiO<sub>2</sub>/Si carrier wafer and substrate removal through RIE deep etching. This method allows for the fabrication of micro-rings, as no underetching is needed due to the large contrast in refractive index between III-nitrides and SiO<sub>2</sub>. The process flow is shown in Fig. 1.42. First (Fig. 1.42(a)), a 2 μm thick SiO<sub>2</sub> layer is deposited on the sample. Then (Fig. 1.42 (b)), the sample is bonded on a SiO<sub>2</sub>/Si carrier wafer using benzocyclobutene (BCB). In Fig. 1.42 (c) the Si substrate is removed using RIE deep etching. Then (Fig. 1.42 (d)), an SiO<sub>2</sub> hard mask is deposited. Next (Fig. 1.42 (e)), the UVIII or UV5 resist is spin-coated on the sample, and (Fig. 1.42 (f)) the pattern is written using e-beam lithography and the resist is developed. We etch (Fig. 1.42 (g)) the SiO<sub>2</sub> mask using RIE or ICP and (Fig. 1.42 (h)) we etch the III-nitride using ICP. Then (Fig. 1.42 (i)), we remove the remaining SiO<sub>2</sub> mask using RIE. A sketch of the top-view of the finished device is shown in Fig. 1.42 (j).

The main challenge in this case is the bonding and substrate removal. The substrate is removed by RIE using SF<sub>6</sub> gas, which also attacks III-nitrides. Since we are etching Si, which absorbs in the visible, we have no optical end-point detection of the etching. When trying to determine if the etch is complete, the sample is in air and Si forms a native oxide that then reduces the etch rate of a subsequent RIE step.

For the e-beam lithography, we need to use a slightly smaller dose, 0.25 C · m<sup>-2</sup>, due to the insulating SiO<sub>2</sub> layer underneath the III-nitride.

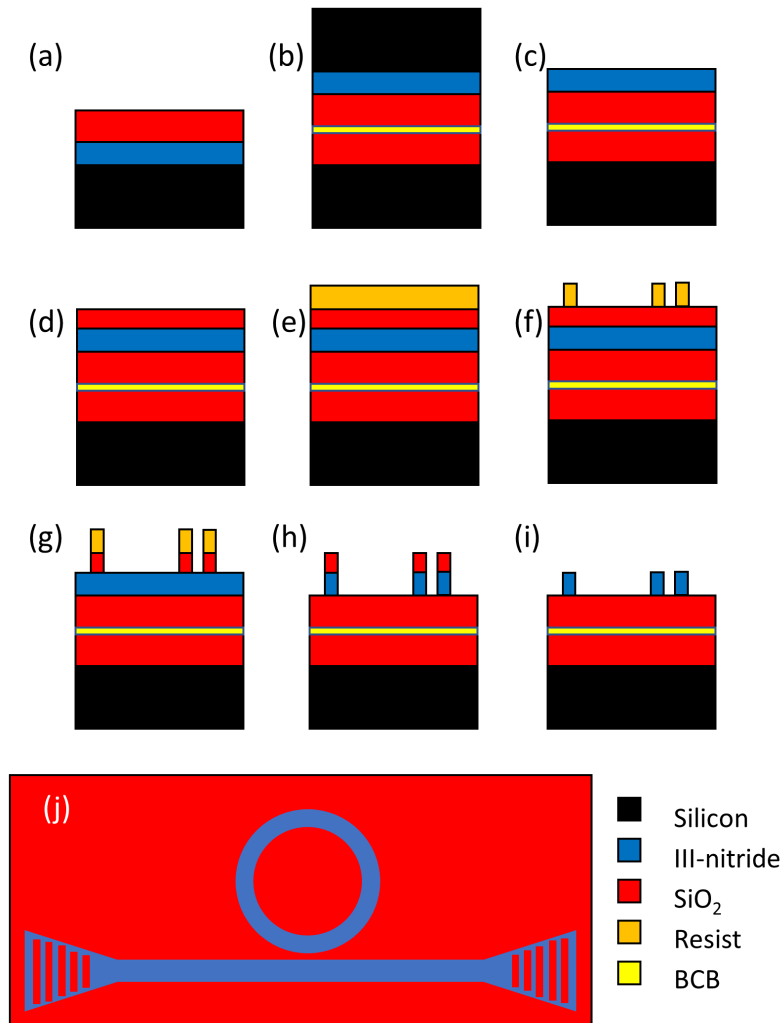


Figure 1.42: Process flow of a passive microring coupled to a waveguide terminated by out-coupling gratings and bonded on SiO<sub>2</sub>. (a) deposition of SiO<sub>2</sub>, (b) BCB bonding to carrier wafer (SiO<sub>2</sub> on Si), (c) removal of Si substrate by RIE deep etching, (d) deposition of SiO<sub>2</sub> hard mask, (e) spin coating of e-beam resist, (f) e-beam lithography, (g) RIE etching of SiO<sub>2</sub> mask, (h) ICP etching of III-nitride layer, (i) RIE etching of SiO<sub>2</sub> mask, (j) top-view of finished device.

### 1.3.7 Fabrication of III-nitride PhC slabs

The process flow of 2D PhC slab cavities is depicted in Fig. 1.43. First (Fig. 1.43 (a)), we deposit an SiO<sub>2</sub> hard mask. Then (Fig. 1.43 (b)), we spin-coat ZEP520A resist and (Fig. 1.43 (c)) define the pattern using e-beam lithography and use e-beam irradiation to harden the resist in preparation for RIE etching of the SiO<sub>2</sub> mask (Fig. 1.43 (d)). Then (Fig. 1.43 (e)), we etch the III-nitride using ICP and (Fig. 1.43 (f)) underetch the membrane using XeF<sub>2</sub>. Fig. 1.43 (g) shows a sketch of the top-view of a finished device.

Fig. 1.44 shows L3 PhC cavities (a) with and (b) without resist hardening. We can see that

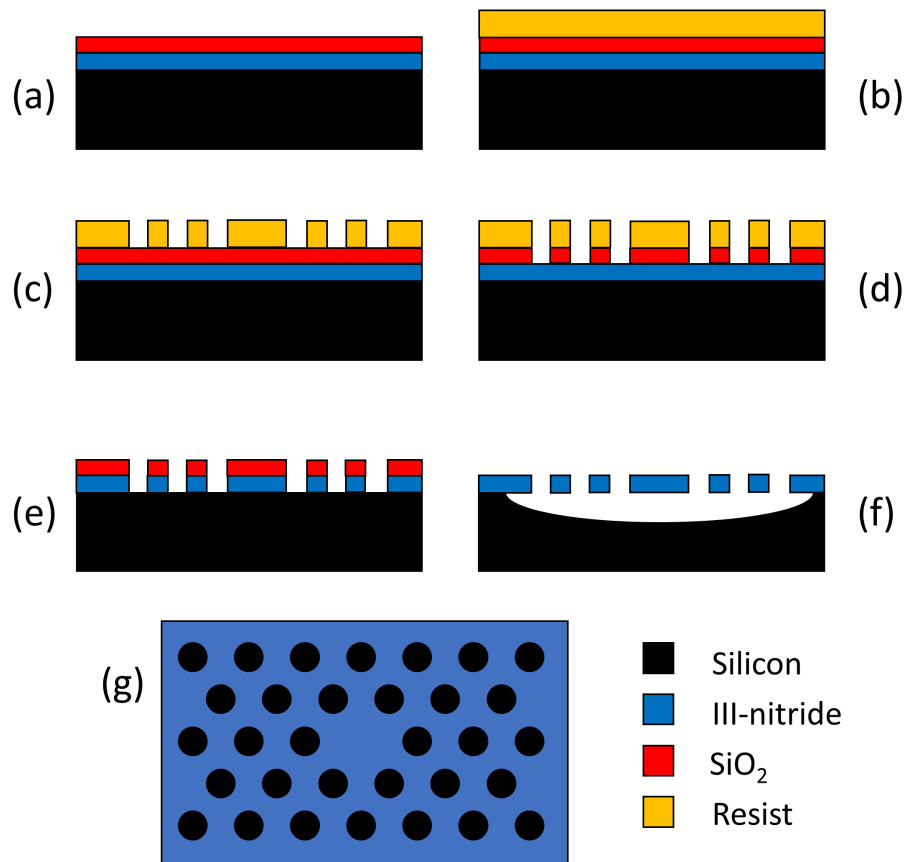


Figure 1.43: Process flow of an active 2D PhC slab cavity. (a) deposition of  $\text{SiO}_2$  hard mask, (b) spin-coating of e-beam resist, (c) e-beam lithography and e-beam irradiation, (d) RIE etching of  $\text{SiO}_2$  mask, (e) ICP etching of III-nitride, (f) underetching of Si by  $\text{XeF}_2$ , (g) top-view of finished device.

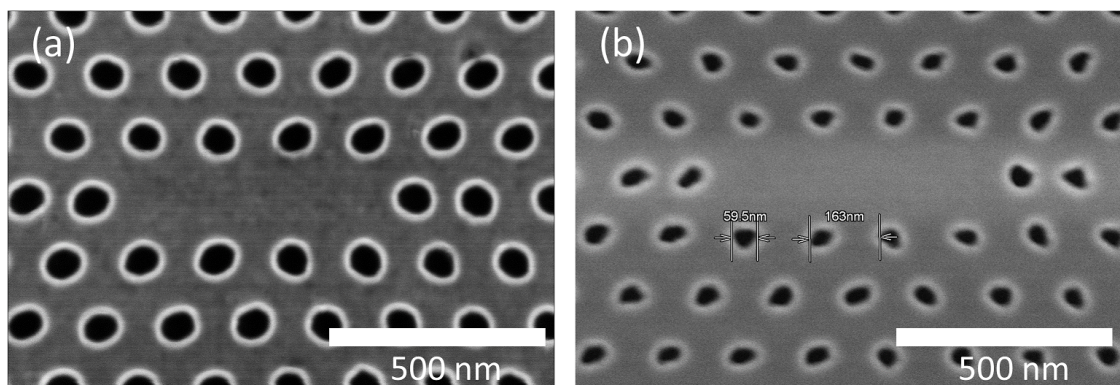


Figure 1.44: SEM images of 2D PhC cavities. (a) with resist hardening, (b) without resist hardening.

the holes are smaller and deformed when the resist was not irradiated before RIE etching of the  $\text{SiO}_2$  mask.

## 1.4 Optical spectroscopy setups

We will discuss the optical spectroscopy setups for the UV/blue spectral range that we use at the University of Montpellier and at CEA-IRIG in Grenoble.

### 1.4.1 $\mu$ -PL setups

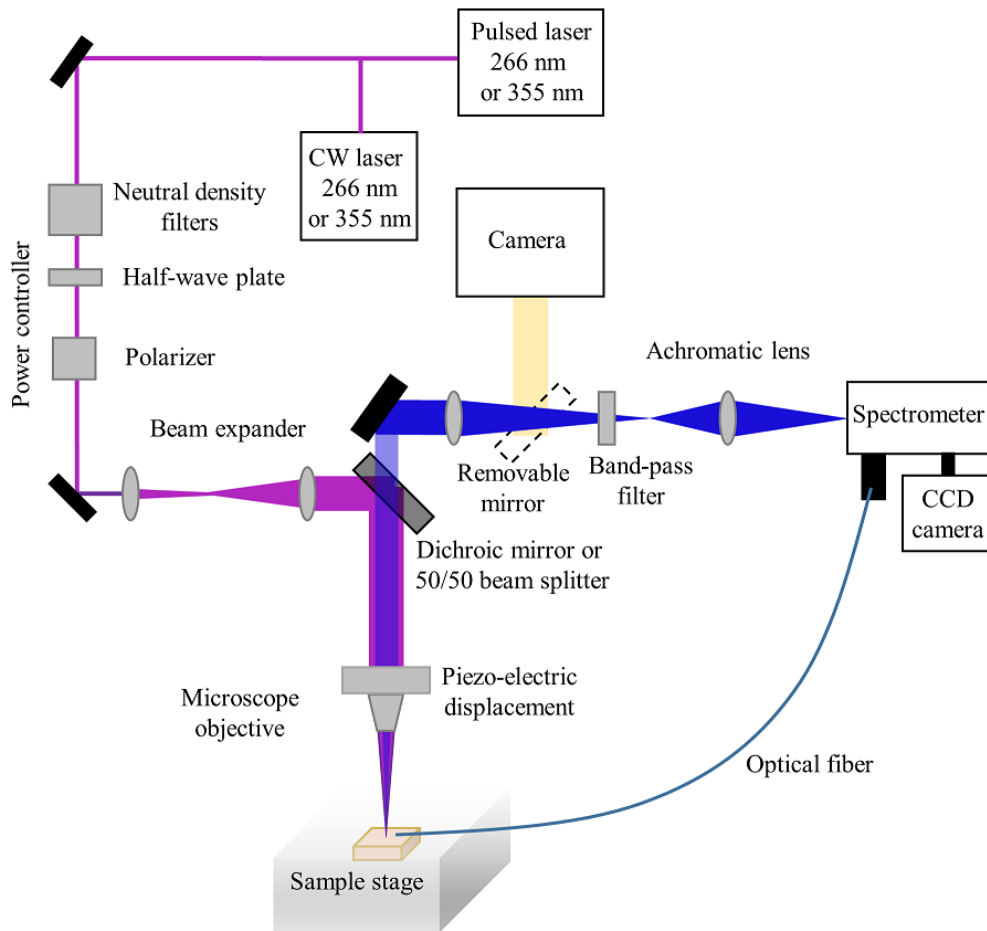


Figure 1.45:  $\mu$ -PL setup in Montpellier. Adapted from Ref. [58].

Fig. 1.45 shows the  $\mu$ -PL setup that we use in Montpellier. Four different lasers can be used, a pulsed and a CW laser at  $\lambda = 266$  nm and at 355 nm. The lasers are frequency-quadrupled and -tripled Nd:YAG lasers emitting at 1064 nm. The pulsed lasers are Q-switched and the CW lasers use non-linear crystals for frequency conversion. The sample is placed on a stage. The laser beam passes through a half-wave plate and a polarizer to control the optical power and gets broadened before getting focused onto the sample using a microscope objective controlled by piezo-electric motors. The emission of the microdisks can be collected from the top using the microscope objective or from the side using an optical fiber. The advantage of side-collection

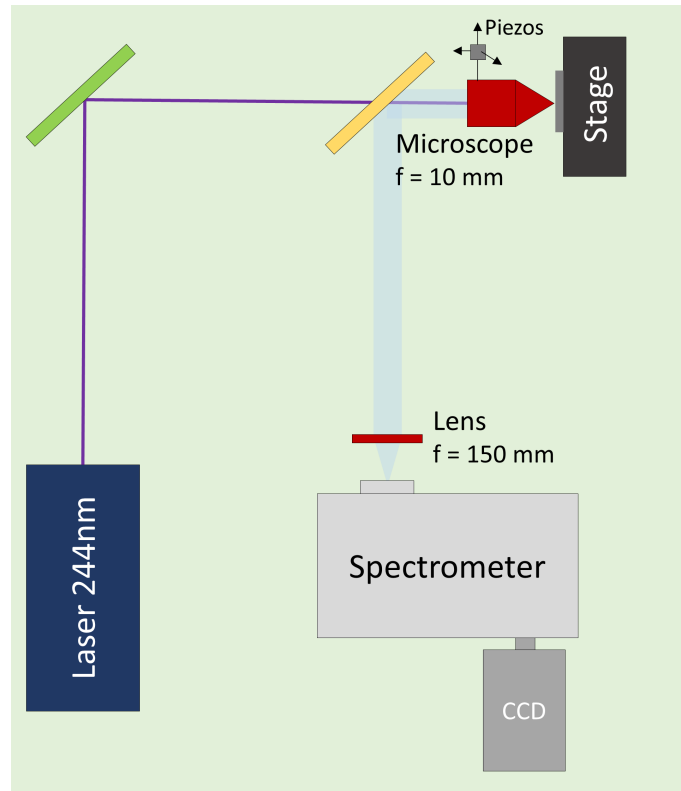


Figure 1.46: Scheme of the  $\mu$ -PL setup in Grenoble.

is that the WGMs radiate preferentially in-plane. Thus, they can be measured with a better signal to background ratio. For photonic circuits with out-couplers, top-collection is preferential. The emission spectrum is measured using a spectrometer and a charge coupled device (CCD) camera cooled by Peltier elements. A digital camera is used to visualize the sample and align the laser beam onto a microdisk.

Fig. 1.46 shows a schematic of the CW  $\mu$ -PL setup we use in Grenoble. A 488 nm solid-state laser (Coherent) is frequency-doubled to 244 nm and focused on the sample, which is placed on a stage, using a microscope objective that is controlled by piezo elements. The light emitted by the sample is collected from the top by the microscope objective and focused into the slit of a spectrometer and measured using a liquid nitrogen cooled CCD camera.

## 1.5 Conclusion

In conclusion, this chapter gave an introduction to the III-nitride material system and photonic devices as well as their design and fabrication. A reader, unfamiliar with this field but with university-level knowledge of semiconductor physics, optics, and electromagnetism should be able to understand the following chapters with the here presented thematic introduction.

III-nitrides are a good candidate for next generation photonics from the UV to the NIR be-

cause of the large transparency window and band gap tunability from the UV to VIS. Active and passive devices can be integrated monolithically on-chip using epitaxial growth. Growth on silicon allows to underetch the III-nitride layers, providing the necessary refractive index contrast for vertical confinement.

The cleanroom fabrication of III-nitrides is fairly advanced. Near-vertical smooth side-walls can be achieved with ICP etching in  $\text{Cl}_2$  and  $\text{BCl}_3$ . However, problems during e-beam lithography or during the etching of the hard mask can cause unwanted roughness. Using a resist that directly acts as the hard mask, like HSQ, can mitigate this problem. The suspension of the photonic circuits can be problematic when strain release causes nanotethers to break. Bonding to  $\text{SiO}_2$  and removing the substrate is a good alternative but difficult to implement for active structures that require etching of the QWs to avoid re-absorption.

## Summary of Chapter 1

In this chapter, we presented the relevant information for a basic understanding of photonic devices in the III-nitride on silicon platform. We started by describing the relevant III-nitride material properties. We explained the wurtzite crystal structure and the spontaneous and piezoelectric polarization observed in c-plane nitrides, briefly pointing out semi- and non-polar crystal orientations as alternatives. We discussed the band structure and the possible band gap engineering of the III-nitride alloys, as well as the external quantum efficiencies reported in literature to give an idea of the spectral ranges that can easily be achieved using III-nitrides, which are, notably, blue, green, and UV. We presented the ordinary and extraordinary refractive indices, which are very important parameters for our device design, as they define the speed of light inside the material. Then, we explained the choice of substrate and detailed the growth of III-nitrides on silicon, pointing out the difficulties related to the lattice and thermal mismatch. Next, we discussed theoretically the different photonic components that make up our photonic integrated circuits, including the slab and ridge waveguide, the microdisk cavity, the microdisk to waveguide coupling, the semiconductor laser, the 2D PhC slab, and the grating coupler. We explained the FDTD method and the simulation of the aforementioned devices. We then discussed the fabrication of III-nitride photonic devices on silicon. We first highlighted the four main components of the process, the lithography, the etch mask, the etching, and the underetching. Then, we discussed the process flows of the different photonic devices investigated in this thesis, including the mushroom-type microdisk, active and passive photonic circuits, and 2D PhC slab cavities. We highlighted some of the problems that can occur during fabrication, such as rough side-walls, broken nanotethers, coupling gaps that are not open, broken or irregular gratings, delamination of bonded layers, and non-circular holes. In the end, we discussed the optical spectroscopy setups for the UV/blue spectral range.

## Chapter 2

# III-nitride on silicon microdisk lasers

**I**N THIS CHAPTER, we study individual III-nitride on silicon microdisk lasers. Some of the here presented results have been published in Ref. [131]. This chapter covers:

- A review of the state of the art of both pulsed and continuous-wave optically pumped lasing reported in III-nitride microdisks in literature.
- A review of the results from our collaboration from before the beginning of this thesis.
- A thorough description of nine of our samples, including some structural characterization, photoluminescence measurements, and simulations of the optical confinement and band structure.
- An analysis of the pulsed optically pumped lasing observed at room temperature for microdisks fabricated on the before-mentioned samples, including a discussion of the influence of various parameters on the lasing threshold.

## 2.1 Introduction and state of the art

Small foot-print microresonators, such as microdisks constitute an important building block for integrated photonic circuits. Microdisk lasers have been reported in different material systems and for a variety of applications for nearly three decades [95]. The first ever microdisk lasers were reported by McCall et al. in 1991 using InP/InGaAsP [132]. They used selective wet-etching to undercut the microdisks and achieved lasing at around  $1.5\mu\text{m}$  at liquid nitrogen temperature with a threshold power of  $100\mu\text{W}$ .

### 2.1.1 Lasing under pulsed optical pumping

There have been numerous reports on pulsed optically pumped lasing at room temperature (RT) in the ultraviolet to visible (UV-VIS) spectral range in III-nitride microdisks fabricated on

samples grown on both sapphire and silicon substrates [30–32, 49, 50, 123, 133–136]. The first report was in 2004 by Haberer et al. [30]. Optically pumped III-nitride microdisk lasers in the blue spectral range containing 5 InGaN/GaN quantum wells (QWs) were demonstrated using a thick heterostructure grown on sapphire substrate. The microdisks were fabricated using band gap selective photoelectrochemical (PEC) etching. They observed threshold peak powers of  $64 \text{ MW} \cdot \text{cm}^{-2}$  under pulsed excitation.

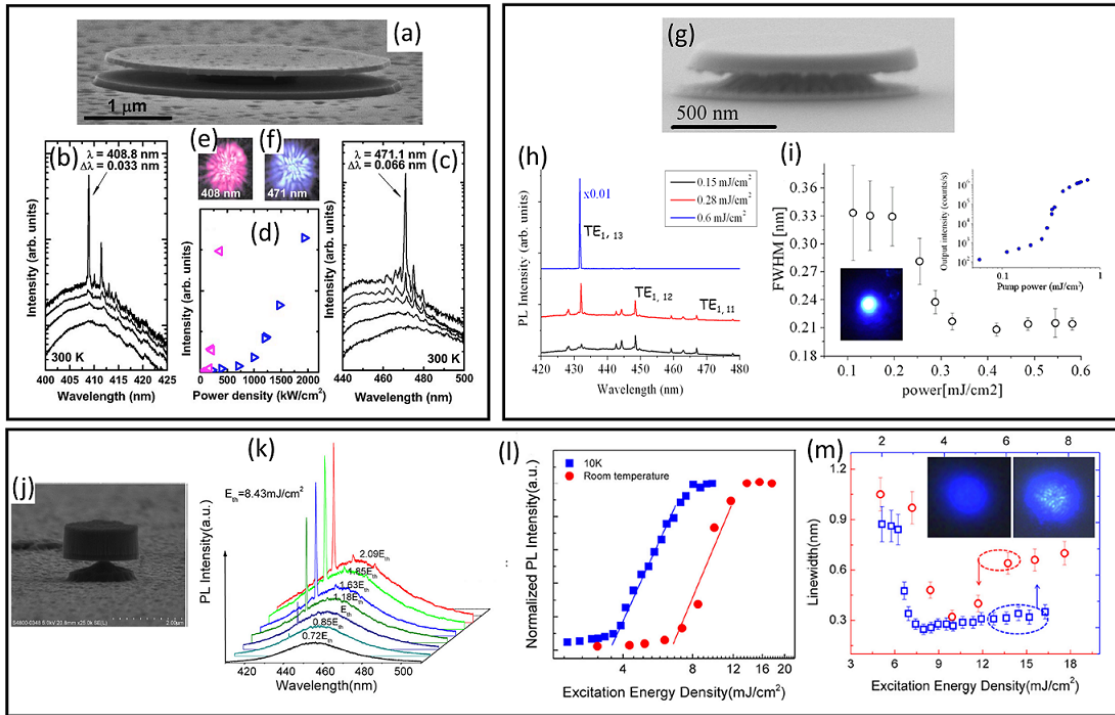


Figure 2.1: Reports of pulsed optically pumped lasing in III-nitride microdisks. (a) SEM image of a  $5 \mu\text{m}$  diameter disk, pump power dependent PL spectra of a mode at (b)  $408.8 \text{ nm}$  and (c)  $471.1 \text{ nm}$ , (d) peak intensity over pump power density for both modes in (b) and (c), (e) and (f) false-color optical microscope images of the emission patterns above threshold of the two modes. (a)-(f) reproduced from Ref. [135]. (g) SEM image of a  $1 \mu\text{m}$  diameter disk, (h) excitation energy dependent PL spectra, (i) FWHM, double-log peak intensity over pump energy, and microscope image above threshold. (g)-(i) reproduced from Ref. [123]. (j) SEM image of a  $2 \mu\text{m}$  diameter disk, (k) excitation energy dependent PL spectra at RT, (l) PL intensity over excitation energy at  $10 \text{ K}$  and RT, and (m) FWHM over excitation energy at  $10 \text{ K}$  and RT and below and above threshold optical images of a microdisk. (j)-(m) reproduced from Ref. [32].

In 2007-2008, using a somewhat different approach but also on sapphire substrate, Simonov et al. fabricated microdisks with a lateral oxidation process of an InAlN sacrificial layer [134, 135]. The sample contained 3 InGaN/GaN QWs. A scanning electron microscope (SEM) image of their  $5 \mu\text{m}$  diameter disk is shown in Fig. 2.1 (a). They used optical lithography to pattern their disks and achieved quality (Q) factors up to 3500. They observed lasing in the

blue spectral range with threshold power densities of  $166 \text{ kW} \cdot \text{cm}^{-2}$  and  $850 \text{ kW} \cdot \text{cm}^{-2}$  at 409 nm and 471 nm, respectively. Pump power dependent PL spectra are shown in Figs. 2.1 (b) and (c), clearly showing lasing. The peak intensity over pump power for the two modes is shown in Fig. 2.1 (d), indicating the thresholds. Optical microscope images above threshold of the two disks are shown in Figs. 2.1 (e) and (f).

In 2013, Aharonovich et al. demonstrated the first optically pumped III-nitride microdisk laser with quantum dots (QDs) in the active region [123]. They used PEC etching to undercut the microdisks grown on sapphire. Fig. 2.1 (g) shows an SEM image of their  $1 \mu\text{m}$  diameter disk and Fig. 2.1 (h) pulse energy dependent PL spectra. The full width at half-maximum (FWHM) is shown in Fig. 2.1 (i), and a reduction is observed at the threshold energy density of  $0.3 \text{ mJ} \cdot \text{cm}^{-2}$  per pulse (peak power of  $1.5 \text{ MW} \cdot \text{cm}^{-2}$ , 200 ps pulse width). They show the output intensity over pump energy in both linear and double-log, both clearly indicating a threshold. The double-log plot is shown in the inset in Fig. 2.1 (i), indicating a clear S-shape.

Zhang et al. demonstrated III-nitride microdisk lasers on silicon containing 5 InGaN/GaN QWs in 2014 using alumina microspheres as the hard mask during inductively coupled plasma (ICP) etching [32]. Fig. 2.1 (j) shows an SEM image of a  $2 \mu\text{m}$  diameter disk with near-vertical side-walls. Pulse energy dependent PL was measured at RT and 10K, indicating thresholds of  $8.4$  and  $3.0 \text{ mJ} \cdot \text{cm}^{-2}$  per pulse ( $2.1$  and  $0.75 \text{ MW} \cdot \text{cm}^{-2}$ , 4 ns pulse width), respectively. The RT spectra are shown in Fig. 2.1 (k). The intensity over excitation energy is shown in Fig. 2.1 (l), showing the thresholds at RT and 10K. A significant reduction in FWHM at both temperatures was observed and is shown in Fig. 2.1 (m) along with below and above threshold optical images of the microdisk.

### 2.1.2 Lasing under continuous-wave optical pumping

We have found three reports of RT continuous-wave (CW) lasing in III-nitride microdisks on sapphire and silicon substrate in the literature [31, 33, 137].

In 2006, Tamboli et al. reported having achieved RT CW lasing with low threshold power densities of  $300 \text{ W} \cdot \text{cm}^{-2}$  using a 325 nm pump laser [31]. They used PEC etching of samples grown on sapphire and e-beam lithography to pattern their disks, as opposed to the optical lithography that this group used before in Ref. [30]. The threshold reported in their article is 5 orders of magnitude lower than in their previous paper [30], which is extraordinary considering that they only discuss having improved the fabrication. Their structure presumably contains  $5 \times 4 \text{ nm In}_{0.14}\text{Ga}_{0.86}\text{N} / 8 \text{ nm GaN}$  QWs, assuming the same layer thickness as in Ref. [30]. We estimate an overlap of the  $\text{TE}_0$  mode with the QWs of 19.7% (the structure is 124 nm thin after undercutting). They report a Q factor of 3700 below threshold. Fig. 2.2 (a) shows an SEM image of their  $1.2 \mu\text{m}$  diameter disk with significant side-wall roughness. They point out that due to the deep undercut the lasing modes are second-order radial modes, which see less of the side-wall roughness, as their maximum intensity is further inside the disk. Fig. 2.2 (b) shows a linear plot of the peak intensity of the lasing mode at 428 nm, shown in Fig. 2.2 (c), for several

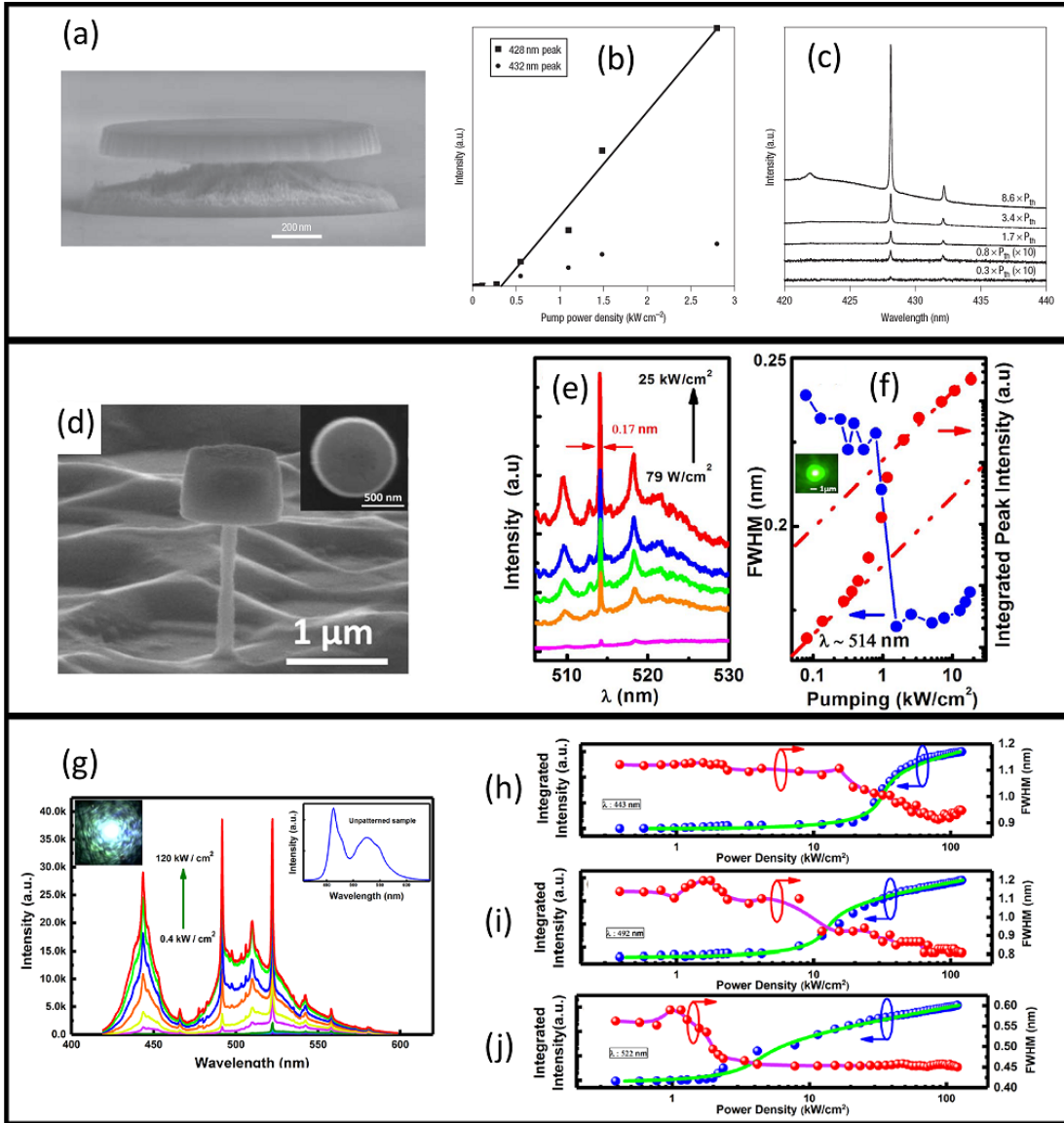


Figure 2.2: Reports of optically pumped RT CW lasing in III-nitride microdisks. (a) SEM image of a 1.2 μm diameter disk, (b) peak intensity over pump power, (c) pump power dependent PL spectra, reproduced from Ref. [31]. (d) SEM images of a 1.2 μm diameter disk, (e) pump power dependent PL spectra, (f) FWHM and log-log plot of integrated peak intensity over pump power, reproduced from Ref. [33]. (g) pump power dependent PL spectra, (h)-(i) FWHM and double-log plot of integrated peak intensity over pump power for the three modes in (g), reproduced from Ref. [137].

excitation power densities. A threshold can be observed at  $300 \text{ W} \cdot \text{cm}^{-2}$ . They do not show a reduction in FWHM, but state that they are limited by the resolution of their spectrometer. They demonstrate a dynamic between peak and background of only a factor of around 8 at  $9P_{th}$ . In Fig. 2.2 (c), the background emission in the spectrum at  $8.6P_{th}$  is significantly increased as opposed to lower excitation powers, which is unusual for a laser. We will point out later that

our calculations suggest that the threshold power density observed by Tamboli et al. is too low for 5 QWs using III-nitrides in the blue. The too low threshold and the very small dynamic between lasing modes and background spontaneous emission, suggests that these results are not correct.

Athanasiou et al. reported RT CW lasing in the green spectral range in 2014 using 1  $\mu\text{m}$  diameter disks on Si and achieving thresholds of  $1 \text{ kW} \cdot \text{cm}^{-2}$  [33]. Their heterostructure was 773 nm thick and contained 5x 2.5 nm  $\text{In}_{0.27}\text{Ga}_{0.73}\text{N}$ / 10 nm GaN QWs. We estimate the overlap of the  $\text{TE}_0$  mode with the QWs to be 0.7%. They used silica microspheres to fabricate the disks. SEM images of one of their devices are shown in Fig. 2.2 (d). They reported a Q factor of 2150. Excitation power dependent PL spectra are shown in Fig. 2.2 (e) with a linear intensity axis. They use a 405 nm pump laser, which means that only the QWs are being pumped. The ratio between the lasing mode and the background spontaneous emission is very small and does not change much with increasing excitation power. They show an S-shaped increase of integrated peak intensity over pump power in a double-log plot, but only a small reduction in FWHM (Fig. 2.2 (f)).

In 2017, Athanasiou et al. reported on RT multi-color blue-green lasing using 1  $\mu\text{m}$  diameter microdisks grown on silicon substrate and fabricated using the microsphere method [137]. They used two sets of 3 and 5  $\text{In}_x\text{Ga}_{1-x}\text{N}$ /GaN QWs with  $x = 0.18$  and  $x = 0.28$  for emission at 450 nm and 530 nm, respectively. They used a CW laser emitting at 375 nm to pump their disks. Power dependent spectra are shown in Fig. 2.2 (g) and double-log plots of integrated intensity over pump power and the FWHM for the three modes are shown in Figs. 2.2 (h)-(i). They observe only a very slight reduction in FWHM, but they do observe S-shapes in the integrated intensity, indicating lasing thresholds of 27, 15, and  $5 \text{ kW} \cdot \text{cm}^{-2}$  for the three modes. Only a very small ratio between the lasing modes and the background spontaneous emission is observed.

The results presented by Athanasiou et al. [33, 137] are not convincing. The linewidth narrowing is less than a factor of 2 in all cases. The peak intensity is not much higher than the background intensity (factor 3 in Fig. 2.2 (g)) and their ratio does not change much with increasing power. Notably, the mode at 443 nm shown in Fig. 2.2 (g) can barely be differentiated from the background [137].

None of these papers discusses the threading dislocation density of their material, which suggests standard values in the range of  $10^{10} \text{ cm}^{-2}$ .

## 2.2 Before this thesis

Our consortium<sup>1</sup> started working on the topic of III-nitride microdisks on silicon in 2009 [56, 138], more than a decade ago. All the microdisk samples from our collaboration from before the beginning of this thesis were grown by molecular beam epitaxy (MBE) on Si (111). All mea-

<sup>1</sup>researchers from CRHEA, C2N, IRIG, and L2C

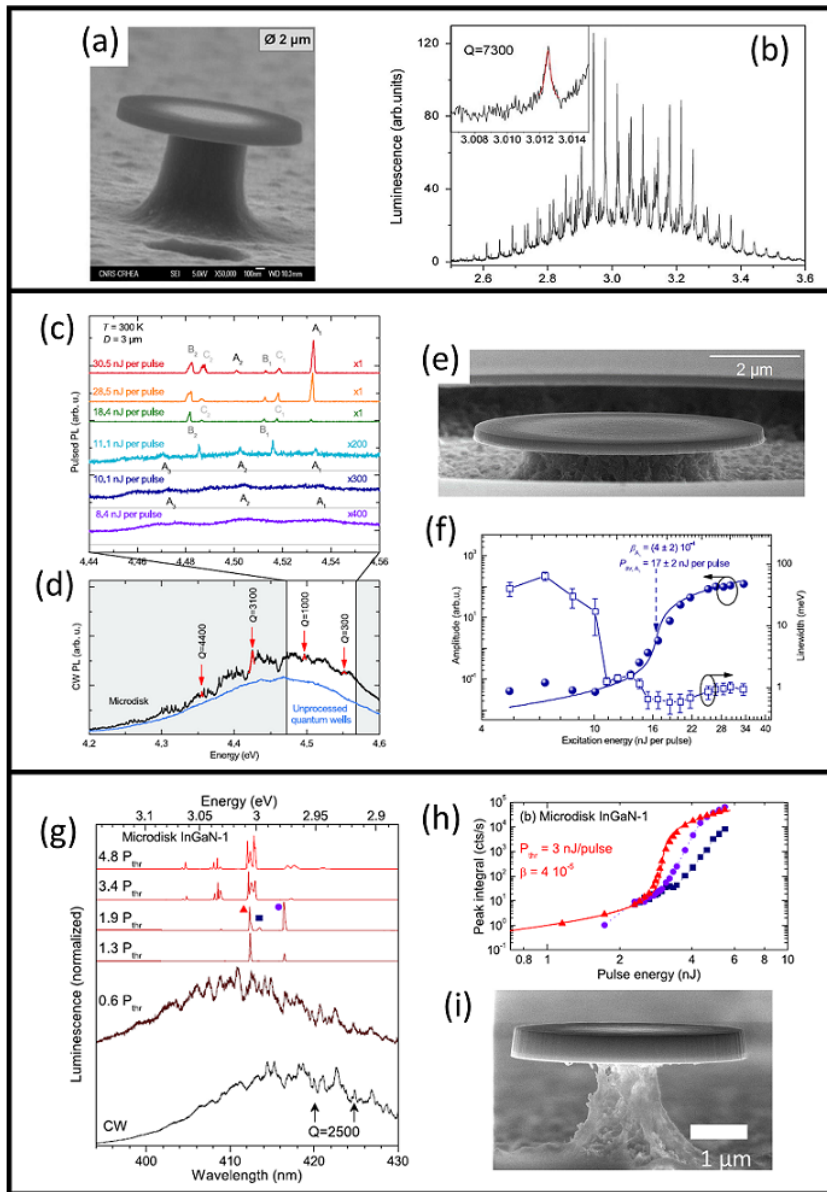


Figure 2.3: III-nitride microdisk resonators and lasers from our collaboration from before 2017. (a) SEM image of a 2 μm diameter disk and (b) RT CW μ-PL spectrum of a 5 μm diameter disk, inset shows zoom-in of a mode with  $Q = 7300$ , reproduced from Ref. [46]. (c) RT excitation energy dependent PL spectra and (d) below threshold CW PL showing Q factors of various modes in the UVC for a 3 μm diameter disk. (e) SEM image of an 8 μm diameter disk. (f) FWHM and peak amplitude over excitation energy in double-log plot for peak A1 in (c). (c)-(f) are reproduced from Ref. [49]. RT CW and pulse energy dependent PL spectra of (g) a 4 μm diameter disk in the blue. (h) Peak integral over pulse energy for the disk in (g) and (i) SEM image of a 4 μm diameter disk of the sample depicted in (g) and (h). (g)-(i) are reproduced from Ref. [50].

measurements were performed at RT. In 2011, they demonstrated high Q factors of  $> 7000$  using a 110 nm thin layer with QDs as the gain material grown on Si substrate by MBE [46]. An SEM image of a 2  $\mu\text{m}$  diameter disk is shown in Fig. 2.3 (a) and a RT CW PL spectrum of a 5  $\mu\text{m}$  diameter disk is shown in Fig. 2.3 (b). The inset shows a zoom-in of a mode with  $Q = 7300$ . This value is state of the art for III-nitride microdisks in the visible and has only been surpassed by Ref. [36]. However, no lasing was observed with microdisks with embedded QD active layers, so our consortium switched to QWs.

Our consortium extended the III-nitride microdisk laser platform into the deep-UV spectral range down to 275 nm in 2016, achieving pulsed lasing thresholds of  $15 \text{ mJ} \cdot \text{cm}^{-2}$  per pulse ( $37.5 \text{ MW} \cdot \text{cm}^{-2}$ ) at RT with a sample containing 20x 0.7 nm GaN/5 nm AlN QWs [49]. Fig. 2.3 (c) shows pulse energy dependent PL spectra and (d) a CW spectrum below threshold indicating several modes and their Q factors as well as a spectrum of an unprocessed sample. An SEM image of a 8  $\mu\text{m}$  diameter disk is shown in Fig. 2.3 (e). A sharp drop in FWHM and a clear S-shape in the double-log plot of peak intensity over excitation energy are shown in Fig. 2.3 (f) for peak A1 in (c), clearly indicating lasing.

Our collaboration also demonstrated pulsed optically pumped lasing at RT from microdisks across the entire UV to blue spectral range using a 266 nm pump laser (see Fig. 2 in the introduction) [50]. Below threshold CW and pulse energy dependent PL spectra are shown in Fig. 2.3 (g) for a sample lasing at 412 nm containing 10 pairs of InGaN/GaN QWs. Fig. 2.3 (h) shows the peak integral over pulse energy for three modes indicated by symbols in (g), showing a clear S-shape for the mode at 412 nm with a threshold of  $3 \text{ mJ} \cdot \text{cm}^{-2}$  per pulse ( $7.5 \text{ MW} \cdot \text{cm}^{-2}$ ). An SEM image of a 4  $\mu\text{m}$  diameter disk of the 412 nm sample (D559) is shown in Fig. 2.3 (i). No correlation between threshold and disk diameter was found in the diameter range of 3 to 12  $\mu\text{m}$ .

## 2.3 Results and discussion

### 2.3.1 Sample description

We will discuss 9 samples that were grown by either MBE or metal organic chemical vapor deposition (MOCVD) or hybrid combinations of both growth methods on silicon (111) substrate by B. Damilano, B. Alloing, S. Rennesson, E. Frayssinet, and F. Semond at CRHEA. Sketches of the heterostructures are depicted in Fig. 2.4. Table 2.1 summarizes some structural characteristics, as well as results obtained from RT low and high excitation power density PL measured on the as-grown samples using a CW laser at 244 nm and a pulsed laser at 266 nm (400 ps pulse width, 7 kHz repetition rate), respectively. When comparing low to high excitation PL, we can clearly see a blue-shift of 5 to 16 nm at higher excitation which is related to the band filling and screening of the QCSE. The table also includes the overlap integral of the  $\text{TE}_0$  optical mode with the QWs (without the barriers), which we estimated using a 1D mode solver (OMS) [97]. Atomic force microscopy (AFM) images of some of the samples are shown in Fig. 2.5 (a). The

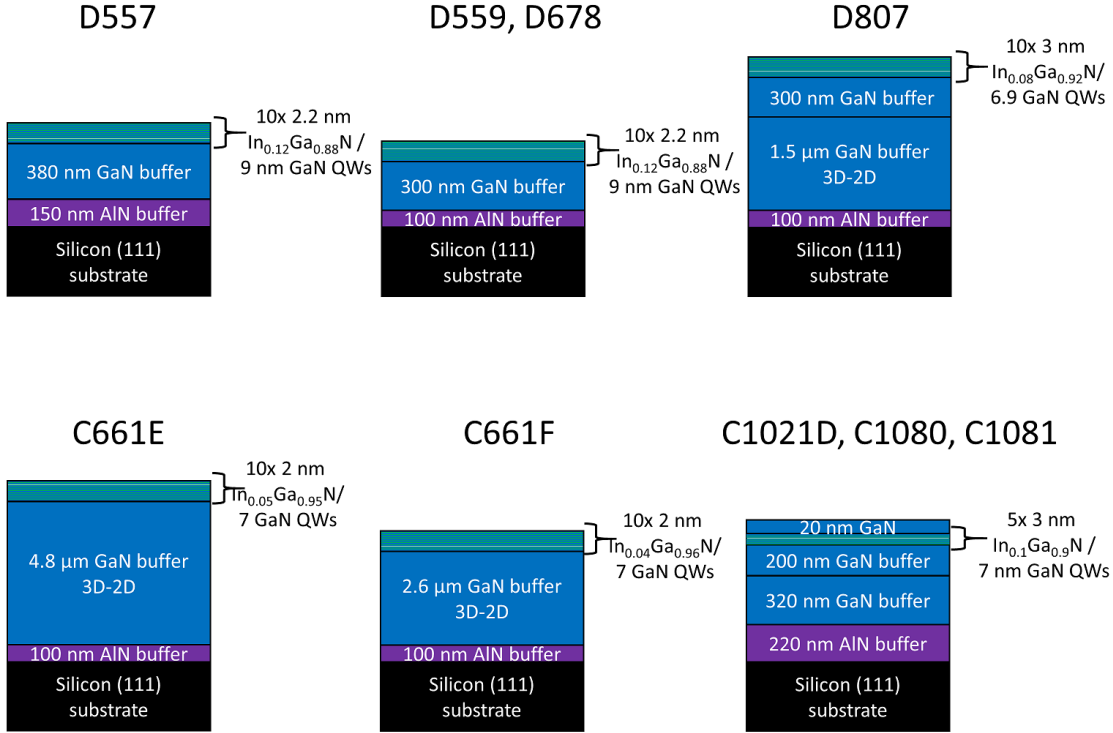


Figure 2.4: Sketches of the heterostructures of the investigated samples. The top row was grown by MBE and the bottom row by MOCVD.

sample	$d$ (nm)	QW growth	QWs	TDD ( $10^9$ $\text{cm}^{-2}$ )	$\lambda$ low (nm)	$\lambda$ high (nm)	FWHM (nm)	rel. peak intensity	Overlap $\text{TE}_0$ (%)
D557	850	MBE	10	10	427	419	38	0.06	1.7
D559	500	MBE	10	/	426	410	25	0.06	2.7
D678	500	MBE	10	24	428	414	23	0.13	2.7
D807	2000	MBE	10	1.3	408	403	29	0.47	0.048
C661E	5000	MOCVD	10	0.57	/	373	22	0.83	0.00081
C661F	2800	MOCVD	10	1.3	381	378	22	1	0.0068
C1021D	810	MOCVD	5	13	412	400	17	0.56	0.40
C1080	810	MOCVD	5	12	419	403	27	0.53	0.42
C1081	810	MOCVD	5	12	433	427	30	0.49	0.44

Table 2.1: Description of the investigated samples with total thickness  $d$ , QW growth method, number of QWs, TDD, and their RT low and high excitation power density PL with center wavelength, and FWHM, peak intensity relative to C661F for high excitation PL, and the overlap of the  $\text{TE}_0$  mode with the QWs.

high excitation power density PL spectra are shown in Fig. 2.6.

The samples D557, D559, and D678 were grown entirely by MBE and have similar heterostructures. First, an AlN buffer layer of 150 nm for D557 and 100 nm for D559 and D678 was grown. This layer was followed by a GaN buffer layer of 380 nm for D557 and 300 nm for

D559 and D678. Finally, 10 pairs of 2.2 nm  $\text{In}_{0.12}\text{Ga}_{0.88}\text{N}$  / 9 nm GaN QWs were grown. In the case of D559, the first 100 nm of the GaN buffer layer were n-doped with a silicon concentration of  $5 \times 10^{19} \text{ cm}^{-3}$ . The threading dislocation density (TDD) as determined by X-ray diffraction (XRD) and AFM and is in the range of 1 to  $2 \times 10^{10} \text{ cm}^{-2}$ . An AFM image of D678 is shown in Fig. 2.5 with pyramids visible around some dislocations. Under high excitation power density PL, the samples emit around 410 to 420 nm with a rather large linewidth and fairly low relative peak intensity (see Table 2.1 and Fig. 2.6 (a)).

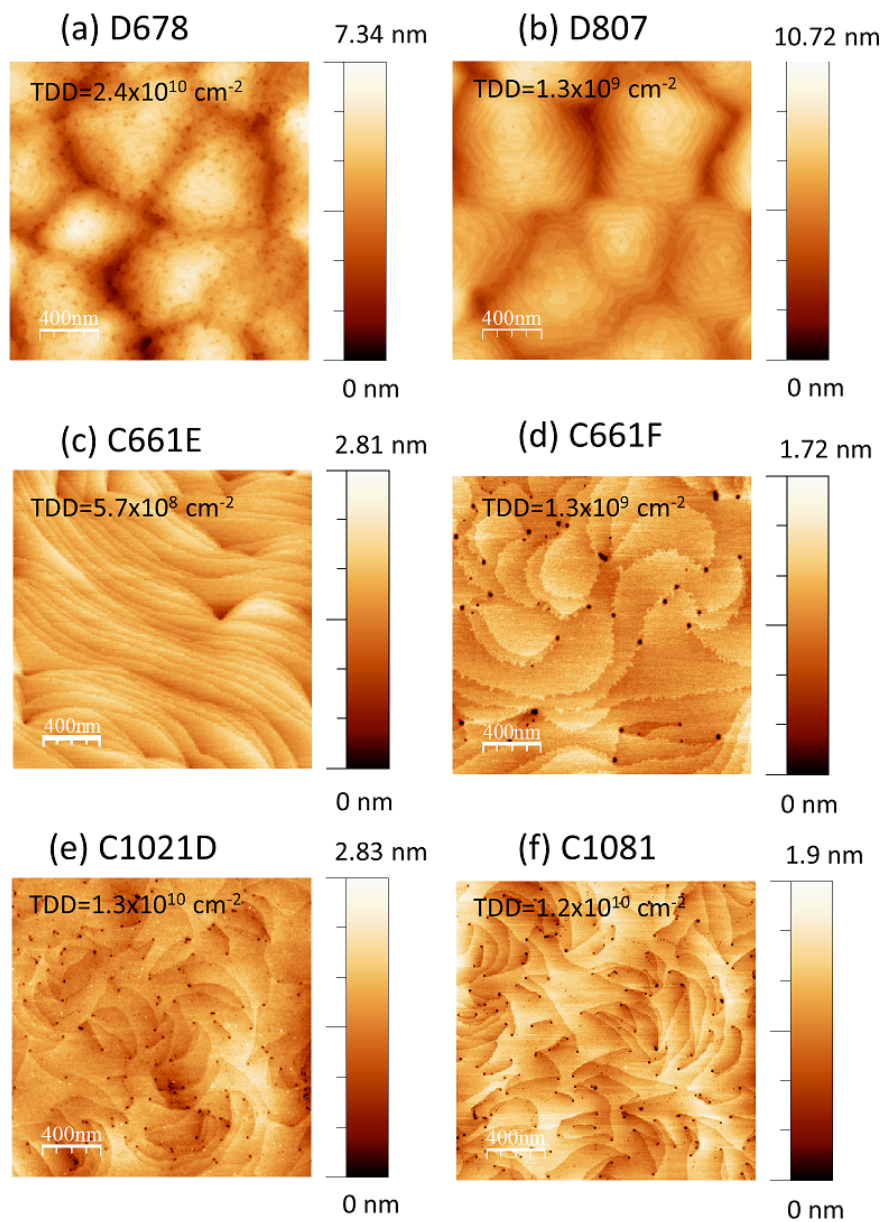


Figure 2.5: AFM images of (a) D678, (b) D807, (c) C661E, (d) C661F, (e) C1021D, and (f) C1081 with TDD, measured by S. Renneson, B. Damilano, and A. Courville at CRHEA.

For sample D807, the 100 nm AlN buffer layer was grown by MBE. Then, to reduce the TDD, 3D GaN islands were grown by MOCVD that were then coalesced into a 2D layer of 1.5  $\mu\text{m}$  thickness. Then, the growth was continued by MBE and a 300 nm GaN buffer layer, followed by 10 pairs of 3 nm  $\text{In}_{0.08}\text{Ga}_{0.92}\text{N}$  / 6.9 nm GaN QWs were grown. Fig. 2.5 (b) shows an AFM image of D807. We can observe pyramids that formed around dislocations. The root mean square (RMS) roughness is 1-2 nm. The TDD is  $1.3 \times 10^9 \text{ cm}^{-2}$ . The high excitation power density PL on the as-grown sample shows a slightly shorter wavelength of 403 nm and a significantly higher intensity than for D557, D559, and D678, as can be seen in Fig. 2.6 (a). The higher intensity is likely related to the improved material quality due to the reduction in TDD. The undulations in the spectra are Fabry-Perot thickness oscillations. Using Eq. 1.39 with  $L = 2h$ , where  $h$  is the sample height,  $\Delta\lambda = 9.2 \text{ nm}$ , and using  $n_g = 4.04$  for GaN at  $\lambda = 398 \text{ nm}$ , we obtain  $h = 2084 \text{ nm}$ , which is very close to the nominal  $h = 2000 \text{ nm}$  (see Table 2.1).

The samples C661E and C661F also use MBE templates of 100 nm AlN on Si (111). However, in the case of C661E, we patterned mesas on the template to perform selective area growth (SAG) in an effort to reduce cracking in thicker layers. The rest of the heterostructure of these two samples was grown by MOCVD during the same growth run. Using a 3D-2D growth transition, a GaN buffer layer thickness of 2.6  $\mu\text{m}$  was targeted. For C661E, this layer ended up being significantly thicker because the growing material concentrated on the mesas. Finally, 10 pairs of 2 nm  $\text{In}_{0.05}\text{Ga}_{0.95}\text{N}$  / 7 nm GaN QWs were grown. AFM images are shown in Fig. 2.5 (c) and (d). Both samples have a similar RMS roughness in the range of 0.2 to 0.6 nm. For C661E we can observe step-flow growth, while C661F grew in spirals. The TDD of C661E is  $5.7 \times 10^8 \text{ cm}^{-2}$  and for C661F it is  $1.3 \times 10^9 \text{ cm}^{-2}$ . These samples emit around 375 nm under high excitation density RT PL. The intensity is much higher than for the MBE-grown samples, which may be due to a higher material quality of QWs grown by MOCVD. The undulations visible for C661F are Fabry-Perot thickness oscillations, which give  $h = 2640 \text{ nm}$  for  $\Delta\lambda = 5 \text{ nm}$  and  $n_g = 5.46$  for GaN at  $\lambda = 383 \text{ nm}$ . This value is very close to the nominal  $h = 2800 \text{ nm}$  (see Table 2.1).

The samples C1021D, C1080, and C1081 were fully grown by MOCVD and have the same nominal heterostructure. First, a template was grown consisting of a 220 nm AlN buffer layer and a 320 nm GaN buffer layer. Then, another 200 nm GaN were grown followed by 5 pairs of 3 nm  $\text{In}_{0.1}\text{Ga}_{0.9}\text{N}$  / 7 nm GaN QWs and a 20 nm GaN cap layer. The growth conditions of the QWs were different for the three samples. However, these differences do not seem to significantly impact the performance. AFM images of C1021D and C1081 are shown in Fig. 2.5 (e) and (f). The surfaces of all three samples look very similar and their TDD is around  $1.2 \times 10^{10} \text{ cm}^{-2}$ . Under high excitation density PL, C1021D and C1080 emit at around 400 nm and C1081 around 430 nm, as can be seen in Fig. 2.6 (b). C1021D has a narrower FWHM than C1080 and C1081. C1081 has a shoulder at 400 nm, which is likely related to emission of an excited state. The intensity of all three samples is very similar (see Table 2.1). They are less intense than C661E and F, and have about the same intensity as D807, which in turn is thicker and has a lower TDD.

The PL results suggest that the samples, whose QWs were grown by MOCVD are better, as

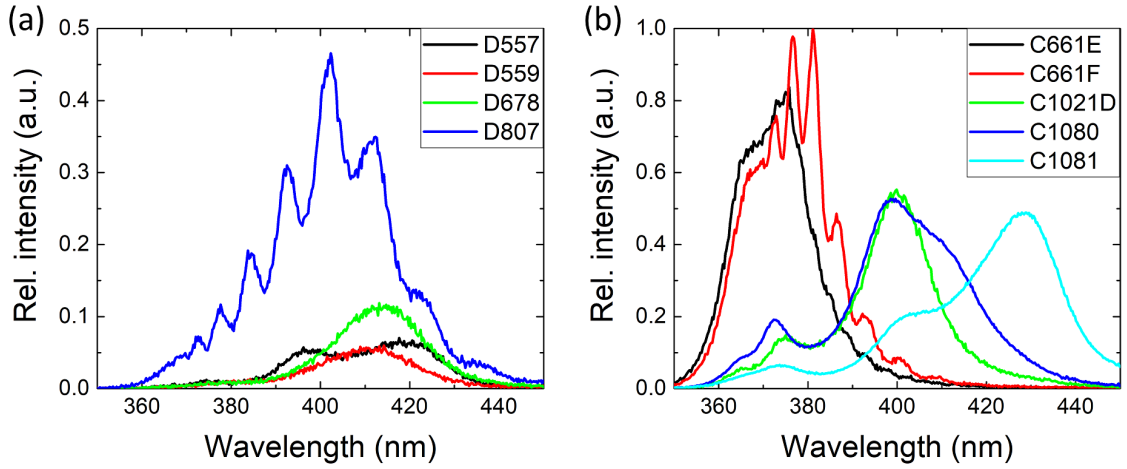


Figure 2.6: High excitation power density pulsed PL spectra from the as-grown (a) MBE and (b) MOCVD samples. Measurements performed by B. Damilano and B. Allong at CRHEA.

their emission is more intense, even though C1021D, C1080, and C1081 have fewer QWs in total. State of the art MBE-grown light emitting diodes (LEDs) show more than an order of magnitude smaller output powers than LEDs grown by MOCVD [139]. The lower efficiency of MBE-grown QWs is said to be due to a higher density of point defects constituting non-radiative recombination centers, which are related to the lower growth temperature [140].

### 2.3.2 Optical confinement

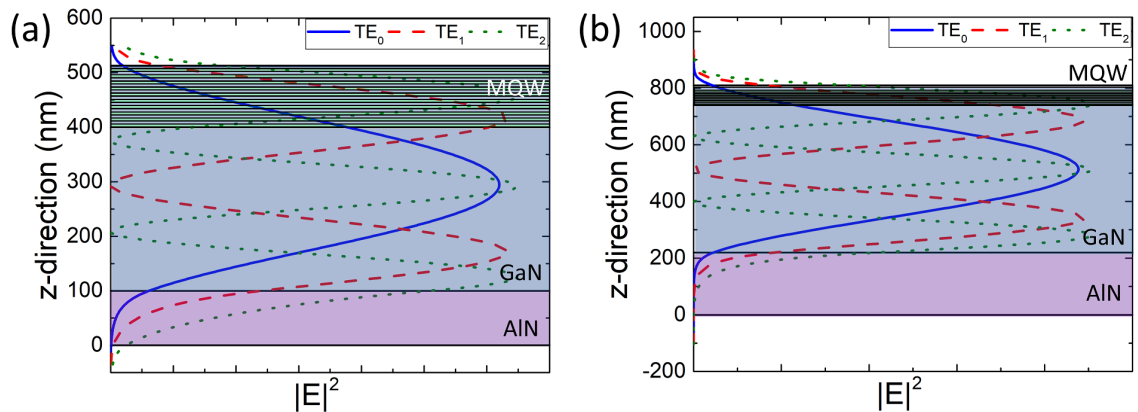


Figure 2.7: Optical confinement of the  $TE_0$ ,  $TE_1$ , and  $TE_2$  modes for (a) D678 at  $\lambda = 416$  nm and (b) C1081 at  $\lambda = 420$  nm.

Fig. 2.7 shows the optical confinement of the  $TE_0$ ,  $TE_1$ , and  $TE_2$  modes for (a) D678 and (b) C1081. We can see that the overlap of these modes with the QWs is rather small. Table 2.2 summarizes the overlap of these three modes with the QWs (without the barriers) for all

investigated samples. For the TE<sub>0</sub> mode the highest values of 2.7% are obtained for the thinnest samples, D559 and D678. For the thickest sample, C661E, the overlap is only  $8.1 \times 10^{-6}$ . The higher order TE<sub>1</sub> and TE<sub>2</sub> modes show a larger overlap with up to 6.4% for the TE<sub>1</sub> mode of D678. We cannot be sure which vertical mode orders lase and even higher order modes are also possible. Since in our heterostructures the QWs need to be located near the surface (top 120 nm, see Fig. 2.4), in order to be optically pumped efficiently, thinner structures are preferable to achieve a larger overlap.

Sample	thickness (nm)	QWs	TE <sub>0</sub> (%)	TE <sub>1</sub> (%)	TE <sub>2</sub> (%)
D557	850	10	1.7	4.8	5.6
D559	500	10	2.7	5.6	5.9
D678	500	10	2.7	6.4	5.8
D807	2000	10	0.048	0.19	0.41
C661E	5000	10	0.00081	0.0032	0.0073
C661F	2800	10	0.0068	0.027	0.061
C1021D	810	5	0.40	1.4	2.7
C1080	810	5	0.42	1.5	2.7
C1081	810	5	0.44	1.6	2.8

Table 2.2: Summary of thickness, number of QWs, and overlap of the TE<sub>0</sub>, TE<sub>1</sub>, and TE<sub>2</sub> modes with the QWs.

It is also possible that we have some weak vertical gain guiding in our structures that shifts the modes more towards the active region. Lateral gain guiding is observed in broad area lasers with a stripe structure, for example [141, 142].

Using cladding layers to confine the mode vertically within the active region could be useful, however, this would result in significantly thicker heterostructures which in turn makes the fabrication of suspended photonic circuits much more challenging.

### 2.3.3 Band structure simulations

We use Nextnano [143], a software for device simulation, to simulate the band structure of the active regions of some of our samples using 6-band **k.p** theory.

Fig. 2.8 shows the conduction band (CB) and three valence bands (heavy hole (hh), light hole (lh), crystal field (ch)), as well as the squared wave functions of the ground state and first excited state of electron (e1, e2) and heavy and light hole (hh1, hh2, lh1, lh2), where 1 signifies the ground state and 2 the first excited state. The InGaN/GaN multi-QW (MQW) is pseudomorphically strained on GaN. Piezo- and pyro-electric polarization are taken into account. Fig. 2.8 (a) shows a 2.2 nm QW and a 7 nm barrier with an e1 to hh1 transition of 2.91 eV, corresponding to 427 nm, the low-power PL center wavelength for sample D559 (see Table 2.1). In our simulation this ground state energy is attained for an In composition of 15.8%, as opposed to the

nominal 12%. This difference is rather small and exemplifies the fact that the QW composition is not that well known and depends on the material parameters used to determine it, i.e. the band gaps, the bowing parameters, etc. Fig. 2.8 (b) shows a 3nm InGaN MQW with 7 nm GaN barriers. The ground state transition is 3.01 eV, which corresponds to 412 nm, the low-power PL center wavelength of sample C1021D. Here, we use an In composition of 11.5% as opposed to the nominal 10%.

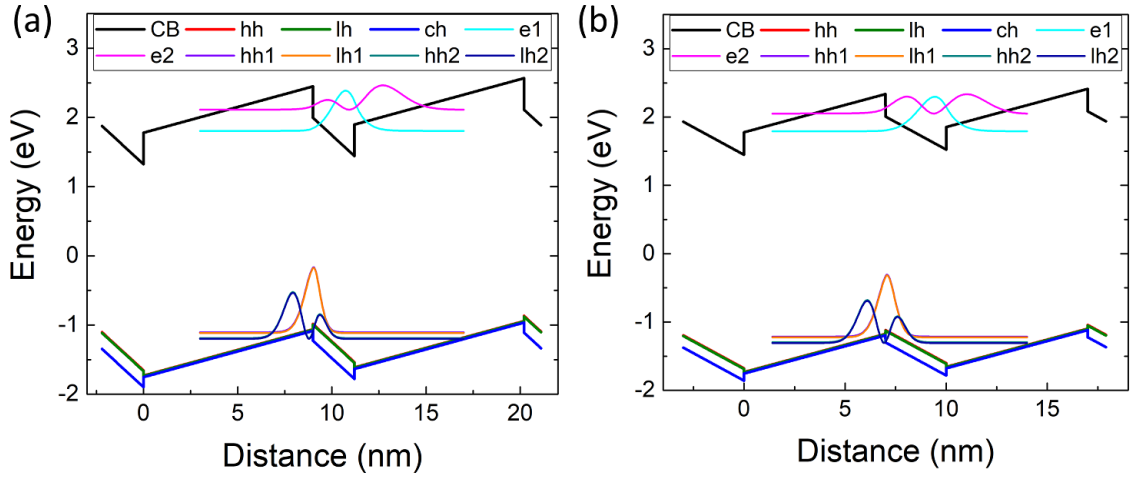


Figure 2.8: Calculated band structure and squared electron and hole wave functions for samples (a) D559 and (b) C1021D.

sample	e1-hh1	e1-hh2	e2-hh1	e2-hh2
D559	2.91 eV (0.24)	3.00 eV (0.11)	3.22 eV (0.23)	3.30 eV (0.028)
C1021D	3.01 eV (0.12)	3.09 eV (0.095)	3.26 eV (0.44)	3.35 eV (0.081)

Table 2.3: Energies and in parentheses oscillator strengths of ground and excited state transitions in the QWs of D559 and C1021D. e to lh transitions are not shown, but can also have large oscillator strengths.

Table 2.3 summarizes the transition energies and their oscillator strengths (in parentheses) for the e1-hh1, e1-hh2, e2-hh1, and e2-hh2 transitions. For D559, we can see that the ground state transition has the largest oscillator strength, followed by the e2-hh1 transition at 3.22 eV (385 nm). For C1021D, the e2-hh1 transition has the largest oscillator strength, followed by the e1-hh1 transition. While we will see in Table 2.5 that this sample lases at 403 nm, we also observed a peak around 375 nm in the high excitation density PL shown in Fig. 2.6 (b) that is likely related to this transition. Besides the oscillator strength, we also need to take the population of the energy levels into account. For example, the e2 level will only be populated at high excitation power. Thus the e2-hh1 transition is less likely to lase than the e1-hh1 transition albeit having similar or larger oscillator strength.

### 2.3.4 Fabrication of microdisks

Mushroom-type microdisks were fabricated on all samples using the fabrication process detailed in section 1.3.4. Samples D557 and D559 were fabricated before the beginning of this thesis by I. Roland. D559 is the same sample as discussed in Figs. 2.3 (g) and (h) [50]. SEM images of microdisks on all 9 samples are depicted in Fig. 2.9. In all cases, except for D678, we can see fairly smooth side-walls. It is not clear why the side-walls of the microdisks on D678 are so rough, perhaps the SiO<sub>2</sub> hard mask was a bit too thin, and the side-walls got damaged during the ICP step. We will see, however, that in this case, the influence of the side-wall roughness on the threshold does not seem to be very strong (see Table 2.5, comparison of D678 with D559). Clear differences in the height of the heterostructures are visible, with Fig. 2.9 (e) showing the thickest sample (C661E). In Fig. 2.9 (e) we can see small spikes that come from micro-masking during the etching.

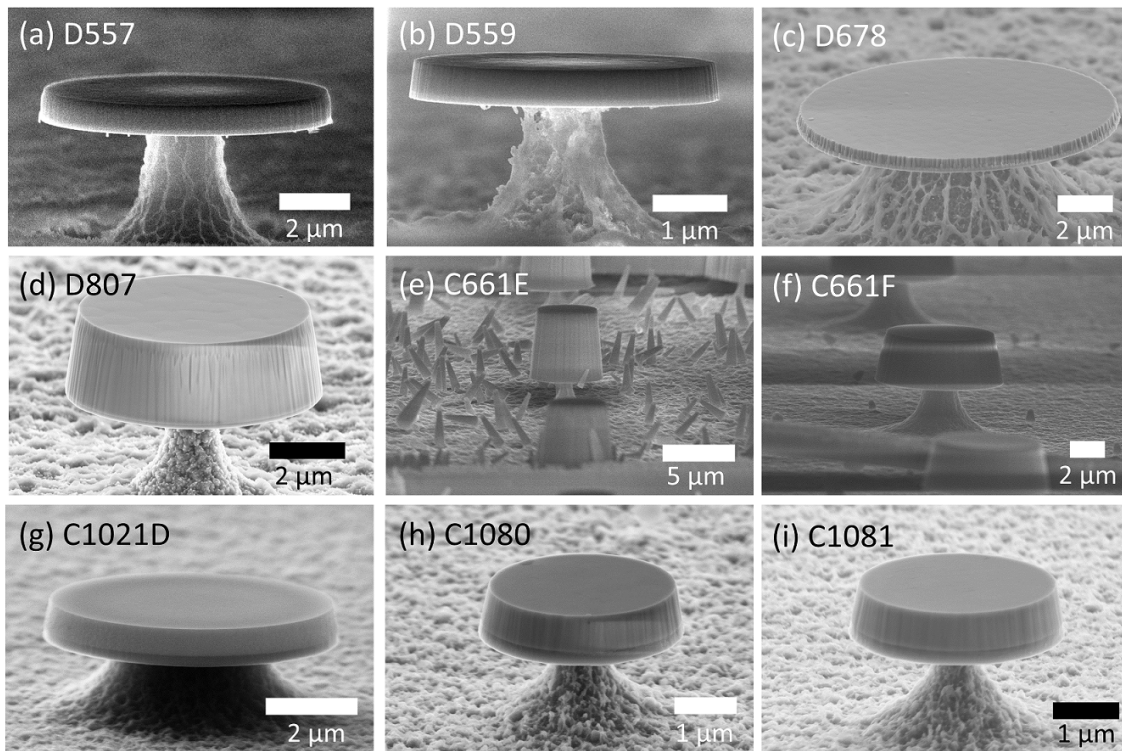


Figure 2.9: Side-view SEM images of (a) an 8 $\mu\text{m}$  disk on D557, (b) a 4 $\mu\text{m}$  disk on D559, (c) a 12 $\mu\text{m}$  disk on D678, (d) a 6 $\mu\text{m}$  disk on D807, (e) a 4 $\mu\text{m}$  disk on C661E, (f) a 6 $\mu\text{m}$  disk on C661F, (g) a 6 $\mu\text{m}$  disk on C1021, (h) an 8 $\mu\text{m}$  disk on C1080, and (i) a 3 $\mu\text{m}$  disk on C1081. (a) and (b) were measured by I. Roland. (c), (d), (h), and (i) were measured by V. Brändli.

### 2.3.5 Quality factor

We have not systematically studied the Q factor of our microdisks below threshold. However, the few measurements we do have indicate that the value of  $Q_{int}$  is generally in the range of 2500 to 7300.

	D559	D677	C1159D	C1081	Mexis et al. [46]	Rousseau et al. [36]
$Q_{int}$	2500	4700	3500	6000	7300	10200
$\lambda$ (nm)	420	442	420	419	411	474

Table 2.4: Q factors of some of our recent samples compared to a paper from our collaboration from 2011 [46] and a paper from Grandjean's group from 2018 [36].

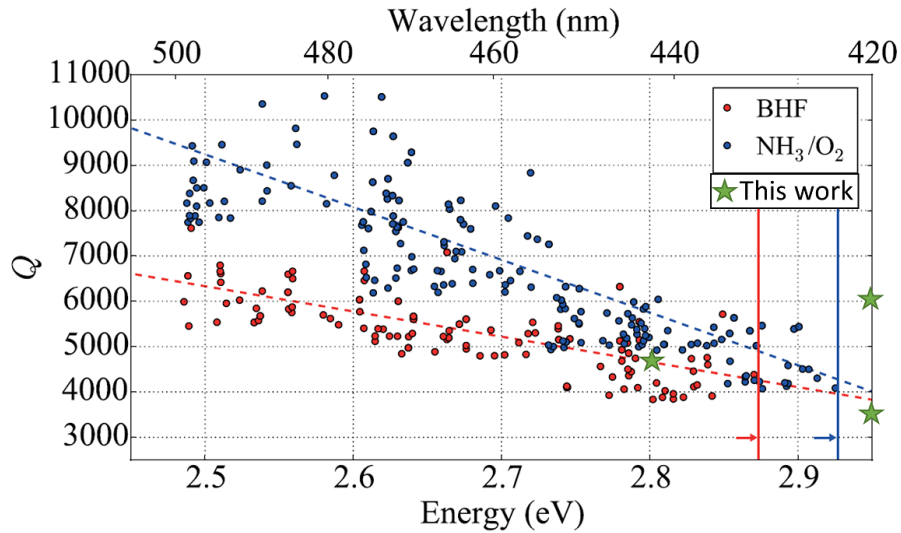


Figure 2.10: Q factor over energy for two different surface treatments measured at 5K in literature. The stars show our work measured at RT. Adapted from Rousseau et al. [36].

Table 2.4 shows the Q factors of WGMs and their corresponding wavelengths of four of our recent samples and compares them to a paper from our collaboration from 2011 [46] and a paper from Grandjean's group from 2018 [36]. The sample D677 has the same heterostructure as D678. Sample C1159D contains 5 QWs and emits at 407 nm under low excitation PL and lases around 380 nm. The Q factors of D677 and C1159D are given for microdisks coupled to bus waveguides. These samples will be discussed in detail in chapters 3 and 4. Our samples, both current and past, have Q factors of a few thousand. The highest value reported in literature for III-nitride microdisks was 10200 at 474 nm by Rousseau et al. (see Fig. 1) [36], who performed surface passivation in oxygen to achieve this record. Fig. 2.10 shows the Q factor over energy for two different surface treatments, reproduced from Ref. [36], as well as the Q factors of three of our samples (D677, C1159D, C1081). We can see a strong decrease in Q with decreasing wavelength in the results from Rousseau et al. [36]. For the wavelength range of 420 to 440 nm,

the Q factors we achieved are in the same range as theirs, suggesting that we have good quality resonators. The Q factor is probably limited by surface absorption and side-wall scattering losses.

### 2.3.6 Pulsed optically pumped lasing

We used the  $\mu$ -PL setup discussed in Fig. 1.45 using the 355 nm pulsed laser. Lasing was observed for all nine investigated samples at RT and the wavelength, threshold, and disk diameter are summarized in Table 2.5. The lowest threshold peak power of  $18 \text{ kW} \cdot \text{cm}^{-2}$  or threshold energy of  $0.07 \text{ mJ} \cdot \text{cm}^{-2}$  per pulse was achieved for C1081.

sample	QW growth	TDD ( $10^9 \text{ cm}^{-2}$ )	Wavelength (nm)	Threshold ( $\text{kW} \cdot \text{cm}^{-2}$ )	Threshold ( $\text{mJ} \cdot \text{cm}^{-2}$ p.p.)	Diameter ( $\mu\text{m}$ )
D557	MBE	10	412	370	1.5	12
D559	MBE	/	412	370	1.5	4
D678	MBE	24	416	340	1.3	12
D807	MBE	1.3	408	160	0.64	6
C661E	MOCVD	0.57	370	250	1.0	5
C661F	MOCVD	1.3	380	720	2.9	6
C1021D	MOCVD	13	403	25	0.1	8
C1080	MOCVD	12	410	20	0.08	3
C1081	MOCVD	12	420	18	0.07	3

Table 2.5: Pulsed RT optically pumped lasing measurements of the investigated samples with QW growth method, TDD, wavelength, threshold peak power density, threshold energy per pulse, and microdisk diameter. Measurements performed by C. Brimont, L. Doyennette, and T. Guillet at L2C.

Fig. 2.11 shows pump power dependent spectra of a  $3 \mu\text{m}$  diameter disk on C1081. Several modes are lasing and we can see clamping of the spontaneous emission. The two strongest modes at 419 and 423 nm have very similar thresholds and are in strong competition. Figs. 2.12 (a) and (b) show the integrated intensity and linewidth over peak pump power for the modes at 419 and 423 nm, respectively. We point out the limited visibility of whispering-gallery modes (WGMs) below threshold in a top-collection setup, as WGMs radiate preferentially in-plane. For the mode at 419 nm (Fig. 2.12 (a)), the narrowest linewidth of 0.07 nm is observed at  $15 \text{ kW} \cdot \text{cm}^{-2}$  peak power and the threshold is around  $18 \text{ kW} \cdot \text{cm}^{-2}$  (or threshold energy per pulse of  $0.07 \text{ mJ} \cdot \text{cm}^{-2}$ ). At higher power densities, a second mode appears at nearly the same wavelength, thus making the linewidth analysis complex. For the mode at 423 nm (Fig. 2.12 (b)), the linewidth starts narrowing at  $8 \text{ kW}/\text{cm}^2$ . A zoom on the onset of the mode dynamics indicates a threshold at  $10 \text{ kW} \cdot \text{cm}^{-2}$  consistent with the linewidth narrowing. There is nonetheless mode competition with the 419 nm mode. Consequently, Fig. 2.12 (b)) indicates an overall threshold to be around  $25 \text{ kW} \cdot \text{cm}^{-2}$ . A close-up of the mode at 423 nm at low pump powers below threshold is shown in Fig. 2.12 (c). A large dynamic between the peak intensity and the

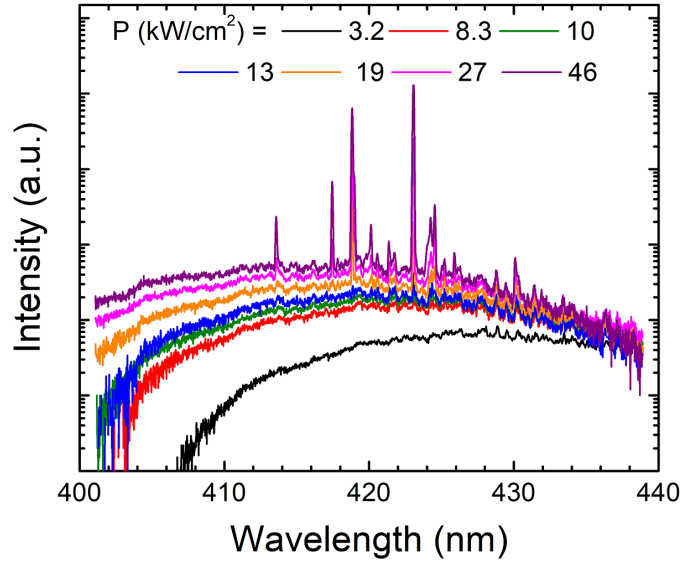


Figure 2.11: Pump power dependent spectra of a  $3\mu\text{m}$  diameter disk. Spectra measured by C. Brimont at L2C.

background spontaneous emission of  $> 300$  can be discerned for the 423 nm mode in Fig. 2.12 (d), where we plot the peak and background intensities over pump power in a double logarithmic plot. At the last point of  $45\text{kW}\cdot\text{cm}^{-2}$  the CCD is saturated.

### 2.3.7 Calculation of the threshold power

Using the rate equation model introduced by Baba and Sano, we get the following formula for the threshold power [144]:

$$P_{th} = \frac{E_{phot}d}{U\eta_{inj}(1-R)} \left( \frac{1-C_{sp}}{\tau_{sp}} + \frac{1}{\tau_{nr}} \right) n_{th}, \quad (2.1)$$

with  $E_{phot}$  the photon energy of the pump laser,  $d$  the total thickness of the active medium,  $U$  the ratio between the homogeneous broadening of the laser mode and the spectral broadening of the spontaneous emission [144],  $\eta_{inj}$  the injection efficiency of the carriers into the QWs,  $R$  the surface reflectivity,  $C_{sp}$  the spontaneous emission factor,  $\tau_{sp}$  the spontaneous emission lifetime,  $\tau_{nr}$  the non-radiative lifetime, and  $n_{th}$  the threshold carrier density, which is given by

$$n_{th} = n_{tr} + \frac{n_g}{c\Gamma g\tau_c}, \quad (2.2)$$

where  $n_{tr}$  is the transparency carrier density,  $n_g$  the group index,  $c$  the speed of light,  $\Gamma$  the overlap of the optical mode with the QWs,  $g$  the dynamic gain, and  $\tau_c$  the photon lifetime. Eq. 2.2 indicates that the first requirement to obtain a net positive gain is to reach transparency. Once transparency is attained, another important factor to reach threshold is  $\Gamma$ . For the  $\text{TE}_0$  mode, we calculate  $\Gamma = 0.44\%$  for the 5 QWs. However,  $\Gamma$  is larger for higher order modes, i.e.

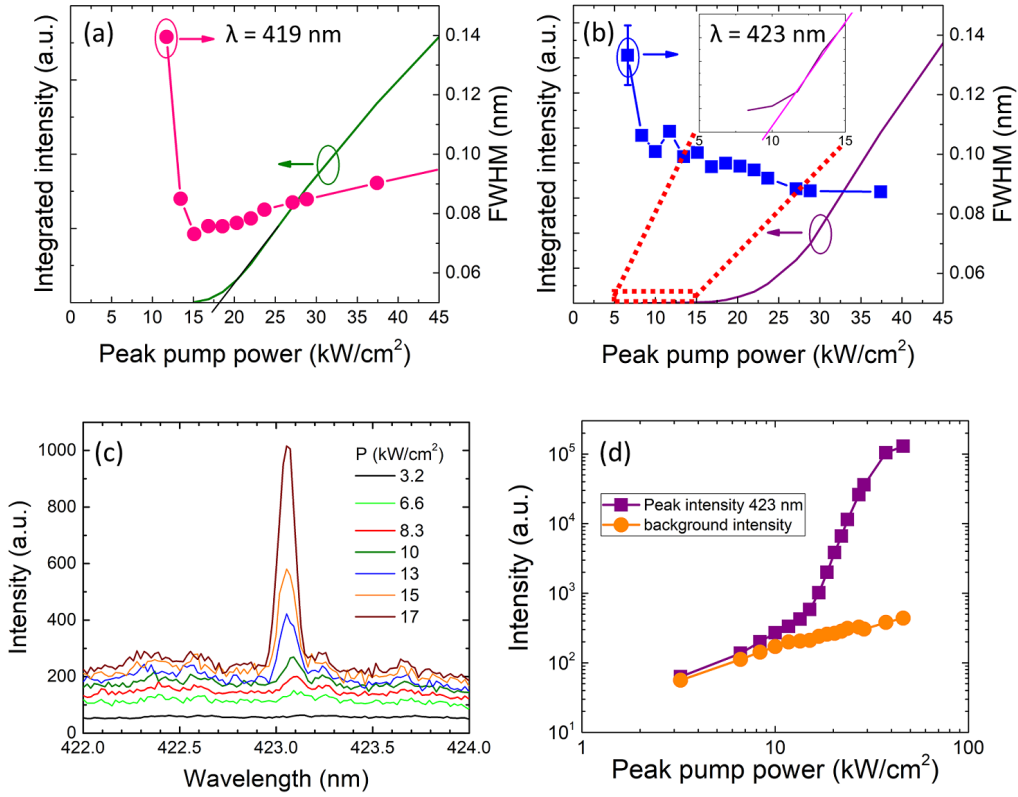


Figure 2.12: Integrated intensity and full-width at half maximum (FWHM) of the modes (a) at 419 nm and (b) at 423 nm. Inset in (b) shows a zoom-in at low power density. (c) Close-up of the spectra at low power density for the 423 nm mode. (d) Peak and background intensities over pump power for the mode at 423 nm.

2.8% for the TE<sub>2</sub> mode, and it is not clear which mode is lasing. We calculate  $n_g = 3.44$  and  $g$  is given by  $g = g_0/n_{tr}$ , where  $g_0$  is the empirical gain coefficient, which we estimate to be  $35000 \text{ cm}^{-1}$ , based on Ref. [34], where they study a fairly similar QW (3 nm, 15% In) and which constitutes a typical value.

The photon lifetime is given by

$$\tau_c = \frac{Q\lambda}{2\pi c}, \quad (2.3)$$

with  $Q$  the quality factor and  $\lambda$  the peak wavelength. We calculate  $Q = 6000$  using the below threshold linewidth, which is in good agreement with our previous samples (see Table 2.4 [50, 145]), and  $\lambda = 420 \text{ nm}$ . We get  $\tau_c = 1.3 \text{ ps}$ .

The sheet transparency carrier density is around  $3 \times 10^{12} \text{ cm}^{-2}$  for InGaN QWs, which gives us  $n_{tr} = 1 \times 10^{19} \text{ cm}^{-3}$  for our 3 nm QWs [34, 146, 147]. Using Eq. 2.2, we thus get  $n_{th} = 1.57 \times 10^{19} \text{ cm}^{-3} = 1.57 n_{tr}$ .

We can calculate  $C_{sp}$  using [144]

$$C_{sp} = \frac{p\Gamma_r\lambda^3}{4\pi^2 n_{eff}^3 V_m} \frac{\lambda}{\Delta\lambda}, \quad (2.4)$$

where  $p$  is the polarization anisotropy of the spontaneous emission,  $\Gamma_r$  is the relative confinement factor,  $n_{eff}$  is the effective refractive index,  $V_m$  is the mode volume, and  $\Delta\lambda$  is the homogeneous broadening. We calculate the mode volume using the finite-difference time-domain (FDTD) method with  $V_m = \int_V \epsilon |\mathbf{E}|^2 dV / [\epsilon |\mathbf{E}|^2]_{max}$  and obtain  $0.22 \mu\text{m}^3$  for a first order radial  $\text{TE}_0$  mode. Note that this weak mode volume is linked to the short wavelength investigated. Using  $p = 1$  (consistent with the formula for  $\beta$  in Ref. [108], p. 562),  $\Gamma_r = 1$  (for a cavity with many modes [148]),  $n_{eff} = 2.49$ , and  $\Delta\lambda = 15 \text{ nm}$ , we get  $C_{sp} = 2 \times 10^{-2}$ . This value is still fairly small and can thus be neglected in Eq. 2.1.

Note that  $C_{sp}$ , the spontaneous emission factor, is in first approximation inversely proportional to the number of allowed cavity modes in the spectral broadening. This spontaneous emission factor is in the literature often presented as  $\beta$  [33, 34, 50]. By accounting for the homogeneous broadening in the calculation of  $C_{sp}$ , we assume to be in the so-called bad emitter regime, i.e. emitter linewidth larger than the cavity linewidth [108, 149]. Note that Eq. 2.1 is the same as in Ref. [108] (p. 252) except for the pre-factor  $U$  that accounts for homogeneous broadening.

Using the standard rate equations given in Ref. [108] (p. 249), we can fit the L-L curve of Fig. 2.12 (b) in the range up to  $25 \text{ kW} \cdot \text{cm}^{-2}$ . We obtain a value of  $6 \times 10^{-3}$  for the spontaneous emission factor, which is within a factor of 3 of the calculated value of  $C_{sp}$ . For the here presented range of microdisk parameters, the equations for the laser threshold are equivalent to those for ridge waveguide lasers [108, 150] where the spontaneous emission factor is weak.

$E_{phot} = 3.49 \text{ eV}$  for our pump laser and  $d = 15 \text{ nm}$  for our 5 QWs. The reflectivity of GaN at  $355 \text{ nm}$  is 19% [151]. We can estimate  $\tau_{sp}$  and  $\tau_{nr}$  using the ABC model [152] with

$$\frac{1}{\tau_{tot}} = \frac{1}{\tau_{sp}} + \frac{1}{\tau_{nr}} = A + Bn + Cn^2, \quad (2.5)$$

where the first term describes Shockley-Read-Hall recombination, the second term describes radiative recombination, and the third term describes Auger-type recombination. We use  $A = 4.2 \times 10^7 \text{ s}^{-1}$ ,  $B = 3 \times 10^{-12} \text{ cm}^3 \text{ s}^{-1}$ , and  $C = 4.5 \times 10^{-31} \text{ cm}^6 \text{ s}^{-1}$  (see Refs. [34, 152]). As discussed below, there is a large spread on these values in the literature. We use the aforementioned values because they have been measured for InGaN laser diodes emitting in the same spectral range as our sample and at high carrier densities. However, the laser diodes studied by Scheibenzuber et al. [152] were grown on bulk GaN, thus having a much smaller dislocation density than our material, which has an influence on the non-radiative lifetime. Assuming a 5 times larger  $A$  would increase  $P_{th}$  by a factor of 2, a 10 times larger  $A$  would result in a factor 3 increase in  $P_{th}$ . Given that our measured thresholds are quite low, the non-radiative lifetime cannot be extremely short. At threshold, we calculate  $\tau_{tot} = 5.1 \text{ ns}$ ,  $\tau_{sp} = 21 \text{ ns}$ , and  $\tau_{nr} = 6.6 \text{ ns}$  using the ABC values of Scheibenzuber et al. [152]. It corresponds to an internal quantum ef-

efficiency of 24% at threshold. This  $\tau_{tot}$  is very close to and a bit larger than the pulse width of 4 ns, which can influence the carrier dynamics and increase the threshold. Meanwhile, a 5 times larger  $A$  would result in a  $\tau_{tot}$  of 2.7 ns, which is significantly shorter than the pulse width, and a factor 2 larger  $P_{th}$ , which would still fit well with our experimental values. Our threshold calculation assumes a pseudo-continuous modeling.

The parameters  $U$  and  $\eta_{inj}$  in Eq. 2.1 are not well-known.  $U$  is the ratio between the homogeneous broadening and the spectral broadening. It is unlikely that all the spontaneous emission participates homogeneously to the laser mode, and  $U$  is certainly less than one. Under non-resonant optical pumping, the carriers are photo-induced in the barriers and subsequently captured in the QWs. Moreover, at RT, a fraction of the carriers can thermally escape from the QWs. There are 5 QWs in our active structure, which are not identical and thus cause some broadening. Considering a  $U$  value of 0.4 (for a spectral broadening of 35 nm and a homogeneous broadening of 15 nm) and a large range of  $\eta_{inj}$  between 0.3 and 0.7, their product is likely in the 0.1-0.3 range.

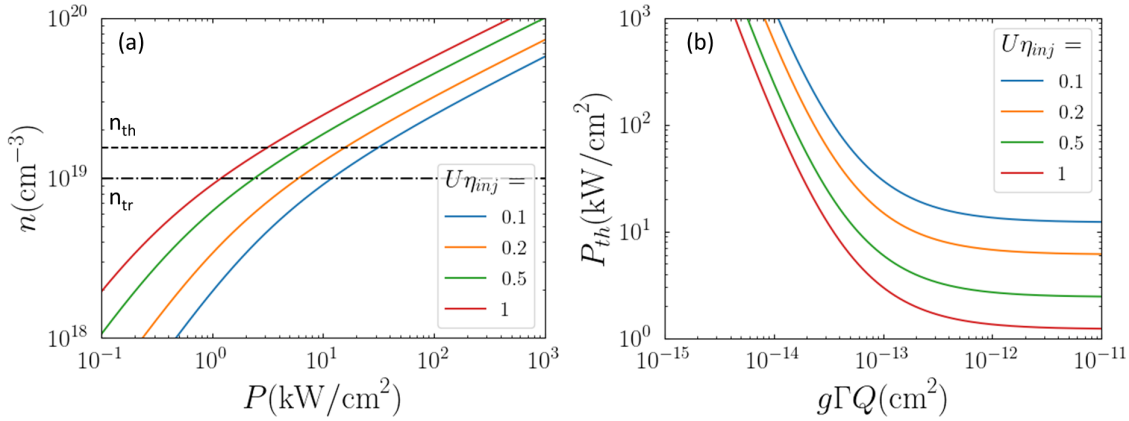


Figure 2.13: (a) Calculation of  $n$  over  $P$  for different values of  $U\eta_{inj}$  using Eqs. 2.1 and 2.5, and indicating the values of  $n_{tr}$  and  $n_{th}$ . (b) Calculation of  $P_{th}$  over  $g\Gamma Q$  for different values of  $U\eta_{inj}$  using Eqs. 2.1, 2.2, 2.3, and 2.5.

In Fig. 2.13 (a), we plot  $n$  over  $P$  below threshold for different values of  $U\eta_{inj}$  between 0.1 and 1 using Eqs. 2.1 (which is valid below and at threshold) and 2.5. The values of  $n_{tr}$  and  $n_{th}$  of our sample are indicated. For  $U\eta_{inj} = 0.18$ , we get  $P_{th} = 18\text{kW}\cdot\text{cm}^{-2}$ , which is the value we observed experimentally, indicating that the parameters considered for the III-nitride microresonators on silicon are relevant. We cannot be sure which vertical mode order is lasing. For the  $\text{TE}_1$  mode, we would have a larger value of  $\Gamma$ , 1.6%, and the same  $P_{th}$  value would be attained for a smaller value of  $U\eta_{inj}$  of 0.1. Alternatively, for the same  $U\eta_{inj}$  of 0.18, we would get  $P_{th} = 9\text{kW}\cdot\text{cm}^{-2}$ . For the  $\text{TE}_2$  mode with  $\Gamma = 2.8\%$ , we would get  $P_{th} = 8\text{kW}\cdot\text{cm}^{-2}$  at  $\eta_{inj} = 0.18$ . This suggests a rather small influence of  $\Gamma$  on the threshold in the range of parameters considered here. A different vertical mode order would, however, also imply a different mode volume, which we have not considered here. For the  $\text{TE}_0$  mode, a  $P_{th} = 10\text{kW}\cdot\text{cm}^{-2}$  would

correspond to a  $U\eta_{inj} = 0.3$ .

In Fig. 2.13 (b), we plot  $P_{th}$  as a function of  $g\Gamma Q$  using Eqs. 2.1, 2.2, 2.3, and 2.5. High gain, high Q and strong overlap are parameters governing the threshold. For large values of  $g\Gamma Q$  (i.e. for a very high-Q cavity),  $P_{th}$  goes towards  $P_{tr}$ , the power needed to reach transparency. We can see that even for an unrealistic  $U\eta_{inj} = 1$  at RT,  $P_{tr}$  is still  $1.2 \text{ kW} \cdot \text{cm}^{-2}$ . Using a single QW, as opposed to 5, can reduce the minimum power needed to reach transparency to  $0.24 \text{ kW} \cdot \text{cm}^{-2}$ . We emphasize that for III-nitrides the relatively large threshold values as compared to other compound semiconductors are directly associated to the large density of states due to the heavy electron and hole effective masses characteristic of III-nitrides.

Achieving a threshold below  $1 \text{ kW} \cdot \text{cm}^{-2}$  for a MQW at RT is thus highly challenging. In the literature, a claim of lasing at threshold powers as low as  $0.3 \text{ kW} \cdot \text{cm}^{-2}$  at a similar wavelength and for a comparable active region (also 5 QWs) was reported in Ref. [31] (see Fig. 2.2 (a)-(c)). They demonstrate a dynamic between peak and background of only a factor of around 8 at  $9P_{th}$ , which is 40 times smaller than in our case. We need to consider the large variability of ABC parameters in literature [153, 154]. In order to achieve  $P_{th} = 0.3 \text{ kW} \cdot \text{cm}^{-2}$  with the parameters of the sample reported by Tamboli et al. [31], a  $\tau_{tot}$  of 110 ns would be required at  $U\eta_{inj} = 0.35$ , which would require  $C$  to be around one order of magnitude smaller as compared to the values of Scheibenzuber et al., [152] along with a smaller  $B$  value and a much smaller  $A$  value, i.e., very long radiative lifetimes and high material quality leading to very long non-radiative lifetimes. This radiative lifetime improvement could be combined with an increase of the  $C_{sp}$  factor by decreasing the cavity size. If a different gain medium was studied, i.e. quantum dots instead of QWs, or generally more localized emitters, the density of states would be different [155], and the threshold could possibly be reduced since  $n_{tr}$  would be lower. Localized states are expected in InGaN QWs, but for the pump powers reported by Tamboli et al. [31] or in this work, it is expected that they are saturated and that a 2D density of states is recovered, thus justifying the QW rate equation analysis.

The here-discussed linewidth of 0.07 nm at threshold is one of the narrowest values reported for III-nitride microdisks. The only smaller value we found, 0.033 nm, was reported by Simeonov et al. [134, 135] for III-nitride microdisks on sapphire with a higher threshold of  $166 \text{ kW} \cdot \text{cm}^{-2}$  (see Fig. 2.1 (a)-(f)). As for III-nitride microdisk lasers on silicon, we have not found any narrower values.

### 2.3.8 Pump laser

Most of the optically pumped lasing results discussed in this thesis were obtained using a pulsed laser emitting at 355 nm with 7 kHz repetition rate and 4 ns pulse width. However, most results that pre-date 2019 (i.e. the results discussed in Fig. 2.3) were obtained using a pulsed laser emitting at 266 nm with 4 kHz repetition rate and 400 ps pulse width. We will compare the thresholds obtained for sample D559 using these two lasers and we will discuss why the thresholds are different. The heterostructure of D559 is given in Fig. 2.4 and Table 2.1. The

active region consisting of 10 QWs makes up the top 112 nm of the sample.

The attenuation of the light intensity  $I(z)$  inside a material as a function of depth  $z$  is given by Lambert-Beer's law

$$I(z) = I_0 e^{-\alpha z}, \quad (2.6)$$

where  $I_0$  is the initial intensity and  $\alpha$  is the absorption coefficient.

The penetration depth  $d_p$ , the depth at which the intensity is reduced to  $1/e$  is then given as

$$d_p = \frac{1}{\alpha}. \quad (2.7)$$

Table 2.6 gives  $\alpha$  and  $d_p$  for GaN at 355 nm and 266 nm according to Ref. [151]. We note that the penetration depth is more than twice as large for the 355 nm laser than for the 266 nm laser. This means that the lower QWs are not pumped by the 266 nm laser.

However, we also need to take the carrier diffusion length  $d_{diff}$  into account, which is in the order of a few hundred nm [156, 157] and will allow the carriers to diffuse into all QWs.

$\lambda$ (nm)	$\tau_p$ (ns)	$E_{phot}$ (eV)	$\alpha$ GaN ( $10^4 \text{ cm}^{-1}$ )	$d_p$ (nm)	$E_{th}$ ( $\text{mJ} \cdot \text{cm}^{-2}$ )	$P_{th}$ ( $\text{kW} \cdot \text{cm}^{-2}$ )	$R$ (%)	$d$ (nm)
355	4	3.49	9.67	103	1.49	370	19	22
266	0.4	4.66	22.4	44	3	7500	21	22

Table 2.6: Summary of some parameters of Eqs. 2.7 and 2.1 for D559 for the two lasers. Values for  $\alpha$  and  $R$  are taken from Ref. [151].

Using the 266 nm laser the threshold energy per pulse for D559 is  $E_{th} = 3 \text{ mJ} \cdot \text{cm}^{-2}$  or  $P_{th} = 7.5 \text{ MW} \cdot \text{cm}^{-2}$  for the threshold peak power, where  $P_{th} = E_{th} / \tau_p$ . These results are shown in Fig. 2.3 (g) and (h) and Ref. [50]. Using the 355 nm laser, we obtain  $E_{th} = 1.5 \text{ mJ} \cdot \text{cm}^{-2}$  per pulse or  $P_{th} = 370 \text{ kW} \cdot \text{cm}^{-2}$ . The threshold peak power is reduced by a factor 20 by changing to the 355 nm laser.

We can use Eq. 2.1 to analyze the difference in threshold observed with the two lasers.

The most important difference between the two lasers is a factor 10 in the pulse width  $\tau_p$ , which likely causes a factor of around 10 difference in the carrier lifetime  $\tau_{tot}$  and consequently in  $P_{th}$ . In steady state, we would assume a  $\tau_{tot}$  of a few ns. When the pulse width is shorter than the carrier lifetime, the microlaser cannot reach a steady state and the threshold increases accordingly.

The remaining difference of a factor 2, presumably comes from the difference in photon energy and injection efficiency. The photon energies of the two lasers are 3.49 eV and 4.66 eV, while the band gap of GaN is 3.39 eV and 2.97 eV for the InGaN QWs. The difference in energy is lost as heat. This means that the device heats up significantly more using the 266 nm laser, which increases the threshold. The difference in injection efficiency can be seen in the above-

mentioned difference in penetration depth.

The reflectivity  $R$  of GaN is also slightly different for the two pump wavelengths and is given in Table 2.6.

A difference in threshold of a factor of 2-3 was also observed by Martens [158], who investigated 405 nm lasers using 193 nm and 266 nm pump lasers. The thresholds were larger using the 193 nm laser. However, in his case the pulse widths were 5 ns for both lasers and were thus more directly comparable.

One must keep in mind that a comparison of lasing thresholds obtained using pump lasers with different wavelengths and pulse widths is not always straightforward. This can complicate the comparison with literature.

### 2.3.9 Growth method

When comparing the lasing thresholds of the seven samples that lase in the blue spectral range between 403 and 420 nm, we can see a clear trend that MOCVD-grown devices show more than an order of magnitude lower thresholds than MBE-grown ones. Just like for the high excitation power density PL presented in Fig. 2.6, the higher threshold of MBE-grown samples can be explained by the lower radiative recombination rate in MBE QWs due to a higher density of point defects caused by the lower growth temperature [140]. MBE-grown InGaN lasers reported in literature have higher thresholds and are less developed than their MOCVD counterparts [159, 160].

However, another important aspect to take into account is that the three samples with very low thresholds have only 5 QWs as opposed to the 10 QWs of all other samples. For fewer QWs, transparency and lasing are achieved at lower pump powers, while the output power will be higher for more QWs. It is more likely that all QWs are pumped to population inversion when fewer QWs are present. It would be interesting to compare two samples with identical structures: one grown by MBE and the other by MOCVD to have a clearer understanding of the difference in lasing threshold resulting from the growth method.

### 2.3.10 Dislocation density

The TDD of our samples ranges from  $5.7 \times 10^8$  to  $2.4 \times 10^{10} \text{ cm}^{-2}$ .

We can compare C661E and C661F. The only difference between these two samples is that C661E was grown using SAG on a patterned template. Both samples were grown with a 3D-2D growth mode to reduce the TDD. The TDD of C661E is more than a factor of two lower than for C661F which might be due to the increased thickness and an increased effect of the 3D-2D transition. The lasing threshold of C661E is nearly a factor of three lower than for C661F, which might be related both to the reduced TDD and to the reduced strain through the SAG. However, the SAG requires further optimization to become a viable growth method for microcavities. In the case of C661E, the layer thickness was uncontrolled due to the large masked areas. The

400 $\mu\text{m}$  diameter circular mesas were spaced in a rectangular lattice with 600 $\mu\text{m}$  period. We have designed a new SAG mask with 10 $\mu\text{m}$  spacing between 300 $\mu\text{m}$  or 600 $\mu\text{m}$  wide mesas. Unfortunately, this mask has not yet been used to fabricate a new sample.

We can also compare the MBE-grown samples emitting in the blue. For D807, we used a 3D-2D growth mode to reduce the TDD, while for D557, D559, D678 we used regular 2D growth. D807 has an order of magnitude lower TDD but only about a factor of two lower threshold than D557, D559, and D678. This suggests that the influence of the TDD in the range of  $10^9$  to  $10^{10}$   $\text{cm}^{-2}$  on the lasing threshold is not very large. But we also need to take the increased height into account, which results in a smaller overlap of the optical mode with the QWs.

Kneissl et al. reported a simulated IQE curve as a function of TDD for AlGaIn QWs [161], which indicates an IQE of only a few percent for dislocation densities in the  $10^{10}$   $\text{cm}^{-2}$  and around 65% for  $5 \times 10^8$   $\text{cm}^{-2}$ . As discussed previously, a higher TDD results in higher SRH recombination ( $A$  value in the ABC-model), which could increase the threshold by a factor 2-3, for a factor 5-10 higher  $A$ . Given all the influences on the threshold, such as process variability, the effect of the TDD is ultimately not that high in our case.

We can conclude that a lower TDD is favorable for reducing the lasing threshold. However, our lowest thresholds have, nonetheless, been achieved with samples showing high TDD around  $1.2 \times 10^{10}$   $\text{cm}^{-2}$ . It would be interesting to study a sample like C1081 with a 3D-2D buffer layer and SAG in order to have a low TDD and MOCVD-grown QWs emitting in the blue. However, we will see in the following chapters that there is an interest in having continuous thin layers ( $< 1\mu\text{m}$ ) for the fabrication of photonic circuits.

### 2.3.11 Chemical treatment

We performed a chemical treatment on microdisks fabricated on samples C1021D and C1080 after the ICP etch and before the underetch. We used two pieces ( $10 \times 11 \text{ mm}^2$ ) of C1021D and cleaved them into two parts and one piece of C1080 that we cleaved into four parts. The pieces were dipped into 40°C AZ400K developer for 0 to 10 min with the goal to remove ICP etch damage. ICP etch damage of III-nitrides was reported to be rather shallow, in the range of 15 nm [162], and to especially affect the breakdown voltage of LEDs [163]. The damage is probably due to the formation of point defects in the material, such as nitrogen vacancies [164]. By etching the side-walls in AZ400K, part of this damage should be removed.

Fig. 2.14 shows side-view SEM images of microdisks on the different pieces of C1021D after chemical treatment. For 1, 7, and 10 min we can see crystallographic facets emerging that become more pronounced with increasing treatment time. For 10 min and 0 min, which are from the same  $10 \times 11 \text{ mm}^2$  piece, the top edge of the microdisks is rounded, perhaps due to damage to the mask during ICP etching. Strangely, both samples were etched at the same time. Perhaps the position of the sample on the ICP sample holder influences the etch quality, if the plasma is not homogeneous everywhere. Or perhaps the etch mask was thinner due to thickness fluctuations during the plasma enhanced chemical vapor deposition (PECVD) of

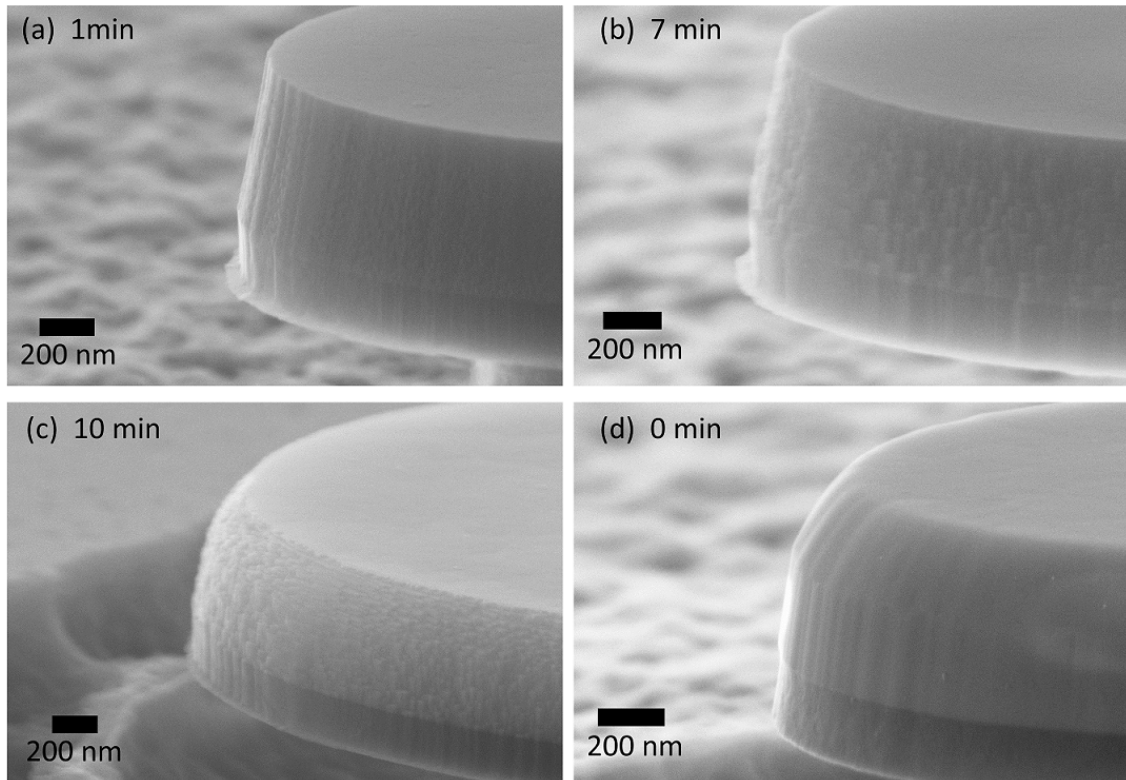


Figure 2.14: SEM images of the four pieces of C1021D after AZ400K treatment of (a) 1 min, (b) 7 min, (c) 10 min, and (d) 0 min.



Figure 2.15: Schematic of a  $3\mu\text{m}$  diameter disk with truncated edges and depicting the  $H_z$  field of a first order radial mode.

$\text{SiO}_2$ .

Table 2.7 summarizes the chemical treatment time and lasing thresholds for the different samples. For sample C1021D, at 0 min and 10 min of chemical treatment, no lasing is observed. For 1 min and 7 min the threshold peak power densities are  $35$  and  $25\text{ kW}\cdot\text{cm}^{-2}$ . We can explain the absence of lasing for 0 and 10 min with the round edges observed in the SEM images in Figs. 2.14 (c) and (d). Fig. 2.15 shows a schematic of a  $3\mu\text{m}$  diameter disk with truncated edges and depicting the  $H_z$  field of a first order radial mode. We can see that the maximum of the mode is located close to the edge of the microdisk (in a perfect disk). The lateral extension of the etch damage seen in Fig. 2.14 (d) is about  $170\text{ nm}$ . Given that the QWs are located in the top  $70\text{ nm}$  of the structure (see Fig. 2.4), there are no QWs remaining where the radial maximum of the

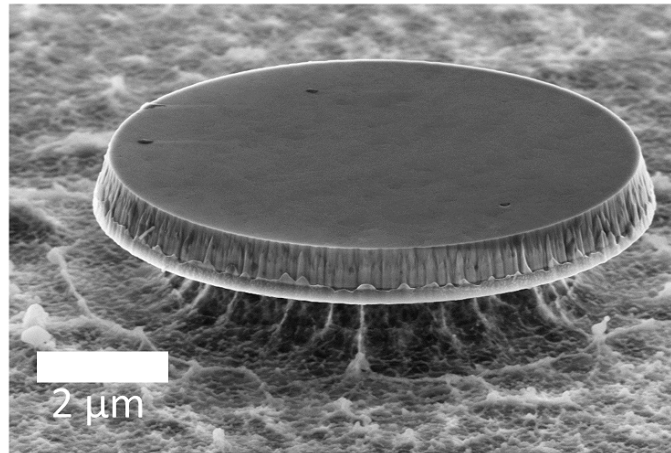


Figure 2.16: SEM image of an 8 $\mu\text{m}$  diameter disk on a different piece of C1021D, measured by V. Brändli.

first-order mode would be, which could explain why no lasing is observed. The mode would have a slightly different shape in a truncated disk, but the overlap with the QWs is certainly significantly less than in an ideal structure. Meanwhile, the influence of the chemical treatment on the threshold remains inconclusive, as the values for 1 min and 7 min are very similar and there is no direct comparison to 0 min.

We fabricated microdisks independently on a different piece of C1021D without any chemical treatment. An SEM image of an 8 $\mu\text{m}$  diameter disk is shown in Fig. 2.16, depicting very rough side-walls. There must have been some problem during the ICP etching of either the SiO<sub>2</sub> or the III-nitride. These microdisks lased, but with an order of magnitude higher threshold, 220 kW $\cdot\text{cm}^{-2}$  peak power density. Clearly, fairly smooth side-walls are required for low-threshold lasing.

For C1080, all four parts come from the same 10 x 11 mm<sup>2</sup> sample that was cleaved after ICP etching. SEM images of 5 $\mu\text{m}$  diameter disks are shown in Fig. 2.17. Near vertical side-walls and crystallographic facets, that become more noticeable with increased chemical treatment time, are visible. The lasing thresholds are between 20 and 38 kW $\cdot\text{cm}^{-2}$  (see Table 2.7) with no correlation to the chemical treatment time. This suggests that the etch damage that can be removed by AZ400K does not limit the performance of our devices. However, we can see a correlation between the threshold and the underetch depth (assuming it is homogeneous across one sample piece), which is shown in Fig. 2.18. The microdisks with the smallest underetch (Fig. 2.17 (c)) have the lowest thresholds. The threshold increases linearly with increasing underetch depth in this parameter range (see Table 2.7 and Fig. 2.18). A smaller pedestal implies a lower thermal conductivity and consequently a hotter microdisk. Unfortunately, the underetch is not very controllable.

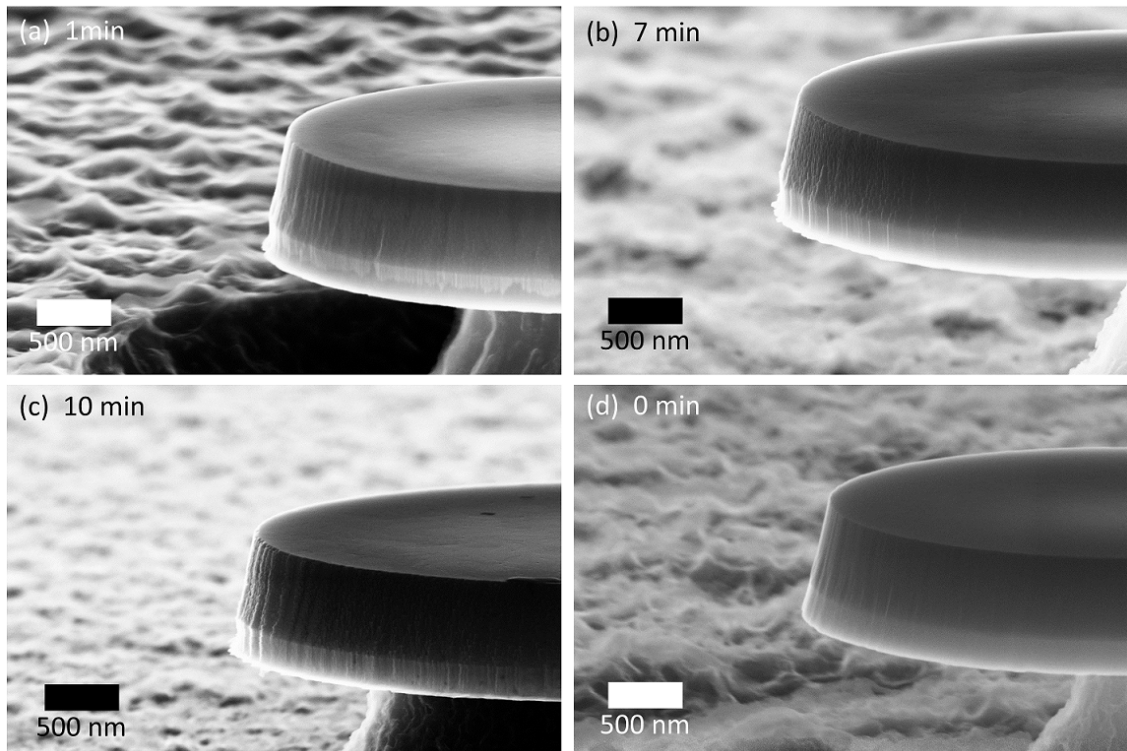


Figure 2.17: SEM images of 5µm diameter disks on C1080 with and without chemical treatment. (a) 1 min, (b) 7 min, (c) 10 min, (d) 0 min of AZ400K treatment. Images were measured by V. Brändli.

Sample	Piece	Time (min)	Threshold ( $\text{kW} \cdot \text{cm}^{-2}$ )	Underetch ( $\mu\text{m}$ )
C1021D	1	0	/	
	2	1	35	
	2	7	25	
	1	10	/	
	3	0	220	
C1080	1	0	28	1.8
	1	1	23	1.3
	1	7	38	2.4
	1	10	20	1.0

Table 2.7: Summary of the AZ400K treatment with sample number, piece number, chemical treatment time, and threshold peak power density.

### 2.3.12 Blue vs. UVA

We can compare the MOCVD-grown samples emitting in the UVA (C661E and C661F) with samples emitting in the blue (C1021D, C1080, C1081). The thresholds of the blue samples are more than an order of magnitude smaller than the thresholds of the UVA samples, even though the UVA samples have much lower TDDs (see Tables 2.1 and 2.5). This suggests that our blue QWs

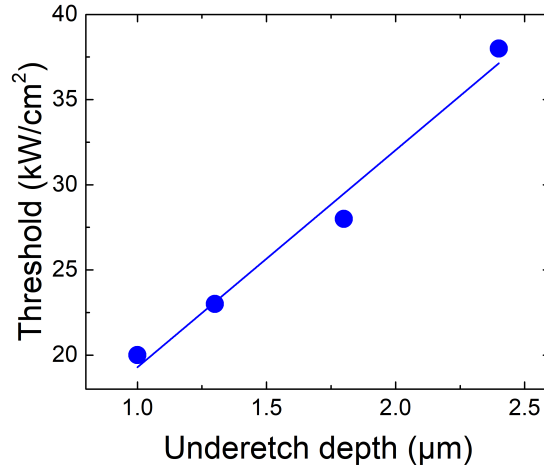


Figure 2.18: Lasing threshold as a function of underetch depth for sample C1080.

are much more efficient than our UVA QWs. An explanation for this observation is that 5% In-GaN/GaN QWs are much shallower than 10% InGaN/GaN QWs, and consequently carriers are much less well confined in the UVA QWs. At high injection power, this carrier escape could thus lead to an increased mobility towards non-radiative defects.

### 2.3.13 Lasing threshold vs. PL

In Fig. 2.19, we compare the lasing thresholds (Table 2.5) with the high excitation power density PL measured on the as-grown samples (Table 2.1). We can conclude that samples that are not very intense in PL tend to have higher thresholds (i.e. the MBE samples). However, the most intense samples (C661E and C661F) have very high thresholds. No conclusion can be drawn from the linewidth of the PL emission.

### 2.3.14 Lasing threshold vs. mode overlap

A larger mode overlap should result in a lower threshold. We plot the threshold over the  $\text{TE}_0$  mode overlap in Fig. 2.20. The threshold decreases with increasing mode overlap except for the three samples with the largest overlap, D557, D559, and D678 (see also Table 2.2). We also need to take the TDD and the growth method into account. Samples D557, D559, and D678 have high TDDs and were grown by MBE, two factors that could increase the threshold in spite of a larger overlap. The very low overlap of the QWs of C661E and C661F with the  $\text{TE}_0$ ,  $\text{TE}_1$ , and  $\text{TE}_2$  modes could explain why the thresholds of these samples were very high, even though their PL was very intense and their TDD very low. However, the shorter wavelengths of these samples also need to be taken into account. When comparing D807 with D557, D559, and D678, the lower overlap of D807 might explain why the threshold was only a factor of two lower

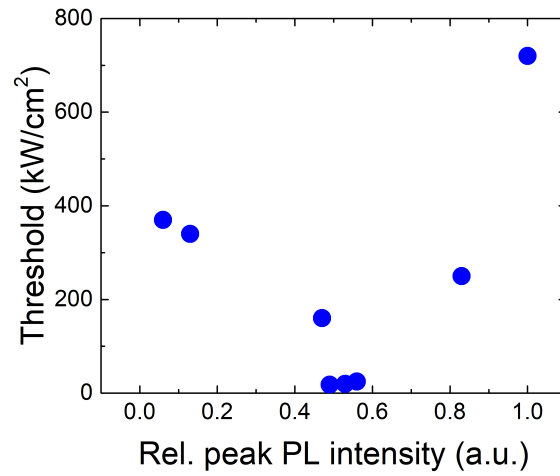


Figure 2.19: Lasing threshold as a function of relative peak PL intensity.

even though the TDD was an order of magnitude lower. In order to precisely characterize the influence of the overlap on the threshold, we would need to investigate two samples grown by the same method, with similar TDD, and emitting at the same wavelength, where the only difference was the thickness of the buffer layer. Unfortunately, this is rather difficult to realize experimentally.

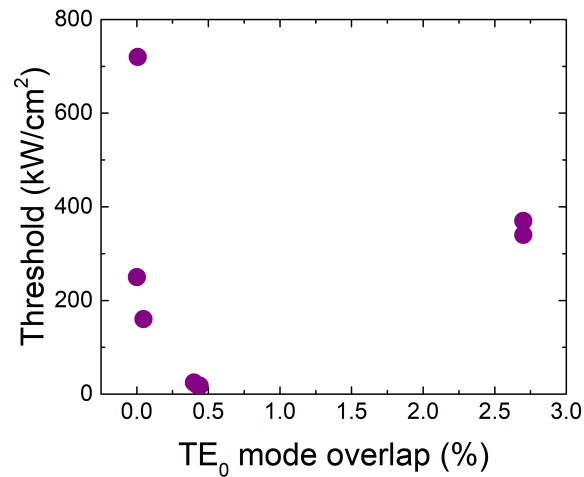


Figure 2.20: Lasing threshold as a function of overlap with the TE<sub>0</sub> mode.

### 2.3.15 Sample on bulk GaN

We will briefly discuss TL73, a sample grown on bulk GaN by MOCVD. The structure consists of 430 nm of n-GaN, 496 nm of 8x 54 nm n-In<sub>0.18</sub>Al<sub>0.82</sub>N/ 8 nm n-GaN bottom cladding, a 110 nm n-GaN waveguide, 4x 2.5 nm InGaN/ 8 nm GaN QWs, a 20 nm Al<sub>0.2</sub>Ga<sub>0.8</sub>N electron blocking

layer, 107 nm p-GaN waveguide, 525 nm of 105x 2.5 nm p-Al<sub>0.14</sub>Ga<sub>0.86</sub>N/ 2.5 nm p-GaN short-period super-lattice top cladding, and a 25 nm p<sup>++</sup>-GaN layer. The TDD is that of the bulk GaN substrate,  $1 - 2 \times 10^7 \text{ cm}^{-2}$ . We fabricated microdisks on this sample and obtained lasing at 389 nm with a threshold energy per pulse of  $0.86 \text{ mJ} \cdot \text{cm}^{-2}$  or threshold peak power of  $214 \text{ kW} \cdot \text{cm}^{-2}$  for a 6  $\mu\text{m}$  diameter disk under pulsed optical pumping with the 355 nm laser. This threshold is in the same order of magnitude as for the MBE samples discussed in Table 2.5. The reason for the high threshold is likely the presence of the pn-junction that creates internal electric fields, as well as the thickness of material above the QWs of nearly 700 nm (400 nm of which are not transparent at 355 nm), which does not allow to efficiently pump the QWs given the penetration depth and diffusion length. Meanwhile, ridge waveguide laser diodes fabricated on this wafer showed threshold current densities of  $6.7 \text{ kA} \cdot \text{cm}^{-2}$  [165]. We have not been able to investigate a sample more adapted for optical pumping grown on bulk substrate. Presumably, it would give better results. However, switching to bulk substrate for microdisks is not that straightforward, as the vertical confinement needs to be provided by thick cladding layers.

## 2.4 Conclusion and Outlook

In conclusion, we studied the influence of several parameters on the lasing threshold of optically pumped mushroom-type microdisk lasers in III-nitrides on silicon. We have not found a material parameter that clearly indicated whether a sample would have a lower threshold. It is thus always necessary to process microdisks and measure the lasing threshold, in order to determine if one sample is better than another, which makes growth optimization a slow process.

Our lowest threshold of  $18 \text{ kW} \cdot \text{cm}^{-2}$  is the lowest value reported for III-nitride microdisks under pulsed optically pumping in literature. However, there have been reports of thresholds of  $0.3 \text{ kW} \cdot \text{cm}^{-2}$  [31] and  $1 \text{ kW} \cdot \text{cm}^{-2}$  [33] under CW pumping of 1  $\mu\text{m}$  diameter disks. These results are, however, not very convincing due to a very low dynamic between lasing mode and background that does not change significantly with increasing pump power. Using a rate equation model, we calculated the minimum power needed to reach the transparency carrier density in our structure and the structure reported by Tamboli et al. [31] (both of which contain 5 QWs), which is in the order of  $1 \text{ kW} \cdot \text{cm}^{-2}$ , suggesting that the results of Tamboli et al. cannot be correct.

While we believe that we cannot reduce the threshold of our microdisks much further (without reducing the number of QWs), we have to date not succeeded to observe lasing under CW pumping. The 355 nm CW laser of our colleagues in Montpellier emits a maximum power of 20 mW, of which about 3.4 mW reach the sample. For a spot diameter of 6  $\mu\text{m}$  this translates into  $12 \text{ kW} \cdot \text{cm}^{-2}$ , for a 3  $\mu\text{m}$  spot even  $48 \text{ kW} \cdot \text{cm}^{-2}$ . We are thus in a regime where the laser power is only barely enough to achieve lasing for a 3  $\mu\text{m}$  diameter disk. Reducing the microdisk diameter and laser spot size to around 1  $\mu\text{m}$  can mitigate this problem. As of June 2020, our low thresh-

old samples have not been studied sufficiently under CW excitation to determine if CW lasing could be achieved. However, a possible reason to not observe lasing, even at a sufficiently high power density, is heating in the microdisk.

## Summary of Chapter 2

In this chapter, we investigated III-nitride microdisk lasers on silicon. We reviewed the state of the art of III-nitride microdisk lasers on both silicon and sapphire substrates. Then, we discussed the results obtained by our collaboration before the beginning of this thesis. We described the nine samples investigated in this chapter and discussed some structural and optical measurements performed on the as-grown samples, as well as simulations of the optical confinement and the band structure. We fabricated mushroom-type microdisks on these samples and performed pulsed optically pumped measurements at RT. We discussed the lasing characteristics, calculated the threshold power of the best sample, which is in good agreement with the experimental results, and investigated the influence of the pump laser. The here observed lowest threshold peak power density of  $18\text{ kW} \cdot \text{cm}^{-2}$  (or  $0.07\text{ mJ} \cdot \text{cm}^{-2}$  per pulse) is state of the art for pulsed optically pumped microdisk lasers in III-nitrides on silicon. We investigated the impact of the growth method, the dislocation density, and a chemical treatment on the lasing threshold. MOCVD-grown devices show lower thresholds than their MBE counterparts. Lower TDDs seem to result in lower thresholds, however, our samples are not easily comparable, and it is noteworthy that we can achieve low thresholds with thin and highly dislocated material. The AZ400K chemical treatment had no clear effect on the lasing threshold. However, we observed that an inexplicably failed process can result in no lasing being observed at all due to damage to the area where the QWs and the lasing mode should be. We further noticed that the threshold increases with increasing underetch depth due to worse thermal management. We also compared blue and UVA samples, discussed the relationship between the threshold and the high excitation power density PL on the as-grown samples, as well as with the mode overlap. Blue samples show significantly lower thresholds than UVA samples. Besides the PL intensity being an indicator of a low or high lasing threshold, no clear correlation between the PL and the lasing threshold was found. A higher mode overlap should result in lower thresholds, but it is difficult to draw clear conclusions from the samples available. We briefly discussed the rather high threshold obtained for a sample grown on bulk GaN that contained a pn-junction in comparison to our samples on silicon. We estimated whether our samples could lase under CW conditions and concluded that for small disk diameters and laser spot sizes, it should be possible given the CW laser we have available.



## Chapter 3

# III-nitride on silicon microlaser photonic circuits in the blue

**I**N THIS CHAPTER, we investigate monolithically integrated photonic circuits containing blue III-nitride on silicon microdisk lasers. The results of this chapter have been published in Refs. [145, 166]. This chapter covers:

- An overview of the different approaches of monolithic integration in active photonic circuits.
- A brief review of the state of the art of heterogeneous integration of III-nitride lasers with passive platforms, as well as critical coupling in III-nitride photonic circuits.
- The design and fabrication of photonic circuits in the III-nitride on silicon platform.
- An analysis of lasing and critical coupling observed in this platform.

### 3.1 Introduction and state of the art

Efficient integration of active devices with passive photonic circuits is a complicated and important issue. Monolithic, hybrid, or heterogeneous integration schemes are possible.

#### 3.1.1 Monolithic integration

The monolithic integration of active photonic components into photonic circuits is an important step towards achieving low-cost and highly functional next generation photonic chips. Complex devices involving multiple schemes have been demonstrated in indium phosphide (InP), for example [26].

Without the use of an integration scheme, the waveguides reabsorb part of the emission of the microlaser. This reabsorption can be reduced by using quantum dots (QDs) as the active

material. Koseki et al. have demonstrated microdisks coupled to waveguides in a geometry very similar to our own, but using the gallium arsenide (GaAs) platform and QDs as the active material [167]. Meanwhile, Gao et al. demonstrated light communication using a photonic circuit containing a microring and absorbing waveguides using III-nitrides [168].

Different integration approaches, including selective regrowth, quantum well (QW) intermixing, and QW etching have been proposed. Fig. 3.1 shows schematics of these three approaches.

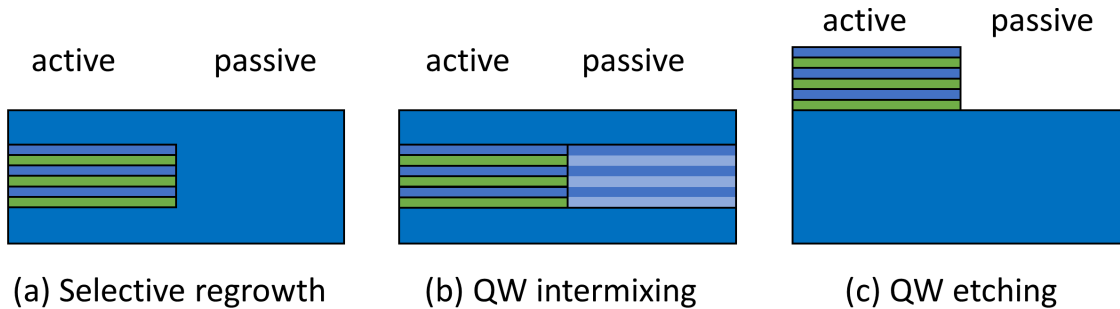


Figure 3.1: Sketch of (a) selective regrowth, (b) QW intermixing, and (c) QW etching as approaches for monolithic integration. Inspired by Ref. [169].

### 3.1.1.1 Selective growth

An efficient approach to avoid re-absorption in the waveguide is to etch away the active layer and to selectively regrow the transparent waveguide. This is schematically illustrated in Fig. 3.1 (a). Coleman et al. discussed this approach for various integrated photonic devices using the GaAs platform [170]. Matsuo et al. demonstrated an InP based photonic crystal laser with a buried QW using selective regrowth [171]. Alternatively, by growing on patterned substrate a difference in the vertical position of the QWs can be achieved that in combination with a post-growth planarization step can allow for monolithic integration of active devices and passive waveguides in a single growth step, as demonstrated for example, by Remiens et al. using the InP platform [172].

Selective area growth (SAG) has been demonstrated in III-nitrides [173], but was mainly used a method to reduce the threading dislocation density (TDD) [174]. However, microrings have also been demonstrated using SAG [175]. Selective regrowth appears to be a feasible option for photonic integration in III-nitrides, but has not yet been demonstrated.

### 3.1.1.2 QW intermixing

QW intermixing is an approach in which the QWs get selectively altered, for example, by ion implantation or annealing in the area that is supposed to be passive to blue-shift their emission/absorption in order to make them transparent at the operating wavelength of the photonic

circuit. Fig. 3.1 (b) shows a schematic of this approach, which is well-established in GaAs and InP [169, 176].

QW intermixing approaches have been demonstrated for InGaN QWs by ion-implantation [177] and metal-intermixing through annealing [178], achieving blue-shifts of the QW emission. These approaches seem like viable options for achieving monolithic integrated photonic circuits.

### 3.1.1.3 QW etching

Another approach for monolithic integration involves selective etching of the active region, which is placed on top of the waveguiding layer. This approach is illustrated in Fig. 3.1 (c). It was utilized, for example, by Mason et al. in the fabrication of a ridge waveguide sampled grating distributed Bragg reflector (DBR) laser using the InP platform and selectively etching the QWs on top of the waveguide [179].

There have been several demonstrations of QW etching in III-nitride photonic circuits. Shi et al. demonstrated a circuit consisting of a transmitter, a waveguide, and a receiver in the blue spectral range, where the waveguide was etched to the passive n-GaN [180]. Floyd et al. demonstrated similar circuits in the UVC with an AlGaN waveguiding layer [181, 182].

As we have discussed in section 1.3.5.1, we also use a QW etching approach to selectively remove the active region from the waveguide. While we have not tried selective regrowth or QW intermixing, we believe that these are also interesting approaches that could be investigated in future work.

## 3.1.2 Heterogeneous integration

As an alternative to monolithic integration, a few heterogeneous integration approaches of blue III-nitride laser diodes with passive photonic circuit platforms have been proposed in simulation [183, 184]. Kamei et al. proposed an integrated platform using a blue InGaN gain medium directly bonded to a TiO<sub>2</sub> waveguide with a vertical coupling scheme, however, they encountered difficulties with the bonding. DBRs in the waveguide are supposed to act as the laser cavity [183]. Meanwhile, Arefin et al. proposed both hybrid and heterogeneous integration of III-nitride blue laser diodes into a passive Si<sub>3</sub>N<sub>4</sub> platform through either flip-chip bonding or transfer printing [184], however, the transfer printing has only been demonstrated using polyethylene terephthalate (PET) substrates [185] and should be difficult to realize on SiN. So far, no experimental realization of heterogeneous or hybrid integration has been reported.

To et al. demonstrated a microdisk directly coupled to a waveguide in GaN using eutectic bonding and laser lift-off of the sapphire substrate, however, no lasing was observed and the waveguides were absorbing [124].

### 3.1.3 Critical coupling in III-nitride photonic circuits

In the literature, most of the demonstrations of critical coupling have been observed by injecting light into a waveguide coupled to a passive microresonator and looking at the transmission. Critical coupling was reported, for example, using silica microspheres coupled to fibers in the near-infrared (NIR) [186, 187] or in the silicon photonics platform using silicon-on-insulator (SOI) [188]. At critical coupling, there is a perfect destructive interference between the transmitted field and the microresonator's internal field coupled to the waveguide, thus leading to quenching of the transmission on resonance.

Using III-nitrides, critical coupling has been observed in passive photonic circuits in the NIR around  $\lambda = 1.55\mu\text{m}$  [29, 38, 39, 52]. Fig. 3.2 (a) shows a microring photonic circuit fabricated in GaN on sapphire with a transmission spectrum at critical coupling shown in Fig. 3.2 (b), reproduced from Bruch et al. [39]. Our consortium observed critical coupling using AlN/GaN on Si microdisks coupled to suspended waveguides, shown in Fig. 2 (b) and (c), before the beginning of this thesis [52]. Achieving critical coupling in the blue spectral range is more difficult due to the requirement of much narrower coupling gaps at the limit of what can be achieved using e-beam lithography.

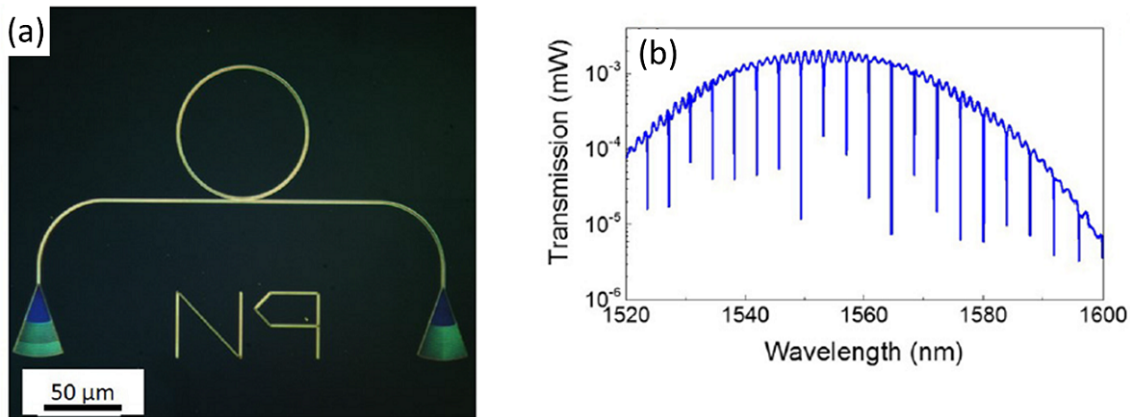


Figure 3.2: (a) Optical microscope image of a passive photonic circuit and (b) transmission spectrum at critical coupling in the NIR, reproduced from Ref. [39].

## 3.2 Design of photonic circuits on D559 and D677

The heterostructure of D559 was discussed in section 2.3. The structure of D677 is the same as of D678, which was also discussed in section 2.3. To briefly summarize the most important aspects, the two samples are 512 nm thick and contain 10 InGaN/GaN QWs that are located in the top 112 nm of the structure and emit in the blue spectral range. The main difference between the two samples is that D559 has 100 nm of n-doped GaN in the buffer layer (see section 2.3 for more details).

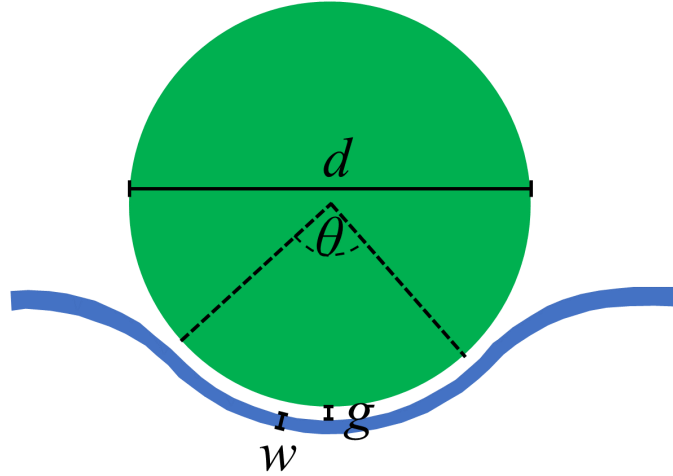


Figure 3.3: Sketch of the microdisk and waveguide coupling region with all the design parameters indicated.

The height  $h$  and wavelength range are defined by the material. Thus the remaining design parameters are the disk diameter  $d$ , the waveguide bending angle  $\theta$ , the gap between the disk and the waveguide  $g$ , and the waveguide width  $w$ . Fig. 3.3 shows a sketch of a disk and waveguide, depicting the four design parameters. We choose  $d = 3$  and  $5\mu\text{m}$  to have a free spectral range (FSR) of around 4 to 8 nm in the blue spectral range. We investigate different angles  $\theta$  from  $0^\circ$  to  $90^\circ$ , where  $0^\circ$  corresponds to a straight waveguide and  $90^\circ$  corresponds to the waveguide being bent around one quarter of the disk's circumference. Fig. 3.3 shows a  $90^\circ$  angle.

In the FDTD simulation, we limit  $Q_{int}$  to experimentally observed values (see section 2.3.5) of around 3700 by introducing some absorption. This allows us to reduce the simulation time. Fig. 3.4 shows simulation results for  $3\mu\text{m}$  diameter disks with  $\theta = 90^\circ$ . We vary  $g$  for a given  $w$  in the simulation to find the parameters of critical coupling. In Fig. 3.4 (a), the transmission spectra for one first-order radial mode are depicted for different gap sizes for  $w = 133\text{ nm}$ . For gaps of 80, 100, and 120 nm the system is under-coupled, at 50 nm it is very close to critical coupling and a transmission minimum, and at 30 nm it is over-coupled. While the transmission should theoretically go down to zero at critical coupling, there are several reasons why this is not observed here. The spatial resolution is not high enough. We use 16 pixels per wavelength in the material, which translates into 11 nm/px. Furthermore, the waveguide is thinner than the disk. This height difference might prevent the transmission from dropping to zero even at critical coupling. Fig. 3.4 (b) shows the loaded Q factor over the gap size for gaps from 30 to 120 nm. For large gaps  $Q_{load} \approx Q_{int}$ . The loaded Q factor decreases with decreasing gap size and reaches  $Q_{load} \approx 1/2 Q_{int}$  at critical coupling around  $g = 50\text{ nm}$ . A further requirement for critical coupling is phase matching, which can be achieved for different combinations of  $g$  and  $w$  and is given at  $g = 50\text{ nm}$  and  $w = 133\text{ nm}$ , in this case. Since it is very challenging to fabricate

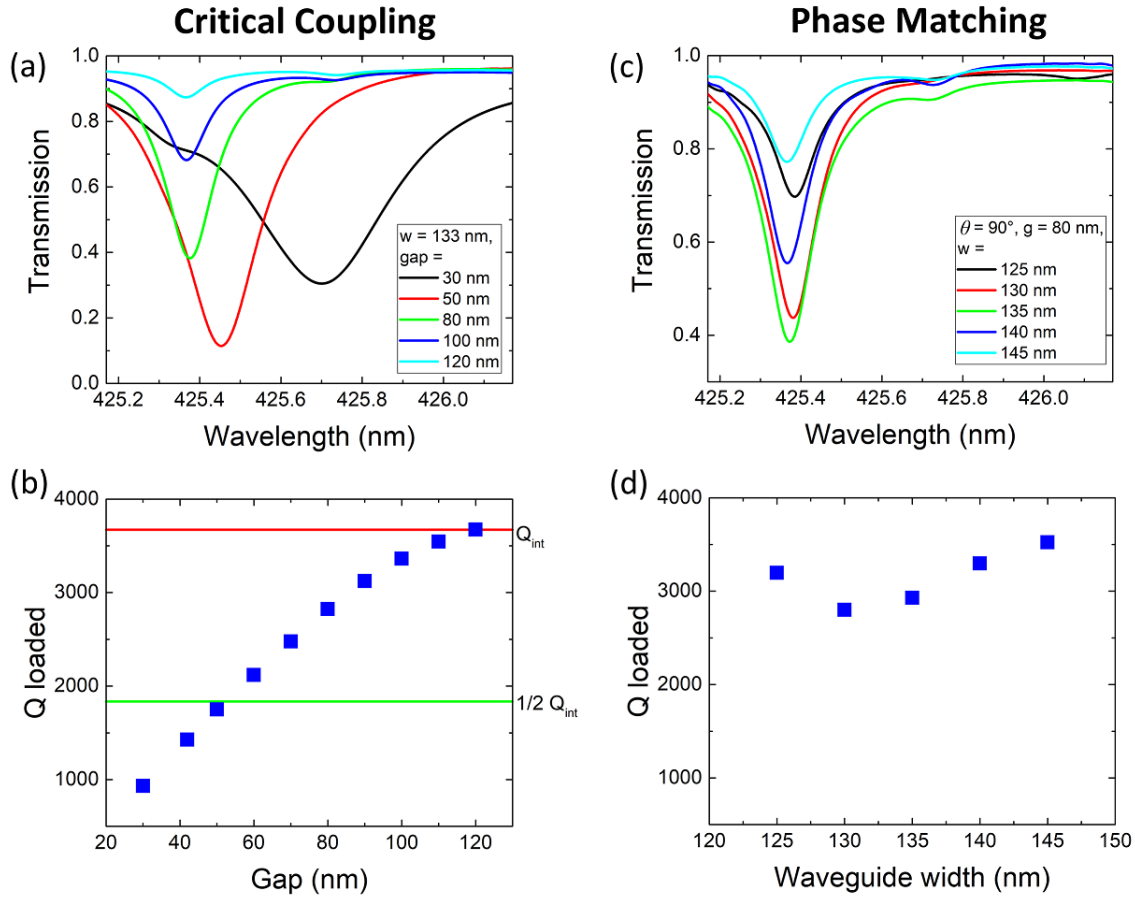


Figure 3.4: FDTD simulations of critical coupling showing transmission and loaded Q factor of devices with a 3 μm diameter disk with  $\theta = 90^\circ$  for different gap sizes and waveguide widths (a) Transmission for devices with  $w = 133$  nm and five different gaps showing the under-coupled (80, 100, and 120 nm), critically coupled (50 nm) and over-coupled (30 nm) regime. (b) Loaded quality (Q) factor in dependence of gap size showing the degradation of the Q factor with increased coupling.  $Q_{\text{load}} \approx Q_{\text{int}}$  for  $g = 120$  nm and  $Q_{\text{load}} \approx 1/2 Q_{\text{int}}$  at  $g = 50$  nm. (c) Transmission for devices with a gap of 80 nm and different waveguide widths showing phase matching around  $w = 135$  nm. (d) Loaded Q factor for different waveguide widths demonstrating its independence from phase matching far away from critical coupling.

small gaps, we decided to investigate the under-coupled regime in a first sample, fabricated from wafer D559, choosing gaps of  $g = 80$  to 120 nm. Fig. 3.4 (c) shows simulated transmission spectra for devices with a gap of 80 nm and different waveguide widths. For a width of around 135 nm a transmission minimum can be observed, which corresponds to phase matching. The corresponding loaded Q factor (depicted in Fig. 3.4 (d)) is not significantly degraded by phase matching when the system is far away from critical coupling, as is the case for a gap of 80 nm. For the second sample, D677, we use smaller gaps of 40 to 120 nm with the goal to observe critical coupling.

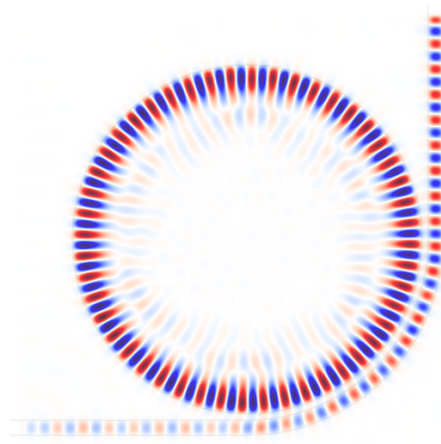


Figure 3.5: Simulation of the  $H_z$  field of a  $d = 3 \mu\text{m}$  diameter disk for a first-order radial mode with azimuthal order  $m = 48$ . The waveguide is bent at a  $\theta = 90^\circ$  angle, the gap is  $g = 50 \text{ nm}$  and the waveguide width is  $w = 133 \text{ nm}$ .

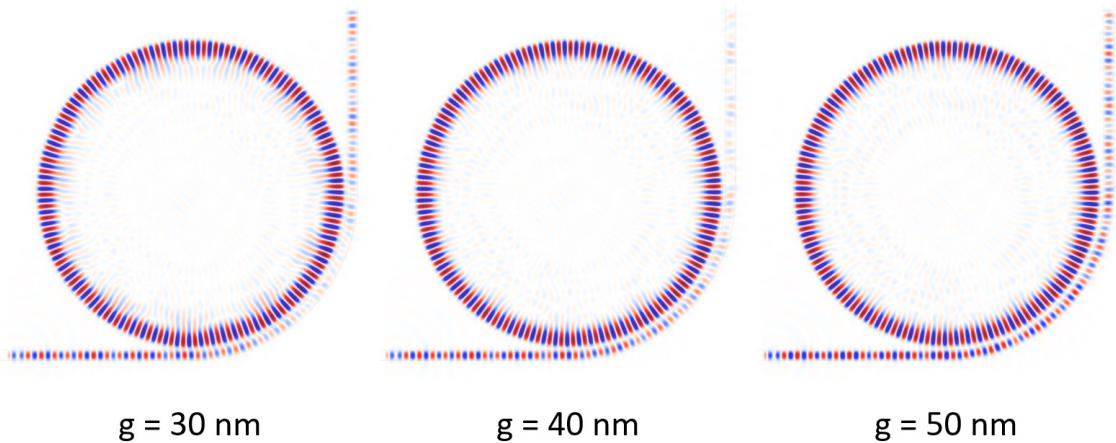


Figure 3.6: FDTD simulations of the  $H_z$  field for devices with  $d = 5 \mu\text{m}$  diameter,  $w = 170 \text{ nm}$ , and  $g = 30 \text{ nm}$  to  $50 \text{ nm}$ .

Fig. 3.5 shows the simulated  $H_z$  field of a  $d = 3 \mu\text{m}$  diameter disk and a waveguide bent at  $\theta = 90^\circ$ . The gap is  $g = 50 \text{ nm}$  and the waveguide width is  $w = 133 \text{ nm}$ . The depicted mode is of order  $n = 1$  and  $m = 48$ . Comparing Fig. 3.5 to Fig. 3.3, we can see that the simulation does not include the curvature of the waveguide away from the disk. While this difference in design does not change anything for the coupling region itself, the additional bend does create some losses, however, these should be rather small.

In Fig. 3.6, we show the simulated  $H_z$  field of devices with  $5 \mu\text{m}$  diameter and  $g = 30$  to  $50 \text{ nm}$ . Good phase matching can be observed for  $g = 40$  and  $50 \text{ nm}$ . The depicted mode is a first-order radial mode with azimuthal order  $m = 79$  at  $\lambda = 441 \text{ nm}$ .

A major difficulty in combining a microdisk laser containing QWs as the active medium with a waveguide is to avoid re-absorption of the emission in the waveguide. We discussed several approaches for monolithic integration in section 3.1.1. We are tackling this issue by

partially etching the waveguide to remove the QWs (QW etch, Fig. 3.1 (c)), which are within 120nm of the surface. It is thus important to investigate whether the reduction in waveguide height has an influence on the coupling. Fig. 3.7 (a) shows a sketch of the device with under-etched microdisk and suspended waveguide with a reduced height. In Fig. 3.7 (b), we show transmission simulations for devices with waveguide heights  $h = 510$  nm (same height as the disk) and  $h = 410$  nm (the case of QW removal). We can see that, while critical coupling is attained for different values of  $g$  for  $w = 133$  nm, the transmission minimum reaches roughly the same value. Consequently, we do not observe any disadvantage in reducing the waveguide height besides needing a slightly smaller gap for efficient coupling.

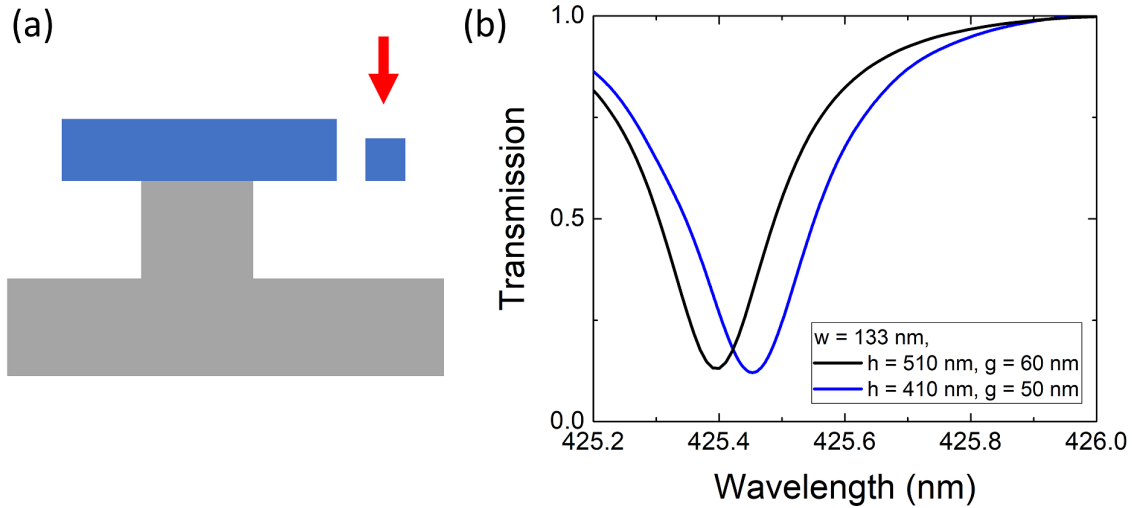


Figure 3.7: (a) Sketch of a microdisk and suspended waveguide with reduced height. (b) Transmission spectra for two devices with different waveguide height and different gap size.

We also etch grating couplers at the extremities of the waveguide to out-couple the guided light. Our grating couplers are not optimized for efficiency or to reduce back reflection. Our goal is just to have near vertical scattering for easy detection in our top-collection setup. Since we are using the microscope objective of the  $\mu$ -PL setup to collect the emission, we are not particularly sensitive to the angle of emission, unlike when using fiber couplers in the NIR. FDTD simulations of the  $xz$ -cross-section of the  $E_y$  field of grating couplers with periods of 170, 190, 210 and 230 nm are shown in Fig. 3.8. The Gaussian source emitting in a 10 nm range around  $\lambda = 425$  nm is placed at the left end of the waveguide. The grating etch depth is 200 nm. The 190 and 210 nm periods give the most vertical emission.

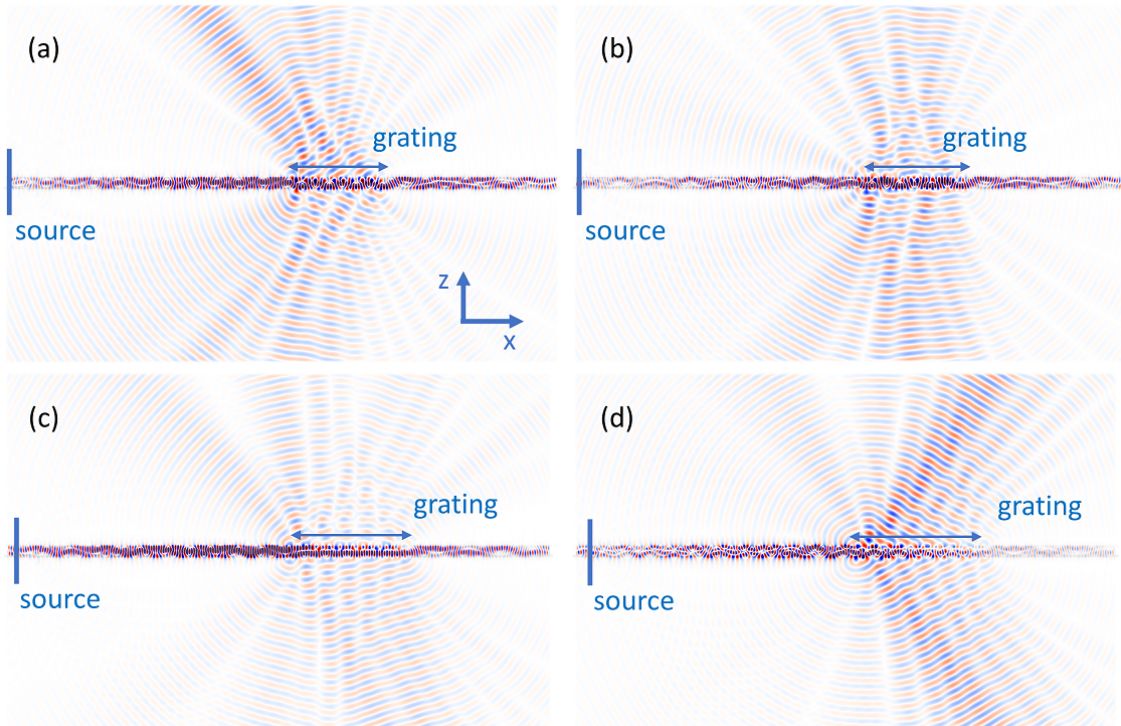


Figure 3.8: FDTD simulations of the  $xz$ -cross-section of the  $E_y$  field of grating couplers with (a)  $P = 170$  nm, (b)  $P = 190$  nm, (c)  $P = 210$  nm, and (d)  $P = 230$  nm in a 10 nm spectral range around  $\lambda = 425$  nm.

### 3.3 Fabrication of photonic circuits on D559 and D677

The fabrication of photonic circuits on samples D559 and D677 follows the process flow described in section 1.3.5.1 and Fig. 1.36. We will discuss especially the aspects that are different from the ideal process. With sample D559, we aimed to demonstrate the first III-nitride microlaser integrated photonic circuit, operating in the under-coupled regime for relative ease of fabrication using gaps in the 80-120 nm range. With sample D677, we aimed to observe critical coupling, so we chose gap sizes of 40 to 120 nm.

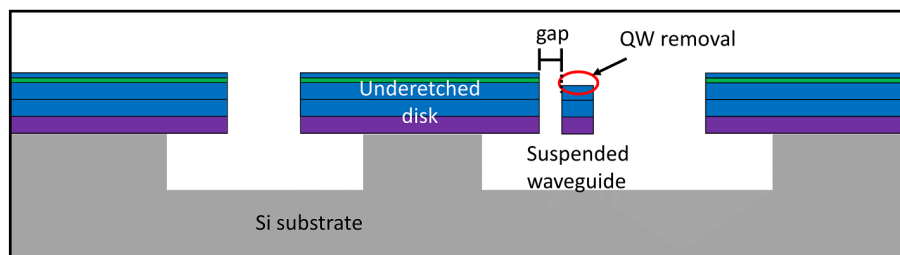


Figure 3.9: Sketch of fabrication process of a microdisk and suspended waveguide.

A schematic cross-sectional view of a device, depicting the disk underetch, waveguide sus-

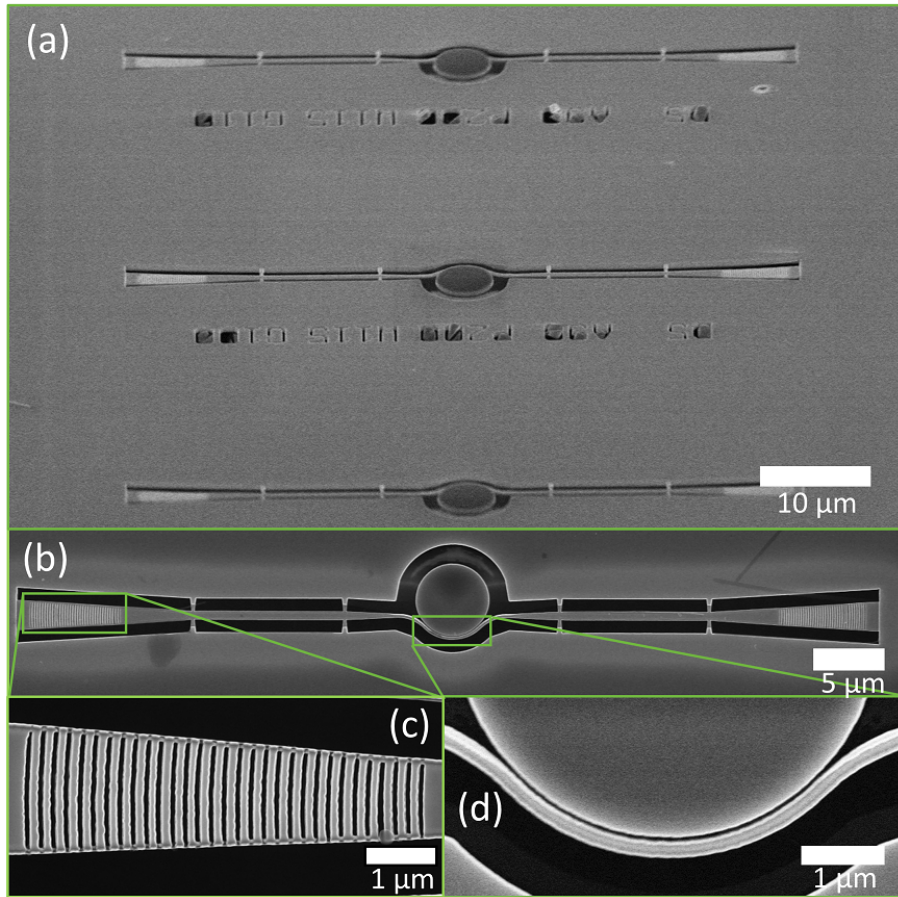


Figure 3.10: SEM image of III-nitride photonic circuit fabricated on sample D559. (a) View of several devices at an angle, (b) top view of one device, (c) close-up of a grating coupler, (d) close-up of the disk and waveguide coupling region.

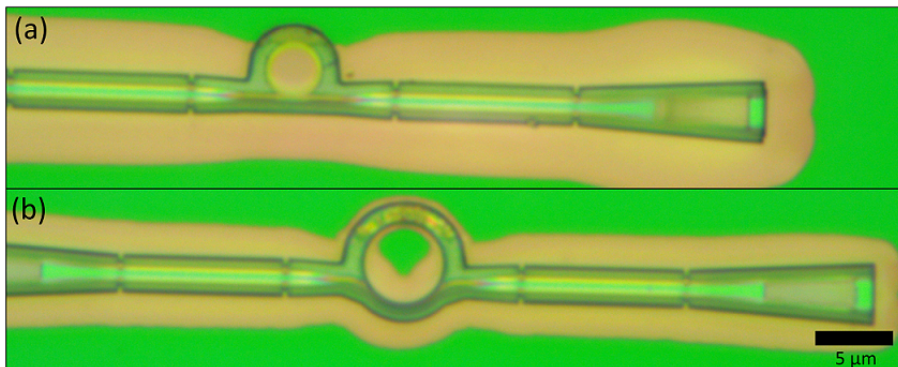


Figure 3.11: Optical microscope images of (a) a 3 $\mu$ m diameter disk with a straight waveguide and (b) a 5 $\mu$ m diameter disk with a 90° bent waveguide fabricated on sample D559. The underetch and silicon pedestal are visible.

pension, and the QW removal is shown in Fig. 3.9. Fig. 3.10 (a)-(d) show SEM images of devices fabricated on sample D559 with close-ups of the grating coupler and the disk-waveguide cou-

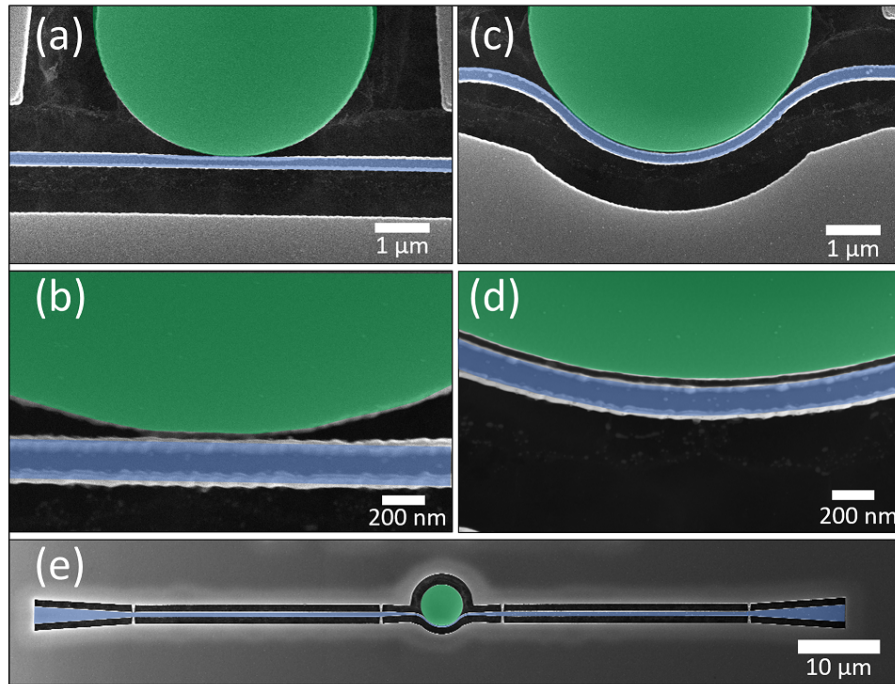


Figure 3.12: (a,b) False colors SEM images of a device with  $\theta = 0^\circ$  and  $g = 45$  nm, (c,d) SEM images of a device with  $\theta = 90^\circ$  and  $g = 45$  nm, (e) SEM image of a full device fabricated on sample D677. The green coloring represents the area with InGaN QWs (i.e. the microdisk) and the blue areas are etched to the GaN buffer layer (i.e. the waveguide).

pling region shown in Figs. 3.10 (c) and (d), respectively. For this sample, the pedestal shape varies based on the device geometry due to the first ICP etch leaving behind a thin layer of AlN. For devices with a  $3\mu\text{m}$  diameter disk (shown in Fig. 3.11 (a)), there is no pedestal remaining after the underetch and the disk is being held in place by the thin AlN layer. For a  $5\mu\text{m}$  diameter disk and  $\theta = 90^\circ$  (as shown in Fig. 3.11 (b)), we observe a triangular decentralized pedestal. The total device length is  $60\mu\text{m}$  with about  $20\mu\text{m}$  between the edge of the disk and the beginning of the grating.

In the case of sample D677, we only performed the first two levels of the process, in other words, there are no gratings due to a malfunctioning cleanroom at the time of fabrication. The device length is  $100\mu\text{m}$ , as can be seen in Fig. 3.12 (e). The end of the waveguide is tapered from  $500$  nm to  $2\mu\text{m}$  width. The  $120$  nm high edge created at the end of the waveguide through the QW removal allows for light extraction by scattering.

We fabricated  $5\mu\text{m}$  diameter microdisks with bent bus waveguides with  $\theta = 0^\circ$  to  $90^\circ$ , a waveguide width of nominally  $w = 135$  nm (measured:  $w = 170$  nm), and nominal gap sizes between the disk and the waveguide of  $g = 40$  to  $120$  nm (measured:  $g = 30$  to  $120$  nm). False color SEM images of devices with  $g = 45$  nm are shown in Fig. 3.12 (a,b) for  $\theta = 0^\circ$  and (c,d) for  $\theta = 90^\circ$ . In the zoom-ins in Fig. 3.12 (b) and (d), it is clearly visible that the small gaps are

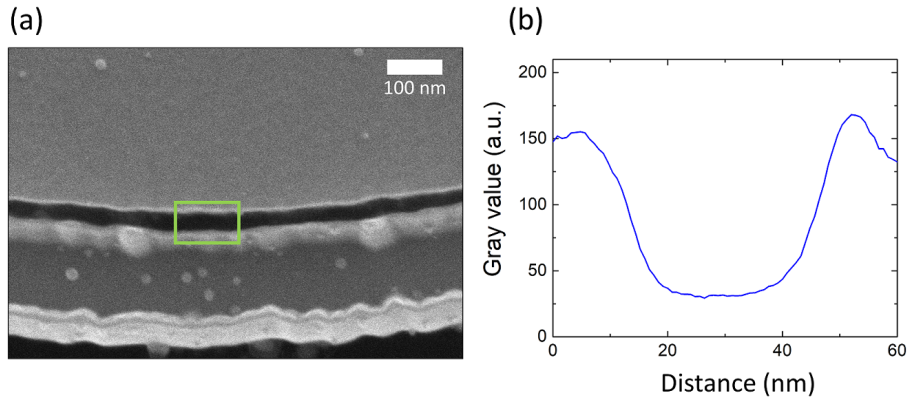


Figure 3.13: (a) SEM image of a nominally 50 nm gap and (b) gray-scale profile along the vertical direction and integrated along the horizontal direction of the rectangle in (a), giving a gap of 45 nm at the top, fabricated on sample D677.

fully open. Fig. 3.13 (a) shows an SEM image of a device with a gap of nominally 50 nm. The gray-scale profile in Fig. 3.13 (b) is measured along the vertical direction and integrated along the horizontal direction of the rectangle in Fig. 3.13 (a). The measurement gives a gap of 45 nm at the top. With this method, we determined the gaps for the devices of this sample and we will refer to the measured gap sizes in the following.

## 3.4 Results and discussion

### 3.4.1 CW spectroscopy of sample D559

We use the  $\mu$ -PL setup in Grenoble depicted in Fig. 1.46 for CW measurements of sample D559 using a laser emitting at 244 nm. Fig. 3.14 (a) shows a 2D map of the charge coupled device (CCD), where the vertical axis is the distance along the device direction and the horizontal axis is the wavelength. In vertical direction, 1 pixel on the CCD map corresponds to a distance of  $0.9\mu\text{m}$  on the sample. The vertical position on the CCD is matched with the SEM image next to it (Fig. 3.14 (b)). The central, over-saturated emission comes from the QW luminescence scattered from the center of the microdisk. Faint emission, spatially separated from the high intensity central region, can be observed from the grating couplers. Fig. 3.14 (c) shows spectra integrated over 5 pixels along the vertical axis of the CCD, which corresponds to  $4.5\mu\text{m}$  on the sample. Clear whispering-gallery mode (WGM) emission is observed from both gratings, while much higher intensity emission without any visible modes is observed from the center of the disk. The free carrier absorption in the n-doped part of the waveguide is only in the range of  $50\text{cm}^{-1}$  [189]. Taking the overlap of the mode with this region (28%) into account, the estimated propagation losses due to doping are negligible. This result demonstrates light routing and extraction using an active blue emitter.

A comparison between experimental and simulated spectra is shown in Fig. 3.15 for a  $3\mu\text{m}$

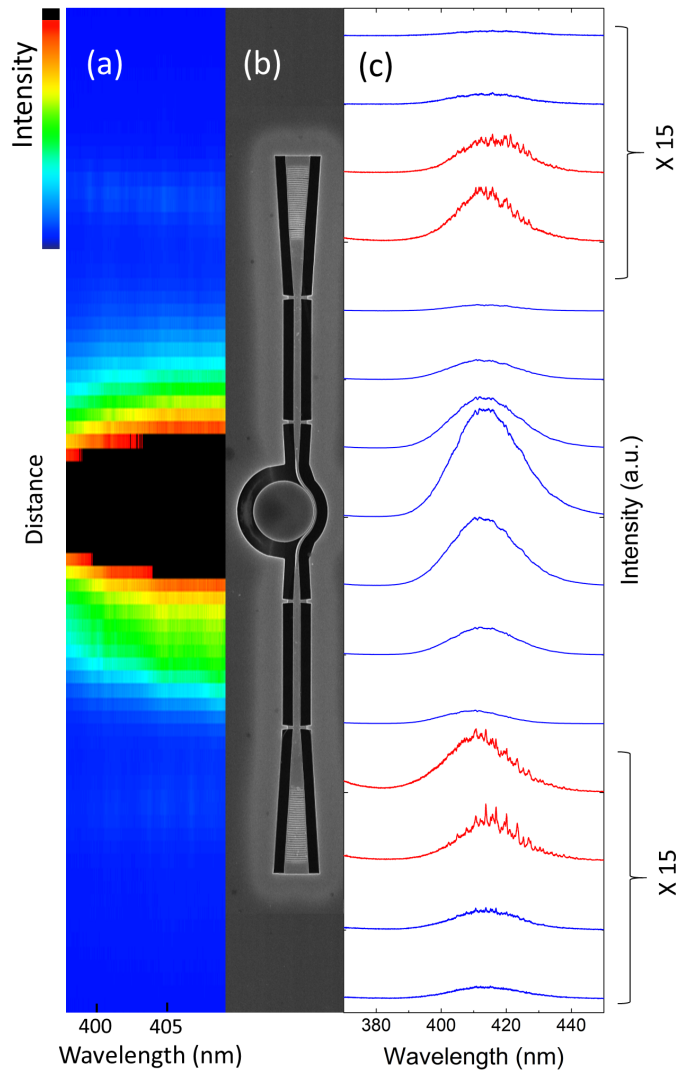


Figure 3.14: Visualization of the spatial distribution of the emission for sample D559. (a) 2D intensity map of the CCD, (b) SEM image of the device matched to the CCD image along the vertical axis, (c) spectra integrated over 5 pixels along the vertical axis corresponding to (a) and (b) in vertical position.

diameter disk. A simulated transmission spectrum is depicted in Fig. 3.15 (a) and compared to an experimental emission spectrum in Fig. 3.15 (b). The mode spacing between first-order radial modes is 5–6 nm and the mode positions match well between simulation and experiment. The azimuthal number of each mode is clearly identified by performing simulations for a 1 nm wavelength range around each mode and counting the nodes in the  $H_z$  field, as depicted in Fig. 3.5.

$\mu$ -PL measurements for different gap sizes and bending angles are shown in Fig. 3.16 for devices with 5  $\mu\text{m}$  diameter disks, integrated spatially over one grating coupler on the CCD. Broad QW luminescence that couples to the waveguide and is outcoupled at the grating is observed

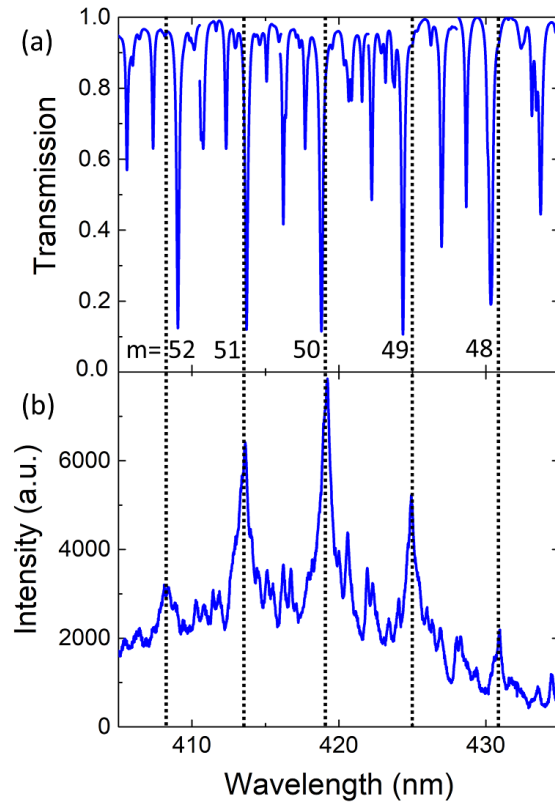


Figure 3.15: Comparison of (a) simulation and (b) measurement for a  $3\ \mu\text{m}$  diameter disk fabricated on sample D559. The mode positions match well and the azimuthal numbers of the first-order radial modes is clearly identified.

in all spectra and decreases in intensity with increasing gap size. WGMs can also be seen in all spectra. Larger contrast WGM resonances are observed for small gaps (Fig. 3.16 (a)) and large angles (Fig. 3.16 (b)), giving loaded Q factors larger than 2000 in the blue, as can be seen in the close-up in Fig. 3.16 (c). We attribute the sharp resonances with high Q factor to the first-order radial modes. The azimuthal number for the first-order radial mode at 422 nm is  $m = 84$ , according to our FDTD simulations. Lower Q factor, broader modes of higher radial order are also detected, indicating the presence of different families of modes. The here observed WGM contrast (defined as mode intensity divided by background intensity) of up to 2.7 is the largest we have measured for such microdisks in a top-collection setup. In previous measurements, we had to use in-plane side-collection to detect the WGMs directly from the disk, since the modes radiate preferentially in the layer plane [46, 50]. The loaded Q factors are very similar compared to the intrinsic Q factors of individual disks, which we have previously determined to be around 2500 for disks fabricated from the sample D559 (see section 2.3.5 and Ref. [50]).

The coupling Q factor,  $Q_C$ , depends on the mode overlap between the WGM and the waveguide mode, the interaction length, and the phase mismatch. It is thus dependent on several parameters including the gap distance, the microdisk radius and the waveguide width. The spatial overlap of the first-order radial mode with the waveguide mode is smaller than the one

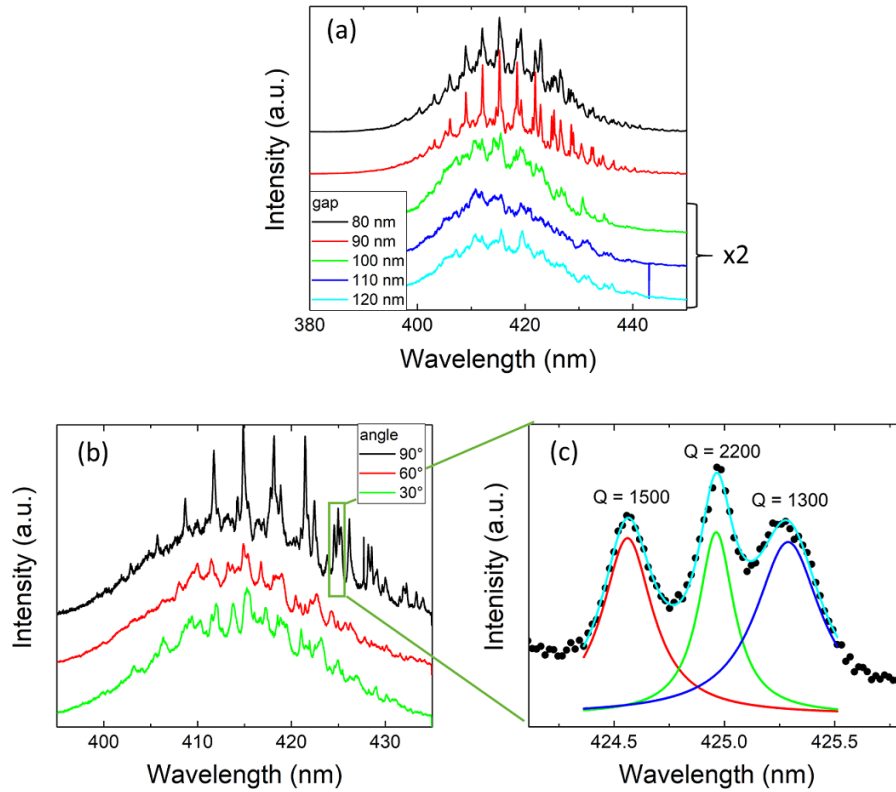


Figure 3.16: PL measurements integrated over one grating coupler on the CCD for devices with a disk diameter of  $5\mu\text{m}$ , a waveguide width of  $155\text{nm}$  and a grating period of  $210\text{nm}$  fabricated on sample D559. (a) The waveguide bending angle is  $90^\circ$  and the gap sizes vary between  $80\text{nm}$  and  $120\text{nm}$ . The spectra for  $g = 100 - 120\text{nm}$  have been multiplied by 2 for better visibility of the modes. (b) The gap is  $90\text{nm}$  and the bending angle has been varied between  $90^\circ$  and  $30^\circ$ . (c) Close-up of three modes of the  $90^\circ$  spectrum in (b) showing Lorentzian fits and the corresponding Q factors.

of higher-order radial modes. As shown by Soltani [190] for the case of silicon-based coupled resonators, the coupling strength (defined as  $\frac{1}{Q_C}$ ) is usually weaker for the first-order radial modes thus leading to higher  $Q_C$  factors as compared to higher-order radial modes. We say "usually", as there might be some specific parameter combinations, where this assumption does not hold because of phase mismatch issues. This feature has a strong impact on the mode visibility, since the emission coupling to the waveguide depends on the values of  $Q_{int}$  and  $Q_C$ , as for the case of transmission with microdisks and bus waveguides [191].

As the gap distance increases,  $Q_C$  will increase exponentially and the fraction of the light transmitted through the waveguide drops very rapidly to zero. According to FDTD modeling (see Fig. 3.4 (b)), the critical coupling distance is  $50\text{nm}$  for the first-order radial modes, i.e. the ones where  $Q_{int} = Q_C$  and thus  $Q_{load} = 1/2Q_{int}$ . For gap distances larger than  $80\text{nm}$ , we are in the under-coupled regime and the loaded Q factor should increase steadily towards the intrinsic Q factor. However, the coupled intensity decreases. In the case of the  $120\text{nm}$  gap,

the first-order radial modes are barely visible in FDTD transmission simulations (see Fig 3.4 (a)). Meanwhile, the higher-order radial modes have both a lower intrinsic quality factor and a lower coupling quality factor as compared to the first-order radial modes. The amplitude of the higher-order radial modes coupled to the waveguide decreases as well with the gap distance, but less sharply than the first-order radial modes. It explains why in Fig. 3.16 (a), the emission spectra for gaps larger than 100 nm are dominated by the low Q factor broad modes and that the mode visibility of the first-order radial modes with high Q factor is quenched above 90 nm. Moreover, there is some scattered spontaneous emission from the disk collected above the waveguide, and this background signal decreases the overall visibility of the modes.

### 3.4.2 Critical coupling in the spontaneous emission regime

For sample D677, we used the  $\mu$ -PL setup in Montpellier that is depicted in Fig. 1.45 using a CW laser emitting at  $\lambda = 355$  nm. We determine the contribution of the disk-waveguide coupling to the Q factor by performing RT measurements on devices with  $\theta = 90^\circ$ . The microdisk is excited with an 8  $\mu$ m diameter spot, and the emission is collected from the top. By defining areas on the CCD, the position of the emission can be discerned (i.e. above the disk or at the end of the waveguide). Spectra of devices with  $g = 30$  to 55 nm measured at the end of the waveguide are shown in Fig. 3.17 (a). First-order radial WGMs are clearly visible and their azimuthal mode orders are identified in Fig. 3.18, which were determined by counting the nodes in the  $H_z$  field. Modes of orders  $m = 85$  to 79 are visible.

We can determine  $Q_{int}$  by investigating a device with  $g = 120$  nm, where the coupling to the bus waveguide becomes negligible ( $Q_{load} \approx Q_{int}$  in the under-coupled regime). Fig. 3.17 (b) shows the spectrum of a mode with  $Q_{int} \approx Q_{load} = 4700$ . The FWHM of the resonance is determined by a Lorentzian fit. The spectrum is measured at the disk for a device with  $g = 120$  nm, where the coupling is very weak, and in the low energy tail of the spectrum, where the contribution of the QW absorption is negligible. We use a spectrometer grating with 3600 grooves/mm to allow for sufficient resolution. We assume that the determined  $Q_{int}$  value is for a first-order radial mode and that we have the same  $Q_{int}$  value at 442 nm for first-order radial modes for all investigated microdisks. Higher order modes would have different  $Q_{int}$  values. We explain the factor 2 improvement of  $Q_{int}$  as opposed to sample D559 by the higher material quality due to the lack of Si-doping.  $Q_{int} = 4700$  is state of the art for III-nitrides in the blue spectral range. A factor two higher values have been achieved using oxygen passivation [36]. The main limitations for the Q factor at short wavelength are scattering loss, which scales with  $\lambda^{-2}$  due to sidewall roughness, as well as surface absorption [36]. At  $\lambda = 420$  nm, we estimate  $Q_{abs,QW} = 5000$  in analogy to Ref. [192] (see chapter 4). At longer wavelength, the QW absorption vanishes, as well as its contribution to  $Q_{load}$ . In Fig. 3.17 (a), the linewidth of the WGMs does not change for  $\lambda > 430$  nm, since the absorption is negligible. As will be shown later,  $Q_C$  is larger than  $10^5$  for a gap size of 120 nm. At critical coupling,  $Q_{load} = 1/2 \cdot Q_{int}$ . The occurrence of critical coupling is associated with a maximum in energy transfer from the microdisk to the waveguide as a func-

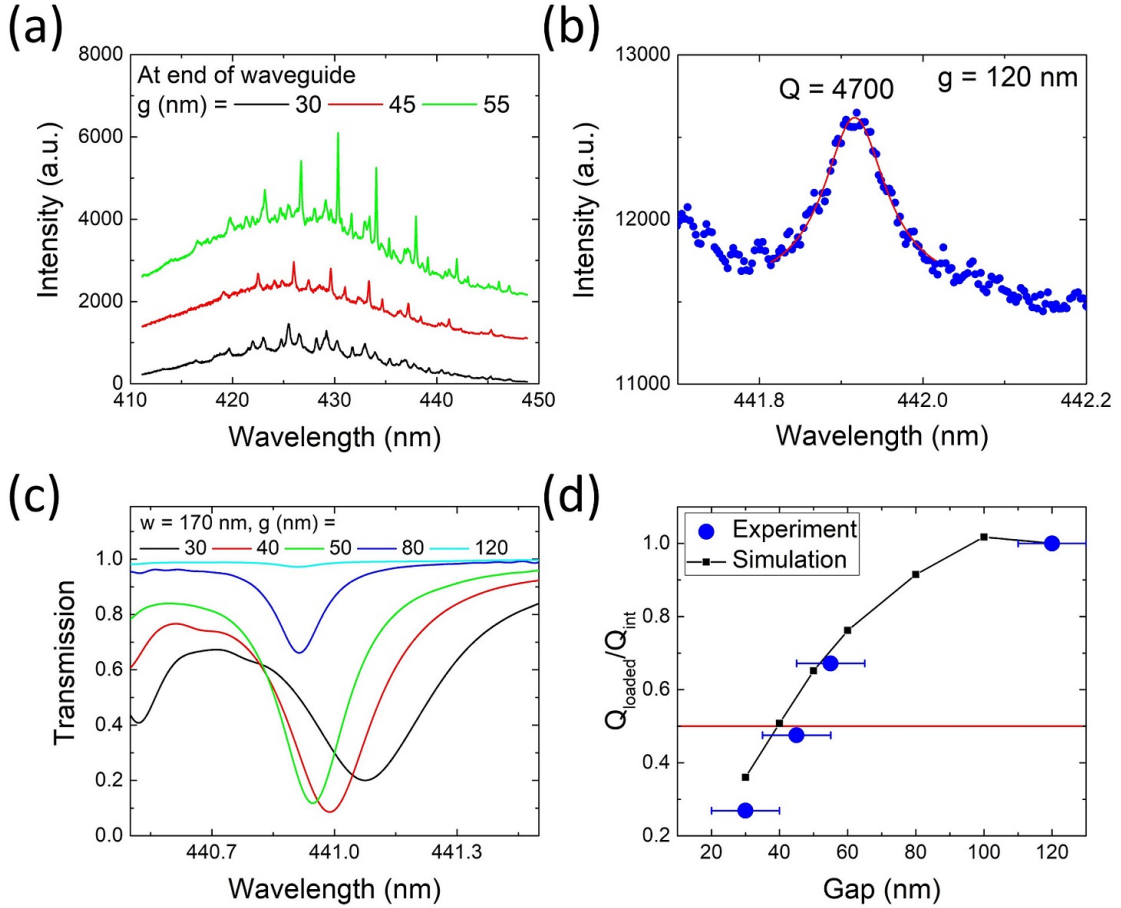


Figure 3.17: Critical coupling of 5 μm diameter disks: (a) CW μ-PL spectra taken at the end of the waveguide for devices with a waveguide bending angle  $\theta = 90^\circ$  and  $g = 30$  to 55 nm, fabricated on sample D677. (b) CW μ-PL spectrum measured above the disk for a device with  $g = 120$  nm using a 3600 grooves/mm grating. The mode is fitted with a Lorentzian, giving  $Q_{int} = 4700$ . (c) FDTD simulation of the radiative flux transmitted through the end of the waveguide of devices with  $g = 30$  to 120 nm. (d) Comparison of experimental and simulated results of  $Q_{load}/Q_{int}$  vs. gap for the 442 nm mode. The red horizontal line indicates critical coupling.

tion of the gap. FDTD simulations show the sensitive dependence of the transmitted radiative flux for a mode at 441 nm in Fig. 3.17 (c) for gaps between 30 and 120 nm for a 5 μm diameter disk. Experimental and simulated  $Q_{load}$  factors are plotted as a function of gap in Fig. 3.17 (d). The experimental values are determined for the 442 nm mode where absorption is negligible, since this is the low-energy end of the QW emission/absorption spectrum. We assume that these are first-order radial modes, which is a fair assumption because the experimental mode positions and spacing match well with FDTD simulations (see Fig. 3.18). Critical coupling is attained at  $g \approx 40 - 45$  nm for both experiment and simulation. Phase matching of the modes in the disk and waveguide is a necessary condition for critical coupling. It is achieved

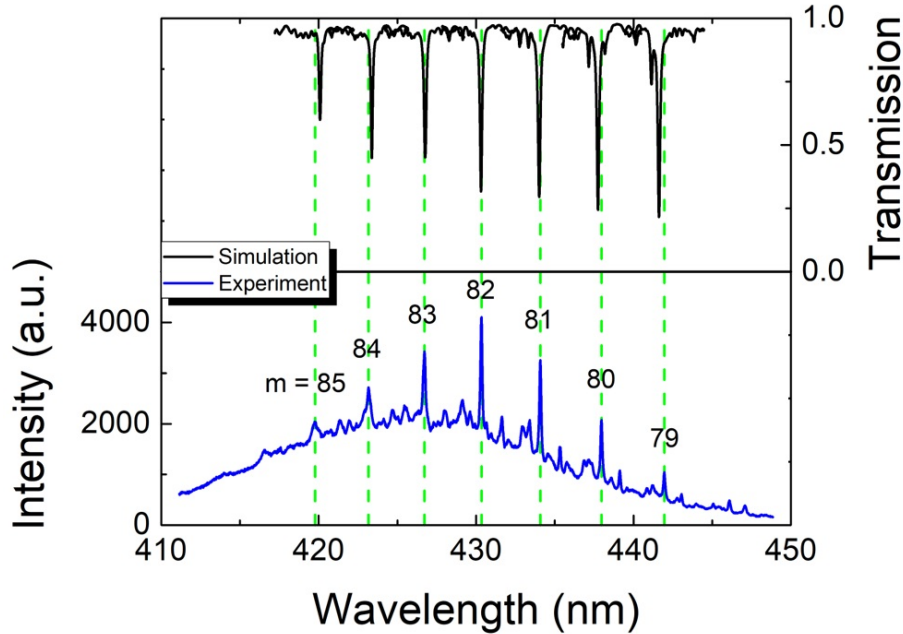


Figure 3.18: Simulated (top) and experimental (bottom) spectra of a device with  $\theta = 90^\circ$  and  $g = 50$  nm (simulated) and 45 nm (experimental), fabricated on sample D677. The azimuthal orders of the first-order radial modes are  $m = 85$  to 79.

by fine-tuning  $w$  and  $g$  to get the mode profiles in the waveguide and disk to match. In FDTD simulation, good phase matching can be observed for both  $g = 40$  and 50 nm (see Fig. 3.6 (b) and (c)).

### 3.4.3 Observation of pulsed lasing in a III-nitride photonic circuit

Using the  $\mu$ -PL setup depicted in Fig. 1.45 and a 266 nm laser under pulsed conditions (400 ps, 4 kHz), lasing was observed at RT for sample D559, for devices with 3  $\mu$ m diameter disks, straight waveguides and 100 to 120 nm gaps. Fig. 3.19 shows power dependent measurements both collected above the disk (Fig. 3.19 (a)) and from the out-coupling grating (Fig. 3.19 (b)), for a device with a gap of 120 nm. The threshold was estimated to be  $15 \text{ mJ} \cdot \text{cm}^{-2}$  per pulse ( $38 \text{ MW} \cdot \text{cm}^{-2}$  peak power), and lasing was observed up to our maximum available energy density of  $16.5 \text{ mJ} \cdot \text{cm}^{-2}$  per pulse. For individual microdisk lasers with a slightly larger diameter of 4  $\mu$ m, fabricated on sample D559, we have previously observed thresholds of  $3 \text{ mJ} \cdot \text{cm}^{-2}$  per pulse (see sections 2.2 and 2.3.8 and Ref. [50]). The here larger threshold is explained by differences in thermal management and heat dissipation issues due to the lack of a silicon pedestal (see the microscope image in Fig. 3.11). The lasing mode and broad QW luminescence can be observed from both the disk and the grating. At the disk, the emission has a higher intensity, while a factor two better contrast between the lasing mode and the QW luminescence is obtained at the grating.

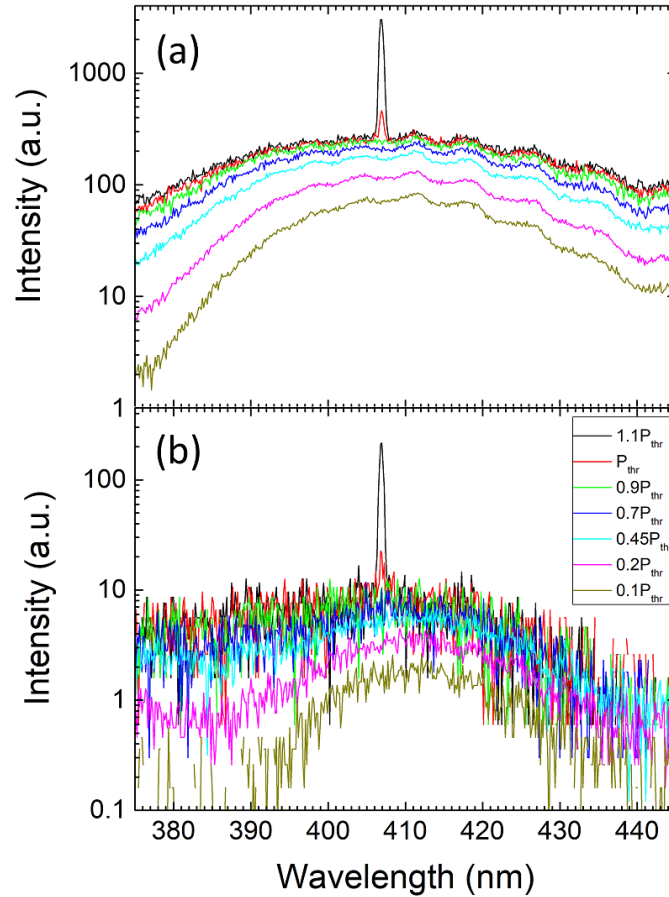


Figure 3.19: Power dependent pulsed lasing spectra of a device with a  $3\mu\text{m}$  diameter disk, a straight waveguide and a  $120\text{ nm}$  gap, fabricated on sample D559, and measured (a) above the disk and (b) above the out-coupling grating. The threshold excitation energy is  $E_{th} = 15\text{ mJ} \cdot \text{cm}^{-2}$  per pulse.

We do not observe lasing from any  $5\mu\text{m}$  diameter disks, which can be explained by the decentralized pedestal near the disk edge causing additional absorption losses. Furthermore, we also do not observe lasing from the devices with  $3\mu\text{m}$  diameter and  $90^\circ$  bent waveguides due to losses in the pedestal, which is decentralized and near the disks edge in this case.

The measurements reported in Fig. 3.19, along with the images shown in Fig. 3.10 and Fig. 3.14, demonstrate the first integrated microlaser photonic circuit in the blue [166].

#### 3.4.4 Dependence of lasing threshold and output signal on Q factor and coupling distance

We demonstrate pulsed lasing at RT of devices fabricated on sample D677 for all investigated values of  $\theta$  and  $g$ . We use the  $\mu\text{-PL}$  setup described in Fig. 1.45 with a pulsed  $355\text{ nm}$  laser with  $7\text{ kHz}$  repetition rate,  $4\text{ ns}$  pulse width and a  $20\times$  microscope objective. Fig. 3.20 shows pulse energy dependent spectra of a device with  $\theta = 90^\circ$  and  $g = 45\text{ nm}$ , corresponding to the

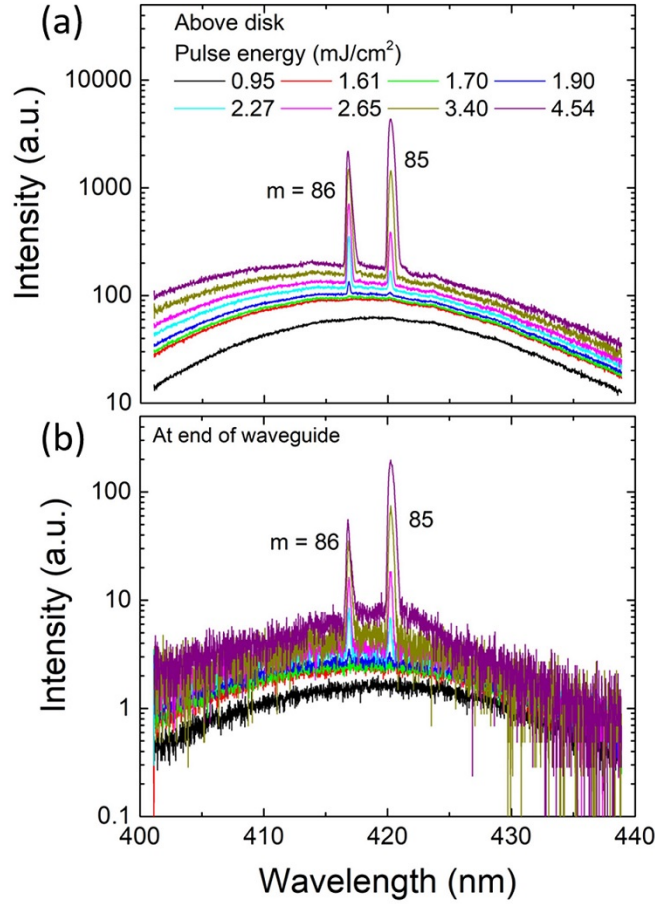


Figure 3.20: Lasing at the critical coupling gap size: pulse energy dependent spectra measured (a) above the disk and (b) at the end of the waveguide, for a device with  $\theta = 90^\circ$  and  $g = 45$  nm, fabricated on sample D677. The azimuthal numbers of the first-order radial modes are  $m = 86$  and  $85$ . The threshold energy density of the  $m = 86$  mode is  $1.7 \text{ mJ} \cdot \text{cm}^{-2}$  per pulse.

critical coupling parameters under CW excitation discussed in Fig. 3.17 (d). The spectra in Fig. 3.20 (a) are taken using top-collection above the disk and in Fig. 3.20 (b) at the end of the waveguide. Two first-order radial modes at 416 and 420 nm are lasing. Their azimuthal numbers are determined to be  $m = 86$  and  $85$ , by comparison with FDTD simulations (see Figs. 3.6 and 3.18). The threshold energy density is determined as the value where the mode starts to become clearly visible in the spectrum. For the  $m = 86$  mode,  $E_{th} = 1.7 \text{ mJ} \cdot \text{cm}^{-2}$  per pulse (or  $P_{th} = 425 \text{ kW} \cdot \text{cm}^{-2}$ ). The other below-threshold modes are not visible due to the pulsed excitation with top-collection, a configuration that does not allow for easy detection of modes below threshold [49]. Similar lasing spectra for devices with  $g = 30$  nm and  $g = 55$  nm are shown in Fig. 3.21 measured both above the disk and at the end of the waveguide. The thresholds are  $E_{th} = 2.5 \text{ mJ} \cdot \text{cm}^{-2}$  per pulse ( $P_{th} = 625 \text{ kW} \cdot \text{cm}^{-2}$ ) for  $g = 30$  nm and  $E_{th} = 1.4 \text{ mJ} \cdot \text{cm}^{-2}$  per pulse ( $P_{th} = 350 \text{ kW} \cdot \text{cm}^{-2}$ ) for  $g = 55$  nm. The threshold clearly decreases with increasing gap.

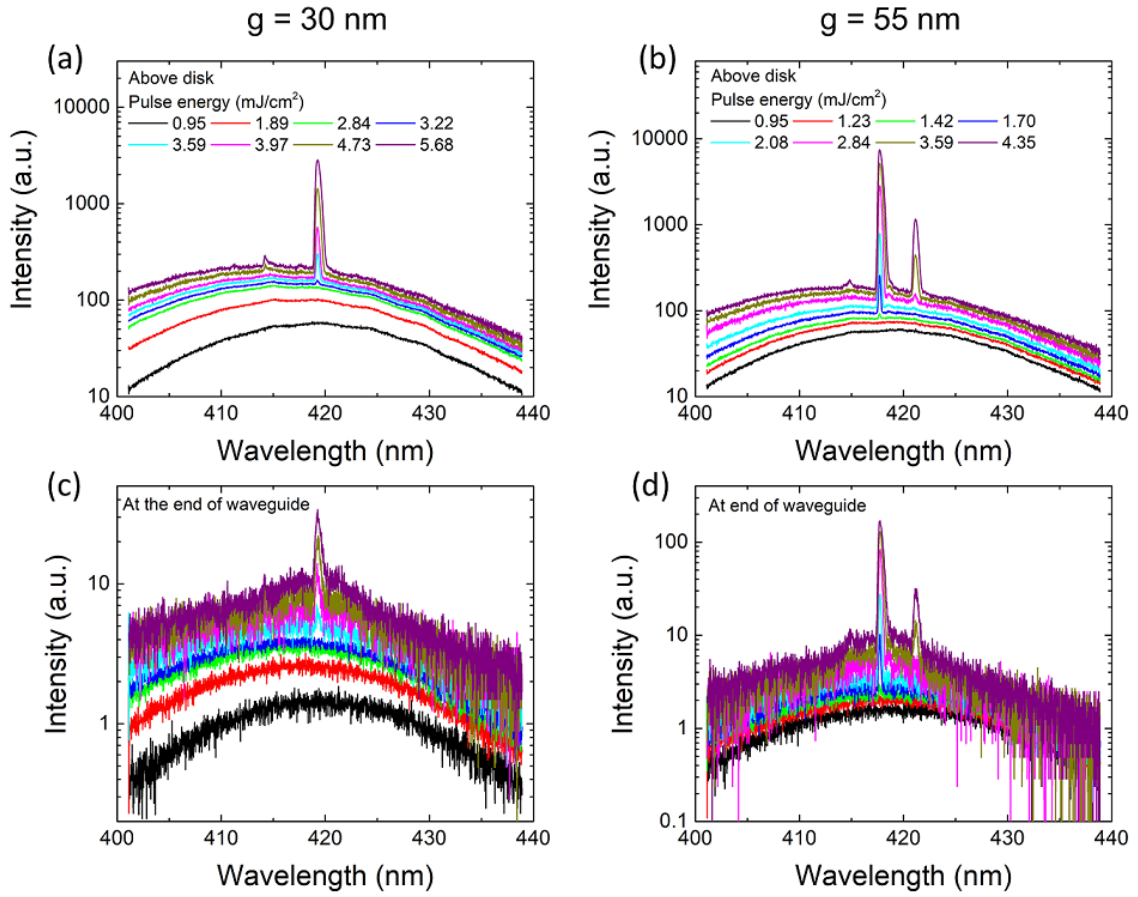


Figure 3.21: Lasing spectra measured above the disk for (a)  $g = 30$  nm and (b)  $g = 55$  nm, and at the end of the waveguide for (c)  $g = 30$  nm and (d)  $g = 55$  nm, for devices fabricated on sample D677.

Fig. 3.22 (a) shows pulse energy dependent spectra around the threshold for a device with  $\theta = 90^\circ$  and  $g = 120$  nm. The threshold is determined to be  $E_{th} = 1.2 \text{ mJ} \cdot \text{cm}^{-2}$  per pulse ( $P_{th} = 300 \text{ kW} \cdot \text{cm}^{-2}$ ). The linewidth over pulse energy is shown in Fig. 3.22 (b), indicating a linewidth narrowing of more than a factor of 2. The inset in Fig. 3.22 (b) shows the integrated intensity over pulse energy.

The lasing mode integral vs. pulse energy is shown in Fig. 3.23(a) and (b) for devices with different gaps and for  $\theta = 90^\circ$  and  $0^\circ$ , respectively. Fig. 3.23 (c) summarizes the thresholds for both angles. As previously observed in Fig. 3.17 (a)-(c) in the spontaneous emission regime, the impact of the gap size on the lasing behavior is very strong for values near the spontaneous emission critical coupling point. A larger effect of the gap size on the threshold is observed for  $\theta = 90^\circ$  than for  $0^\circ$ . A geometry with  $\theta = 90^\circ$  allows for critical coupling at a larger distance than the straight waveguide configuration due to the increased coupling length [193]. For  $\theta = 0^\circ$ , the critical coupling distance is shorter and was not reached experimentally. The lowest threshold of  $1.2 \text{ mJ} \cdot \text{cm}^{-2}$  per pulse is observed for  $\theta = 90^\circ$  and  $g = 120$  nm, as depicted in Fig. 3.22.

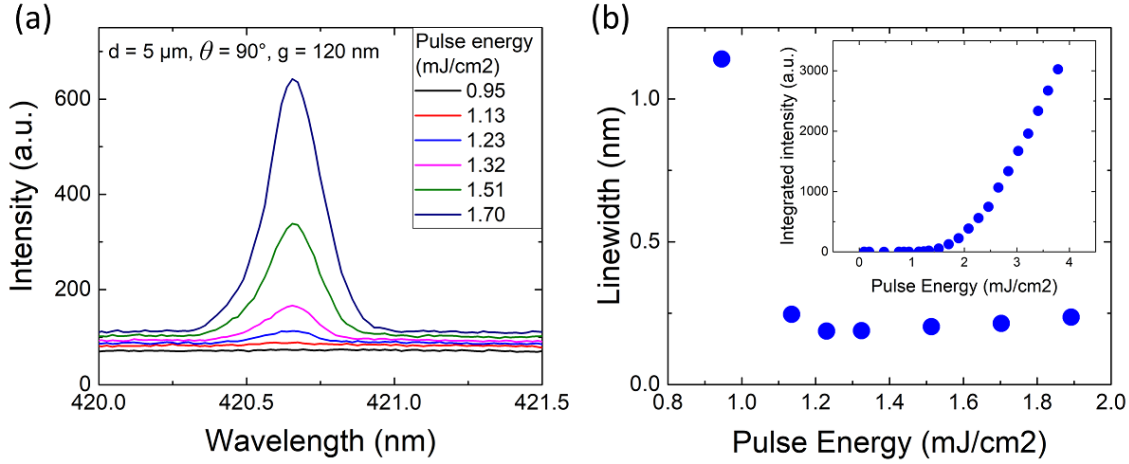


Figure 3.22: (a) Pulse energy dependent spectra around threshold for a device with  $\theta = 90^\circ$  and  $g = 120$  nm, fabricated on sample D677. The threshold is at  $1.2 \text{ mJ} \cdot \text{cm}^{-2}$  per pulse. (b) Linewidth vs. pulse energy of the mode in (a) and (inset) integrated intensity vs. pulse energy for the same mode.

Fig. 3.23 (d) shows the lasing threshold as a function of  $Q_{load}$  using the below-threshold CW  $Q_{load}$  values from Fig. 3.17 and the threshold values from Fig. 3.23 (c). It is interesting to quantitatively analyze the microlaser threshold and the collected laser emission as a function of the coupling strength. The threshold is given as [144, 194]

$$P_{th} \propto G_{th} = \frac{2\pi n_g}{\Gamma \lambda Q_{load}} + G_{tr}, \quad (3.1)$$

$$P_{th} = B \cdot \left( \frac{1}{Q_{int}} + \frac{1}{Q_C} \right) + F, \quad (3.2)$$

with  $G_{th}$  the threshold gain,  $n_g$  the group index in the material,  $\Gamma$  the energy confinement factor,  $\lambda$  the resonant wavelength,  $G_{tr}$  the gain needed to achieve transparency, and  $B = 2070$  and  $F = 0.79$  fit parameters. The red curve in Fig. 3.23 (d) is given by Eq. 3.2 and matches well with the experimental data, showing that the laser threshold can be controlled by tuning  $Q_{load}$  by adjusting the gap size.

As seen in Fig. 3.23, the threshold depends on the coupling gap between the microdisk and the bus waveguide, as well as on  $Q_{load}$ . The energy extracted at the end of the waveguide depends also on  $Q_C$  and there is an optimal  $Q_C$  providing maximum extracted energy. In the case of standard ridge lasers, the optimization of the output power is well-known and the maximum out-coupled power depends on the mirror reflectivity  $R$  [96]. For high-power lasers, a small  $R$  is chosen, providing large out-coupled power but a higher threshold, while for low-power lasers,  $R$  needs to be large and the out-coupled power and threshold are small. The cases of microsphere, microdisk or microring lasers coupled with bus waveguides have been thoroughly investigated as well. In most cases, the pump energy was injected through the bus waveguide

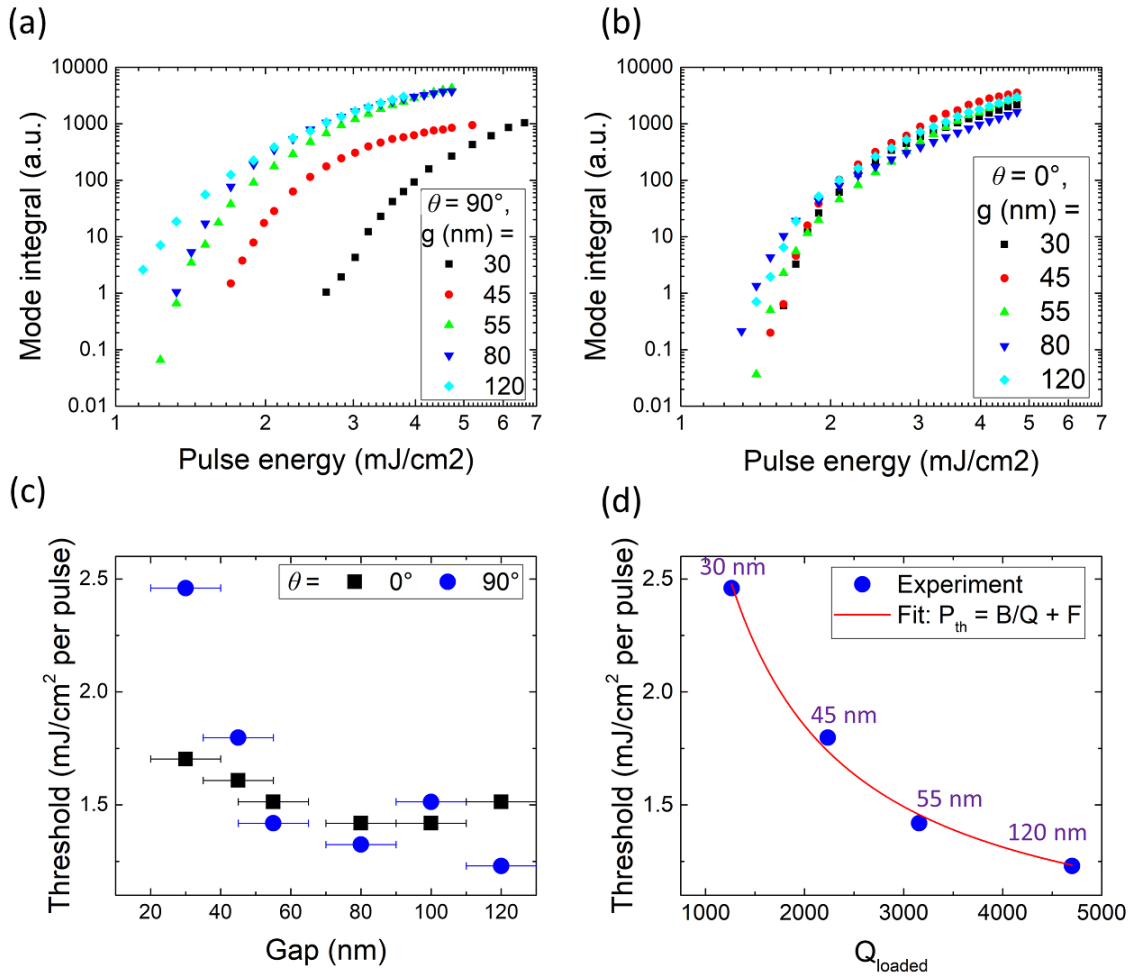


Figure 3.23: Mode integral over pulse energy for different gap sizes for a  $5\mu\text{m}$  disk for (a)  $\theta = 90^\circ$  and (b)  $\theta = 0^\circ$ . (c) Threshold vs. gap for  $\theta = 90^\circ$  and  $\theta = 0^\circ$  for devices fabricated on sample D677. (d) Threshold vs.  $Q_{\text{load}}$  for  $\theta = 90^\circ$  using the  $Q_{\text{load}}$  values from CW excitation in Fig. 3.17 (a,b) and fitted with Eq. 3.2.

[186, 188, 195, 196], which results in the laser characteristics being doubly dependent on the coupling to waveguides for both pump injection and laser emission. In the case investigated here, population inversion is achieved through an external pump that is not linked with the bus waveguide. For this type of configuration, which is also relevant for an electrical injection scheme, the know-how to achieve optimum out-coupled power is essential. This optimum depends on the pump energy as well as the microdisk to waveguide coupling. In the spontaneous emission regime, the energy transfer is most efficient at critical coupling. However, in the lasing regime, the gap distance providing maximum energy transfer does not necessarily coincide with the spontaneous emission critical coupling. It is thus necessary to investigate the dependence of the output signal on the pump energy and coupling. Fig. 3.24 shows the output signal measured at the end of the waveguide and integrated over one mode as a function of  $Q_C$  for

different pump powers  $P_{pump}$  for devices with  $\theta = 90^\circ$ . This signal is proportional to the out-coupled power  $P_{out}$  and is integrated over the mode that shows lasing first. The experimental data points are shown as well as the theoretical curves given by [95, 96, 195, 197, 198]

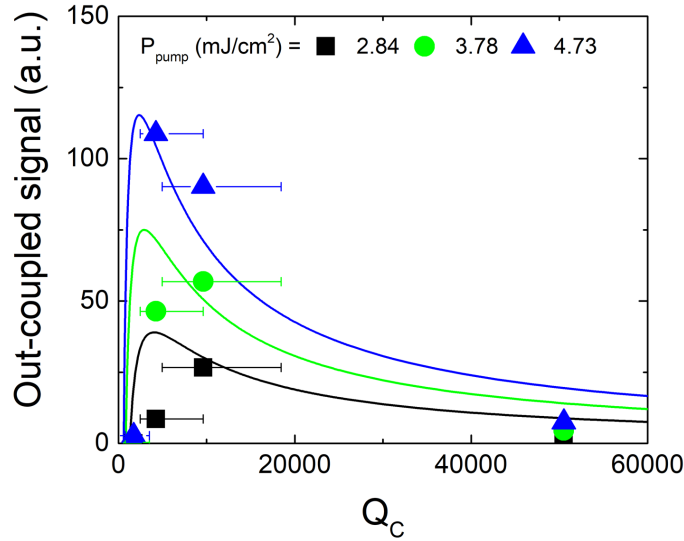


Figure 3.24: Out-coupled signal integrated over one mode as a function of  $Q_C$ , for  $\theta = 90^\circ$  measured at the end of the waveguide (symbols) and the theoretical curve of Eq. 3.3 for devices fabricated on sample D677.

$$P_{out} = C \cdot \frac{\frac{1}{Q_C}}{\left(\frac{1}{Q_{int}} + \frac{1}{Q_C}\right)} \cdot (P_{pump} - P_{th}), \quad (3.3)$$

where  $C = 66$  is a fit parameter and  $P_{th}$  is given by Eq. 3.2 and the fit in Fig. 3.23 (d). This equation reflects the external quantum efficiency, given by the ratio between coupling losses and global losses, and the threshold condition of the laser. The  $Q_C$  values were determined using Eq. 1.75, where  $Q_{int} = 4700$  is taken from Fig. 3.17 (b), and  $Q_{load}$  values are taken from Fig. 3.17 (d). The error bars are determined via an exponential fit between  $Q_C$  and gap and the  $\pm 10$  nm error assumed for the gaps. The maximum of  $P_{out}$ , representing maximum energy transfer, shifts towards smaller  $Q_C$  with increasing  $P_{pump}$ . For large values of  $Q_C$ , the power quickly drops towards zero. Experiment and calculation match rather well, however, this is limited by the accuracy of the gap values and by the limited number of experimental data points.

In order to determine the  $Q_C$  value where  $P_{out}$  becomes maximal for a given  $P_{pump}$ , we calculate  $dP_{out}/dQ_C = 0$ , which gives

$$P_{pump} = F + \frac{BC}{Q_C^2} \cdot \frac{(Q_{int} + Q_C)^2}{CQ_{int}}. \quad (3.4)$$

Fig. 3.25 shows the resulting maximum output  $Q_C$  over  $P_{pump}$ . In the experimentally investigated range of 2 to 5 mJ · cm<sup>-2</sup> per pulse, maximum  $P_{out}$  is achieved for  $Q_C$  values in the

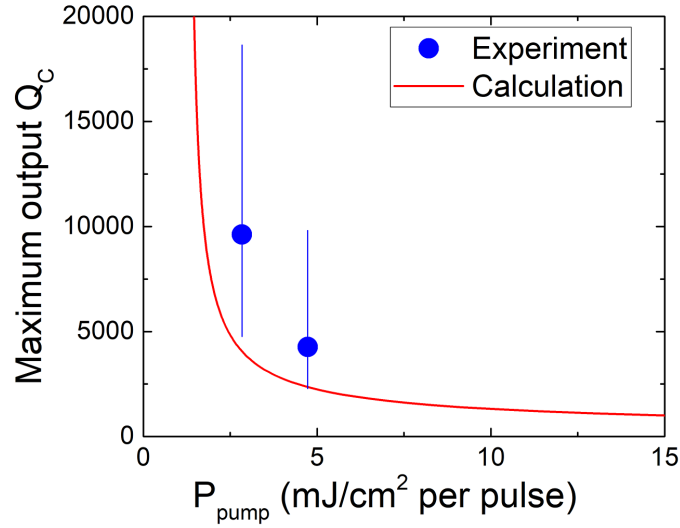


Figure 3.25: Maximum output  $Q_C$  as a function of  $P_{pump}$ , according to Eq. 3.4 and with the experimental values from Fig. 3.24 with error bars.

range of 7000 to 2000. The experimental values are taken from Fig. 3.24. There are many parameters that go into the theoretical curve in Fig. 3.25, such as the fit of  $P_{th}$  over  $Q_{load}$  (Fig. 3.23 (d)), the theoretical curve of  $P_{out}$  over  $Q_C$  (Fig. 3.24), and  $Q_{int}$ , all of which have an uncertainty. The here shown theoretical curve is only intended to show a tendency based on the different parameters extracted from Figs. 3.23 and 3.24 and modeling. The maximum energy transfer under lasing conditions does not occur for the same  $Q_C$  and gap as critical coupling ( $Q_C = Q_{int} = 4700$ ) in the spontaneous emission regime, but at slightly smaller values in the investigated range of  $P_{pump}$  (i.e.  $Q_C = 4300$  for  $P_{pump} = 4.73 \text{ mJ} \cdot \text{cm}^{-2}$  per pulse), and the  $P_{pump}$  dependence allows for fine-tuning of the coupling efficiency for a given  $Q_C$  and gap size.

### 3.4.5 Proximity effect

As the coupling distances are in the tens of nm range for blue emitters, the proximity between waveguide and microresonator is an issue for monolithic integrated circuits as opposed to systems like a microsphere coupled to an external tapered fiber. We have thus investigated the impact of this proximity on the spectral mode resonance for sample D677. Fig. 3.26 (a) shows the 421 nm mode of devices with  $\theta = 90^\circ$  for different gap sizes. With decreasing gap size, the mode position red-shifts and subsequently blue-shifts, which is plotted in Fig. 3.26 (b). The red-shift is expected because of the change in the effective index seen by the WGM as the coupling distance decreases. A 0.5 nm red-shift is observed going from a 120 to a 55 nm gap. A small red-shift is also observed in FDTD simulations. For small gaps between 55 and 30 nm, a 0.8 nm blue-shift per 10 nm decrease in gap size is observed. This blue-shift is caused by a reduction in disk diameter during the fabrication process due to the proximity of the waveguide [188]. The FDTD simulations in Fig. 3.27 show that a 10 nm decrease in diameter for a 5  $\mu\text{m}$  disk

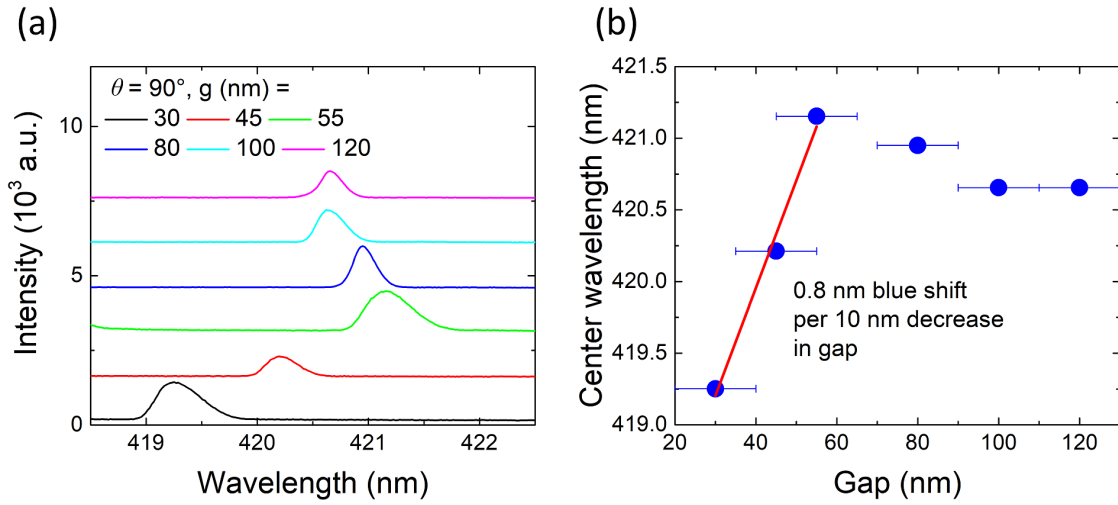


Figure 3.26: (a) Pulsed lasing spectra measured at the disk for devices with  $\theta = 90^\circ$  and different gap sizes fabricated on sample D677. (b) Peak wavelength as a function of gap for the spectra in (a).

(0.2%) causes a 0.8 nm blue-shift. The inset shows the corresponding transmission simulations for a mode at 441 nm. This phenomenon is observed experimentally due to the proximity effect of the waveguide with decreasing gap during the fabrication process. The reduction in disk diameter is thus roughly directly proportional to the decrease in gap size and in agreement with the experimental observation.

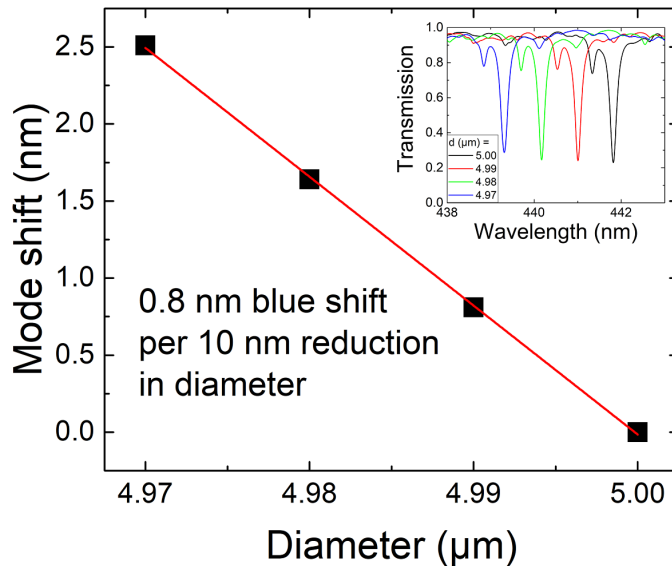


Figure 3.27: Mode shift over diameter. The linear fit gives a 0.8 nm blue-shift per 10 nm reduction in diameter. The inset shows the FDTD transmission simulations of the 420 nm mode.

The effect of the bending angle on mode position is investigated in Fig. 3.28. Fig. 3.28 (a)

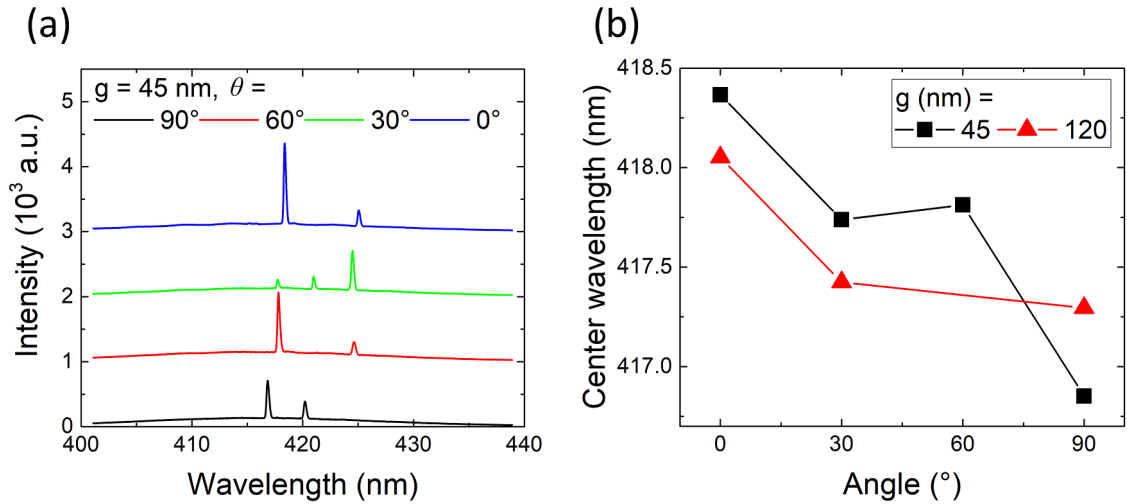


Figure 3.28: (a) Pulsed lasing spectra measured at the disk for devices with  $g = 45$  nm for different angles, fabricated on sample D677. (b) Peak wavelength as a function of angle for  $g = 45$  nm and  $g = 120$  nm.

shows spectra for devices with  $g = 45$  nm and angles from  $\theta = 0^\circ$  to  $90^\circ$ . Fig. 3.28 (b) shows the peak wavelength vs.  $\theta$  for  $g = 45$  and  $120$  nm. For small angles, a constant 0.3 nm blue-shift is observed when going from  $g = 45$  to  $120$  nm due to the change in effective refractive index. For small angles, the diameter reduction due to waveguide proximity is negligible. At  $\theta = 90^\circ$ , a 0.4 nm red-shift is observed when going from  $g = 45$  to  $120$  nm due to the increase in disk diameter of approximately 5 nm, given by Fig. 3.26. With increasing angle a blue-shift is observed due to a reduction in disk diameter, which is more pronounced at a smaller gap size. The blue-shifts of 2 nm at  $g = 45$  nm and 1 nm at  $g = 120$  nm correspond to 20 nm and 10 nm reduction in disk diameter, respectively. The proximity effect is less pronounced for small angles due to a reduced coupling length.

These measurements highlight the strong sensitivity of the microresonator system on the coupling distances. A short distance, i.e. in the range of tens of nm, is mandatory for efficient coupling. Meanwhile, we reach a regime where the distances set new challenges for fabrication, as the gap needs to be open, and where the distances have an impact on the microresonator resonances through a loading effect. This effect needs to be taken into account for the design of integrated photonic circuits in the blue spectral range.

### 3.5 Conclusion and perspectives

The here presented results are an important step in demonstrating the viability of the III-nitride on silicon nanophotonic platform for real-world applications at short wavelength. More complex photonic circuits using active microlasers operating near critical coupling can be used for visible-light communication [199] and lab-on-chip applications [200]. An important step will

be to integrate electrical injection into this nanophotonic platform, which we will discuss in chapter 5. Going towards the UV spectral range, which we will do in chapter 4, can also be interesting, for example for germicidal irradiation, however, smaller gap sizes or larger waveguide bending angles will be necessary for critical coupling, which is more difficult to master experimentally. Using a bonding process, III-nitride thin films can also be transferred onto SiO<sub>2</sub>-on-Si substrates, which would eliminate the necessity of underetching, allowing for the fabrication of ring resonators, for example, which we will study in chapter 6.

## Summary of Chapter 3

In this chapter, we investigated monolithically integrated active III-nitride photonic circuits in the blue, consisting of a microdisk laser, a bus waveguide, and grating couplers. We discussed different monolithic integration approaches found in literature, as well as the state of the art of heterogeneous integration and of critical coupling in III-nitride photonic circuits. We elaborated on the design and fabrication process of III-nitride photonic circuits on silicon specific to two samples, which were grown by MBE and contain 10 InGaN QWs emitting around 420 nm. The first sample had microdisks coupled to waveguides with larger gaps for operation in the under-coupled regime, to demonstrate lasing in a photonic circuit in the blue. The second sample had smaller gaps to allow us to observe critical coupling in the spontaneous emission regime, and to investigate how the lasing threshold and out-coupled signal depend on  $Q_{load}$ .

We showed results obtained under CW and pulsed optical pumping conditions from these two samples. We discussed CW  $\mu$ -PL obtained from the first sample, demonstrating an active photonic circuit in the blue. Loaded Q factors greater than 2000 were observed at the out-coupling grating for devices with small gaps and large waveguide bending angles. We demonstrated the first blue microlaser integrated into a photonic circuit using III-nitrides on silicon. Pulsed lasing was observed for devices with large gaps and straight waveguides with a threshold of  $15 \text{ mJ} \cdot \text{cm}^{-2}$  per pulse ( $38 \text{ MW} \cdot \text{cm}^{-2}$  peak power). Using the second sample, we demonstrated critical coupling and lasing in an active III-nitride on silicon nanophotonic circuit, utilizing a microdisk and a bent bus waveguide in the blue spectral range. This study was meant to identify the salient features associated with critical coupling and lasing in the blue. Low threshold energies of  $1.7 \text{ mJ} \cdot \text{cm}^{-2}$  per pulse ( $425 \text{ kW} \cdot \text{cm}^{-2}$  peak power) at the critical coupling gap and  $1.2 \text{ mJ} \cdot \text{cm}^{-2}$  per pulse ( $300 \text{ kW} \cdot \text{cm}^{-2}$ ) in the under-coupled regime were observed. Large  $Q_{int}$  factors of 4700 were measured in the under-coupled regime, and a reduction in  $Q_{load}$  of a factor of 2 was observed at critical coupling for a gap of 45 nm. A strong dependence of  $P_{th}$  on  $Q_{load}$  was shown that perfectly matched the expectation.  $P_{out}$  was investigated as a function of  $Q_C$ , and we analyzed the dependence on  $P_{pump}$ , finding a good agreement between the experimental data and the analytical formula. A proximity effect of the waveguide on the disk was shown to cause a shift in mode position, emphasizing the impact of an optimized design and fabrication on the intrinsic properties of the microresonator.

## Chapter 4

# Integrated microlaser photonic circuits and 2D photonic crystal slabs in the ultraviolet

**I**N THIS CHAPTER, we investigate two photonic devices in the ultraviolet: monolithically integrated microlaser photonic circuits and 2D photonic crystal slab cavities. The here reported results have been published in Refs. [192] and [201]. This chapter covers:

- A review of ultraviolet photonic circuits in literature.
- A review of III-nitride photonic crystal slab cavities in literature.
- The design, fabrication, and pulsed optically pumped lasing of monolithically integrated photonic circuits in the ultraviolet in III-nitrides on silicon.
- Continuous-wave  $\mu$ -photoluminescence of 2D L3 and H2 photonic crystal slab cavities in the ultraviolet.

### 4.1 Introduction and state of the art

In recent years, there has been a significant interest in ultraviolet (UV) emitters, such as light emitting diodes (LEDs) and optically pumped lasers, for a variety of applications, including germicidal sterilization and gas sensing [75, 202]. UVC light can be used to destroy the DNA of bacteria and viruses in water or air, for example, a currently very relevant application. The material system of choice for active devices in the UV is III-nitride due to its band gap tunability from the UVC to the visible.

III-nitride microcavity photonics is a very active field of research [6]. Individual microlasers in the UV spectral range have been realized under pulsed optical pumping [49, 50, 136], as we have discussed in chapter 2, and electrical injection [44], which we will discuss in chapter 5.

### 4.1.1 UV photonic circuits

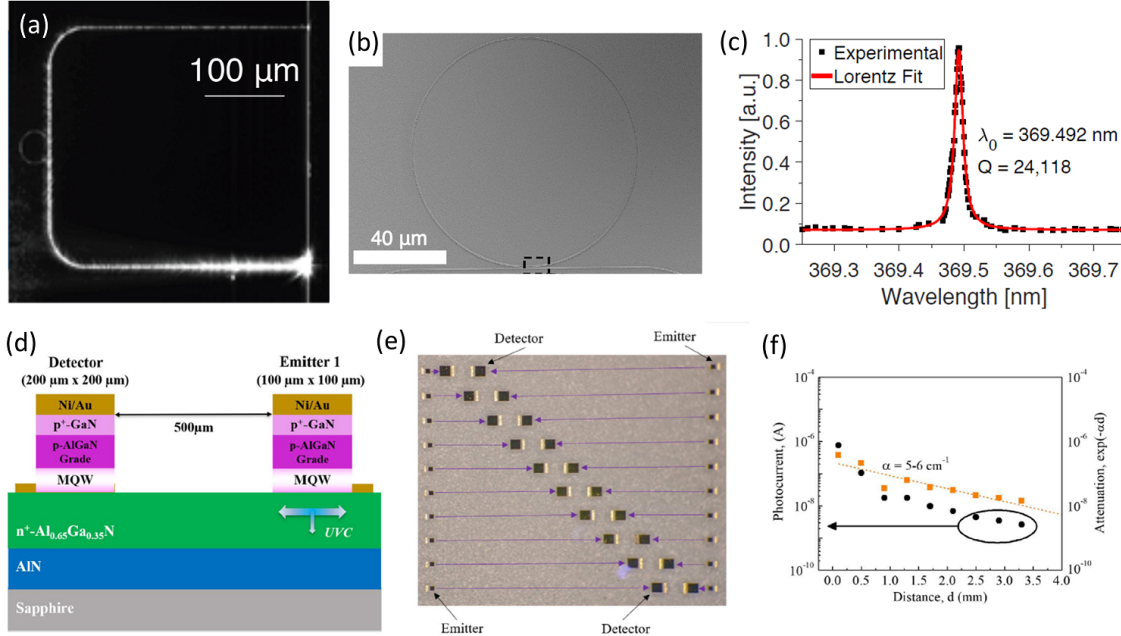


Figure 4.1: (a) Optical image, (b) SEM image, and (c) spectrum of a passive photonic circuit operating at 370 nm with  $Q = 24000$ , reproduced from Ref. [41]. (d) Device sketch, (e) optical microscope image, and (f) photo-current and attenuation over distance of an active photonic circuit operating in the UVC, reproduced from Ref. [182].

Photonic circuits in the UV have also recently gained popularity, with potential applications including atomic clocks or precision metrology [7]. Several passive circuits have been demonstrated using AlN [10, 41, 42, 203] or aluminum oxide ( $\text{Al}_2\text{O}_3$ ) [204]. Stegmaier et al. demonstrated a passive photonic circuit consisting of a waveguide and grating couplers operating down to 370 nm using polycrystalline AlN on  $\text{SiO}_2$  with losses of  $650 \text{ dB} \cdot \text{cm}^{-1}$  at 400 nm [10]. Lu et al. demonstrated passive photonic circuits with microrings using a crystalline sputtered AlN layer on sapphire and operating at 370 nm, as shown in Fig. 4.1 (a-c). They fabricated large microrings coupled to waveguides and obtained quality (Q) factors of 24k and a corresponding propagation loss of  $75 \text{ dB} \cdot \text{cm}^{-1}$  [41]. Liu et al. demonstrated passive microring photonic circuits using epitaxial AlN on sapphire, and demonstrated Q factors as large as 200k and losses of  $8 \text{ dB} \cdot \text{cm}^{-1}$  at 390 nm (see Fig. 1 (e-g) in the introduction) [42]. The main differences between the structures of Lu et al. and Liu et al. are the thickness and width of the microring, which are 200 nm and 250 nm for Lu et al. and 500 nm and 400-800 nm for Liu et al [41, 42]. The thicker and wider rings result in lower losses and consequently larger Q factors for Liu et al. Recently, West et al. demonstrated propagation losses as low as  $3 \text{ dB} \cdot \text{cm}^{-1}$  at 370 nm using  $\text{Al}_2\text{O}_3$  [204]. A simple active circuit using AlGaIn LEDs as emitters and detectors has also recently been demonstrated, and is shown in Figs. 4.1 (d-f) [181, 182]. They measured attenuation losses of  $22\text{-}26 \text{ dB} \cdot \text{cm}^{-1}$ .

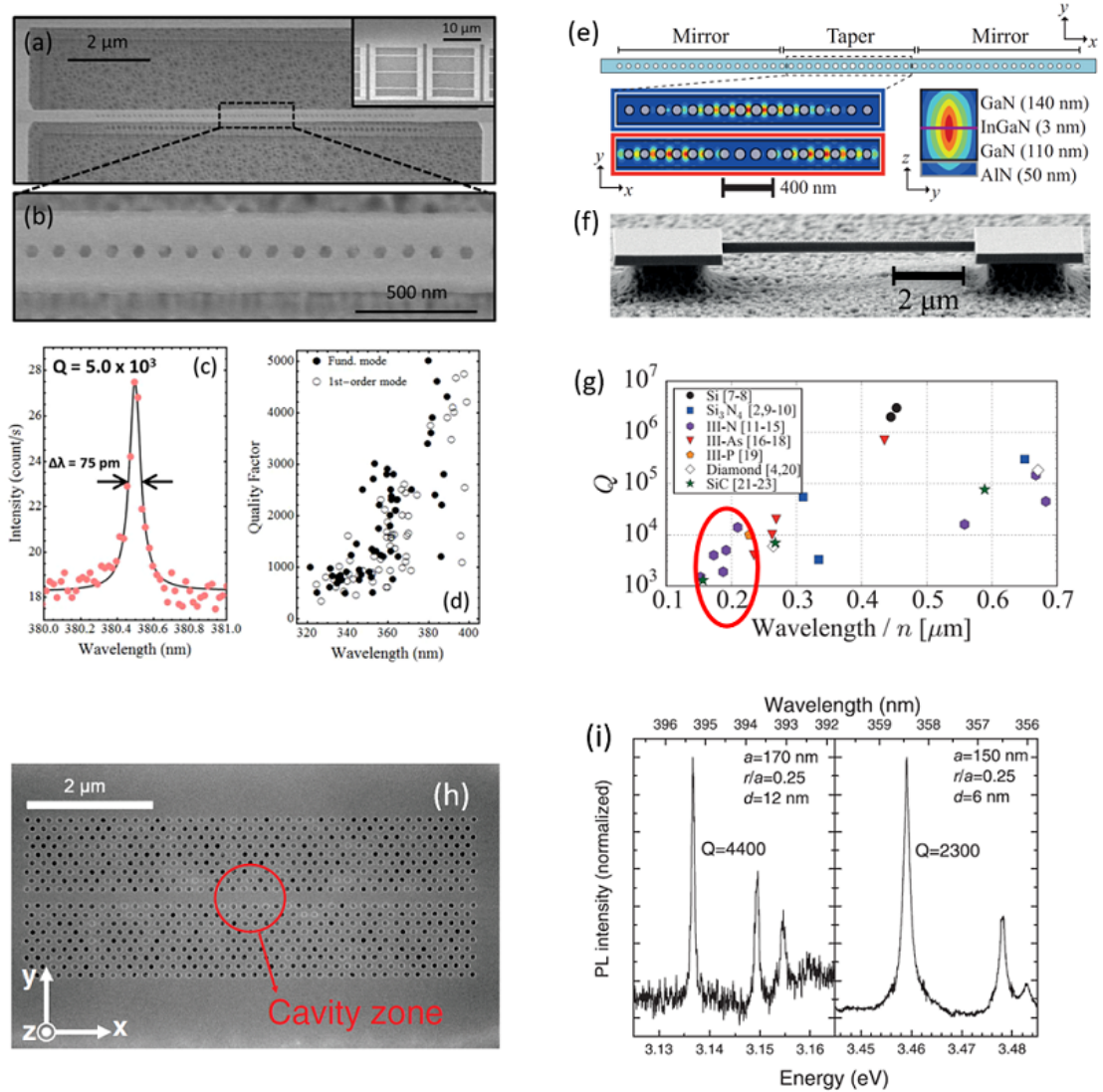


Figure 4.2: (a,b) SEM images of 1D nanobeam cavities, (c) PL spectra showing a Q factor of 5000 at 380 nm and (d) Q factor over wavelength in the blue-UV spectral range, reproduced from Ref. [205]. (e) Design and (f) SEM image of a 1D nanobeam cavity and (g) Q factor over wavelength/ $n$  for different cavities reported in literature, reproduced from Ref. [35]. (h) SEM image of a 2D width-modulated waveguide cavity and (i) PL spectra showing Q factors of 4400 at 395 nm and 2300 at 358 nm, reproduced from Ref. [47].

No demonstrations of active photonic circuits containing microlasers in the UV have been reported, while this would constitute an important step for the development of next generation photonic circuits.

### 4.1.2 III-nitride photonic crystal slab cavities

In the past decade, there have been numerous reports of 1D and 2D photonic crystal (PhC) slab cavities using III-nitrides on Si, SiC, or sapphire substrate for passive photonic circuits in the IR [51, 206, 207], non-linear frequency conversion [53, 54, 208] and active emitters and lasers in the blue-UV spectral range [34, 35, 37, 47, 205, 209–214]. Q factors up to 44000 have been reported in the IR around 1500 nm [208]. Going to shorter wavelength, the Q factor decreases drastically (see section 4.3). In the blue to UVA spectral range (420 to 380 nm), Q factors around 4000-5000 have been achieved using 1D and 2D PhC slab cavities [47, 205, 212–214]. Optically pumped lasing was reported in L3 and H2 cavities around 370 nm with Q factors up to 1700 [211]. When going to shorter wavelengths (< 350 nm), much lower Q factors (< 1000) were observed for PhCs [212]. Figs. 4.2 (a)-(g) show the results obtained by Sergent et al. and Rousseau et al. on 1D nanobeam cavities in the blue to UVA spectral range. Both observed Q factors around 5000 in the blue and reported a strong decrease in Q factor with decreasing wavelength (Figs. 4.2 (d) and (g)).

Before the beginning of this thesis, our collaboration worked on blue/UVA and near-infrared (NIR) PhC cavities with III-nitrides on Si, mainly using a width-modulated waveguide cavity (see Fig. 4.2 (h)). They demonstrated Q factors of 34000 at 1575 nm [51] and reported both second and third harmonic generation [53, 54]. They also demonstrated Q factors of 2300 at 358 nm and 4400 at 395 nm using GaN QDs in AlN suspended on Si, as shown in Figs. 4.2 (h) and (i) [47], indicating the same trend as reported in Refs. [212] and [35].

## 4.2 Microdisk laser photonic circuits

### 4.2.1 Design and fabrication

The investigated sample was grown by metal organic chemical vapor deposition (MOCVD) on silicon (111). First, a 220 nm AlN buffer layer was grown, followed by 300 nm of GaN. Then, the active region containing 5 pairs of 2 nm  $\text{In}_x\text{Ga}_{1-x}\text{N}$  / 9 nm GaN quantum wells (QWs) (nominal indium composition  $x = 0.1$ ) was grown, followed by a 20 nm GaN cap layer. The total thickness is around 600 nm. The heterostructure is illustrated in Fig. 4.3 (a).

With decreasing wavelength, the coupling efficiency decreases for the same device parameters. One can either further decrease the gap size or increase the coupling length to improve the coupling efficiency. In chapter 3, we have investigated photonic circuits in the blue spectral range with a waveguide with a bending angle  $\theta = 90^\circ$  around the disk. In this section, we chose  $\theta = 180^\circ$  to double the coupling length, since we are not able to further decrease the gap size due to fabrication constraints. Fig. 4.3 (b) shows finite-difference time-domain (FDTD) transmission simulations for devices with a 3  $\mu\text{m}$  diameter, a  $180^\circ$  angle, a 125 nm wide waveguide, and gaps between 40 and 80 nm. The simulations were performed with a resolution of 8 pixels

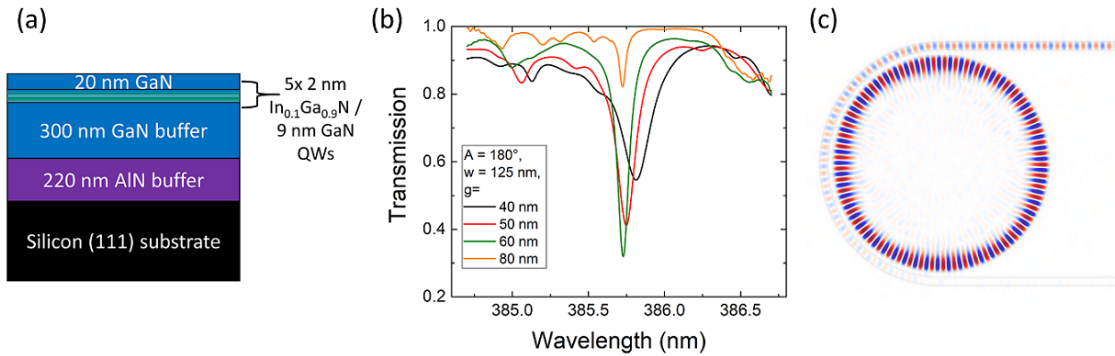


Figure 4.3: (a) Heterostructure of sample C1159D. (b) FDTD transmission simulations for a  $180^\circ$  angle, 125 nm waveguide and 40 to 80 nm gap. (c)  $H_z$  field of the first-order radial mode in (b) with azimuthal order  $m = 57$  and 60 nm gap.

per wavelength in the material or 20 nm per pixel. While the resolution is not very high, these simulations allow us to get an idea of optimal coupling conditions. The lowest transmission dip is observed for a 60 nm gap, indicating near-critical coupling. The transmission dip only goes to around 30%, which is likely related to the insufficient resolution or the difference in height between disk and waveguide (see also the discussion related to Fig. 3.4). Fig. 4.3 (c) shows the  $H_z$  field of the first-order radial mode with azimuthal order  $m = 57$  for the device with 60 nm gap from Fig. 4.3 (b). The Gaussian source is placed in the bottom right end of the waveguide.

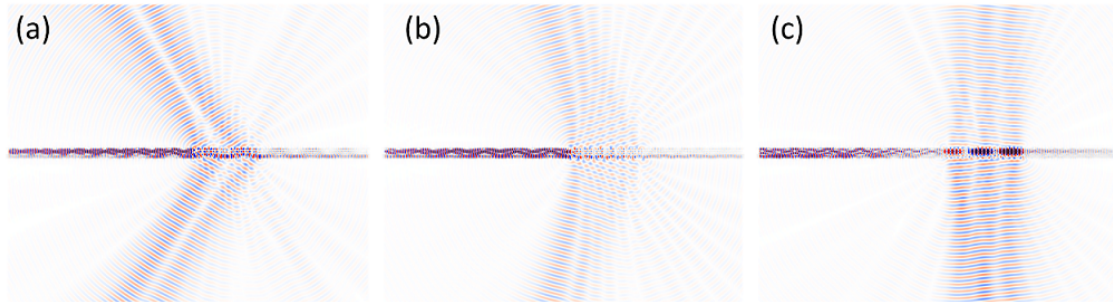


Figure 4.4: 2D FDTD simulations of the  $xz$ -cross-section of the  $E_y$  field of fully etched gratings with a fill-factor of 60% (80% for the first period) and periods of (a) 180 nm, (b) 200 nm, and (c) 220 nm at  $\lambda = 380$  nm.

Fig. 4.4 shows 2D FDTD simulations of the  $xz$ -cross-section of the  $E_y$  field of fully etched gratings with a fill-factor of 60%, and with periods between 180 and 220 nm. The first period has a fill-factor of 80% to reduce reflection. The Gaussian source is placed at the left side of the waveguide and emits at 380 nm with a width of 10 nm. We can see that for both 200 and 220 nm periods (Figs. 4.4 (b) and (c)), the emission is fairly vertical. Since we are using a microscope objective to collect the emission, we are not very sensitive to the angle and do not see any measurable difference between 200 and 220 nm grating periods.

We fabricated microdisk photonic circuits using the 2-level process described in section 1.3.5.1. We used proximity effect correction at the gap, as discussed in Fig. 1.32 and a higher

e-beam dose for the grating coupler. After the first ICP etch, we performed a chemical treatment with AZ400K developer at 40°C to smooth the side-walls. We fabricated devices with 3 μm diameter disks and waveguides with an angle of 180° around the disk, with nominally 125 nm width in the proximity of the disk, and 500 nm width away from the disk. The distance from the center of the microdisk to the end of the straight waveguide is 50 μm. The grating couplers have a period of 200 nm. The gap between the disk and the waveguide is varied between 40 and 100 nm. These devices are particularly challenging to fabricate due to the fairly long suspension length of the waveguide with the 180° bend. For larger microdisks, we observe cracking of the nanotethers that hold the waveguide, which then falls. For suspension lengths smaller than 12 μm, the devices are stable. Thus, our devices are at the fabrication limit of suspended photonic circuits in this platform. The reason for using a 180° waveguide bend is the increase in coupling length that allows to have efficient coupling at larger gaps. Using FDTD simulations, we estimate that the critical coupling gap is 20 nm larger than for a 90° angle (60 nm instead of 40 nm), corresponding to the maximum coupling.

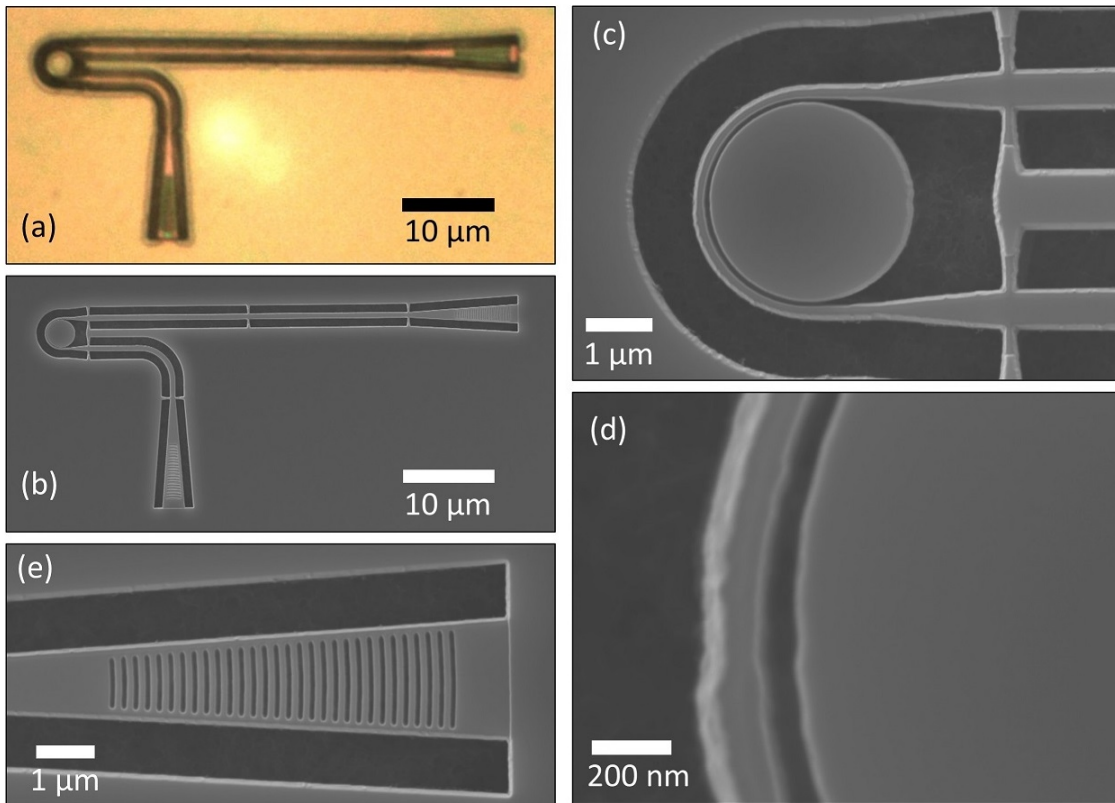


Figure 4.5: (a) Optical microscope image and (b) SEM image of a photonic circuit. Zoom-ins of (c) the microdisk, (d) the coupling region, and (e) the grating coupler.

Fig. 4.5 (a) shows an optical microscope image of a fabricated device, clearly showing the underetched areas as well as the waveguide etch through color-contrast. Fig. 4.5 (b) shows a scanning electron microscope (SEM) image of a device, also indicating the underetch and

clearly showing the nanotethers that hold the waveguide. Zoom-ins of the microdisk, the gap, and the grating coupler are shown in Figs. 4.5 (c)-(e). In Fig. 4.5 (d), we can see the roughness of our very thin waveguides (nominally  $w = 125$  nm), which is visible due to the large zoom.

## 4.2.2 Results and discussion

We use the  $\mu$ -photoluminescence ( $\mu$ -PL) setup in Montpellier, discussed in section 1.4 and Fig. 1.45 with a continuous-wave (CW) laser emitting at 355 nm and a 20x microscope objective. A map of the CCD allows to differentiate between the emission from the disk and from the grating by integrating over different areas (see Fig. 4.9). We pump the microdisks at RT, in order to determine the loaded Q factors of our devices. The bottom part of Fig. 4.6 shows a CW spectrum of a device with 100 nm gap measured from the top at the out-coupling grating. Many modes are visible and their identification is difficult. We observe first-order modes with an FSR of 4 nm at 407.7 nm, 411.8 nm, and 415.4 nm with  $Q_{load}$  in the range of 1400 to 1800, which are limited by QW absorption. The maximum  $Q_{load}$  for the 100 nm gap is 3500 at 419.7 nm (potentially the next first-order mode), which is shown in the inset in Fig. 4.6. We note that under low power density CW excitation the QW emission is centered at around 407 nm. The modes are not, or barely, visible above the microdisk under CW excitation in our top-collection setup, as whispering-gallery modes (WGMs) radiate preferentially in-plane. Based on the  $Q_{load}$  of the 100 nm gap device, we assume that the intrinsic Q factor,  $Q_{int}$ , is 3500, which is in the same order of magnitude as for our previously investigated microdisks [46, 50, 145] (see chapters 2 and 3). The  $Q_{load}$  at 380 nm will certainly be lower due to the GaN absorption.  $Q_{int}$  might be limited by side-wall roughness or surface absorption [36]. We do not perform any surface passivation, such as deposition of an  $\text{SiO}_2$  cladding, which would improve the Q factor, but would be difficult to implement due to the suspension and the small gaps that can create air pockets.

We can estimate the effective propagation losses of the microdisk using [215]

$$\alpha_{disk} = \frac{\lambda_0}{Q_{int} \cdot FSR \cdot r}, \quad (4.1)$$

with  $\lambda_0$  the resonance wavelength,  $FSR$  the free spectral range, and  $r$  the radius of the disk. We obtain  $\alpha = 0.08 \text{ dB} \cdot \mu\text{m}^{-1}$  when extrapolating at  $\lambda_0 = 380$  nm,  $FSR = 4$  nm,  $Q_{int} = 3500$ , and  $r = 1.5 \mu\text{m}$ , which is two orders of magnitude larger than reported by Liu et al. for AlN microrings at 390 nm [42] and in the same order of magnitude as reported by Stegmaier et al. for polycrystalline AlN waveguides at 400 nm [10] (see section 4.1.1). When comparing with Ref. [42], we need to take into account several factors. Firstly, the different waveguiding material, GaN vs. AlN: GaN will have higher losses due to larger material absorption at 380 nm, an absorption of  $100 \text{ cm}^{-1}$  would result in a  $Q_{abs}$  of 4200. Secondly, the much higher radiation loss due to strong bending of a small microdisk ( $r = 1.5 \mu\text{m}$ ) as compared to a large microring ( $r = 30 \mu\text{m}$ ) [216]. Thirdly, the different refractive index contrasts between waveguide and cladding (air vs.  $\text{SiO}_2/\text{Al}_2\text{O}_3$ ): a smaller index contrast results in significantly lower scattering loss due to rough-

ness. Lastly, the growth substrate, Si vs sapphire: a smaller dislocation density, which can be more easily achieved on sapphire, can induce lower internal losses. Furthermore, we employ much smaller gaps between the resonator and the waveguide than Liu et al., which renders our process more complex, but leads to better cavity to waveguide coupling.

In analogy to Ref. [42], we calculate  $H_{z,s}^2 / (\int H_z^2 dx dz)$ , where  $H_{z,s}$  is the maximum field at the side-wall of the disk, and the integral is taken over the  $xz$ -cross-section, where  $z$  is the out-of-plane direction, as shown in Fig. 4.7 using FDTD. For our microdisk, we obtain  $2.3 \mu\text{m}^{-2}$ , which is an order of magnitude larger than the value obtained by Liu et al. for wide microrings [42]. The higher field at the interface can be explained by the larger curvature of a small disk compared to a large ring and results in larger side-wall losses, explaining in part the lower Q factor we observe.

The root mean square (rms) surface roughness of our sample after growth is 1 nm, as determined from a  $10 \times 10 \mu\text{m}^2$  atomic force microscopy (AFM) image. This small roughness, which is a quite normal value for epitaxial III-nitrides, allows to minimize light scattering on the surface [217]. The ICP etching of the QWs can cause the surface roughness of the waveguide to increase further.

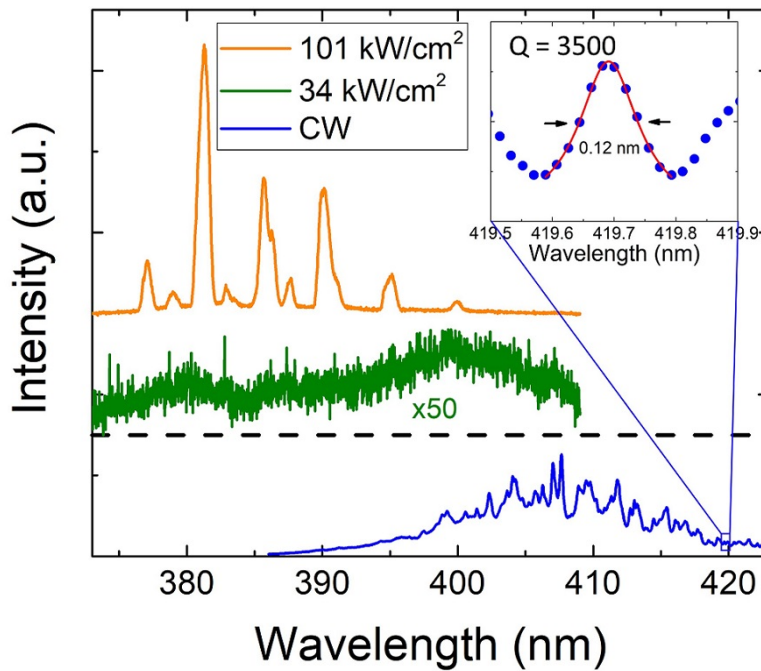


Figure 4.6: Spectra below and above threshold taken at the out-coupling grating for devices on C1159D with 100 nm gap. Bottom: Low-excitation power density CW spectrum below threshold. The inset shows the maximum Q factor of 3500 at the low energy side of the spectrum at 419.7 nm. Top: Pulsed spectra below and above threshold. The spectra are displaced along the y-axis and the CW spectrum has a different y-scale.

Lasing is observed at RT under pulsed optical conditions using a laser at 355 nm with 7

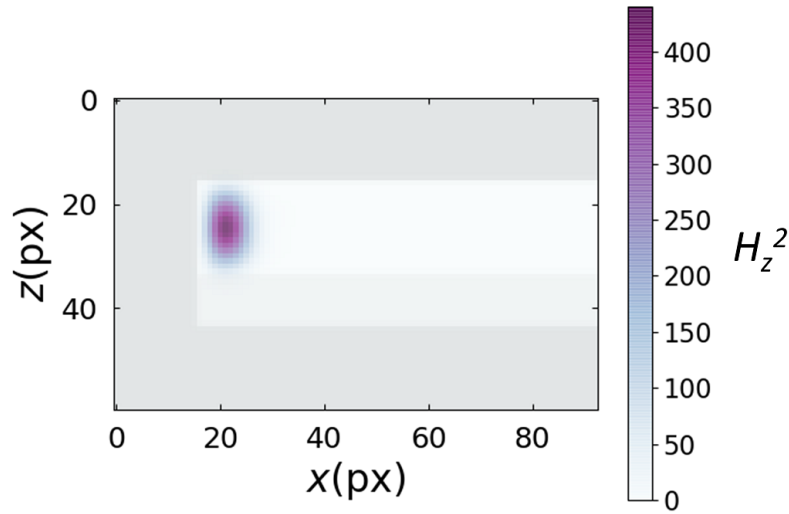


Figure 4.7: FDTD simulation of the  $xz$ -cross-section of a  $3\mu\text{m}$  diameter disk, showing half the disk and the  $H_z^2$  of a first-order radial mode at  $387\text{ nm}$ .

kHz repetition rate and  $4\text{ ns}$  pulse width. Fig. 4.6 shows pulsed spectra at peak powers of  $34\text{ kW}\cdot\text{cm}^{-2}$  ( $0.9E_{th}$ ) and  $101\text{ kW}\cdot\text{cm}^{-2}$  ( $2.7E_{th}$ ) measured at the out-coupling grating for a device with  $100\text{ nm}$  gap. A strong blue-shift of around  $25\text{ nm}$  is observed with increasing excitation power, as we go from CW to pulsed excitation far above threshold. The blue-shift can be explained both by quantum confined Stark effect screening at large carrier density and by state-filling of localized states of the InGaN QWs. A smaller blue-shift was observed in our previous samples, as they were grown by molecular beam epitaxy (MBE) where less localization is observed [145]. Furthermore, it is very likely that excited states in the QWs are lasing. Considering the e1 (electron ground state) to hh1 (heavy hole ground state) transition at  $3.05\text{ eV}$  or  $407\text{ nm}$ , the center emission wavelength under low excitation CW pumping, an indium composition of  $13.5\%$  in the QWs is deduced from 6 band  $\mathbf{k}\cdot\mathbf{p}$  simulations (using Nextnano [143]), without considering carrier interactions. The band diagram with electron and hole wave functions is shown in Fig. 4.8. The e1-hh1 transition has an oscillator strength of  $0.34$ . The QWs are very asymmetric, which makes the cross-transitions (e2-hh1 and e1-hh2, where 2 denotes the first excited state) very intense. The oscillator strength of the e2-hh1 transition at  $3.31\text{ eV}$  or  $375\text{ nm}$  is  $0.23$ . For the e1-hh2 transition at  $3.13\text{ eV}$  or  $396\text{ nm}$ , we get an oscillator strength of  $0.12$ . The emission thus encompasses the entire lasing spectral range of our devices.

The lasing modes are rather broad. The mode at  $381.2\text{ nm}$  at  $2.7E_{th}$  has a full-width at half maximum (FWHM) of  $1\text{ nm}$ . Generally, under pulsed pumping, linewidths are broader than under CW pumping, since the carrier density changes strongly in the microlaser during one pulse (here  $4\text{ ns}$ ). We do not observe linewidth narrowing near the threshold, since the modes are not visible below threshold due to the limited signal to noise ratio under these low duty-cycle conditions.

Fig. 4.9 shows 2D CCD maps of the  $50\text{ nm}$  gap device at different pump energies. The y-axis

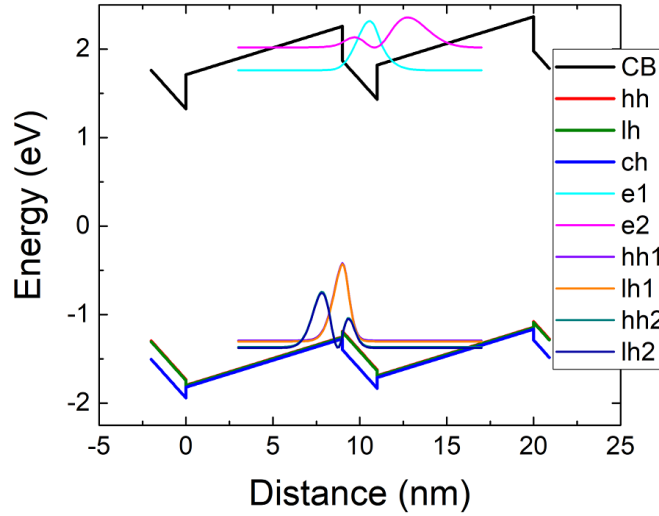


Figure 4.8: Band diagram and electron and hole wave functions of the QWs of sample C1159D, with e1-hh1 transition at 3.05 eV or 407 nm, and with an indium composition of 13.5% in the QWs.

is the distance in pixels along the straight waveguide, where 1 pixel is around  $0.4\mu\text{m}$ . An SEM image of a device is shown next to the map to illustrate the position on the sample. The x-axis shows the wavelength. The microdisk emission is indicated with dashed lines and the grating with dotted lines. Fig. 4.9 (a) is measured at  $0.6E_{th}$  and we can see the spontaneous emission at the disk and at the grating. At  $1.1E_{th}$  (Fig. 4.9 (b)), we can see a first mode lasing at 382 nm. With higher pump energy, more modes start to lase in Figs. 4.9 (c) and (d). We integrated the emission spatially over the white dashed rectangles in the CCD maps to obtain the spectra presented in Fig. 4.10.

Figs. 4.10 (a) and (c) show pulse energy dependent spectra measured above the microdisk for devices with 50 nm and 90 nm gaps, respectively. Spectra measured on the same devices, but at the out-coupling grating, are depicted in Figs. 4.10 (b) and (d). Lasing modes are observed from 374 nm to 399 nm. The lowest threshold energy of  $0.14\text{mJ}\cdot\text{cm}^{-2}$  per pulse or threshold peak power of  $35\text{kW}\cdot\text{cm}^{-2}$  is observed for the 80 nm gap (not shown). The calculated overlap of the vertical  $\text{TE}_0$  mode with the QWs (excluding the barriers) is 1.0%. This value could be increased by using cladding layers, but those would result in a much thicker structure that makes suspended photonic circuits more difficult to fabricate.

The first-order radial WGMs are visible for both 50 nm and 90 nm gaps (Fig. 4.10) with a spacing of 3.6 to 4.6 nm and azimuthal mode orders of  $m = 60$  at 374 nm to  $m = 54$  at 399 nm, as determined by FDTD simulations. Initially, one and then several first-order modes lase, followed by other modes of higher order, which are especially visible at high energy for the larger gaps (Figs. 4.6 and 4.10 (c,d)). We observe a very large dynamic of the peak to background emission of around 200 at  $3E_{th}$  for the 50 nm gap device at the grating coupler, with only a factor 10 observed directly at the disk. The improvement of this dynamic with increased coupling is

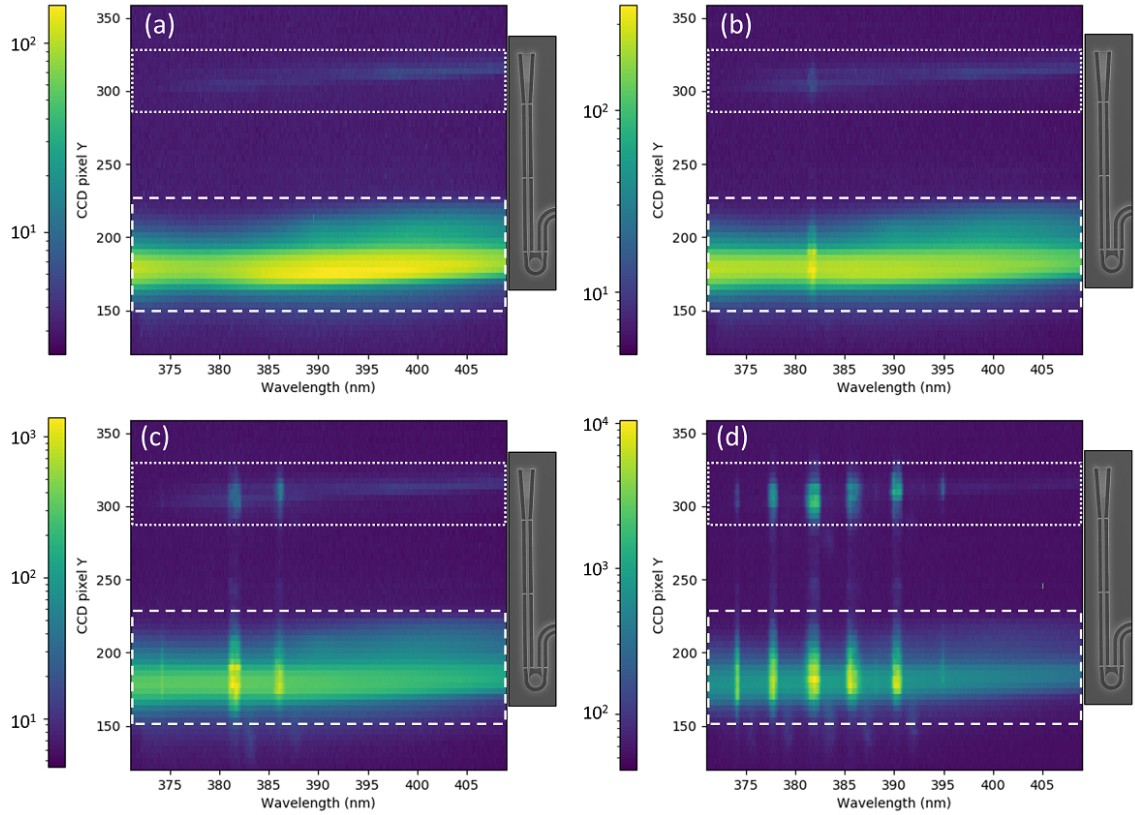


Figure 4.9: 2D CCD maps of the device with 50 nm gap at (a)  $0.6E_{th}$ , (b)  $1.1E_{th}$ , (c)  $1.5E_{th}$ , and (d)  $3E_{th}$ . The dashed lines indicate the emission from the disk and the dotted lines indicated the emission from the grating. The intensity scale is logarithmic. An SEM image is shown next to the CCD maps to indicate the position on the sample.

due to the fact that the WGMs radiate preferentially in-plane, while the spontaneous QW emission radiates mainly out-of-plane. In FDTD transmission simulations, we obtain a maximum coupling of 70% for a gap of 60 nm (see Fig. 4.3).

The here reported threshold peak powers for pulsed III-nitride microdisk lasers are lower than what we have found in literature. Simeonov et al. reported  $166\text{kW}\cdot\text{cm}^{-2}$  at 409 nm [135] and Zhu et al.  $180\text{kW}\cdot\text{cm}^{-2}$  at 380 nm [136]. We reported lasing thresholds of  $300\text{kW}\cdot\text{cm}^{-2}$  for microdisk photonic circuits operating at 420 nm in chapter 3 and Ref. [145]. In chapter 2, we discussed thresholds as low as  $18\text{kW}\cdot\text{cm}^{-2}$  for sample C1081 at 420 nm. The threshold reduction of one order of magnitude for our samples is primarily due to a change in growth method from MBE to MOCVD for our QWs. MBE grown QWs have a higher non-radiative recombination rate due to a higher concentration of point defects caused by the lower growth temperature [140], as we have discussed in section 2.3.9. The 2 times higher threshold of C1159D, as compared to C1081, can be explained mainly by the shorter wavelength and resulting shorter carrier lifetime [218]. We can compare our thresholds to pulsed electrically injected lasing reported by Wang et al. with a threshold current density of  $250\text{kA}\cdot\text{cm}^{-2}$  (or at least  $800\text{kW}\cdot\text{cm}^{-2}$  assuming

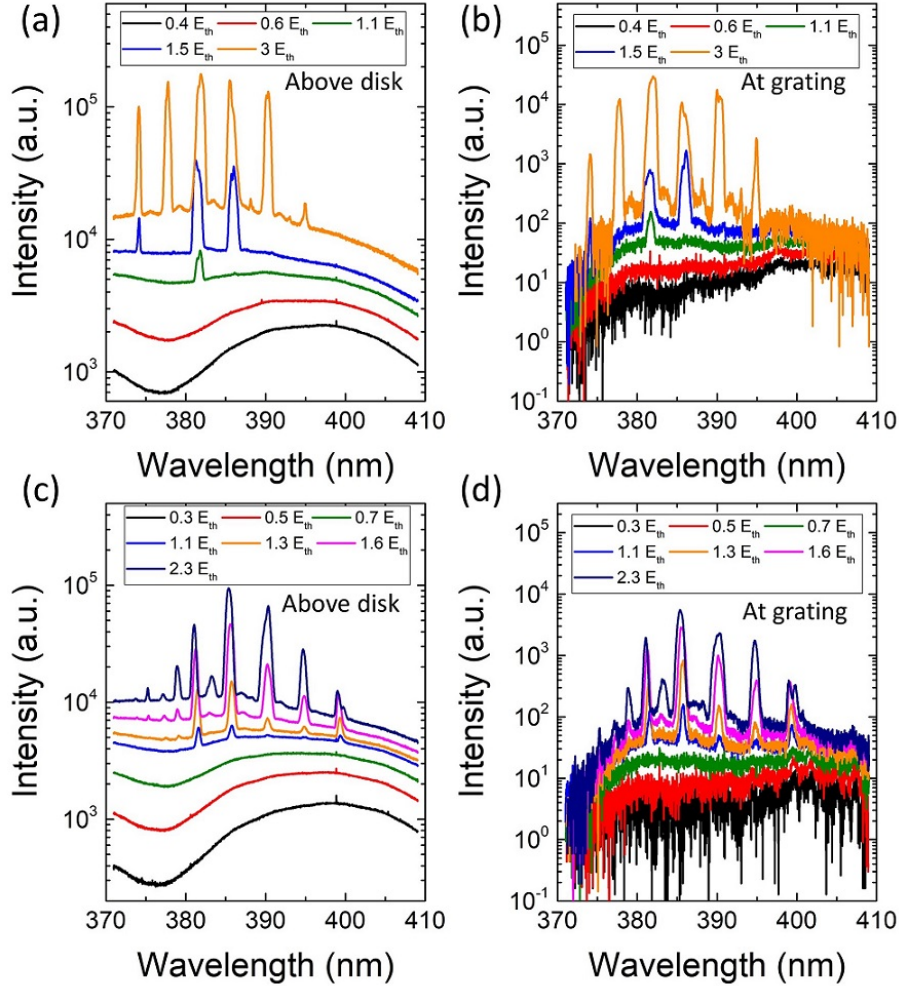


Figure 4.10: Energy dependent pulsed optically pumped spectra of devices on C1159D measured (a,c) above the disk and (c,d) at the grating coupler, for devices with (a,b) a 50 nm gap and (c,d) an 90 nm gap. The thresholds are  $0.18 \text{ mJ} \cdot \text{cm}^{-2}$  per pulse for the 50 nm gap and  $0.15 \text{ mJ} \cdot \text{cm}^{-2}$  per pulse for the 90 nm gap.

operation at least 3.2 V) at 386 nm [44] for a  $6.5 \mu\text{m}$  thick heterostructure.

It is important to take into account that we are very close to the band gap of GaN (365 nm) in this spectral range (374 - 399 nm). Our waveguides consist to 58% of GaN and to 42% of AlN with 99% of the  $\text{TE}_0$  and 94% of the  $\text{TE}_1$  modes confined in the GaN layer. Consequently, there is a non-zero absorption loss that needs to be considered. The precise value of below band gap GaN absorption varies from one growth reactor to another but could be in the range of  $1000 \text{ cm}^{-1}$  at 380 nm [219]. We are thus at the absolute wavelength limit of what can be achieved with a GaN waveguide. In order to descend further in wavelength, we would need to use a waveguide consisting only or mostly of AlN to reduce the absorption loss. Furthermore, using  $\text{Al}_x\text{Ga}_{1-x}\text{N}/\text{Al}_y\text{Ga}_{1-y}\text{N}$  ( $y > x$ ) instead of InGaN/GaN QWs would allow to reduce the emission wavelength into the UVB and UVC. Such photonic circuits are feasible, but remain

very difficult to implement, due to a need for even smaller gaps for efficient coupling, as well as difficulties in growing high quality material.

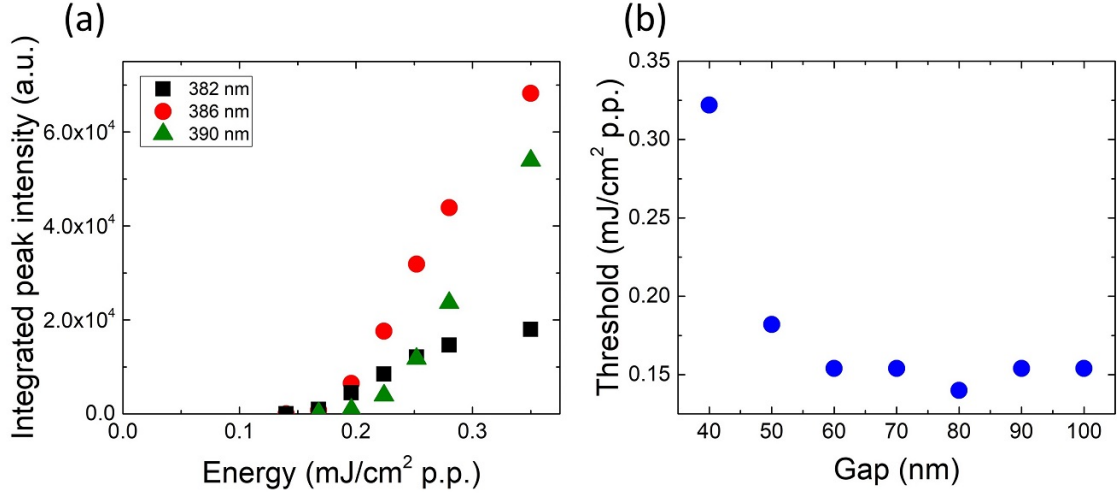


Figure 4.11: (a) Integrated peak intensity over pulse energy for the modes at 382, 386, and 390 nm for the device with 90 nm gap shown in Fig. 4.10 (c,d). (b) Threshold energy over nominal gap size.

In Fig. 4.11 (a), we show the integrated peak intensity over the energy per pulse for the modes at 382, 386, and 390 nm, for the device with 90 nm gap (Figs. 4.10 (c,d)). The lasing thresholds at  $E = 0.15$  and  $0.19 \text{ mJ} \cdot \text{cm}^{-2}$  per pulse are clearly visible. The threshold energy as a function of nominal gap size is shown in Fig. 4.11 (b). We can see that the threshold decreases with increasing gap, which is to be expected, since  $E_{th} \propto 1/Q_{load}$  and since  $Q_{load}$  decreases with increased coupling (see section 3.4.2 and Ref. [145]). For the 40 nm gap, the threshold is particularly high because the gap is not fully open, since these distances are at the limit of what can be achieved using e-beam lithography with UV5 resist.

### 4.3 2D photonic crystal slab cavities

For 2D PhC slabs, the sample needs to be quite thin, in the order of  $h \approx \frac{\lambda}{2n_{eff}}$ . We investigated sample A2083, which was grown by MBE on Si (111) substrate. It consists of a 50 nm AlN buffer layer and 5 pairs of 1.2 nm GaN / 5 nm AlN QWs emitting at a wavelength of 310 nm. The heterostructure is depicted in Fig. 4.12(a).

The cleanroom process described in section 1.3.7 is used to fabricate triangular lattice L3 and H2 PhC cavities. SEM images of typical L3 and H2 cavity suspended membranes are shown in Figs. 4.12 (b-e). We investigate L3 and H2 cavities with periods  $a = 130$  and  $120$  nm and nominal radius over period ratios  $r/a$  of 0.28 to 0.31. For the L3 cavities, we use  $d/a = 0.15$  to 0.25 for the hole displacement.

FDTD simulations show Q factors in the range of 1600 to 5000 for the L3 cavities. Larger Q

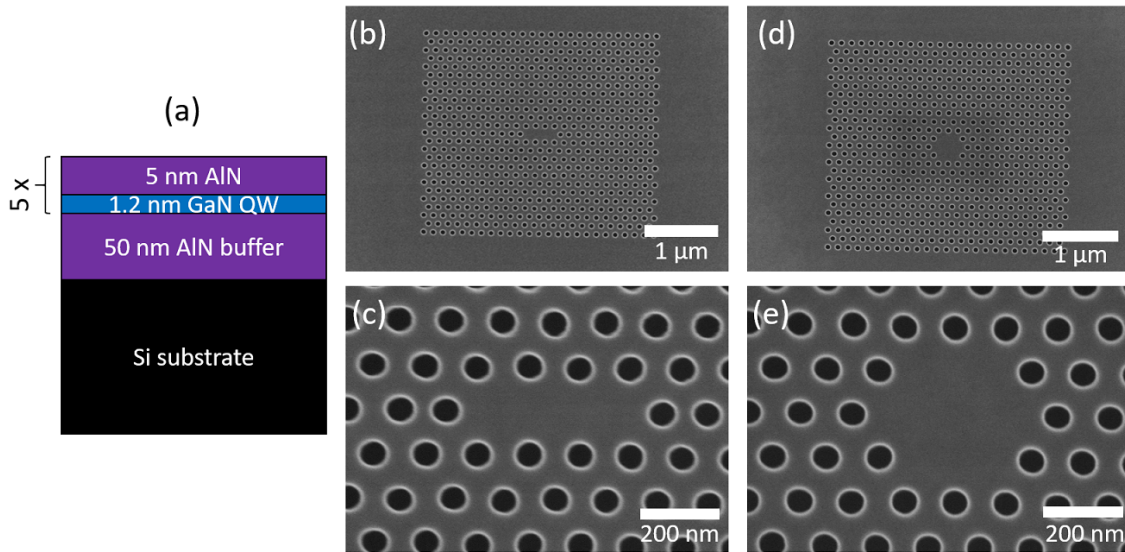


Figure 4.12: (a) Layer stack of sample A2083 grown on Si. (b,c) SEM images of a typical L3 cavity. The period  $a$  is 130 nm, the nominal  $r/a$  is 0.28, and the holes adjacent to the L3 cavity in the direction of the defect line are displaced by  $0.10a$ . (d,e) SEM images of an H2 cavity with  $a = 130$  nm, and  $r/a = 0.28$ .

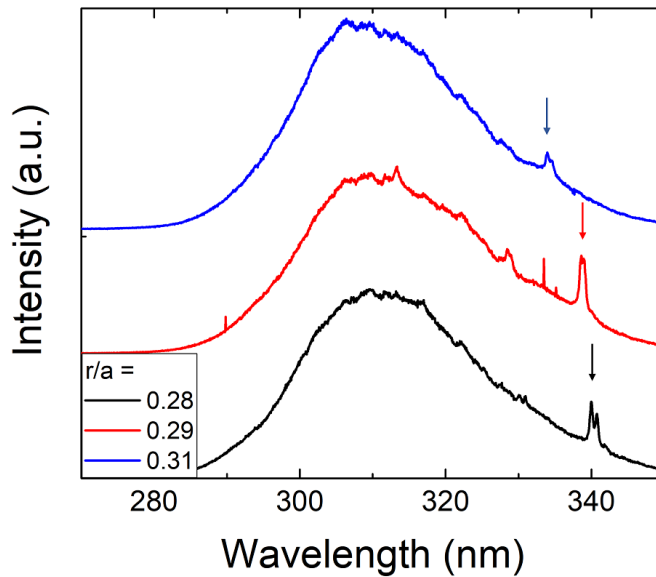


Figure 4.13:  $\mu$ -PL spectra of H2 cavities with  $a = 130$  nm for the different  $r/a$  moved along the y-axis for clarity. Arrows indicate fundamental modes with Q factors in the range of 600-700.

factors can be achieved for smaller  $r/a$ . Using  $d/a = 0.25$  and  $r/a = 0.22$  for these L3 cavities would result in a large theoretical Q factor of more than 10000, however, such cavities are much harder to fabricate due to the much decreased hole sizes. Some theoretical papers suggested hole optimization schemes for L-type cavities, reaching Q factors of  $1 - 2 \times 10^6$  [120, 220].

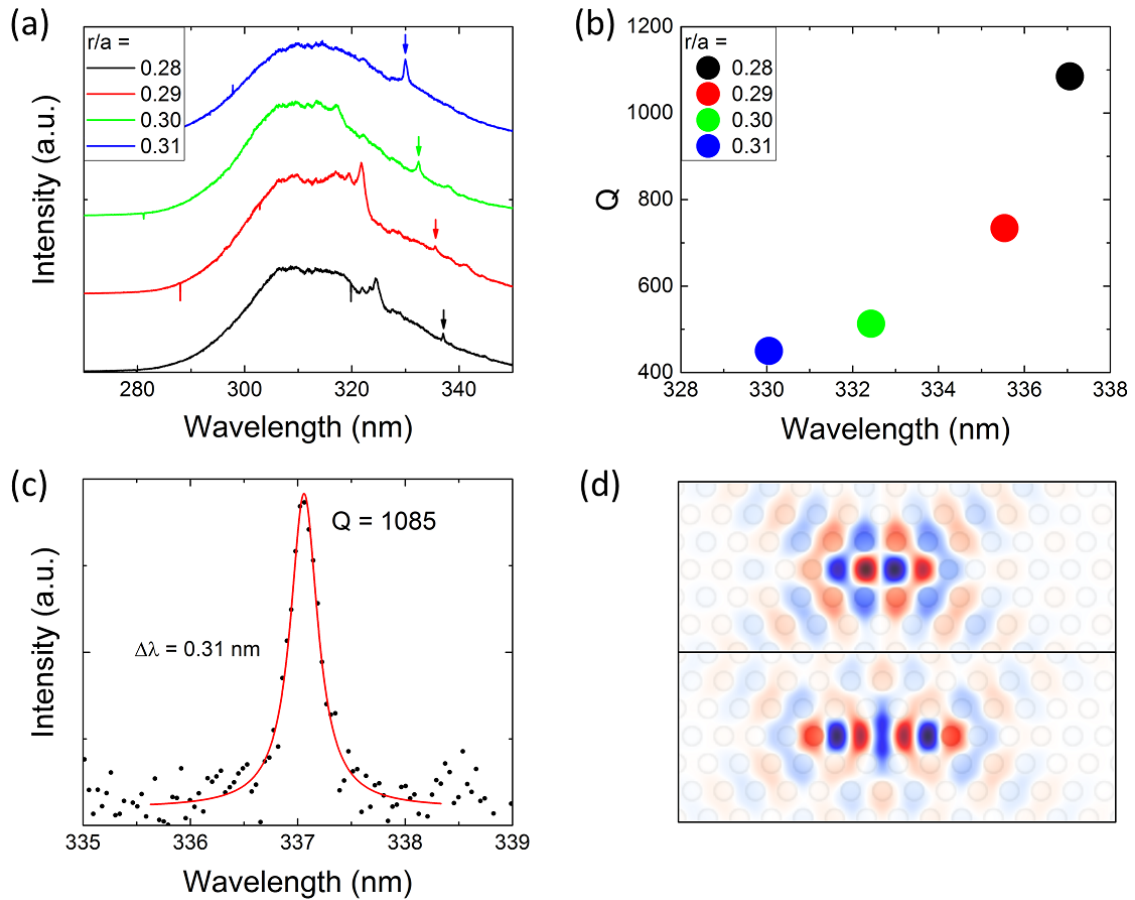


Figure 4.14: L3 cavities with period  $a = 130$  nm, hole displacement  $d/a = 0.15$ , and nominal radii  $r/a = 0.28$  to  $0.31$ . (a)  $\mu$ -PL spectra for the different  $r/a$  moved along the y-axis for clarity. Arrows indicate fundamental modes. (b) Q factors for the fundamental modes in (a). (c) measured spectrum (dots) and Lorentzian fit (line) of the fundamental mode of the L3 cavity with  $r/a = 0.28$  shown in (a). (d) FDTD simulations of the Hz field of (top) the fundamental mode and (bottom) the first-order mode of an L3 cavity depicted in (a) with  $r/a = 0.28$ .

The PhC cavities are investigated at RT using the  $\mu$ -PL setup in Grenoble described in Fig. 1.46 using a 244 nm CW laser.

Fig. 4.13 shows  $\mu$ -PL spectra of H2 cavities with  $a = 130$  nm for the different values  $r/a$ . The broad emission, centered around 310 nm, comes from the QWs. Fundamental modes with Q factors around 600-700 are visible around 330 to 340 nm. Fig. 4.14(a) shows  $\mu$ -PL spectra of L3 cavities with a period of 130 nm. The long wavelength resonances between 330 and 340 nm are the fundamental modes of the L3 cavity and the shorter wavelength peaks between 320 and 330 nm are the first-order modes. Shorter-wavelength modes cannot be seen because they are re-absorbed by the QWs. In Fig. 4.14(b), the Q factors of the fundamental modes shown in Fig. 4.14(a) are plotted as a function of the wavelength. With increasing  $r/a$ , a blue shift and decrease in Q factor are observed, which matches well with calculations, as well will show later.

The zoom-in of the spectrum and Lorentzian fit of the fundamental mode of the L3 cavity with  $r/a = 0.28$  from Fig. 4.14(a) is shown in Fig. 4.14(c). The FWHM is  $\Delta\lambda = 0.31$  nm and the Q factor is 1085 at  $\lambda = 337$  nm, which is the highest we obtained. FDTD simulations of the  $H_z$  field of the fundamental (top) and first-order (bottom) modes for  $r/a = 0.28$  are shown in Fig. 4.14 (d). An extensive classification of similar modes was reported by Chalcraft et al. [221].

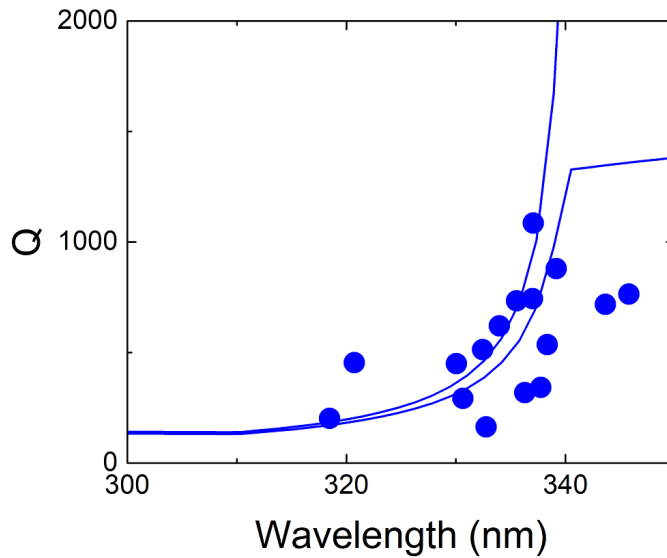


Figure 4.15: The dots are measured Q factors of fundamental modes of various L3 cavities with varying  $a$ ,  $r/a$ , and  $d/a$ . The lines take both the QW absorption and the residual absorption of AlN into account and are fitted using two different values of  $Q_{design}$ , i.e. 1600 and 5000.

Going to shorter wavelengths reduces the Q factor, as can be seen in Fig. 4.15 and is also observed by Sergent et al. [205] and Rousseau et al. [35] (see Fig. 4.2). So far, this phenomenon is rather unclear. Side-wall tapering, dispersion of holes, and surface and side-wall roughness, which cause increased scattering losses with decreasing wavelength, have been suggested as the underlying cause [35, 205]. Another factor that contributes to the reduction in Q factor is the residual absorption of AlN grown on Si. The absorption could be caused by point defects, such as Al vacancies (center energy at 3.6 eV) in the AlN-Si interface region, which are known to be absorption centers in bulk AlN [83, 222, 223]. To confirm this hypothesis, we investigated several samples with varying AlN thicknesses between 50 and 100 nm on Si (111) by spectroscopic ellipsometry (SE) [224]. In the model, we use a two-layer stack consisting of an optically unknown Cauchy film (AlN) on top of a silicon substrate, for which we use literature  $n$  and  $k$  values, which take the substrate absorption into account. Using the Cauchy formulas, we determine  $n$  and  $k$  for the AlN layers:

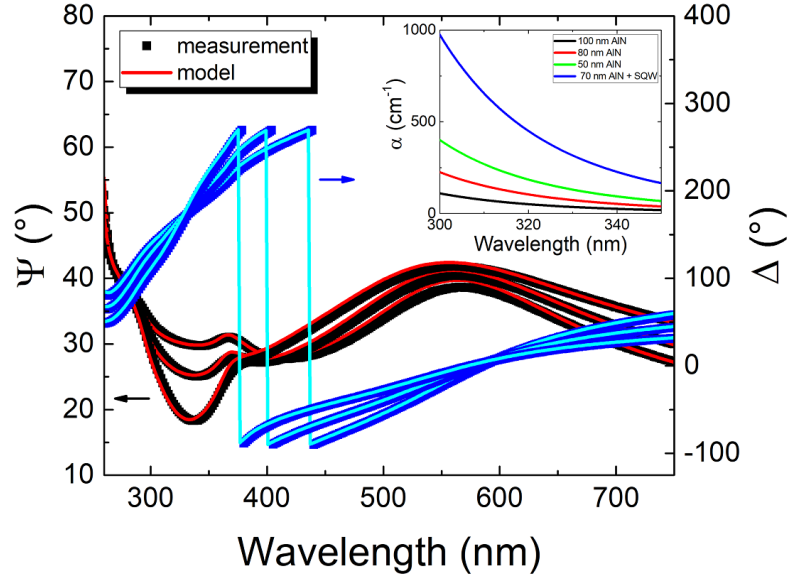


Figure 4.16: Spectroscopic ellipsometry measurement (squares) and model (lines) for angles of incidence of  $65^\circ$ ,  $70^\circ$  and  $75^\circ$  for a sample with 80 nm of AlN grown on Si (111). The inset shows the AlN absorption coefficient  $\alpha$  for samples with different AlN thicknesses.

$$n = A + \frac{B}{\lambda^2} + \frac{C}{\lambda^4}, \quad (4.2)$$

$$k = \alpha \exp \beta \left( 12400 \left( \frac{1}{\lambda} - \frac{1}{\gamma} \right) \right), \quad (4.3)$$

with  $A$ ,  $B$ ,  $C$ ,  $\alpha$ ,  $\beta$  being fit parameters [225]. The fits were performed by taking  $n$  from the Cauchy model of the sample with 50 nm AlN and determining  $k$  by fitting the ellipsometry data of each sample to the Cauchy model ( $n$  and  $\beta$  constant for all samples). Fig. 4.16 shows SE measurements (squares), highlighting the standard phase difference  $\Psi$  and the amplitude ratio  $\Delta$ , and a Cauchy fit model (lines) for a sample with 80 nm AlN for angles of incidence of  $65^\circ$ ,  $70^\circ$  and  $75^\circ$ . The set of Cauchy parameters that gives a good fit of  $\Psi$  and  $\Delta$  is not unique, resulting in small variations of  $n$  and  $k$ . The inset in Fig. 4.16 shows the absorption coefficient  $\alpha$  for the samples with different AlN thickness and a sample with a thin QW, where the AlN buffer layer was grown under different conditions (lower ammonia). The absorption coefficient  $\alpha$  was determined using Eq. 1.65.

The trend first shows a systematic increase of absorption when going to shorter wavelengths. It also shows an increase in absorption with a decrease in thickness. However, the sample with the thin QW and the lower ammonia shows a higher absorption, although the QW absorption is outside of the depicted range at around 280 nm. Presumably the material absorption is strongly dependent on the growth parameters and ammonia flux. SE is a very sensitive

method, and the results discussed here should only be considered as a possible trend.

The full lines in Fig. 4.15 show the fit model of the loaded Q factor of the PhC sample determined by

$$\frac{1}{Q_{load}} = \frac{1}{Q_{abs,QW}} + \frac{1}{Q_{abs,AlN}} + \frac{1}{Q_{design}}, \quad (4.4)$$

where  $Q_{abs,AlN}$  is given by Eq. 1.64 and is determined using  $\alpha$  from the 80 nm AlN sample.

The 5 QWs contribute to the absorption that limits the Q factor. We approximate the QW absorption as  $\alpha_{QW} = 3000 \text{ cm}^{-1}$  below 310 nm using [226]

$$\alpha_{QW} \times L \approx \frac{\pi e^2}{2h} \times \Gamma = 6 \times 10^{-3} \times \Gamma, \quad (4.5)$$

with the thickness of the QW  $L = 1.2 \text{ nm}$ , the overlap factor between the 5 QWs and the mode  $\Gamma \approx 0.06$ , the fundamental charge  $e$ , and Planck's constant  $h$ . We assume a linear decrease of  $\alpha$  down to  $0 \text{ cm}^{-1}$  at 340 nm, close to the PL cut-off. We consider two values of  $Q_{design}$ , 1600 and 5000 from FDTD simulations, giving two results for the loaded Q, as shown in Fig. 4.15. The effect of  $Q_{design}$  is minimal in this range. The modeling matches very well with the measured data. This means that for the here investigated PhC sample the limitation in Q factor stems mainly from QW absorption and partly from residual absorption in AlN. However, considering samples with fewer QWs or QDs, where the absorption by the active region would be significantly reduced compared to here, the residual absorption in AlN grown on Si would ultimately be the limitation for the Q factor at short wavelengths, i.e. 2000 at 300 nm, the latter value being obtained from the measured absorption of the 80 nm thick sample.

The results in the inset of Fig. 4.16 indicate a reduction in absorption with increasing AlN thickness, which may be related to the material quality improving during the longer growth. In the AlN/Si interface region, point or extended defects that are annihilated after several tens of nm cause a large dislocation density. In a thicker AlN layer, the mode sees less of the more absorptive interface region. It explains why higher Q factors could be obtained in thicker microdisks at the same wavelength.

## 4.4 Conclusion and outlook

In conclusion, we have demonstrated active microlaser photonic circuits in the UVA spectral range using the III-nitride on silicon platform, which is very promising for both active and passive photonic components for next generation photonic integration. Our devices operate at the limit of what can be achieved using GaN as the waveguiding layer. The wavelength could be further reduced by switching from InGa<sub>N</sub>/GaN to Al<sub>x</sub>Ga<sub>1-x</sub>N/Al<sub>y</sub>Ga<sub>1-y</sub>N ( $y > x$ ) QWs and the absorption losses could be reduced by using AlN instead of GaN/AlN for the waveguide. While critical coupling would be challenging to achieve given the small gap sizes required, microlasers integrated into photonic circuits are feasible.

Furthermore, we have demonstrated high Q factor resonances in the UVA with L3 and H2 PhC slab cavities fabricated on a III-nitride on silicon sample. The Q factor at 340 nm is limited experimentally to around 1000. Residual absorption, possibly related to point or extended defects in the interface region, in AlN grown on Si may constitute a significant limiting factor when no active layers are present. Our results suggest that achieving high Q factors at short wavelengths down to the UVC is extremely challenging for very thin AlN layers (< 100 nm) grown on silicon and would require specific optimization of the material growth. Unfortunately, we have not had the opportunity to test our L3 and H2 cavities under pulsed optical pumping, so it is unclear if they could lase. We can compare our devices to the 2D PhC cavity lasers discussed by Lin et al. [211]. We observed similar Q factors at a similar wavelength, suggesting that our structures should be able to lase as well. The main limitation might be that our membranes are very thin (80 nm) as compared to 180 nm (Ref. [211]) and 310 nm (Ref. [34]), which may result in the material's damage threshold being reached before the lasing threshold.

## Summary of Chapter 4

In this chapter, we investigated two photonic devices operating in the UV: monolithically integrated microlaser photonic circuits and 2D PhC slab cavities. First, we reviewed the state of the art of both UV photonic circuits and III-nitride photonic crystal slab cavities. We designed and fabricated suspended microdisk photonic circuits operating in the UVA around 380 nm with a 180° angle of the waveguide around the disk. We observed loaded Q factors around 3500 at 420 nm under CW excitation and lasing modes from 374 to 399 nm under pulsed optical pumping. We estimated the effective propagation losses to  $0.08 \text{ dB} \cdot \mu\text{m}^{-1}$  and compared this value to literature. The wavelength shift between CW and pulsed operation was related to lasing of excited states. The lasing modes showed low threshold energies of  $0.14 \text{ mJ} \cdot \text{cm}^{-2}$  per pulse or threshold peak powers of  $35 \text{ kW} \cdot \text{cm}^{-2}$  for an 80 nm gap and we observed a large peak to background dynamic of around 200 at the out-coupling grating for a device with 50 nm gap. The devices showed the expected reduction in threshold with increasing gap size. These devices operate at the wavelength limit of GaN. In order to go further towards the UVC, AlN needs to be used as the waveguiding layer together with AlGaN QWs. Furthermore, we investigated L3 and H2 PhC cavities in III-N membranes suspended on Si with GaN/AlN QWs. We observed resonances with Q factors up to 1085 at 337 nm. We investigated the reduction of Q factor with decreasing wavelength. Besides the QW absorption below 340 nm, a noteworthy contribution is attributed to the residual absorption present in thin AlN layers grown on silicon, as measured by spectroscopic ellipsometry. This residual absorption could ultimately limit the Q factor to around 2000 at 300 nm when no active layer is present. These devices could possibly lase but have not been studied under pulsed excitation.



## Chapter 5

# Electrical injection in III-nitride microdisks and microrings on silicon

**I**N THIS CHAPTER, we investigate electrical injection in III-nitride mushroom-type microdisks and microrings on silicon substrate. Some of the here presented results were published in Ref. [227]. This chapter covers:

- A review of the state of the art of electrical injection in III-nitride microdisks and photonic circuits.
- III-nitride on silicon mushroom-type microdisks under electrical injection: fabrication, electroluminescence, and vertical current path.
- Fabrication and electroluminescence of mushroom-type microrings under electrical injection.
- White microring light emitting diodes.

### 5.1 Introduction and state of the art

Nakamura et al. developed the first InGaN-based laser diode (LD) in 1996 [228] using metal organic chemical vapor deposition (MOCVD) on sapphire substrate. They achieved lasing at  $\lambda = 417\text{ nm}$  at room temperature (RT) with a threshold current density of  $4\text{ kA}\cdot\text{cm}^{-2}$ . In the following years, the blue LD was continuously improved and commercialized for use in Blu-ray disc and HD DVD readers, for example.

What remains challenging to date is to achieve light emitting diodes (LEDs) and LDs at shorter wavelengths in the ultraviolet (UV) spectral range due to issues with efficient doping of AlGaIn with high Al content. Currently, the shortest lasing wavelength under electrical injection is  $271.8\text{ nm}$  using MOCVD growth on bulk AlN substrate [229].

Another challenge is to achieve electrically injected lasing in materials grown on cheaper substrates, such as Si. The first III-nitride laser diode on Si was only achieved in 2016 by Sun et al. [87]. Major difficulties in achieving low threshold and long lifetime electrically injected lasing are to sufficiently reduce the threading dislocation density (TDD) (usually in the order of  $10^9 - 10^{10} \text{ cm}^{-2}$ ) in GaN grown on silicon, which is caused by the large lattice mismatch of 17%, and to reduce cracking due to the large difference in thermal expansion coefficient of 116% between GaN and silicon [86, 87]. However, a significant dislocation density does not prevent to observe lasing. For example, Sun et al. [87] had a TDD of  $6 \times 10^8 \text{ cm}^{-2}$ . Lasing has also been achieved with higher TDDs [230].

A third challenge is the miniaturization of the laser and its integration into photonic circuits. The same can be said for  $\mu$ -LEDs, which are significantly more challenging to realize than regular LEDs. As mentioned in chapter 2, mushroom-type microdisk lasers have been achieved under optical pumping using both QWs and QDs as the active medium in the blue, green, and UV spectral ranges [31–33, 49, 50, 123, 135, 137], and we have reported their integration into photonic circuits in the blue and UVA in chapters 3 and 4 [145, 166, 201]. Several of the reports of microlasers in literature are doubtful, which highlights the microlaser challenge. The monolithic integration of microlasers with passive components in a photonic circuit is difficult and requires specific approaches to remove or "deactivate" the QWs as discussed in section 3.1.1. Usually, it is necessary to underetch these devices to provide a sufficient refractive index contrast in the vertical direction, which can be challenging depending on the choice of substrate. This need to underetch also creates an additional complexity for electrical injection that we will address in this chapter.

Electrical injection was utilized only in very few cases in III-nitride microdisk cavities or photonic circuits [43–45, 168, 180, 182, 227, 231], yet a main interest in using III-nitrides is to have active emitters, which are much more feasible for applications if electrically driven as opposed to optically pumped. Efficient electrical injection continues to pose a challenge in thin III-nitride layers on Si. However, the advantage of using silicon as a substrate for III-nitride nanophotonics is the possibility of monolithic integration into a well-established photonic platform, extending it to encompass UV-VIS emitters.

There have been some attempts at electrical injection in III-nitride photonic circuits for light communication [168, 180–182], but not using microresonators. Gao et al. integrated an LED, a waveguide, a ring resonator, and a photodiode in a suspended  $5 \mu\text{m}$  thick III-nitride on silicon layer operating at  $\lambda = 443 \text{ nm}$  [168]. The dimensions of the devices were large (i.e. gap between ring and waveguide of  $2.5 \mu\text{m}$ ) due to the use of optical lithography, resulting in inefficient coupling. Yet they demonstrated data transmission rates of  $30 \text{ Mb} \cdot \text{s}^{-1}$ . Meanwhile, Shi et al. integrated a transmitter, a waveguide, and a receiver into a suspended III-nitride on Si layer [180]. The photonic circuit operated at  $453 \text{ nm}$  with a turn-on voltage of  $2.8 \text{ V}$ , and they achieved  $120 \text{ Mb} \cdot \text{s}^{-1}$  data transmission rates. Floyd et al. recently demonstrated III-nitride on sapphire based photonic circuits in the UVC [181, 182], as we have already discussed in section

## 4.1.1.

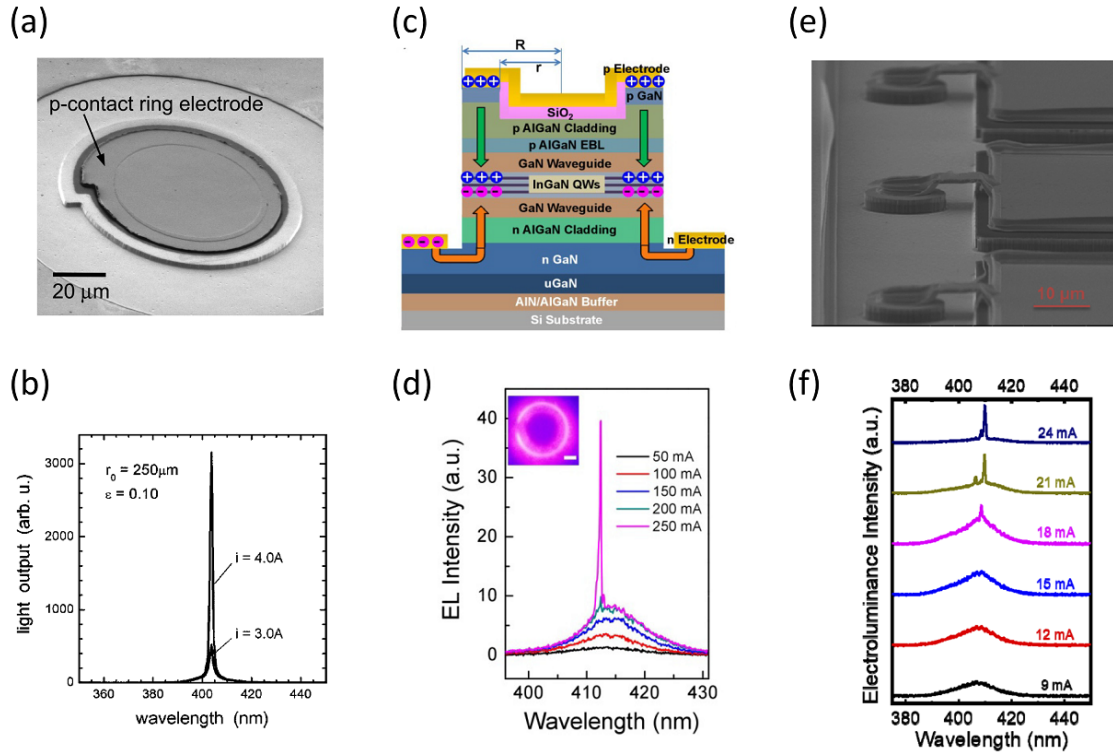


Figure 5.1: III-nitride microdisk lasers. (a,b) Spiral-shaped III-nitride on sapphire microdisk laser reproduced from Kneissl et al. [231]. (c)-(f) "Sandwich"-type microdisk lasers in III-nitride on Si reproduced from Feng et al and Wang et al. [43, 45].

There have been only a few reports on microdisk lasers under electrical injection using III-nitrides [43–45, 231], all of them operating at RT and mainly under pulsed excitation. Already in 2004, Kneissl et al. observed lasing in spiral-shaped III-nitride on sapphire microdisks, shown in Figs. 5.1 (a) and (b) [231]. The disks had  $500\mu\text{m}$  diameter and the lasing threshold was  $7.8\text{kA}\cdot\text{cm}^{-2}$ . In 2018, Feng et al. [43] demonstrated lasing under electrical injection in III-nitride "sandwich"-type microdisks on silicon at  $413\text{nm}$  with a threshold current density of  $25.5\text{kA}\cdot\text{cm}^{-2}$  (see Figs. 5.1 (c) and (d)). They used  $5.8\mu\text{m}$  thick heterostructures with  $3\times 2.4\text{nm}$   $\text{In}_{0.1}\text{Ga}_{0.9}\text{N}$  /  $7.5\text{nm}$   $\text{In}_{0.02}\text{Ga}_{0.98}\text{N}$  quantum wells (QWs) and side contacts and a TDD of  $6\times 10^8\text{cm}^{-2}$ . The same group demonstrated in 2019 lasing in the UVA from "sandwich"-type microdisks with an air-bridge p-contact and a threshold current density of  $250\text{kA}\cdot\text{cm}^{-2}$  [44]. In 2020, they demonstrated the first continuous-wave (CW) microdisk laser under electrical injection at RT with a threshold current density of  $9\text{kA}\cdot\text{cm}^{-2}$ , as shown in Fig. 5.1 (e) and (f) [45]. They reduced the current and voltage of their devices by improving the p-GaN growth to reduce carbon incorporation. However, looking at their electroluminescence (EL) spectra in Fig. 5.1 (d) the peak to background dynamic is quite low (factor 5) as opposed to the factor 30 observed by Kneissl et al. (Fig. 5.1 (b)) [231]. Furthermore, they are using the full spec-

tral broadening of the spontaneous emission below threshold to determine a narrowing of the linewidth, as opposed to only looking at the mode as is more commonly done. When looking only at the mode, one could argue that the threshold was not necessarily reached, but rather that the current density was increased only up to the point where modes became visible, while still being below threshold.

## 5.2 Microdisk under electrical injection

### 5.2.1 Fabrication of microdisks under electrical injection

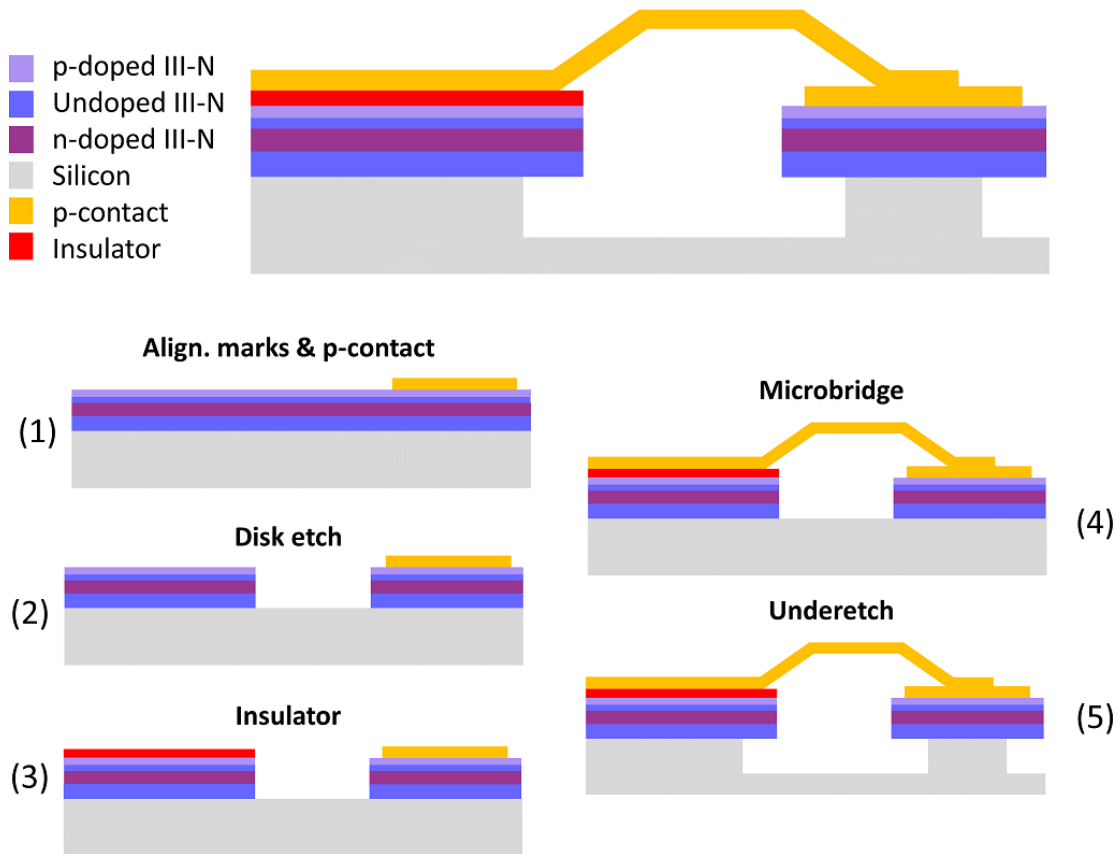


Figure 5.2: Schematic of the process flow of a III-nitride on Si microdisk under electrical injection.

Our initial approach to fabricating microdisks under electrical injection was to use the same scheme as for optical pumping, i.e. mushroom-type disks with underetching, but with a circular p-contact on top of the disk that is connected to a larger p-pad via a suspended mechanically stable metallic microbridge, as shown in Fig. 5.2. The n-contact is taken from the backside of the sample through the conductive Si substrate. The microbridge allows for easy probing of small disks, while avoiding absorption at the edge of the disk in the metal. The circular p-

contact is a few microns smaller than the disk, also with the aim to avoid absorption of the WGMs in the metal, as they propagate at the periphery of the disk. The vertical confinement of the modes is only given by the refractive index contrast to air. We use thin III-nitride layers of usually  $< 1 \mu\text{m}$  thickness for ease of fabrication and limitation of the number of modes in the vertical direction.

The process flow is depicted in Fig. 5.2, and a top-view schematic is shown in Fig. 5.3 (a). First (step (1)), Ni/Au alignment marks and p-contacts are deposited using optical lithography and an e-beam evaporator and annealed for 5 min at  $500^\circ\text{C}$  using rapid thermal annealing (RTA). Then (step (2)), using an  $\text{SiO}_2$  hard mask, e-beam lithography, RIE, and ICP etching microdisks are defined in analogy to Fig. 1.33. In step (3), we deposit  $\text{SiO}_2$  as an insulator and using optical lithography and RIE etching, we remove it on and around the microdisk. The insulator remains where the larger p-pad will be deposited, in order to direct the current path through the microdisk. Next (step (4)), using a two-level optical lithography step, we define the microbridge, which is shown schematically in Fig. 5.3 (b). In the first level, we make a bridge holder using S1818 resist and we use a resist-reflow temperature gradient from  $110$  to  $150^\circ\text{C}$  for 50 min. The second level uses AZ5214E or TI35ESX image-reversal resist to define the microbridge and p-pad over the first resist layer. We then deposit a  $500 \text{ nm}$  Ti/Au layer. Finally (step (5)), we underetch the microdisk using  $\text{XeF}_2$ .

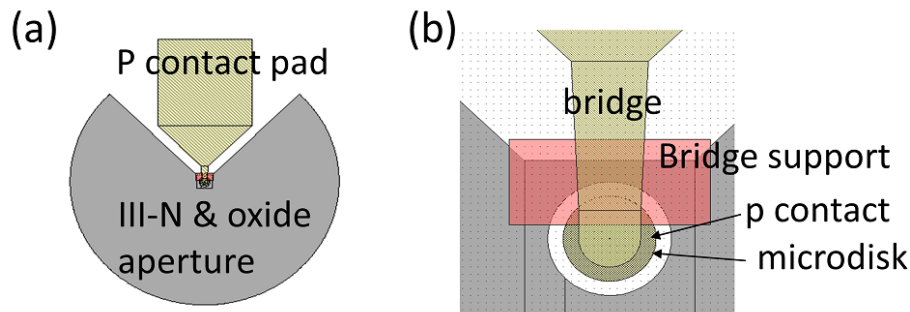


Figure 5.3: Schematic of (a) the full device and (b) a zoom-in into the microdisk and microbridge, showing the bridge holder layer.

### 5.2.2 EL results obtained from sample C404

We fabricated microdisks for electrical injection on sample C404 using the above-mentioned process. The heterostructure of sample C404 is depicted in Fig. 5.4 (a). First, a  $100 \text{ nm}$  AlN buffer layer was grown by molecular beam epitaxy (MBE). Then,  $400 \text{ nm}$  of Si-doped GaN (doping concentration  $4 \times 10^{18} \text{ cm}^{-3}$ ) was grown by MOCVD, followed by 5 pairs of  $2 \text{ nm}$   $\text{In}_{0.16}\text{Ga}_{0.84}\text{N}$  QWs and  $13 \text{ nm}$  GaN barriers. Then, a  $20 \text{ nm}$  Mg-doped  $\text{Al}_{0.2}\text{Ga}_{0.8}\text{N}$  electron blocking layer (EBL) (doping concentration  $4 \times 10^{19} \text{ cm}^{-3}$ ),  $100 \text{ nm}$  GaN:Mg (doping concentration of  $4 \times 10^{19} \text{ cm}^{-3}$ ) and  $15 \text{ nm}$  GaN:Mg (doping concentration of  $1 \times 10^{20} \text{ cm}^{-3}$ ) were deposited.

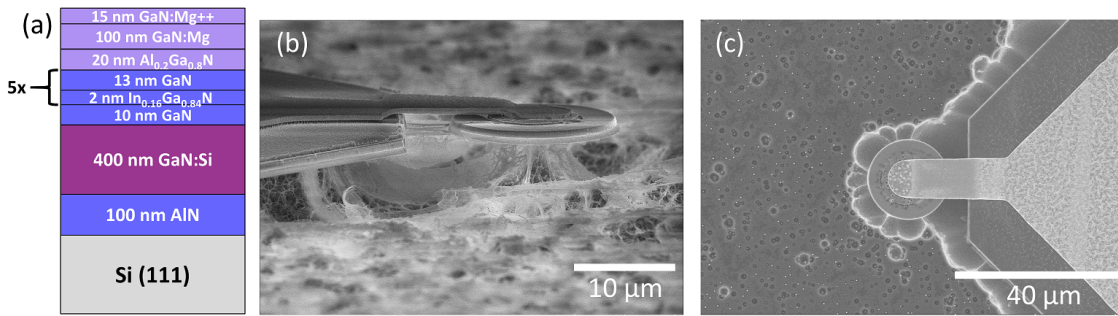


Figure 5.4: (a) Heterostructure of sample C404. (b) Side-view SEM image of a 16µm diameter disk. (c) Top-view SEM image of a 20µm diameter disk.

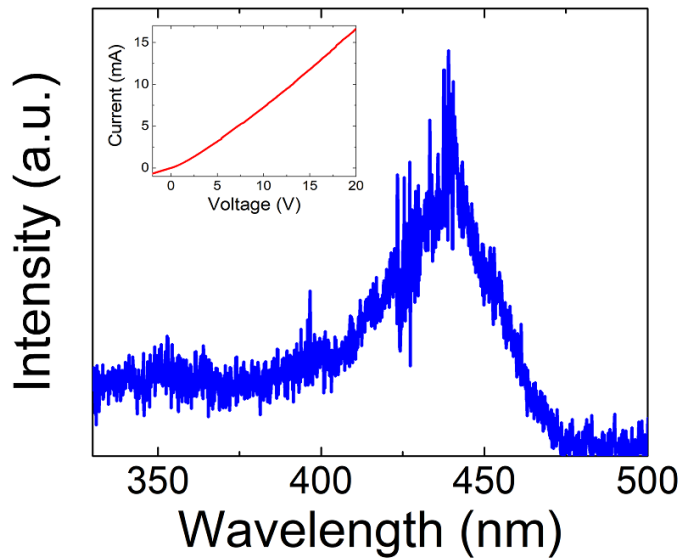


Figure 5.5: EL spectrum of a microdisk fabricated on sample C404. The inset shows the corresponding IV curve.

SEM images of microdisks fabricated on sample C404 are shown in Fig. 5.4 (b) and (c). A side-view of a 16µm diameter disk is depicted in Fig. 5.4 (b) and a top-view of a 20µm diameter disk is shown in Fig. 5.4 (c). The suspended bridge and underetched disk are clearly visible.

A direct current (DC) EL spectrum of a 16µm diameter microdisk measured at 15mA and 18V with an integration time of 20s is shown in Fig. 5.5. The inset shows the current-voltage (IV) curve. The EL is very weak, but provides a proof of concept for the microbridge contact. It also represents a first demonstration of EL from an underetched microdisk, which is a challenge in itself. However, the low intensity indicates a problem with the current path that needs to be investigated in more detail.

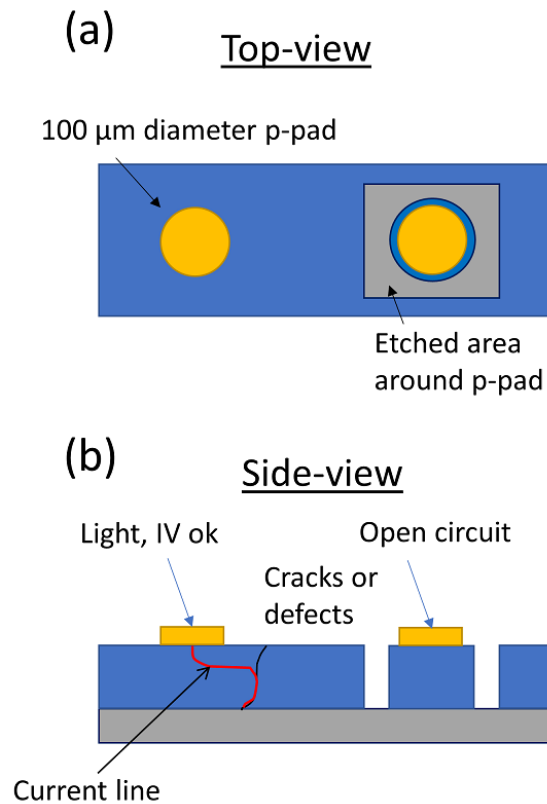


Figure 5.6: (a) Top-view and (b) side-view of test devices with a p-contact and without (left) and with (right) a mesa.

### 5.2.3 Current path through defects in undoped buffer layers

We will look at the path the current takes through the device, in order to understand why the EL in Fig. 5.5 (b) is so weak. Our samples contain undoped buffer layers of AlN (and GaN). One would assume that these layers are not conductive. However, when performing indium-dot tests on the as-grown wafer, we observe light-emission and conductivity through the full vertical stack with the n-contact taken from the backside. Thus, we assumed that the material was sufficiently conductive and performed the fabrication process detailed in Fig. 5.2. However, we noticed that when we etched mesas in the order of 100  $\mu\text{m}$  diameter, the vertical conductivity is often lost, and we observe an open circuit. Initially, we thought that this might be related to ICP etch damage destroying the electrical properties of our QWs, and it took some time to understand that this was not the case. Fig. 5.6 shows a sketch of test devices with and without a mesa. The device on the left consists of a 100  $\mu\text{m}$  diameter p-pad, while the device on the right also has a mesa etched around the p-pad all the way to the Si substrate. For the device on the left, we observe light output and around 13 V at 20 mA, while for the device on the right, we generally observe an open circuit. The vertical conductivity is not simply driven by the dislocation density. We attribute this phenomenon to current flowing through macroscopic defects in the buffer layer and at the AlN/Si interface that might result from dislocation formation, dis-

location bundles, inter-diffusion, and possibly cracks in large mesas. This phenomenon can likely be observed in other vertical devices, such as transistors, as well. Perhaps defect-driven current injection could be exploited for large-scale vertical devices. However, for microdisks, this is challenging and a different injection approach should be favored.

### 5.3 Microrings under electrical injection

We thus propose a new strategy for electrical injection in a vertical device, where we bypass the before-mentioned quasi-insulating buffer layers currently required in our epitaxial scheme for growth of high material quality GaN on silicon. This new scheme is compatible with thin layers (1-2 $\mu\text{m}$ ) and allows for the fabrication of side-coupled bus waveguides with small gaps (less than 100 nm) necessary for efficient coupling in the blue to UV spectral range. Instead of microdisks, we use microrings with a central top buried n-contact that connects the n-GaN to the Si substrate. A microbridge contact allows for easy probing of a larger p-pad. The back contact is taken from the n-doped silicon, without metalization. This technology is scalable to complex integrated photonic circuits and will provide an asset to the field.

Via etching to make an electrical connection to the Si substrate was previously used for field effect transistors by Hikita et al. [232, 233]. They used a "source-via-grounding" approach in a vertical device structure to connect the source to the Si substrate, which was grounded and acted as a field plate. This approach reduced the device size, the parasitic inductance, and the on-state resistance [232]. They etched 20 $\mu\text{m}$  deep and electroplated a thick gold layer. While we use the same basic idea of via etching to reach the Si substrate, the function and dimensions of the via are quite different. In our case, its main purpose is to allow to underetch the microring, and it is only a few microns wide and only 1-2 $\mu\text{m}$  deep. Furthermore, we do not connect the sample surface, but the n-GaN, to the substrate. Another interesting approach to bypass the buffer layers, as well as the Si substrate was proposed by Zhang et al. [234], where they etched vias from the backside to remove the substrate and buffer layers for all vertical power diodes.

#### 5.3.1 Fabrication of electrically injected microrings

We use an 8-step optical and e-beam lithography process that is depicted schematically in Fig. 5.7 to fabricate electrically injected mushroom-type microrings with 30 to 50 $\mu\text{m}$  diameter and microbridge contacts. The p-GaN is very sensitive in these devices and care needs to be taken not to contaminate it. For this reason, we need to start with the p-contact. We first deposit a 1.5 nm thin Ni layer to protect the surface from contamination by photoresist. We use AZ5214 image reversal resist to pattern 2 to 5 $\mu\text{m}$  wide ring contacts and alignment marks and use an e-beam evaporator to deposit 20 nm Ni/ 380 nm Au. The metal layer is lifted off in an acetone bath and the sample is annealed for 5 min under N<sub>2</sub> using RTA at 500°C. The Ni/Au ring p-contact is illustrated in Fig. 5.7 (1). We deposit a layer of PECVD SiO<sub>2</sub> that acts as a hard mask during

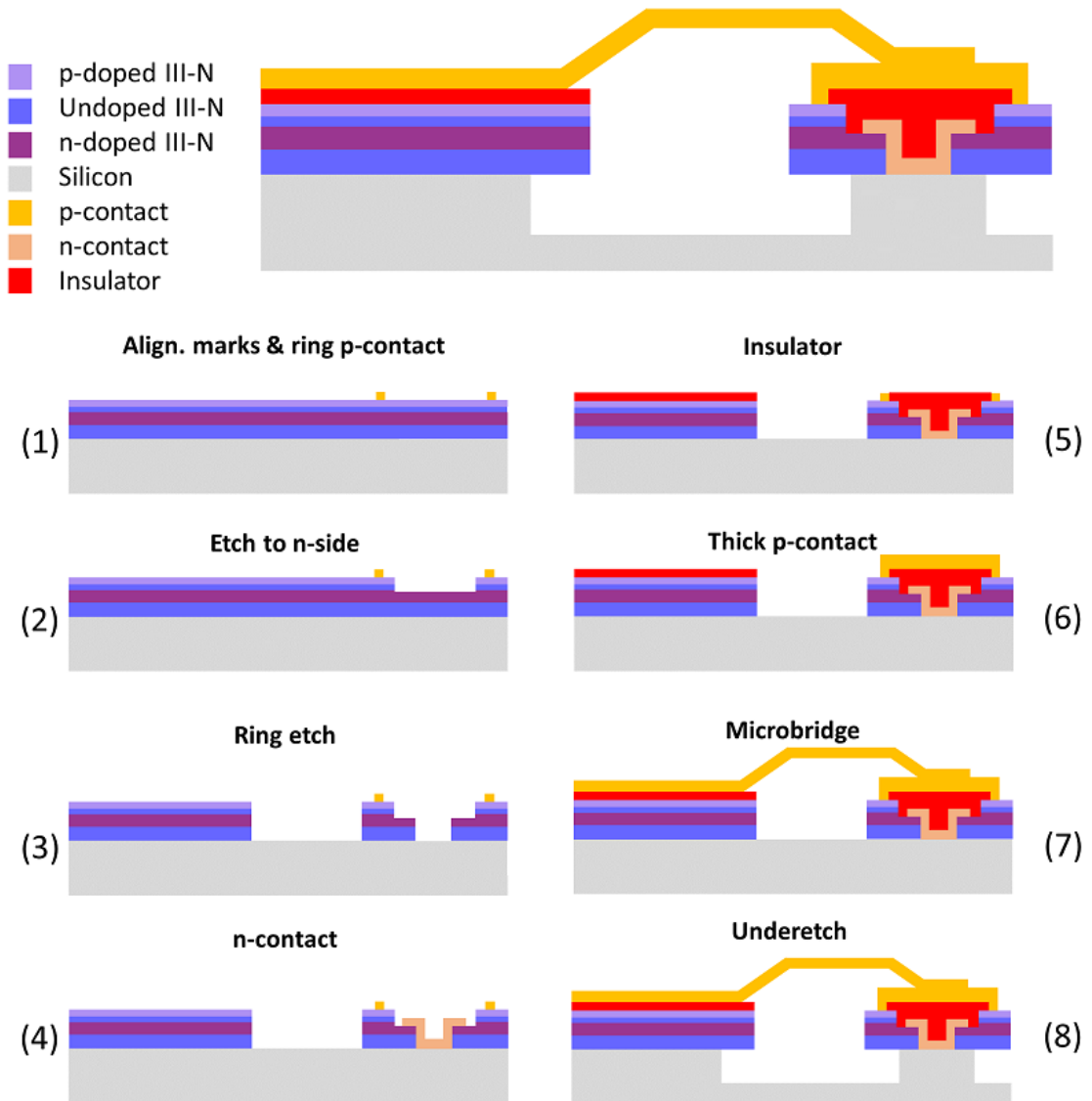


Figure 5.7: Process flow of microrings for electrical injection.

RIE and ICP etching. The second level of optical lithography consists of defining circles in the center of the rings using AZ5214 resist. We etch the  $\text{SiO}_2$  using RIE or ICP and etch the III-nitride using ICP to the n-GaN by knowing the etch rate and the sample heterostructure precisely, and remove the remaining  $\text{SiO}_2$  mask through dry-etching (see Fig. 5.7 (2)). We deposit a new  $\text{SiO}_2$  hard mask using PECVD. In the third level, we use e-beam lithography with UVIII or UV5 resist to define the microring (see Fig. 5.7 (3)). We leave 2 to 6  $\mu\text{m}$  free between the ring p-contact and the edge of the disk to allow for misalignment and to reduce the overlap of the optical mode with the metal. The pattern is subsequently etched into the hard mask using RIE or ICP and into the III-nitride and down to the silicon substrate using ICP etching. The remaining hard mask is removed by RIE or ICP etching. In the fourth step, we use TI35ESX resist and image reversal to open circles in the center of the rings that uncover part of the n-GaN and the central

via to the Si. We e-beam evaporate a thick Ti/Al/Ni/Au (100 nm/400 nm/100 nm/200 nm) n-contact and lift-off the metal in an acetone bath. No annealing is performed at this step, as not to damage the p-contact. The n-contact connects the n-GaN to the silicon substrate, bypassing the insulating buffer layers, which is schematically shown in Fig. 5.7 (4). The distance between the n-contact and the edge of the microring is between 7 and 16  $\mu\text{m}$ . Next, we deposit PECVD  $\text{SiO}_2$  as an insulating layer. We use AZ5214 resist and open it at the edge of the microring to uncover the p-ring and outside of the microring where the Si is exposed. We etch the  $\text{SiO}_2$  using RIE or ICP (Fig. 5.7 (5)). In the sixth step, we use TI35ESX image reversal resist to define circles at the center of the microring, uncovering the insulator and the p-ring. We e-beam evaporate a thick circular Ni/Au (20 nm/480 nm) p-contact and lift-off the metal in an acetone bath (Fig. 5.7 (6)). If the heterostructure is too thick or the resist layer too thin, this lift-off does not work well and the sample is lost at this step. In the seventh step, we define the microbridge contact and p-pad using the 2-step lithography detailed in section 5.2. We deposit a thick Ti/Au (20 nm/780 nm) layer and lift-off the metal in acetone and clean away the bridge holder using a short low-power  $\text{O}_2$  plasma. The microbridge is schematically depicted in Fig. 5.7 (7). In the eighth and final step, the microrings are underetched using  $\text{XeF}_2$  gas after a brief RIE etch to remove the native oxide on the Si (Fig. 5.7 (8)).

A further reduction in device size could be realized by switching to a full e-beam lithography process. Devices in the 10  $\mu\text{m}$  diameter range would be feasible. Finding a way to make the entire heterostructure conductive can also decrease device size, as it would allow for the fabrication of standard mushroom-type microdisks, as described in section 5.2. Alternatively, we could use a "sandwich"-type structure like Feng et al. with cladding layers for light confinement and lateral current injection [43].

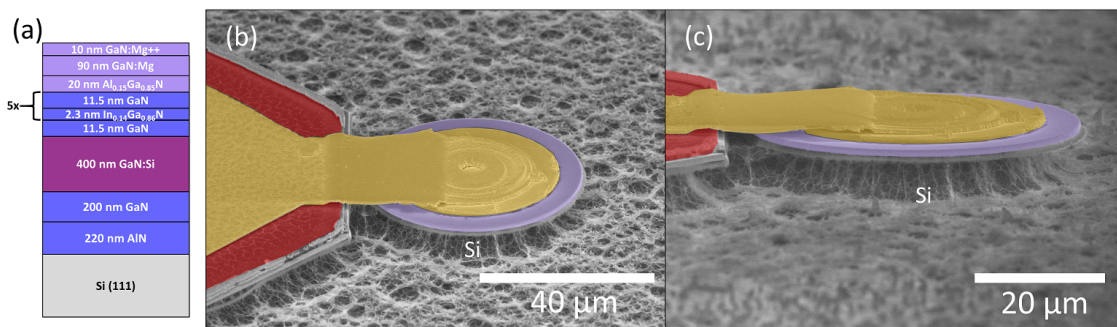


Figure 5.8: (a) Heterostructure of sample C522. (b) False color SEM images of a 50  $\mu\text{m}$  diameter microring for electrical injection. (c) Same device but from a different angle to emphasize the underetching of the microring. The metal microbridge and p-contact are highlighted in yellow, the insulator in red, and the III-nitride in purple. The rough gray area is the etched silicon.

The investigated sample, C522, was grown on a 2 inch n-type (doping concentration  $5 \times 10^{18} \text{cm}^{-3}$ ) silicon (111) wafer using MOCVD. The heterostructure is illustrated in Fig. 5.8 (a). First, an undoped buffer layer of 220 nm AlN and 200 nm GaN was grown, followed by the LED

heterostructure consisting of 400 nm GaN:Si ([Si] of  $5 \times 10^{18} \text{ cm}^{-3}$ ), 11.5 nm of undoped GaN, 5 pairs of 2.3 nm  $\text{In}_{0.14}\text{Ga}_{0.86}\text{N}$  QWs and 11.5 nm GaN barriers, a 20 nm Mg-doped  $\text{Al}_{0.15}\text{Ga}_{0.85}\text{N}$  EBL ([Mg] of  $4 \times 10^{19} \text{ cm}^{-3}$ ), 90 nm of GaN:Mg ([Mg]  $4 \times 10^{19} \text{ cm}^{-3}$ ), and 15 nm of GaN:Mg ([Mg]  $1 \times 10^{20} \text{ cm}^{-3}$ ). The TDD estimated from X-ray diffraction (XRD) and atomic force microscopy (AFM) is in the range of  $5 \times 10^9$  to  $2 \times 10^{10} \text{ cm}^{-2}$  and the root mean square (rms) roughness is 1 nm as determined by an atomic force microscopy (AFM) scan of  $10 \mu\text{m} \times 10 \mu\text{m}$ . The device scheme proposed in this section allows for much simpler heterostructures than required for the devices reported by Feng et al. [43], as no cladding layers are used.

False color SEM images of a tilted  $50 \mu\text{m}$  diameter microring are shown in Fig. 5.8 (b) and (c) for two different angles. The undercut of the microring and the bridge suspension are clearly visible. The rough area around the ring is the silicon substrate after isotropic etching by  $\text{XeF}_2$  gas.

### 5.3.2 Results and discussion

In this section, we will discuss some simulations of the device structure of C522, as well as the EL results obtained from microrings on this sample.

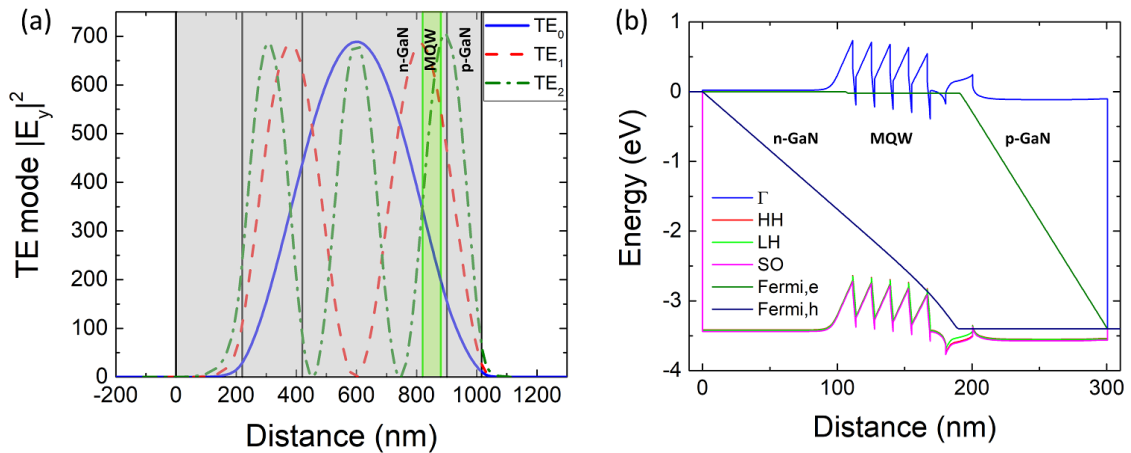


Figure 5.9: (a) Simulated mode confinement of the  $\text{TE}_0$ ,  $\text{TE}_1$ , and  $\text{TE}_2$  modes in C522, the MQW region is highlighted in green, the heterostructure in gray. (b) Energy band structure of sample C522 at 3.4 V bias.

It is important to simulate the vertical mode confinement and look at the overlap of the optical mode with the QWs, as well as with the p-GaN, which is absorbing. Simulations of the  $\text{TE}_0$ ,  $\text{TE}_1$ , and  $\text{TE}_2$  modes are shown in Fig. 5.9 (a) for an underetched disk. The overlap of these modes with the QWs (without barriers) are 0.96 %, 2.4 %, and 2.0 %, respectively. By increasing the thickness of the p-GaN cap layer, for example, we could increase this overlap of the  $\text{TE}_0$  mode to a maximum of 1.6 % for a 400 nm cap thickness. Laterally, the mode is confined by total internal reflection at the edge of the disk, extending over around  $1 \mu\text{m}$  for first-order radial modes. The overlap of the optical mode with the p-GaN is 2.7 % for the  $\text{TE}_0$ ,

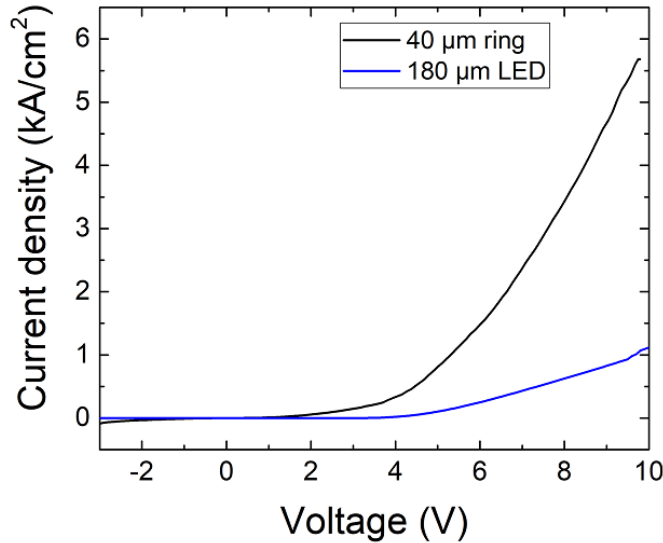


Figure 5.10: JV curves of a 40 $\mu\text{m}$  diameter microring and a 180 $\mu\text{m}$  lateral LED for reference.

8.5 % for the  $\text{TE}_1$  and 15.8% for the  $\text{TE}_2$  mode. The absorption of Mg-doped GaN is around  $100\text{ cm}^{-1}$  [235]. Given the large overlap of the optical mode with the p-doped region, this loss may significantly increase the lasing threshold beyond current densities that can be attained before device breakdown. In this case, a structure with cladding and waveguiding layers would be favorable to reduce the lasing threshold.

A simulation of the band structure is shown in Fig. 5.9 (b) under a 3.4 V bias, which corresponds to the GaN bandgap. Simulations of the radiative recombination show that the carrier density is higher in the QWs closer to the p-side and thus fewer wells may lead to an enhanced performance, which has also been demonstrated experimentally in Ref. [236]. Our 5 QWs would likely not all reach population inversion, making this not the most optimal structure. Many laser diodes in literature often have 3 QWs [87, 202]. Going to 3 QWs would be a reasonable next step for our heterostructure design.

A typical current density over voltage (JV) curve of a 40 $\mu\text{m}$  diameter microring is shown in Fig. 5.10 and is compared to the JV curve of a lateral LED with a 180 $\mu\text{m}$  diameter p-contact and top n-contact on the n-GaN. The turn-on voltages are similar in both cases, which shows that the microring process with its multiple etch steps and small device dimensions, as well as taking the n-contact through the silicon substrate, do not have any negative influence on the device performance. The surface area of both p-contacts is very different, and a direct comparison of the current densities at a given voltage is not straightforward. For microrings, the current density is quite elevated. The overall high voltage in forward direction is due to the resistive p-GaN. The microring also shows a slightly leaky behavior in reverse bias.

We performed direct current RT EL measurements on these devices using probe tips placed on the large p-pad and near the sample on the copper block for the n-contact through the silicon substrate. The emission is collected from the side of the sample with a microscope ob-

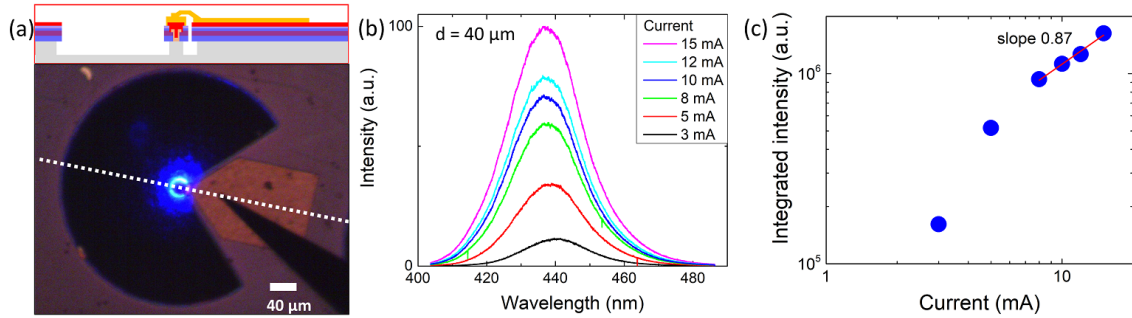


Figure 5.11: Measurement results: (a) Top: Cross-sectional view of the device along the white dashed line. Bottom: Photo of a powered 40 μm diameter device emitting blue EL. (b) Spectra of a device with a 40 μm diameter at different injection currents. Maximum current density  $4.2 \text{ kA} \cdot \text{cm}^{-2}$ . (c) Integrated intensity of the measurements in b).

jective and the light is guided through air into a grating monochromator with a liquid nitrogen cooled CCD as detector. Fig. 5.11 (a) shows a photo of a 40 μm microring emitting blue EL. A cross-sectional view of the device along the white dashed line is shown at the top of the figure. The microring is at the center of a black 3/4 circle, which is etched to the Si substrate by ICP and isotropically underetched by XeF<sub>2</sub> gas. On the right side of this circle is a  $140 \times 140 \mu\text{m}^2$  p-pad that connects to the microring via a microbridge. Fig. 5.11 (b) shows spectra of a 40 μm diameter ring for currents from 3 to 15 mA measured using a 600 grooves/mm grating, an 80 μm slit width, and 0.01 s integration time. A slight blue-shift is observed with increasing current. The maximum current of 15 mA corresponds to a current density of  $4.2 \text{ kA} \cdot \text{cm}^{-2}$ , which is not sufficient to achieve lasing. Device degradation and breakdown are observed at currents between 15 and 30 mA, possibly due to the not optimized insulator between the p- and n-contacts at the center of the microdisk. We also tried using silicon nitride (Si<sub>3</sub>N<sub>4</sub>) instead of SiO<sub>2</sub>, however, the device performance did not improve significantly. Wang et al. reported a lasing threshold of  $9 \text{ kA} \cdot \text{cm}^{-2}$  for devices with 16 μm diameter, while Kneissl et al. observed lasing at  $7.8 \text{ kA} \cdot \text{cm}^{-2}$  for 500 μm diameter devices on sapphire [45, 231]. Under optical pumping, we have observed rather high threshold peak powers of around  $333 \text{ kW} \cdot \text{cm}^{-2}$  for 12 μm diameter disks fabricated on sample C522.

No WGMs are observed using a 3600 grooves/mm grating with a spectral resolution of 0.02 nm. The FSR of first-order modes in such a 40 μm diameter ring is expected to be around 0.4 nm, as extrapolated from FDTD simulations for smaller devices. However, there are many competing families of modes, and it is not evident that the large spectral density of modes allows for an observation of WGMs below threshold. Neither Kneissl et al. nor Wang et al., who used devices in a similar diameter range, observed any modes below threshold [45, 231]. Another issue is the lateral current spreading in such devices due to the distance from the p-ring to the edge of the microdisk, and tunnel junctions will be investigated as a potential solution in future work. Fig. 5.11 (c) shows a double-logarithmic plot of the integrated intensity over current,

depicting a slope of around 1 at high current injection, suggesting dominant radiative recombination, while non-radiative processes dominate at low current, which implies a fairly good material quality.

We performed polarization measurements (not shown) at 0, 45, and 90°, indicating that the microring emission is mainly of TE polarization, as expected for InGaN/GaN QWs [237].

Using an integrating sphere, we determined the output power of a 40μm diameter microring corresponding to the IV response in Fig. 5.10 to be 2μW at 20 mA, giving an output power density of 440mW·cm<sup>-2</sup> at a current density of 5.7kA·cm<sup>-2</sup>. This power density is three orders of magnitude lower than the one reported for micro-LEDs fabricated on a commercial LED on sapphire substrate, which was 655 W·cm<sup>-2</sup> [238], but in the latter case a full optimization of collection efficiency was performed. Here, the microring radiates preferentially in the layer plane, which is detrimental for collection efficiency, but an asset for in-plane coupling and nanophotonic circuits, as described below.

## 5.4 White LED

We will briefly discuss our first demonstration of a white microring-LED during the Milagan project (see Introduction). This was in collaboration with our colleagues at the University of Hong Kong during my stay there at the end of 2018.

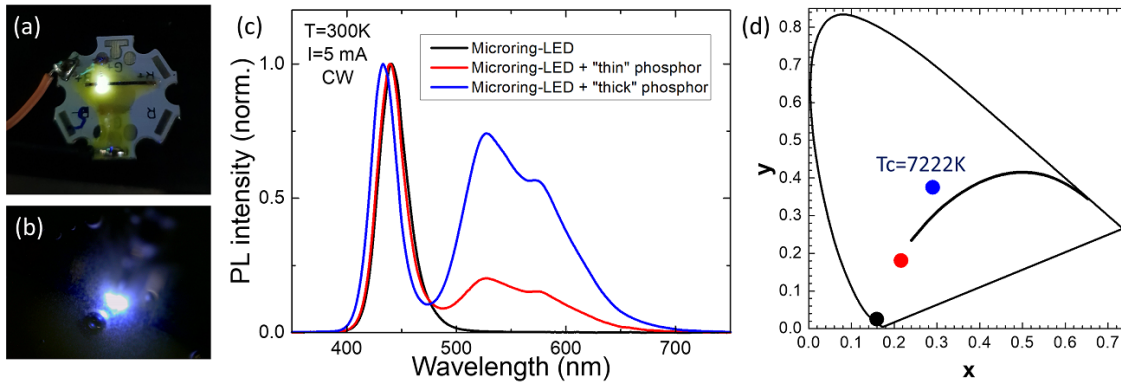


Figure 5.12: White microring LED on C522. (a,b) Photos of packaged LEDs with yellow phosphor coating showing white light emission. (c) normalized PL spectra of three different microring-LEDs. (d) Chromaticity diagram showing the three microring-LEDs and black body radiation. (c,d) measured by B. Damilano at CRHEA.

A common way to fabricate white LEDs is to use a blue LED and a yellow phosphor. The mixing of these colors makes white light. The above-mentioned sample, C522, was diced into bars of 500μm width. The bars were mounted on submounts and the contacts were wire-bonded to metal pads, which in turn were contacted with wires. Then, a yellow phosphor was deposited on top of the bars. Photos of these white microring-LEDs are shown in Fig. 5.12 (a) and (b). CW RT PL spectra of microring-LEDs without and with different amounts of phosphor

are depicted in Fig. 5.12 (c) at a current of 5 mA and their position in the chromaticity diagram is shown in Fig. 5.12 (d). The microring-LED with a thick phosphor layer emits a bluish white corresponding to black body radiation at 7222 K.

One goal of Milagan is to make white light sources based on microlasers. A difficulty of this objective is to avoid having the phosphor affect the Q factor and threshold of the microlaser through absorption. One solution might be having the phosphor not directly touch the microdisk but be strategically placed in its vicinity.

## 5.5 Conclusion and outlook

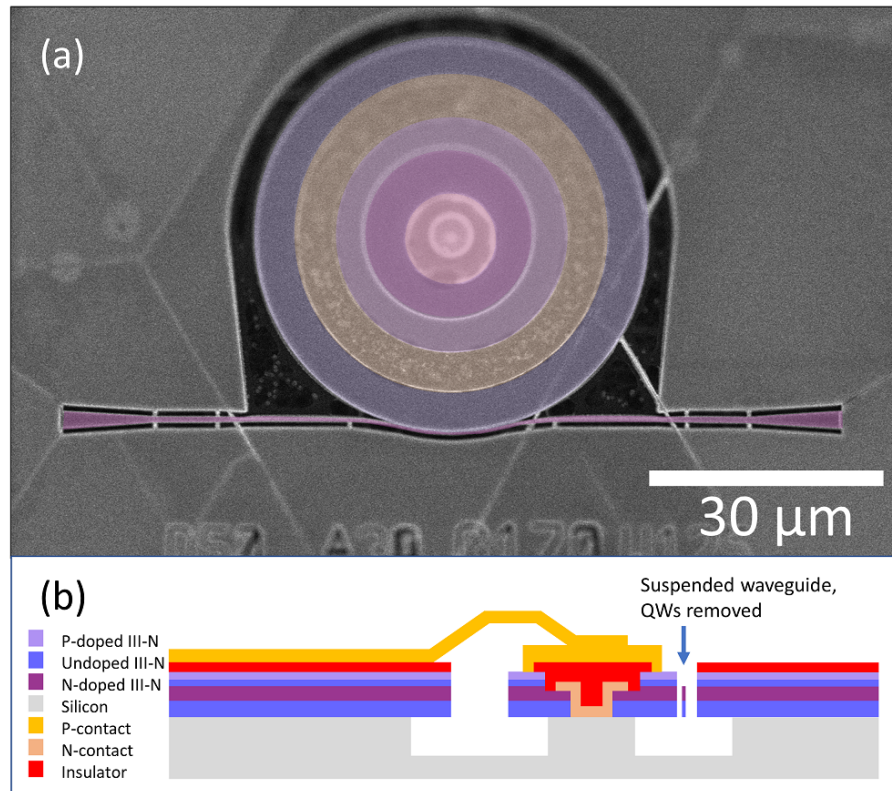


Figure 5.13: Microring under electrical injection with bus waveguide side coupling: a) False color SEM image of device with a 50 μm diameter ring and a 100 μm long bus waveguide after several processing steps. b) Side-view sketch of a full device.

In conclusion, we have presented two approaches towards achieving vertical electrically injected microdisk lasers in III-nitrides on silicon. However, lasing has not yet been observed. Several possible next steps could be investigated, in order to try to achieve lasing in such thin microring structures. Improving the lateral current spreading through the use of tunnel junctions could help. Currently, the p-contact is not at the same location as the optical mode and p-GaN does not allow for a good current spreading. The vertical confinement and mode over-

lap could be improved by replacing the n-GaN layer with n-AlGaN. Combining a 3D-2D growth transition to lower the dislocation density and selective area growth to reduce cracking are also an interesting approach. However, in that case more sophisticated cladding and waveguiding layers would become necessary.

Furthermore, we envision to demonstrate a photonic circuit consisting of an electrically injected microring, a side-coupled bus waveguide with a small gap in the order of 100 nm, and grating out-couplers terminating the waveguide, as illustrated in Fig. 5.13, and as previously demonstrated under optical pumping (see chapters 3 and 4 and Refs. [145, 166, 201]). This process is very challenging, as alignment precision between 20 nm for the e-beam lithography steps and 1  $\mu\text{m}$  for the optical lithography steps are required, and proximity effect correction is needed when defining the microring and bus waveguide. Note that the etching of small gaps and narrow waveguides, which is essential for efficient evanescent coupling in the blue, requires the total heterostructure thickness to be less than 2  $\mu\text{m}$ . Such devices would allow to demonstrate the viability of the III-nitride on silicon nanophotonic platform for consumer applications.

Since lasing has not yet been achieved using thin III-nitride on silicon layers, we decided to try a full waveguiding structure in vertical direction including cladding layers, to increase the mode overlap with the QWs and reduce the overlap with the highly doped layers. However, this approach can significantly increase the thickness of the heterostructure. It further eliminates the necessity of underetching, since the vertical confinement is provided by the cladding layers. Consequently, the n-contact can be taken from the side, since the etch can be stopped in the n-cladding. The heterostructure would be closer to what has been demonstrated in Refs. [43–45].

We grew a first such sample, C1162D, whose heterostructure is shown schematically in Fig. 5.14 (a). Using MOCVD on Si (111), we grew 200 nm AlN, 700 nm n-Al<sub>0.07</sub>Ga<sub>0.93</sub>N cladding ([Si] of  $5 \times 10^{18} \text{ cm}^{-3}$ ), 50 nm n-GaN ([Si] of  $10^{18} \text{ cm}^{-3}$ ), 80 nm In<sub>0.03</sub>Ga<sub>0.97</sub>N waveguide,  $3 \times 4$  nm InGaN/7 nm GaN QWs, 20 nm of p-Al<sub>0.15</sub>Ga<sub>0.85</sub>N electron blocking layer (EBL) ([Mg] of  $10^{19} \text{ cm}^{-3}$ ), 50 nm p-In<sub>0.03</sub>Ga<sub>0.97</sub>N waveguide ([Mg] of  $10^{19} \text{ cm}^{-3}$ ), 500 nm p-Al<sub>0.07</sub>Ga<sub>0.93</sub>N cladding, and 20 nm of p<sup>++</sup>-GaN contact layer ([Mg] of  $10^{20} \text{ cm}^{-3}$ ). The vertical mode confinement of the TE<sub>0</sub> mode is shown in Fig. 5.14 (b) at 420 nm. The overlap of the mode with the 3 QWs is 3.8%. Meanwhile, 33% of the mode is confined in the p-doped region. The advantage of this heterostructure, as opposed to the one of C522 is that we have control over the modes. This structure certainly favors the TE<sub>0</sub> mode, while for C522 higher order modes are possible and likely.

We have designed a lithography mask to fabricate sandwich-type microdisks of 5 to 200  $\mu\text{m}$  diameter with a lateral n-contact in a process with 7-levels of lithography. Here, we aim to fabricate the n-contact before the p-contact, since a contact on n-AlGaN is certainly better when annealed around 900°C. Unfortunately, the Covid-19 nation-wide shutdown started while we were doing the processing and as of June 2020 the process remains unfinished.

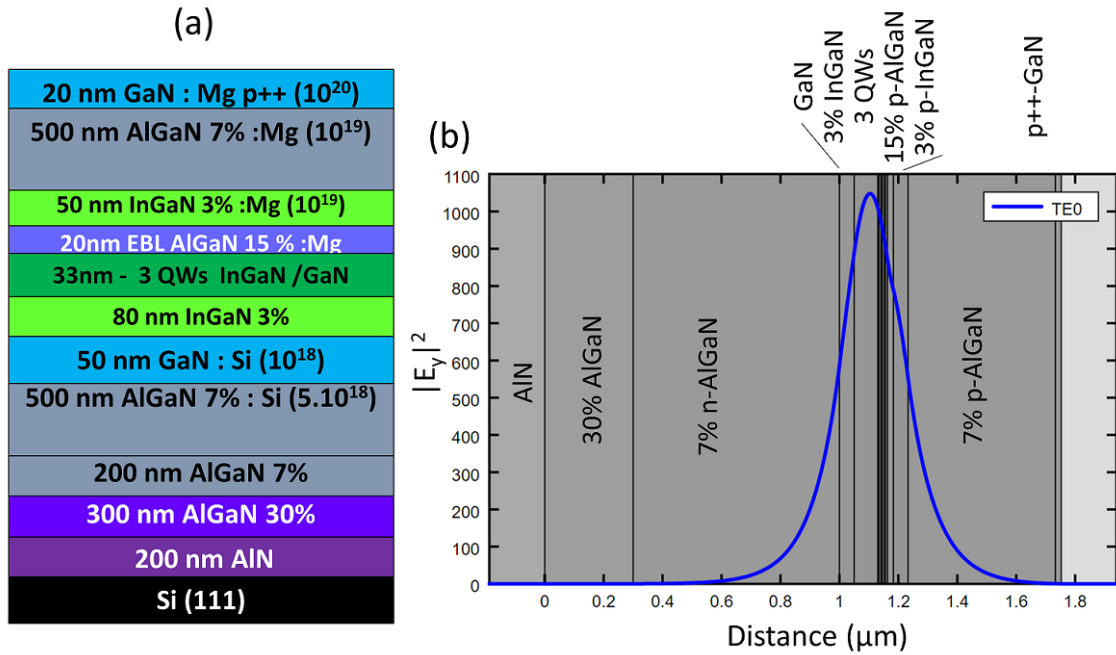


Figure 5.14: (a) Heterostructure of sample C1162 and (b) optical confinement of the TE<sub>0</sub> mode.

## Summary of Chapter 5

In this chapter, we investigated electrical injection in vertical III-nitride microdisks and microrings on silicon. We reviewed the state of the art of lateral sandwich-type microdisk lasers and electrically injected photonic circuits using III-nitrides. We demonstrated two schemes for vertical electrical injection in thin III-nitride microdisks and microrings on silicon. In our initial approach, we assumed sufficient conductivity of the buffer layers, since vertical conductivity was observed for large areas. However, only very weak EL was observed from such devices. The current path was defect-driven and conductivity disappeared for mesas in the 100  $\mu\text{m}$  range. Consequently, we developed a complex process for microrings with a buried n-contact that bypasses the insulating buffer layers. It is compatible with thin III-nitride epilayers on silicon and with microlaser diodes coupled to integrated photonic circuits, as it allows for device under-etching and the possibility of fabricating side-waveguides with small gaps of less than 100 nm, necessary for efficient coupling in the blue-UV spectral range. We demonstrated EL of such microrings contacted with a metallic microbridge with  $440 \text{ mW} \cdot \text{cm}^{-2}$  output power density at 20 mA and demonstrated white microring-LEDs. Lasing has not been achieved, which may be due to the large overlap of the mode with the p-doped region and the small overlap with the QWs, or due to the bad current spreading in p-GaN and the distance between the p-contact and the optical mode at the edge of the disk. Future work includes trying to achieve lasing for either thin mushroom-type or thicker sandwich-type structures, as well as the integration into photonic circuits.



## Chapter 6

# III-nitride photonic circuits in the near-infrared

**I**N THIS CHAPTER, we discuss the design and fabrication of passive photonic circuits in the near-infrared spectral range around 780 nm (and 1560 nm) on III-nitride layers grown on silicon and bonded on SiO<sub>2</sub> or suspended in air. No optical measurements have been performed on the fabricated samples as of June 2020 due to the Covid-19 shut-down. This chapter covers:

- The state of the art of III-nitride photonic circuits in the near-infrared.
- The design and fabrication of passive photonic circuits in III-nitride layers bonded on SiO<sub>2</sub>, operating at 780 nm and containing a microdisk or microring, a waveguide, and grating couplers.
- The design and fabrication of passive suspended photonic circuits at 780 nm, consisting of a microdisk, a waveguide, and grating couplers in III-nitride layers grown on Si (100).
- Initial design considerations for degenerate parametric down-conversion and second-harmonic generation in III-nitride microrings on SiO<sub>2</sub>.

### 6.1 Introduction and state of the art

Two prominent platforms for photonic integrated circuits in the near-infrared (NIR) are silicon on insulator (SOI) [25] and InP [26]. However, non-linear effects, such as two-photon absorption, can occur in both Si [239] and InP [28], which reduce transmission. Si is only transparent for wavelengths longer than 1100 nm, and InP for wavelengths longer than 925 nm, as indicated in Fig. 6.1.

Next generation photonic devices require wide band gap materials for linear and non-linear applications from the ultraviolet (UV) to the NIR [7]. Promising platforms include silicon ni-

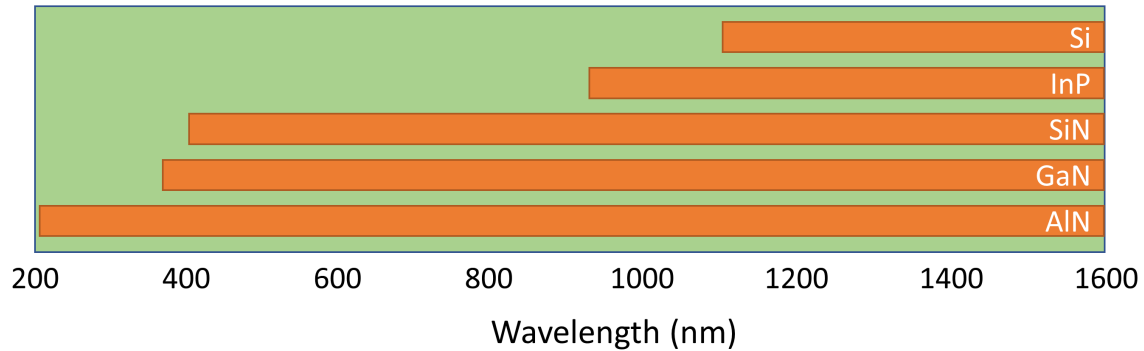


Figure 6.1: Transparency ranges of different materials that can be used for photonic circuits.

tride ( $\text{Si}_3\text{N}_4$ ) [240], aluminum oxide [204], and III-nitrides [39, 52, 241].  $\text{Si}_3\text{N}_4$  is transparent down to around 400 nm with very low waveguide losses of  $< 1 \text{ dB} \cdot \text{cm}^{-1}$  around 650 nm [7]. AlN is transparent down to 205 nm and GaN to 365 nm. The transparency windows of these materials are indicated in Fig. 6.1 for comparison. Of particular interest regarding III-nitrides are the large  $\chi(2)$  and  $\chi(3)$  optical non-linearities, which can be exploited for second- and third-harmonic generation (SHG and THG) [53–55, 242, 243], frequency combs [16, 38, 244], spontaneous parametric down-conversion [15], and optical parametric oscillators (OPOs) [18, 19]. For frequency combs and OPOs, very high-Q resonators are required to reduce the threshold to attainable powers. Figs. 6.2 (a)-(d) show the first on-chip OPO using AlN on sapphire [18]. Bruch et al. used microrings with intrinsic Q factors up to  $1 \times 10^6$  (see also Fig. 1 (c,d)) and achieved an OPO threshold of 12 mW. They pumped the microrings around 780 nm and observed signal and idler signals around 1560 nm, which could be tuned with temperature (see Fig. 6.2 (c,d)) [18]. Liu et al. demonstrated frequency combs using microrings in AlN on sapphire with loaded Q factors up to  $1.1 \times 10^6$  and a threshold of 25 mW [16, 244]. Figs. 6.2 (e)-(g) show the  $\chi(3)$  comb generation around 1560 nm and a subsequent  $\chi(2)$  frequency conversion to 780 nm.

Before the beginning of this thesis, our collaboration demonstrated suspended III-nitride microdisks coupled to waveguides with Q factors of  $8 \times 10^4$  at around 1550 nm (see Fig. 2 (b,c)) [52]. They also demonstrated phase-matched SHG in this platform [55]. In order to be able to reach OPO and comb thresholds, higher Q factors are required, which are more easily attainable with microrings than with microdisks, due to lower bending losses. In this chapter, we will thus investigate a platform that allows for the fabrication of microrings, based on III-nitrides bonded on  $\text{SiO}_2$ . As stated in the introduction, we present preliminary work of the Opoint project that started in 2020 with the goal of achieving OPOs.

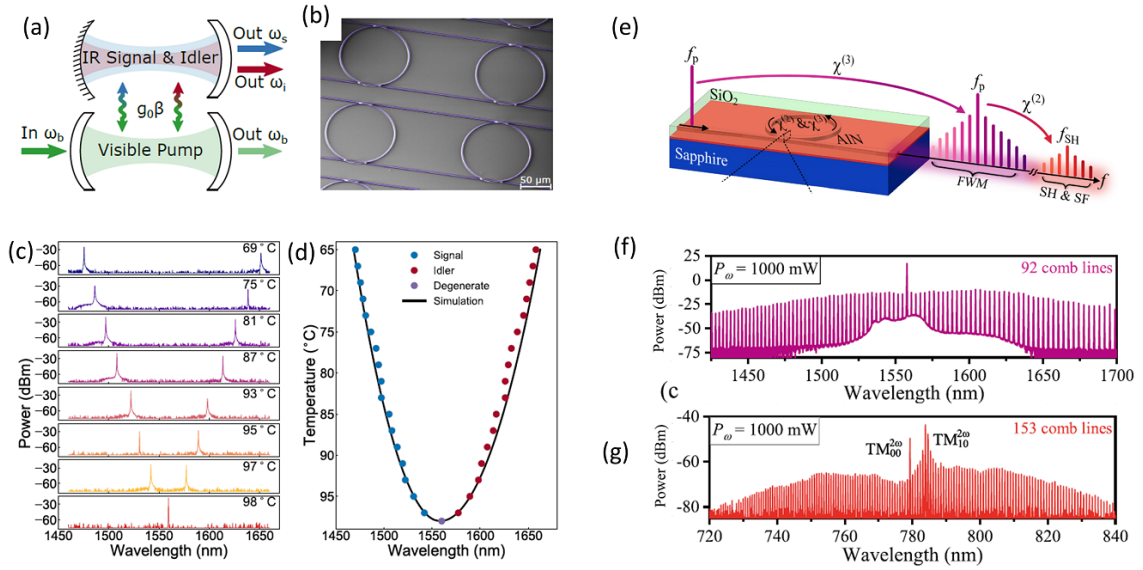


Figure 6.2: (a) OPO principle, (b) SEM image of microrings coupled to waveguides, (c) IR signal and idler signals for different temperatures, and (d) temperature over OPO wavelength, reproduced from Ref. [18]. (e) Schematic of  $\chi^{(3)}$  frequency comb generation and  $\chi^{(2)}$  frequency conversion, (f) frequency comb around 1560 nm and (g) frequency comb around 780 nm, reproduced from Ref. [244].

## 6.2 Design and fabrication of passive photonic circuits on SiO<sub>2</sub>

In order to fabricate microrings, we need a transparent substrate with a low refractive index to confine the optical mode in the ring by refractive index contrast in the vertical direction without the need for underetching. We use bonding and substrate removal to transfer a III-nitride layer grown on silicon onto SiO<sub>2</sub>.

Sample A2390 was grown on Si (111) by molecular beam epitaxy (MBE). First, a 50 nm AlN buffer layer was grown followed by 280 nm of GaN, as depicted in Fig. 6.3 (a). Using the process described in section 1.3.6 and Fig. 1.42, we deposited a 2  $\mu$ m plasma enhanced chemical vapor deposition (PECVD) SiO<sub>2</sub> layer on the sample and bonded it to a SiO<sub>2</sub>/Si carrier wafer using benzocyclobutene (BCB). We then removed the Si substrate through deep reactive ion etching (RIE). The final structure of the sample is shown in Fig. 6.3 (b).

Fig. 6.4 shows a photo of sample A2390 after bonding and substrate removal and before saw dicing. We can see some delaminated areas on the left and good areas on the right. The bonding of sample A2390 was performed by I. Sagnes and co-workers and the substrate removal by E. Herth at C2N.

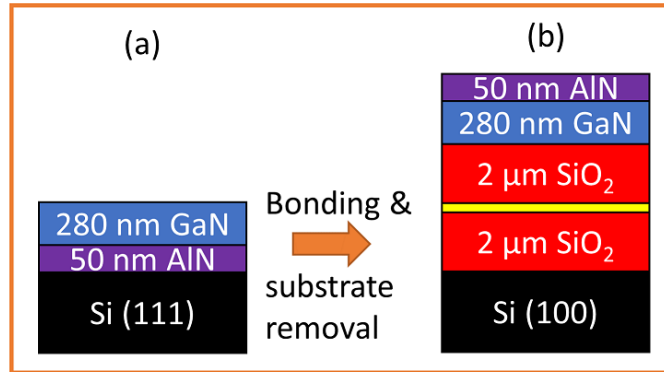


Figure 6.3: Sketches of samples A2390 (a) as grown and (b) after bonding and substrate removal.

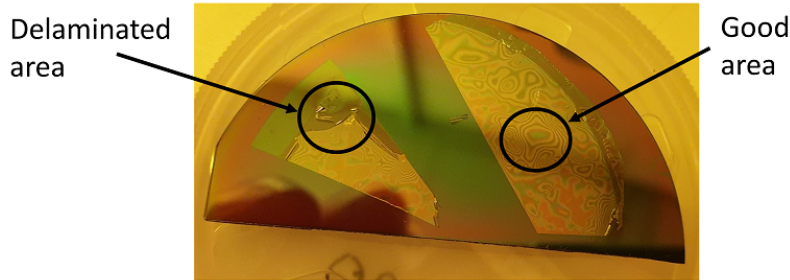


Figure 6.4: Photo of sample A2390 after bonding and substrate removal. Both delaminated and good areas are visible.

### 6.2.1 Choice of wavelength

Initially, we intended to use sample A2390 for photonic circuits operating around 1550 nm. However, simulations of the transverse mode profile of a waveguide using a 2D mode solver (EIMS [98]) indicated that the fundamental mode was not well confined in this layer thickness of 330 nm on SiO<sub>2</sub>, as depicted in Fig. 6.5 (a) for a waveguide width of 1200 nm. Only 76% of the TE<sub>00</sub> mode is confined in the III-nitride layer. While this sample is too thin for a wavelength of 1550 nm, it is well suited for 780 nm, as can be seen in Fig. 6.5 (b) for a waveguide width of 800 nm. The overlap of the TE<sub>00</sub> mode with the III-nitride layer is 94%.

We also performed 3D finite-difference time-domain (FDTD) simulations of 8 μm diameter disks coupled to straight waveguides at 1550 nm for different sample thicknesses on SiO<sub>2</sub>, depicted in Fig. 6.6. The thickness of 330 nm corresponds to sample A2390. The transmission spectrum shows low transmission and very low Q resonances due to the small overlap of the optical mode with the waveguide. A thicker layer is required for high Q resonances. For a thickness of 640 nm, we get a  $Q_{load}$  of 8k at 1543 nm (see Fig. 6.6), which is still rather low. Here, the Q factor is strongly limited by the radiation losses in this relatively small microdisk [190]. For a 13 μm diameter disk, the loaded Q factor near critical coupling increases to 48k for the thickness of 640 nm. This thickness corresponds to sample A2610, which we will discuss further in

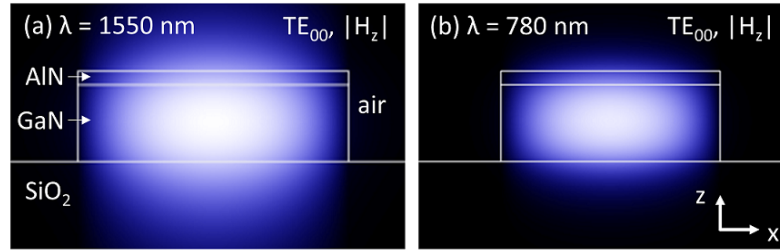


Figure 6.5: Transverse profiles of the  $|H_z|$  field of the  $TE_{00}$  mode for sample A2390 with (a) a waveguide width of 1200 nm at  $\lambda = 1550$  nm and (b) a waveguide width of 800 nm at  $\lambda = 780$  nm.

section 6.4. The radial and azimuthal mode orders are indicated as  $(n,m)$  in Fig. 6.6 for both layer thicknesses. First- and second-order radial modes are visible. For a given wavelength, the azimuthal mode order decreases with decreasing thickness due to a reduction in  $n_{eff}$ . For the thickness of 640 nm, the transmission drops nearly to zero for the mode at 1543 nm, indicating near-critical coupling. For some resonances (notably for even azimuthal orders), we observe splitting of the clockwise and counter-clockwise modes, which may be related to some artefacts in the simulation, possibly due to the limited resolution. Experimentally, this splitting can occur due to side-wall roughness of the microdisk.

### 6.2.2 Design of microring to waveguide coupling on A2390 at 780 nm

Since only the thin sample, A2390, was available, we designed passive photonic circuits around  $\lambda = 780$  nm to work towards a first demonstration of the utility of this III-nitride on SiO<sub>2</sub> photonic platform. All designs are for transverse-electric (TE) polarization.

For the design and fabrication of the microrings on sample A2390, we chose to work with ring diameters of 20  $\mu\text{m}$  and 60  $\mu\text{m}$ . The bending angle  $\theta$  of the waveguide around the microring was set to 90°. For the 20  $\mu\text{m}$  rings, we chose ring widths,  $WR$ , of 800 nm and 1200 nm. To have shorter simulation times, we used varFDTD simulations using Lumerical Mode Solutions [122] for the microrings, which is intended for waveguide and microring simulations and uses a 2.5D effective index approach. However, we need to keep in mind that this 2.5D method accounts for fewer loss mechanisms than 3D FDTD, thus resulting in larger simulated Q factors. For example, a 10  $\mu\text{m}$  diameter ring on A2610 (640 nm III-nitride on SiO<sub>2</sub>) with  $WR = 1050$  nm,  $WG = 900$  nm, and  $g = 500$  nm around  $\lambda = 1560$  nm has a loaded Q factor of 70k using 3D FDTD (MEEP [105]) and 340k using varFDTD (Lumerical Mode [122]).

Initially, we performed simulations with very short simulation times, which indicated critical coupling of first-order radial modes for a waveguide width,  $WG$  of 400 nm and a gap of 120 nm for  $WR = 800$  nm. However, the simulated transmission spectra showed strong oscillations, which indicates an insufficient simulation time. After fabricating samples with these initial parameters, we performed more rigorous simulations with significantly longer simulation

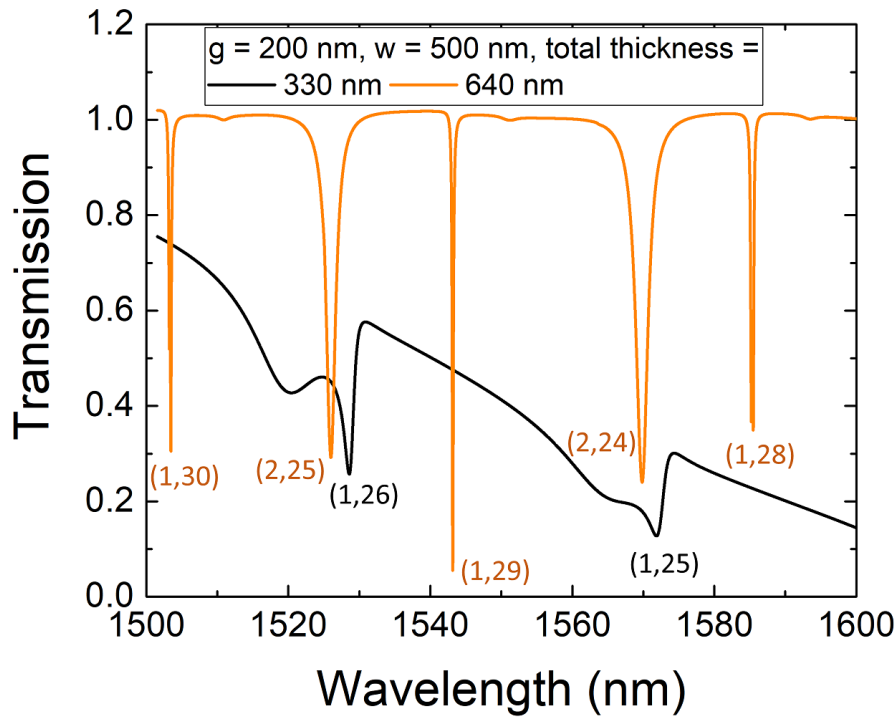


Figure 6.6: 3D FDTD simulations around 1550 nm of an 8  $\mu\text{m}$  diameter disk coupled to a straight waveguide with a width of 500 nm and a gap of 200 nm for two different III-nitride thicknesses on  $\text{SiO}_2$ . 330 nm corresponds to sample A2390 and 640 nm to A2610 (see section 6.4). The radial and azimuthal mode orders are indicated as (n,m) in the corresponding colors.

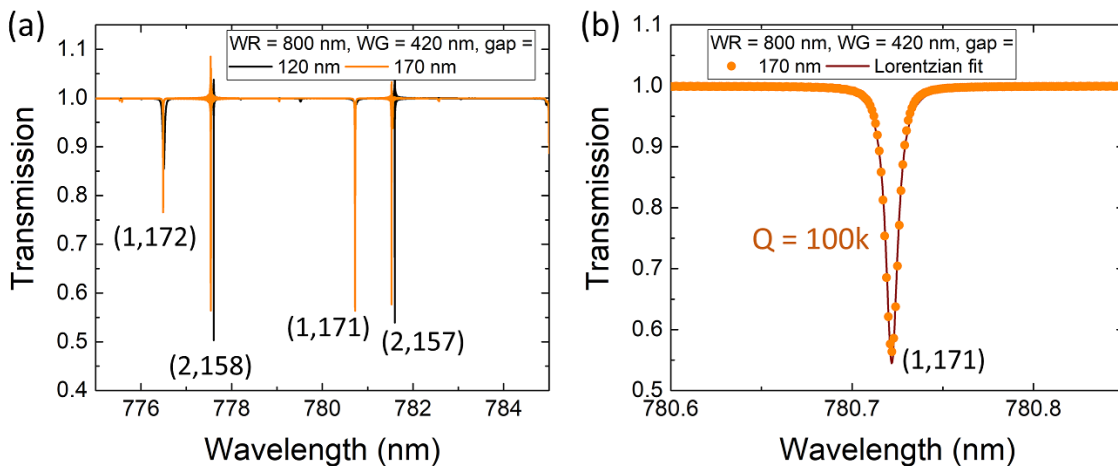


Figure 6.7: (a) VarFDTD transmission simulations of 20  $\mu\text{m}$  diameter microrings with 800 nm ring width, 420 nm waveguide width, and a 90° angle of the waveguide around the ring for gaps of 120 nm and 170 nm. Radial and azimuthal mode orders are indicated as (n,m). (b) Zoom-in of a first-order mode for the 170 nm gap showing a Q factor of 100k.

times and observed that critical coupling was achieved for larger gaps in the order of 200 nm for 20  $\mu\text{m}$  diameter rings (see Table 6.1). The fabricated microrings should thus operate in the over-coupled regime for first-order radial modes. For the 60  $\mu\text{m}$  diameter rings, the initial simulations suggested critical coupling at gaps of 100 nm for ring and waveguide widths of 400 nm. We have not yet been able to perform the required longer simulations for these large rings due to a lack of the necessary computing power.

sample	$d$ ( $\mu\text{m}$ )	$\theta$ ( $^\circ$ )	$WR$ (nm)	$WG$ (nm)	$g_{crit}$ (nm)	$g_{fab}$ (nm)
A2390	20	90	800	420	200	80-170
A2390	8	90	-	370	160-180	80-170
A2587	8	0	-	390	180-200	100-190

Table 6.1: Coupling parameters of first-order radial modes of microrings and microdisks on samples A2390 and A2587.

varFDTD transmission simulations of 20  $\mu\text{m}$  diameter microrings with  $WR = 800$  nm,  $WG = 420$  nm, and  $\theta = 90^\circ$  are shown in Fig. 6.7 (a) for gaps of 120 nm and 170 nm. The radial and azimuthal mode orders,  $(n,m)$ , are indicated. The devices operate in the over-coupled regime for all fabricated gap sizes. A close-up of the first-order mode at 780.7 nm for the 170 nm gap is shown in Fig. 6.7 (b) together with a Lorentzian fit giving a loaded Q factor of 100k. At  $g = 170$  nm, the device is not far from critical coupling, which is given for gaps around 200 nm (see Table 6.1). The second-order modes in Fig. 6.7 (a) have even higher Q factors, for example  $Q_{load} > 360\text{k}$  for the second-order mode at 781.5 nm. The simulation time and spectral resolution are not sufficient to determine their transmission dips precisely. The free spectral range (FSR) is 4.2 nm between first-order and 4.0 nm between second-order radial modes.

### 6.2.3 Design of microdisk to waveguide coupling on A2390 at 780 nm

Besides microrings, we also wanted to fabricate microdisks coupled to bent waveguides. To design such a coupling region, we use 3D FDTD using MEEP [105], as discussed in section 1.2.8.2 and as used previously in chapters 3 and 4. Fig. 6.8 (a) shows transmission spectra of 8  $\mu\text{m}$  diameter disks with 370 nm waveguide width,  $\theta = 90^\circ$ , and gaps of 140 nm to 180 nm on sample A2390 (330 nm III-nitride on SiO<sub>2</sub>). Three first-order radial modes with azimuthal orders 64, 63, and 62 are visible with a FSR of 10 nm. We can see some oscillations for the 160 nm and 180 nm gaps, which means that a slightly longer simulation time would be required to more accurately determine the Q factors and the transmission minima. However, these simulations already took around 10 days. A close-up of the mode at 779.2 nm is depicted in Fig. 6.8 (b), the inset shows the xy-cross-section of the  $H_z$  field of the mode. Near-zero transmission is observed for gaps of 160 nm and 180 nm, indicating near-critical coupling. A Lorentzian fit depicts a loaded Q factor in the range of 136k for the 160 nm gap. The smaller gaps are in the over-coupled regime and have smaller  $Q_{load}$ . The coupling parameters are summarized in

Table 6.1.

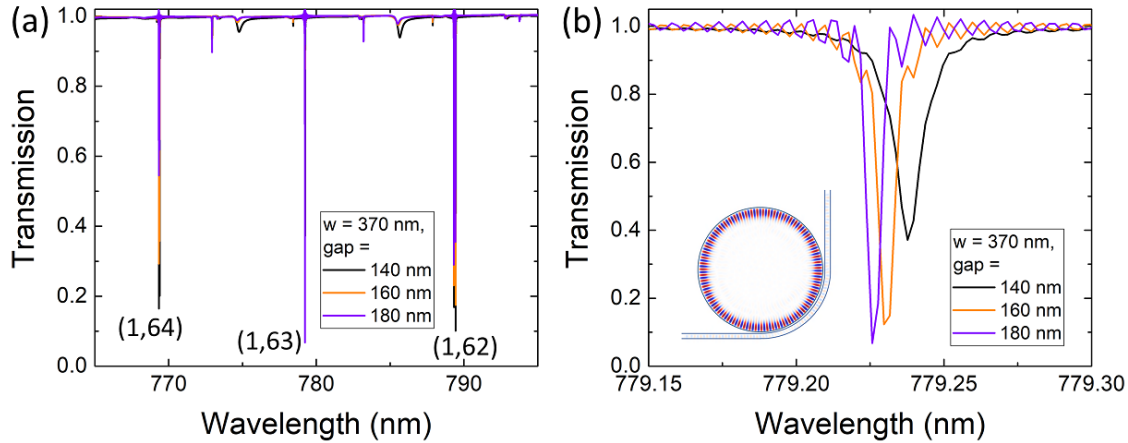


Figure 6.8: (a) 3D FDTD transmission simulation of  $8\mu\text{m}$  diameter microdisks with 370 nm waveguide width, and a  $90^\circ$  angle of the waveguide around the disk for gaps of 140 nm to 180 nm for sample A2390. Radial and azimuthal mode orders are indicated as  $(n,m)$ . (b) Zoom-in of a first-order mode at 779.2 nm. The inset shows the  $H_z$  field of the mode with  $m = 63$ .

#### 6.2.4 Design of grating couplers on A2390 at 780 nm

For grating couplers, we use 2D FDTD simulations of the  $xz$ -cross-section, as discussed in section 1.2.8.4. Our grating coupler design is not optimized, but should be sufficient for an initial demonstration of this photonic platform. A full optimization will be done in future work.

Fig. 6.9 shows simulations of the  $E_y$  field for TE-polarization of fully etched grating couplers with different grating periods on sample A2390 operating at 780 nm (Gaussian pulse source with 10 nm width) with a fill-factor of 70%, except for the first two periods, which have a fill-factor of 80% to reduce reflection. The grating period increases from 480 nm in Fig. 6.9 (a) to 520 nm in Fig. 6.9 (c). The emission angle for  $\lambda = 780$  nm changes from  $8^\circ$  for  $P = 480$  nm to  $16^\circ$  for  $P = 520$  nm. In order to be able to couple to two optical fibers without their holders being too close together, a coupling angle in the range of  $10$  to  $20^\circ$  is ideal. Fig. 6.9 (d) shows simulated transmission spectra of gratings with different periods using a mono-mode fiber (780-HP Nufern) at a  $10^\circ$  angle. The spectra red-shift with increasing grating period. While the largest transmission is observed for a period of 520 nm, a 500 nm period is more suited for collecting emission around 780 nm. In Fig. 6.9 (e), we show simulated transmission spectra for  $P = 500$  nm and different angles of the mono-mode optical fiber. The maximum transmission of 26.4% is obtained at 773 nm for an angle of  $10^\circ$ .

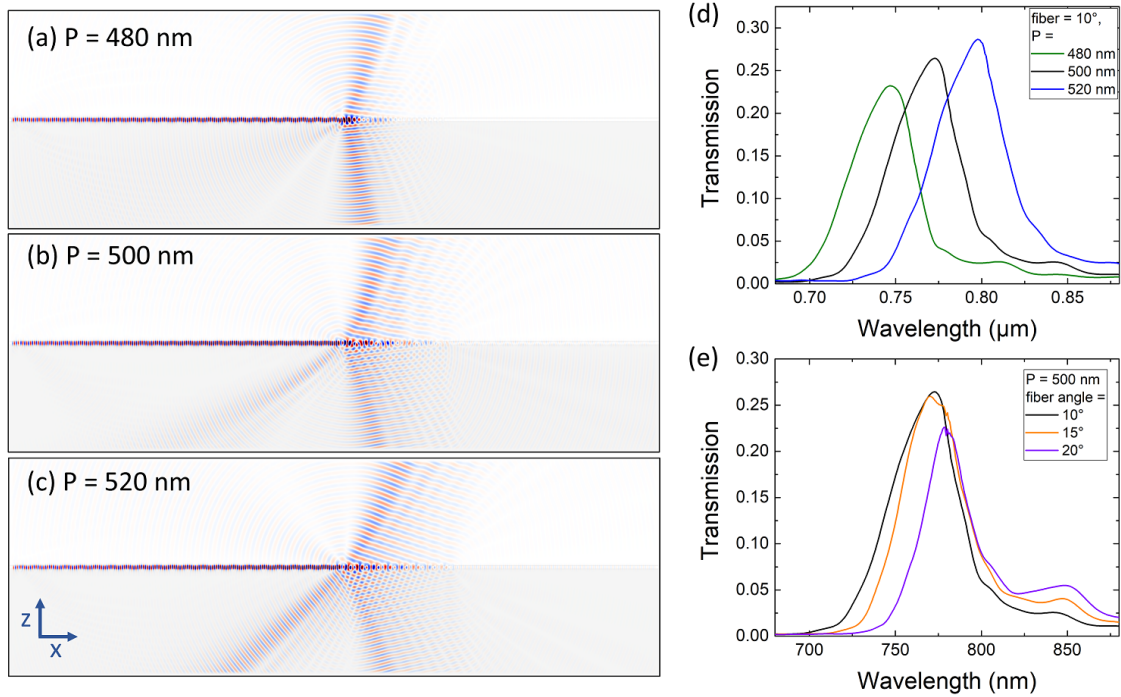


Figure 6.9: 2D FDTD simulations of the  $E_y$  field of a waveguide with grating coupler for sample A2390 for a Gaussian pulse at 780 nm with a 10 nm pulse width with a fill-factor of 70% and a period and emission angle of (a) 480 nm and  $8^\circ$ , (b) 500 nm and  $11^\circ$ , and (c) 520 nm and  $16^\circ$ , respectively. Simulated transmission spectra of (d) gratings with different periods and a mono-mode fiber at a  $10^\circ$  angle and (e) a grating with 500 nm period and different fiber angles.

### 6.2.5 Fabrication of microring and microdisk photonic circuits on A2390 at 780 nm

Using the process described in Fig. 1.42, we fabricated passive photonic circuits consisting of a microring or microdisk and a bus waveguide terminated by grating couplers on sample A2390. We fabricated  $20\mu\text{m}$  diameter rings with ring widths  $WR$  of 800 nm and 1200 nm,  $60\mu\text{m}$  diameter rings with  $WR$  of 360 nm to 400 nm, and  $8\mu\text{m}$  diameter disks. The total device length is  $400\mu\text{m}$ . Optical microscope and SEM images of the microring devices are shown in Fig. 6.10. Figs. 6.10 (a-c) show the  $60\mu\text{m}$  diameter rings and (d-f) the  $20\mu\text{m}$  diameter rings. In Figs. 6.10 (c) and (f), we can see close-ups showing the ring to waveguide coupling region. At the large magnification of Fig. 6.10 (c), we can see some side-wall roughness.

Fig. 6.11 shows the photonic circuits with  $8\mu\text{m}$  diameter disks. Optical microscope images are depicted in Figs. 6.11 (a) and (b). A microdisk with bent waveguide can be seen in Fig. 6.11 (c) and part of a waveguide in Fig. 6.11 (d). A grating coupler with a nominal 500 nm period and 70% fill-factor (80% for the first two periods) is depicted in Fig. 6.11 (e), as well as a close-up of it in Fig. 6.11 (f). From Fig. 6.11 (f), we determine the actual fill-factor of the grating to be

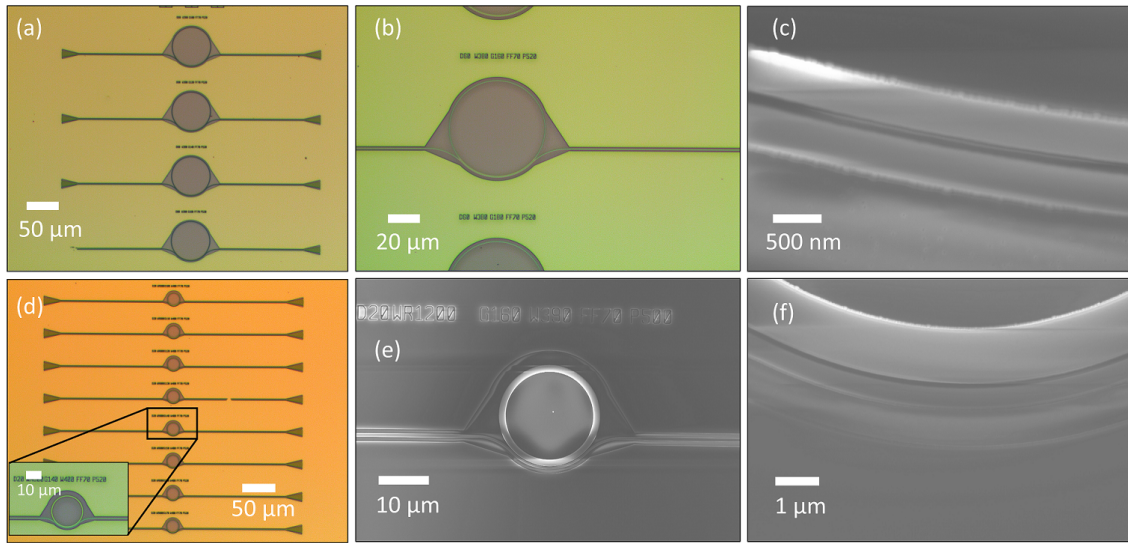


Figure 6.10: Optical microscope and SEM images of passive microring photonic circuits fabricated on A2390. (a,b) Optical microscope and (c) SEM image of devices with  $60\mu\text{m}$  diameter rings. (d) Optical microscope and (e,f) SEM images of devices with  $20\mu\text{m}$  diameter rings. The inset in (d) shows a zoom-in of the ring.

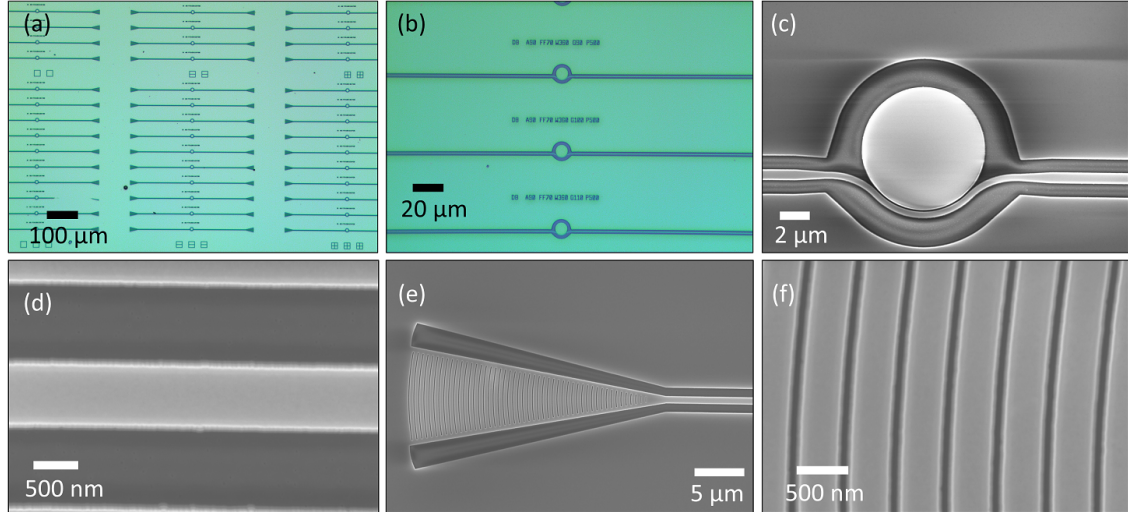


Figure 6.11: Optical microscope and SEM images of passive microdisk photonic circuits fabricated on A2390. (a,b) Optical microscope and (c) SEM image of a microdisk device. SEM images of (c) a piece of waveguide, (e) a grating coupler with  $500\text{nm}$  period and  $70\%$  fill factor and (f) a zoom-in of the grating shown in (e).

around  $72\%$  at the top and  $89\%$  at the bottom (faint color contrast between III-N and  $\text{SiO}_2$ ). This variation is expected to have an influence on the emission angle of the grating. Using an average fill-factor of  $80\%$  in the FDTD simulation, we get an angle of  $22^\circ$  for the  $500\text{nm}$  period. It will be important to verify this experimentally.

As previously mentioned in section 1.3.6, a fabrication challenge was to find the good doses

for e-beam lithography, due to the insulating  $\text{SiO}_2$  substrate. We used a smaller dose of  $0.25 \text{ C} \cdot \text{m}^{-2}$  for the disk and waveguide and increased the dose for the grating couplers to  $0.30 \text{ C} \cdot \text{m}^{-2}$ . When using a larger dose for the waveguide it would lift off and move. For the gap between the disk/ring and the waveguide, we also used a dose of  $0.30 \text{ C} \cdot \text{m}^{-2}$ . We encountered problems with  $\text{SiO}_2$  etching following regular machine maintenance that required a small change in etch parameters to find once again fairly smooth and vertical side-walls.

### 6.3 Design and fabrication of passive photonic circuits suspended on Si(100)

The heterostructure of sample A2587 consists of 330 nm AlN grown by MBE on Si (100), as depicted in Fig. 6.12 (a). This structure is of particular interest because it was grown on "standard" silicon, which allows the use of up to 300 mm substrates, as well as more easy integration of CMOS functions. When growing on Si (100), we are limited to thin layers of AlN, up to around 400 nm before the layer starts cracking. An atomic force microscopy (AFM) image of sample A2587 is shown in Fig. 6.12 (b). The root mean square (RMS) roughness is 1 nm, which is a factor 2 higher than what we usually have on Si (111) for an equivalent structure. The material quality is lower on Si (100) because there are two in-plane epitaxial relationships,  $\langle 01 - 10 \rangle$  and  $\langle -2110 \rangle$  AlN on  $[110]$  Si with a  $30^\circ$  angle between the two, which causes an increased number of defects [245]. Along the growth axis the relationship is  $[0001]$  AlN on  $[001]$  Si. On Si (111), for comparison, the epitaxial relationship in the plane is  $\langle 11 - 20 \rangle$  AlN on  $[1 - 10]$  Si.

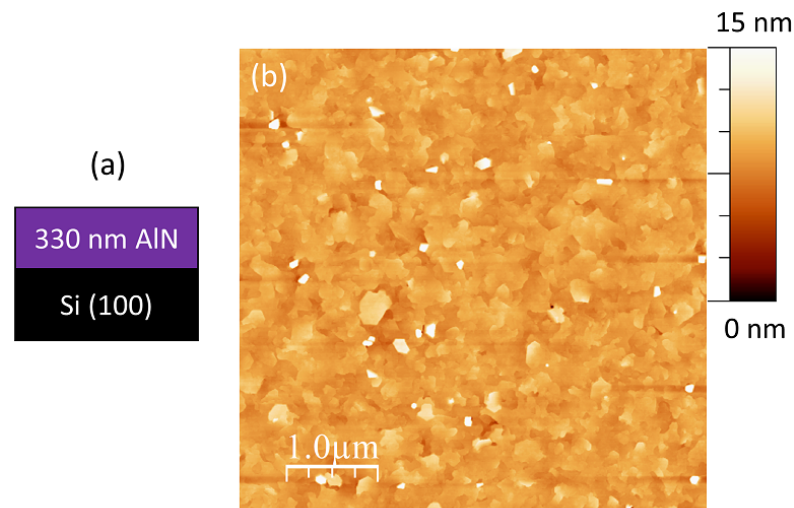


Figure 6.12: (a) Heterostructure of A2587. (b) AFM image of A2587 with 1 nm RMS roughness, measured by A. Courville at CRHEA.

For sample A2587, we have a similar situation regarding the choice of wavelength as we did for A2390. Fig. 6.13 shows the calculated  $|H_z|$  field for the  $\text{TE}_0$  mode in 1D (slab waveguide)

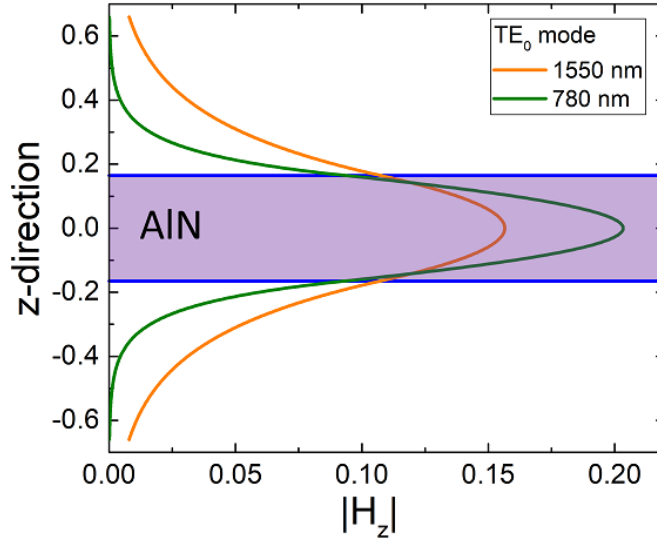


Figure 6.13: Calculation of the  $|H_z|$  field of the  $TE_0$  mode in 1 dimension (slab waveguide) for 1550 nm and 780 nm for A2587 suspended in air.

at 1550 nm and 780 nm, using a 1D mode solver software (OMS [97]). We can clearly see that the mode at 780 nm is much better confined in the AlN layer than the mode at 1550 nm. The overlap is 75% at 1550 nm and 95% at 780 nm. We consequently chose an operating wavelength around 780 nm for this sample.

### 6.3.1 Design of microdisk to waveguide coupling on A2587 at 780 nm

For sample A2587, we are limited to mushroom-type microdisks, since we did not perform a bonding and substrate removal step. 3D FDTD (MEEP [105]) transmission simulations of  $8\mu\text{m}$  diameter disks with 390 nm waveguide width and straight waveguides are shown in Fig. 6.14 (a) for gaps of 140 nm to 180 nm. Two first- and two second-order radial modes are visible with FSRs of 11.4 nm and 11.7 nm, respectively. The azimuthal mode orders are 55 and 54 for the first-order and 50 and 49 for the second-order radial modes, as indicated in Fig. 6.14 (a). The simulation time is not sufficient to accurately determine the loaded Q factor of first-order modes, as indicated by the oscillations around the modes, but it is certainly more than 150k for the 180 nm gap. A close-up of the mode at 773.3 nm is shown in Fig. 6.14 (b), the inset shows the xy-cross-section of the  $H_z$  field of the mode. The transmission drops near zero, suggesting near-critical coupling. The smaller gap is over-coupled. As mentioned before, initial simulations with shorter simulation time suggested smaller gaps at critical coupling, based on which we fabricated the sample discussed hereafter. For the second-order mode at 780 nm, we estimate a Q factor of 100k from the 180 nm gap spectrum. The coupling parameters for first-order radial modes are summarized in Table 6.1.

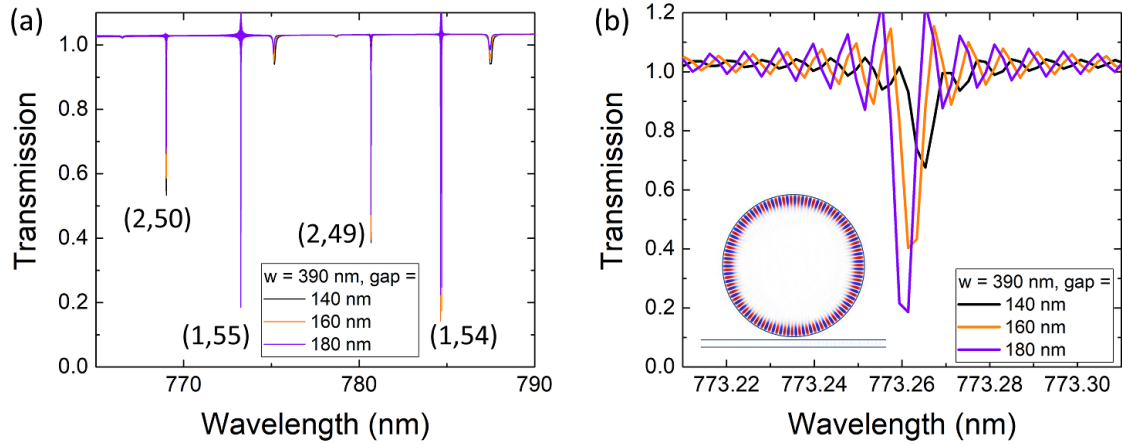


Figure 6.14: (a) FDTD transmission simulation of  $8\mu\text{m}$  diameter microdisks with 390 nm waveguide width, and straight waveguides for gaps of 140 nm to 180 nm for sample A2587. Radial and azimuthal mode orders are indicated as  $(n,m)$ . (b) Zoom-in of a first-order mode at 773.3 nm. The inset shows the  $H_z$  field of the mode with  $m = 55$ .

### 6.3.2 Design of grating couplers on A2587 at 780 nm

2D FDTD simulations of the  $E_y$  field of fully etched grating couplers on sample A2587 (330 nm AlN) are shown in Fig. 6.15. They have a fill-factor of 70% (first two periods 80%). The grating period varies from 560 nm in Fig. 6.15 (a) to 600 nm in Fig. 6.15 (c) and the emission angle for a mode at 780 nm changes from  $10^\circ$  to  $18^\circ$ . For the period of 600 nm (Fig. 6.15 (c)), there is a strong reflection. Consequently, the period of 580 nm should be best for measuring the transmission. Fig. 6.15 (d) shows simulated transmission spectra of gratings with different periods using a mono-mode fiber (780-HP Nufern) at a  $15^\circ$  angle. The transmission spectra are red-shifted with increasing period, while the shape of the curve stays fairly constant. In Fig. 6.15 (e), simulated transmission spectra of a grating with  $P = 580$  nm and different angles of a mono-mode fiber are shown. The maximum transmission of 32.4% is obtained for an angle of  $15^\circ$  at 783 nm. Comparing these gratings to the ones of sample A2390 (330 nm III-nitride on  $\text{SiO}_2$ ), we can see that here slightly larger periods are needed for the same emission angles due to the lower refractive index of AlN as compared to GaN. Furthermore, the transmission is 6% higher.

### 6.3.3 Fabrication of suspended microdisk photonic circuits on A2587 at 780 nm

Using the process described in Fig. 1.41, we fabricated suspended passive photonic circuits consisting of an  $8\mu\text{m}$  diameter disk and a waveguide terminated by grating couplers. The total device length is  $400\mu\text{m}$ . An SEM image of a full device is depicted in Fig. 6.16 (a). A micro-

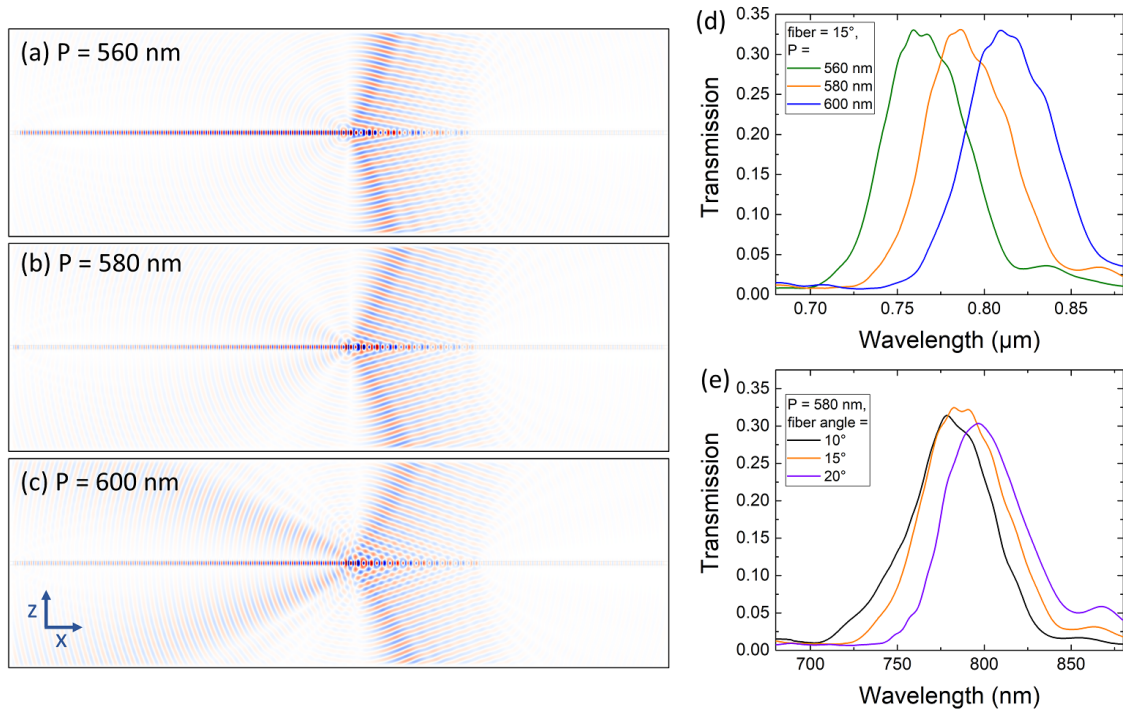


Figure 6.15: 2D FDTD simulations of the  $E_y$  field of a waveguide with grating coupler for sample A2587 for a Gaussian pulse at 780 nm with a width of 10 nm. The gratings have a fill-factor of 70% (except for the first two periods, which have a fill-factor of 80%). The grating periods and emission angles are (a) 560 nm and  $10^\circ$ , (b) 580 nm and  $15^\circ$ , and (c) 600 nm and  $18^\circ$ , respectively. Simulated transmission spectra for (d) different grating periods with a mono-mode fiber at  $15^\circ$  and (e) a 580 nm period grating and a mono-mode fiber at different angles.

disk with straight waveguide is shown in Fig. 6.16 (b) with a zoom-in of the coupling region depicted in (c). A grating coupler is shown in Fig. 6.16 (d). We have had some difficulty with the suspension of devices on this sample due to the strain in the AlN layer that is released when underetching. We previously did not have any problems underetching samples consisting of 50 nm AlN and 280 nm GaN with the same total thickness of 330 nm [55]. This is due to the fact that AlN is tensilely strained on Si and GaN is compressively strained on AlN. Thus GaN allows to mitigate the strain. Upon releasing the tensilely strained AlN layer, many of the nanotethers that hold the devices cracked. We have tried using nanotethers of different sizes from 100 nm to 300 nm on the waveguide side and 300 nm to 600 nm on the other side. Fig. 6.17 (a) shows a partly broken and (b) a fully broken set of nanotethers. We also encountered problems with the suspension of disks with bent waveguides, as can be seen in Fig. 6.18 (a). Some grating couplers also broke and fell partially, as depicted in Fig. 6.18 (b).

In future work, we will aim towards improving the growth of the AlN buffer layer on Si (100) with the goal of having only one epitaxial relationship, either one of the two mentioned previously, which could be achieved by using a  $4$  to  $6^\circ$  disoriented Si (100) substrate, for example

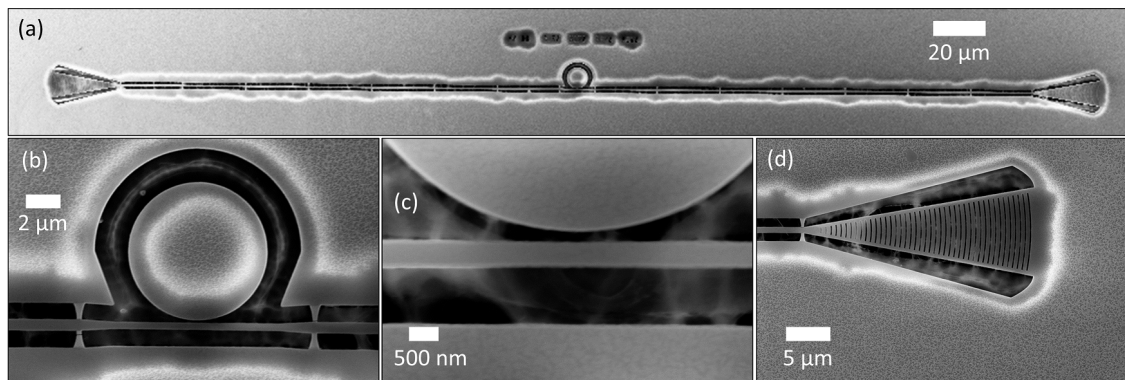


Figure 6.16: SEM images of suspended passive photonic circuits fabricated on A2587, showing (a) a full device (b) a microdisk coupled to a straight waveguide, (c) a zoom-in of the coupling region, and (d) a grating coupler.

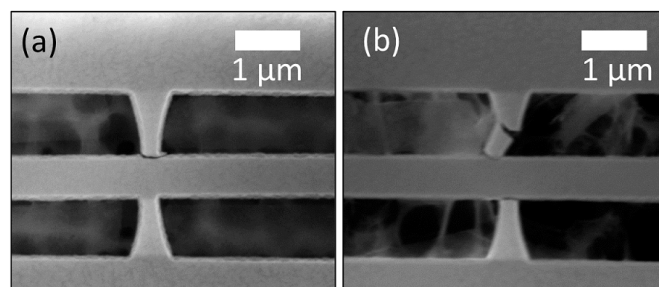


Figure 6.17: SEM images of (a) a partially and (b) a fully broken pair of nanotethers on sample A2587.

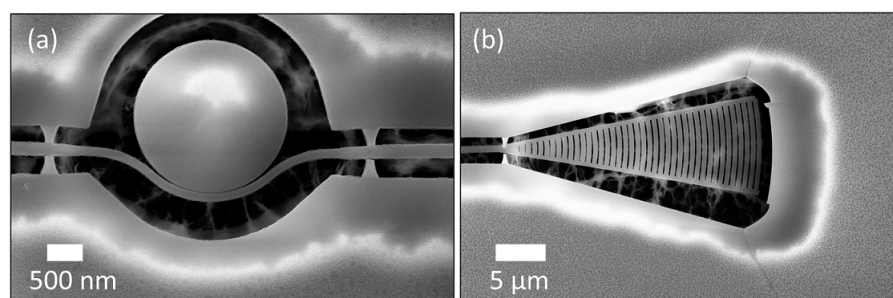


Figure 6.18: SEM images of (a) a microdisk with partially fallen bent waveguide and (b) a fallen grating coupler.

[245]. Certainly, a next step would be to grow GaN on such a sample and fabricate suspended passive photonic circuits for the NIR around 1550 nm. Next, we could grow InGaN QWs and try to fabricate individual mushroom-type microdisk resonators and lasers. If this works, we could proceed to active circuits like the ones we discussed in chapter 3. Using Si (100) as the substrate for such circuits would allow to ultimately go to a 300 mm wafer size and a potential CMOS integration.

## 6.4 Design of a microring photonic circuit on SiO<sub>2</sub> for degenerate parametric down-conversion and SHG

While samples A2390 (330 nm III-nitride on SiO<sub>2</sub>) and A2587 (330 nm AlN) are too thin for operation around 1550 nm, sample A2610 (640 nm III-nitride on SiO<sub>2</sub>) is a good candidate for this wavelength range and consequently for non-linear frequency conversion due to the large  $\chi(2)$  and  $\chi(3)$  non-linearities. The most important component of the  $\chi(2)$  tensor is the  $\chi(2)_{zzz}$  component, which allows for TM/TM mode coupling [55]. With the here investigated sample, we are interested in achieving high loaded Q factors near-critical coupling around 780 nm and 1560 nm. We further want to achieve degenerate (and non-degenerate) parametric down-conversion and inversely SHG in microrings with this sample, similar to what Guo et al. and Bruch et al. have demonstrated in Refs. [15, 18, 242]. Very high loaded Q factors and phase-matched parametric frequency conversion are prerequisites for OPO, in which above a certain threshold power the frequency converted signal and idler waves get amplified through parametric gain, similar to a laser. Since we have so far only investigated TE modes in the previous chapters, we will continue this here, even though these modes would not show any non-linear coupling. We still discuss the simulations as though these modes would couple to demonstrate the need for phase matching. By studying TE modes, we can still verify that we have high Q factors and efficient microring to waveguide coupling at the two wavelengths of interest. A future design will consider TM modes.

To achieve efficient frequency conversion, energy and momentum need to be conserved, that is

$$\omega_p = \omega_s + \omega_i \Rightarrow \frac{1}{\lambda_p} = \frac{1}{\lambda_s} + \frac{1}{\lambda_i}, \quad (6.1)$$

$$k_p = k_s + k_i \Rightarrow \frac{n_p}{\lambda_p} = \frac{n_s}{\lambda_s} + \frac{n_i}{\lambda_i} \quad (6.2)$$

with wavevector  $k$ , refractive index  $n$ , wavelength  $\lambda$ , and angular frequency  $\omega$ . The subscripts  $p$ ,  $s$ , and  $i$  stand for pump, signal, and idler, respectively, in the description commonly used for parametric down-conversion. Here  $\lambda_p$  is at a shorter wavelength, for example, around 780 nm, in our case. Of the two output waves, the shorter wavelength, higher energy one is called the signal and the longer wavelength, lower energy one the idler wave.

Since the azimuthal mode order  $m$  is proportional to  $n/\lambda$ , it follows from Eq. 6.2 that

$$m_p = m_s + m_i. \quad (6.3)$$

In the case of degenerate frequency conversion, signal and idler are the same, that is  $\lambda_s = \lambda_i$  and Eqs. 6.1, 6.2, and 6.3 become

$$\lambda_s = 2\lambda_p, \quad (6.4)$$

$$n_p = n_s, \quad (6.5)$$

$$m_p = 2m_s. \quad (6.6)$$

Eqs. 6.4, 6.5, and 6.6 describe both parametric conversion and the inverse case, SHG, in which two photons of the same frequency combine to create a photon at double the frequency, i.e. two photons at 1560 nm combine and create a photon at 780 nm. In this case, the indices  $p$  and  $s$  should be switched.

Due to chromatic dispersion inside a material (see Fig. 1.7), Eq. 6.5 is generally not true. In a microring, phase-matching can be achieved by careful selection of a higher order optical mode at the pump wavelength, that has the same  $n_{eff}$  as the signal mode [242].

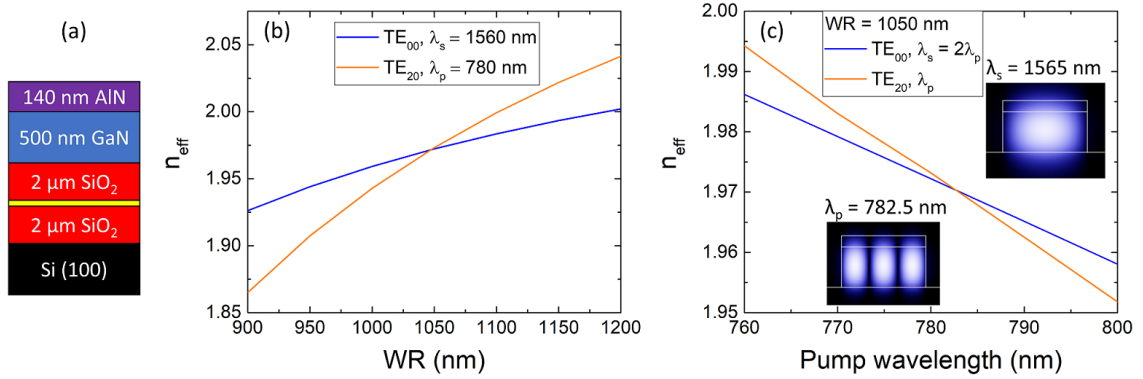


Figure 6.19: (a) Structure of sample A2610. Effective refractive index over (b) microring width and (c) wavelength. Insets in (c):  $|H_z|$  field of the TE<sub>00</sub> mode at 1565 nm and the TE<sub>20</sub> mode at 782.5 nm.

We propose an initial design for a double-resonant microring with the goal of demonstrating degenerate parametric-down conversion (and inversely SHG) with  $\lambda_p$  around 780 nm and  $\lambda_s$  around 1560 nm. We investigate sample A2610, whose structure is depicted in Fig. 6.19 (a) after bonding on SiO<sub>2</sub> and substrate removal. The sample was grown on Si (111) by MBE. First, a 140 nm AlN buffer layer was grown, followed by 500 nm of GaN.

In this case, 93% of the TE<sub>0</sub> mode of a slab waveguide at 1560 nm is confined in the 640 nm thick III-nitride layer, which should allow for high Q resonances.

In Fig. 6.19 (b), we show  $n_{eff}$  over the waveguide width for the TE<sub>00</sub> mode at 1560 nm and the TE<sub>20</sub> mode at 780 nm, calculated using a 2D mode solver (EIMS [98]). The two curves cross at a waveguide width of around 1047 nm. Fig. 6.19 (c) depicts  $n_{eff}$  over the wavelength for a waveguide width of 1050 nm. The crossover is around  $\lambda_p = 782.5$  nm. The insets show the xz-cross-section of the  $|H_z|$  field of the TE<sub>00</sub> mode at  $\lambda_s = 1565$  nm and the TE<sub>20</sub> mode at  $\lambda_p = 782.5$  nm, which have the same  $n_{eff}$ . In TM polarization, this crossing is predicted to

occur for a waveguide width of 765 nm and a lower  $n_{eff}$  of 1.83.

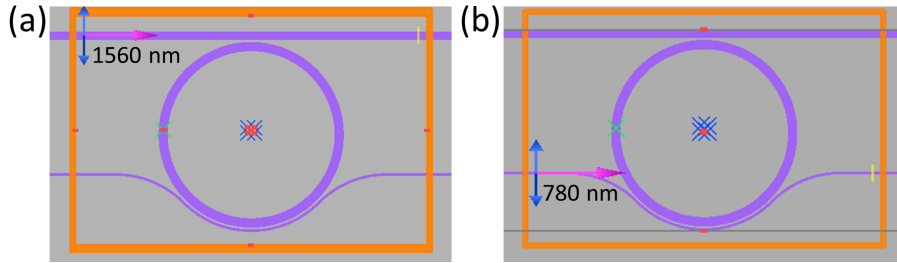


Figure 6.20: Xy-view of the CAD layout of the varFDTD simulation region. The top waveguide is for 1560 nm and the bottom waveguide for 780 nm. In (a) the source is in the 1560 nm waveguide and in (b) in the 780 nm waveguide.

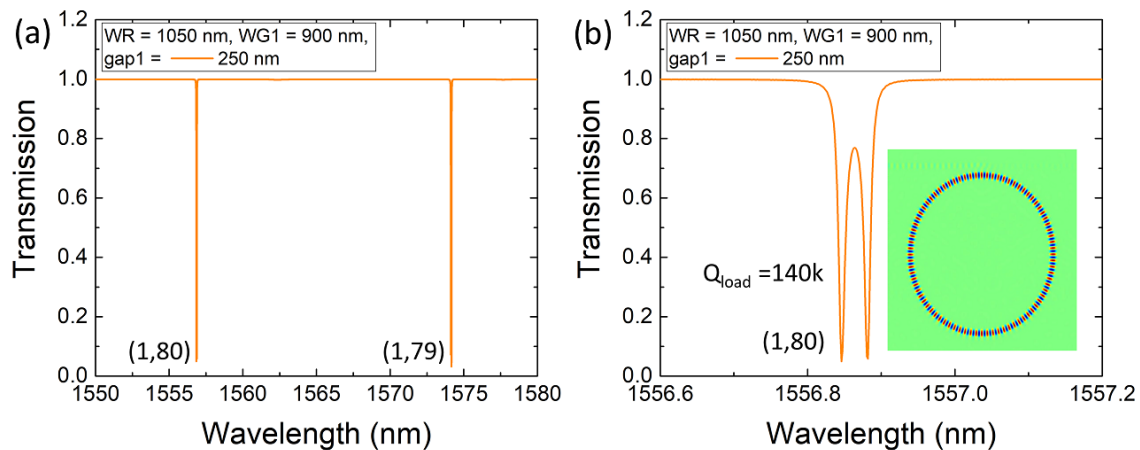


Figure 6.21: (a) VarFDTD transmission spectra of a 20  $\mu\text{m}$  diameter ring with  $WR = 1050$  nm and  $WG = 900$  nm and different gaps for sample A2610 around  $\lambda = 1560$  nm. The radial and azimuthal orders are indicated as (n,m). (b) Close-up of the resonance at 1556.9 nm.

Next, we need to design two separate coupling regions for efficient coupling at both pump and signal wavelengths. The CAD layout of the varFDTD simulation is shown in Fig. 6.20. In Fig. 6.20 (a), a 1565 nm mode source is injected into the top waveguide, while in (b) a 780 nm mode is injected into the bottom waveguide. In the simulation, both waveguides are present to ensure that there is no unwanted coupling with the other waveguide. We start by looking at the  $TE_{00}$  mode at  $\lambda_s$ . Fig. 6.21 (a) shows simulated transmission spectra of 20  $\mu\text{m}$  diameter rings with a straight waveguide for sample A2610 around  $\lambda = 1565$  nm using Lumerical Mode [122]. We use  $WR = 1050$  nm and  $WG = 900$  nm and different coupling gaps. The FSR of the first-order radial modes (or  $TE_{00}$  modes) is 17.3 nm. A close-up of the mode at 1556.9 nm is depicted in Fig. 6.21 (b). The mode is split in two due to the lifting of the degeneracy of clockwise and counter-clockwise modes, which can be caused by backscattering related to an insufficient mesh accuracy in the simulation. For a gap of 250 nm, the transmission nearly goes to 0, indi-

cating near-critical coupling. The loaded Q factor for the 250 nm gap is around 140k. Furthermore, we note that the here presented microring simulations are of low accuracy in both time and space to reduce the simulation time and that the mode positions can shift as accuracy is increased. We limited the diameter to  $20\mu\text{m}$  in our simulation due to limited computing power. The Q factors are larger with varFDTD as opposed to 3D FDTD, as fewer loss mechanisms are taken into account.

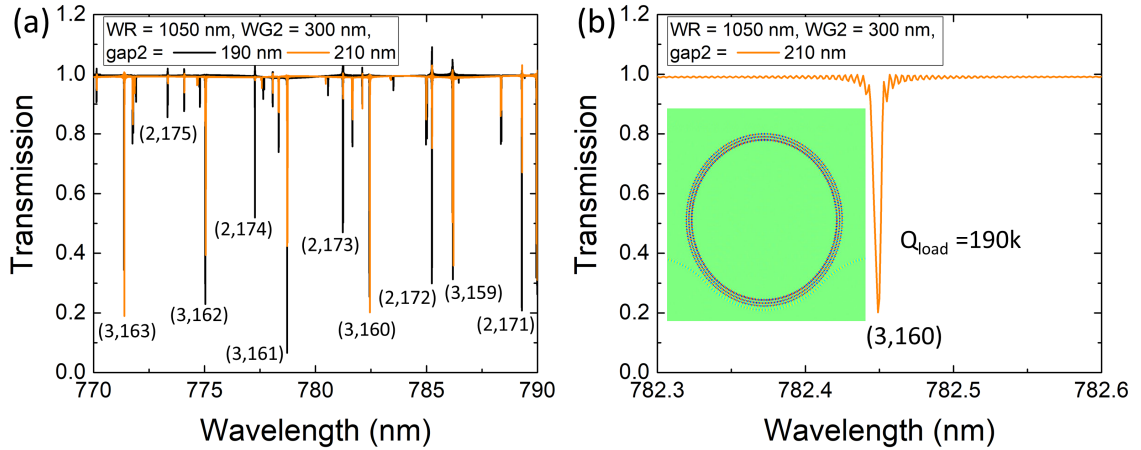


Figure 6.22: (a) VarFDTD transmission spectrum of a  $20\mu\text{m}$  diameter ring with  $WR = 1050\text{ nm}$ ,  $WG = 300\text{ nm}$ ,  $\theta = 90^\circ$ , and gaps of 170 nm to 210 nm for sample A2610 around  $\lambda = 780\text{ nm}$ . The radial and azimuthal orders are indicated as  $(n,m)$ . (b) Close-up of the resonance at 782.43 nm for the 190 nm gap near critical coupling with a  $Q_{load}$  of 220k and the xy-cross-section of its  $H_z$  field.

Next, we design the coupling region for the  $\text{TE}_{20}$  mode at  $\lambda_p$ . Fig. 6.22 (a) shows simulated transmission spectra of a  $20\mu\text{m}$  diameter ring with  $WR = 1050\text{ nm}$ ,  $WG = 300\text{ nm}$ , and  $\theta = 90^\circ$  for gaps of 190 nm and 210 nm. The third-order radial modes or  $\text{TE}_{20}$  modes are near-critical coupling and have an FSR of 3.7 nm. Fig. 6.22 (b) depicts a close-up of the mode (3,160) around 782.45 nm showing a  $Q_{load}$  of 190k for the 210 nm gap. The inset depicts the xy-cross-section of the  $H_z$  field of this mode.

The two modes we investigated in Figs. 6.21 and 6.22 fulfil Eq. 6.6 ( $m_p = 160$  and  $m_s = 80$ ). However, we note that the two wavelengths do not quite fulfil Eq. 6.4, due to a slight mismatch in effective indices as compared to Fig. 6.19. Fig. 6.23 shows Eq. 6.4 as a function of the ring width for the modes (1,80) around 1560 nm and (3,160) around 780 nm. A linear fit indicates that phase-matching is achieved for a ring width of around 1000 nm. The discrepancy with Fig. 6.19 is due to the small change in  $n_{eff}$  caused by the waveguide bend. We thus have a first set of parameters for bus waveguides for injecting and collecting light around 780 nm and 1560 nm for  $20\mu\text{m}$  diameter microrings with a ring width of 1000 nm to 1050 nm that allows for phase-matching of the  $\text{TE}_{00}$  mode around 1560 nm with the  $\text{TE}_{20}$  mode around 780 nm, as depicted in Fig. 6.19 (c) and Fig. 6.23. Experimentally, we can achieve phase matching by slightly varying the ring width across the sample. Ideally, we need to design larger microrings in

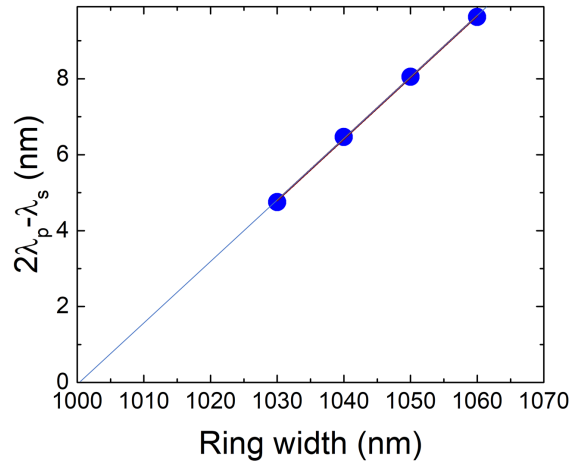


Figure 6.23: Eq. 6.4 as a function of ring width for modes (1,80) around 1560 nm and (3,160) around 780 nm determined using varFDTD simulations for sample A2610. A linear fit indicates phase matching for a  $WR$  of around 1000 nm.

the order of 60 to 100  $\mu\text{m}$  diameter to have a smaller FSR and smaller bending losses, however, at the moment we do not have the required computing power. We could also investigate the case of non-degenerate parametric down-conversion, in which  $\lambda_s$  and  $\lambda_i$  are different. Phase-matching could be achieved for the modes (1,80) and (1,79) depicted in Fig. 6.21 by tuning the temperature, for example. Further detuning of signal and idler waves to several 100 nm is also very interesting, but creates the additional challenge of efficient microring to waveguide coupling at three wavelengths.

We need to point out that these simulations with Lumerical Mode are much less accurate than those that we have shown for microdisks previously, because of the 2.5D effective index approach as opposed to the 3D simulations and also due to a low mesh resolution. Fewer loss mechanisms are taken into account, resulting in larger Q factors using varFDTD. These factors can also have an influence on the precise mode positions.

### 6.4.1 Mask with two waveguides for parametric frequency conversion and SHG

We started the design of an e-beam lithography mask for microrings with two bus waveguides for near-critical coupling at 780 nm and 1560 nm. The mask is shown in Fig. 6.24. The microring has a 20  $\mu\text{m}$  diameter and  $WR = 1050$  nm. The waveguide for coupling at 780 nm has a width of 300 nm, a gap of 210 nm, and an angle of 90° around the ring. Meanwhile, the waveguide for coupling 1560 nm light has a width of 900 nm, a gap of 250 nm and a 0° angle. These parameters correspond to the before-mentioned simulations near critical coupling. The blue areas in the mask are where the e-beam writes, the resist is opened, and the III-nitride layer is etched.

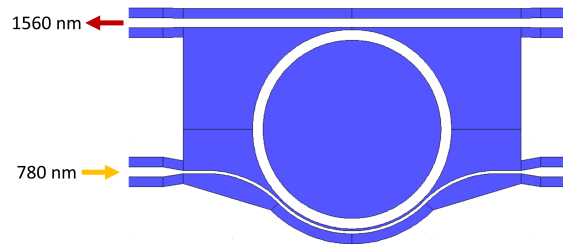


Figure 6.24: Mask showing a 20µm diameter microring with  $WR = 1050\text{nm}$  and two waveguides for near critical coupling at 780nm (bottom) and 1560nm (top) for parametric frequency conversion.

## 6.5 Conclusion and outlook

Unfortunately, as of June 2020 the fabricated samples A2390 and A2587 have not yet been characterized optically due to the Covid-19 nation-wide shut-down. From simulation, it is difficult to say whether one sample is better than the other. A2587 (330nm AlN) shows higher simulated loaded Q factors near critical coupling. Certainly, A2390 (330nm III-nitride on SiO<sub>2</sub>) is more promising for working towards non-linear frequency conversion in high Q factor microresonators, even though it is too thin for operation around 1550nm. With sample A2587, we encountered major fabrication problems due to strain release during underetching. However, once the AlN buffer layer growth is optimized, we could grow GaN on the AlN buffer layer, which would counteract the strain. Suspended passive photonic circuits would be a first step, followed by microdisk resonators and lasers in the blue and finally active photonic circuits. Such a sample could also be bonded to SiO<sub>2</sub> in future work, thus eliminating the need for underetching and allowing the fabrication of microrings.

Meanwhile, sample A2610 (640nm III-nitride), which is much more suited for operation at 1550nm and consequently for non-linear frequency conversion, is still awaiting BCB bonding at C2N. Our collaboration's work in the near future will certainly focus on this sample as well as other similar samples. We have presented initial design considerations for achieving double-resonant degenerate parametric down-conversion and SHG in 20µm diameter microrings on this sample, but more time and computing power should be spent on improving the design, especially expanding it TM modes and to larger microrings. Phase-matched parametric down-conversion is a prerequisite for OPO. As a next step, we need to fabricate devices on sample A2610 for operation around 1560nm and 780nm, in order to demonstrate high Q factor resonances and frequency conversion.

The initial work on the design and fabrication of microring photonic circuits on III-nitrides on SiO<sub>2</sub> presented in this chapter constitutes an important first step towards achieving non-linear optics effects such as OPO and frequency combs in this platform, as very high Q resonators are required to sufficiently reduce the threshold power of these effects. Future work of our collaboration will certainly aim towards achieving these non-linear optics effects in the

framework of the Opoint project (see introduction).

## Summary of Chapter 6

In this chapter, we discussed passive photonic circuits in the NIR in III-nitrides grown on silicon and bonded on SiO<sub>2</sub> or suspended in air. We reviewed the state of the art, focussing on the non-linear optics effects of OPO and frequency combs. We then examined the design and fabrication of photonic circuits on two samples with a III-nitride thickness of 330 nm, one bonded on SiO<sub>2</sub>, the other suspended on Si (100). These layers were too thin to confine light well at 1550 nm. We thus chose an operating wavelength around 780 nm for these two samples. We used FDTD to determine the transmission spectra, obtaining an estimate of the FSR and the loaded Q factor for the different devices. The fabricated devices are expected to operate in the over- and near-critical coupling regimes, since the design of these devices was based on initial simulations suggesting smaller critical coupling gaps. Critical coupling is expected for gaps in the range of 200 nm for 20 μm diameter rings and in the range of 160 nm to 200 nm for 8 μm diameter disks. Very high loaded Q factors around  $1 \times 10^5$  are obtained in simulation in the over- and critically coupled regime, which is the same order of magnitude as demonstrated experimentally in Ref. [18]. Experimental transmission measurements of these samples to determine loaded Q factors are yet to be performed, as the Covid-19 shut-down has delayed the anticipated progress by several months. Meanwhile, we made a preliminary design of a microring for double-resonant phase-matched degenerate parametric down-conversion and SHG for operation at 1560 nm and 780 nm on a sample with 640 nm III-nitride on SiO<sub>2</sub>. We designed 20 μm diameter microrings with a width of 1050 nm with phase-matching of the TE<sub>00</sub> mode at around 1560 nm and the TE<sub>20</sub> mode at around 780 nm. We determined the near-critical coupling parameters of bus waveguides for these two wavelengths. Next steps will include improving this design, especially expanding it to TM modes and towards larger microrings, fabricating such photonic circuits, and measuring the Q factors at both wavelengths, as well as the frequency converted signal.

# Conclusions and future work

**T**HIS chapter summarizes the results obtained in this thesis and gives perspectives for future work.

## Summary

At the beginning of this thesis (chapter 1), we discussed the relevant material properties of III-nitrides, as well as their growth on Si. We then gave a theoretical description of all the photonic devices studied in this work, including the slab and ridge waveguide, the microdisk cavity and its coupling to a waveguide, the semiconductor laser, the 2D photonic crystal slab cavity, and the grating coupler. The design was described next, in general terms, using finite-difference time-domain (FDTD) simulations. We discussed the different components of the cleanroom fabrication process, as well as the process flows of the different types of photonic devices and some common problems that can occur. At the end of the first chapter, we examined the different spectroscopic setups used to experimentally characterize our samples.

Chapter 2 dealt with individual III-nitride microdisk lasers on Si in the blue-UV spectral range. We reviewed the state of the art of pulsed and continuous-wave (CW) lasing, as well as results from our collaboration from before the beginning of this thesis. We then described 9 samples grown by molecular beam epitaxy (MBE) or metal organic chemical vapor deposition (MOCVD) or hybrid combinations of both methods. We discussed their structural properties, photoluminescence (PL) spectra, optical confinement, and band structure and investigated the pulsed optically pumped lasing observed for these samples. The lowest threshold peak power density of  $18 \text{ kW} \cdot \text{cm}^{-2}$  was observed for a sample with MOCVD grown quantum wells (QWs) in the blue. We discussed the influence of the quality (Q) factor and the pump laser, and calculated the threshold using a rate equation model, which was in good agreement with the experimental results. We further evaluated the effect of the growth method, the dislocation density, a chemical treatment, the emission wavelength, high excitation power density PL, and the mode overlap with the QWs on the threshold power density. We compared these samples to one grown on bulk GaN and gave an estimate of whether our samples could lase under CW conditions.

In chapter 3, we investigated monolithically integrated III-nitride on silicon microlaser

photonic circuits in the blue spectral range. First, we gave an overview of different monolithic integration schemes and briefly reviewed the state of the art of critical coupling using III-nitride photonic circuits. We then described the design and fabrication of photonic circuits on two MBE grown samples, one operating in the under-coupled regime and the other at critical coupling. We used a QW etching approach to integrate active emitters into photonic circuits and studied different waveguide bending angles around the disk. We discussed the results obtained from CW  $\mu$ -PL and pulsed optically pumped lasing. We demonstrated the first integrated microlaser photonic circuit in the blue with a threshold of  $15 \text{ mJ} \cdot \text{cm}^{-2}$  per pulse or threshold peak power of  $38 \text{ MW} \cdot \text{cm}^{-2}$  and managed to reduce the threshold to  $1.2 \text{ mJ} \cdot \text{cm}^{-2}$  per pulse (threshold peak power of  $300 \text{ kW} \cdot \text{cm}^{-2}$ ) for the second sample by improving the process and changing the pump laser. We also achieved critical coupling at the shortest wavelength (440 nm) and with the smallest gap size (40 - 45 nm) reported using the second sample and observed large intrinsic Q factors of 4700. We discussed the dependence of the lasing threshold on the gap size and loaded Q factor, as well as the dependence of the output signal on the coupling Q factor. We also described the influence of the proximity effect during e-beam lithography on the mode position.

In chapter 4, we pushed the operating wavelength to the ultraviolet (UV) using microlaser photonic circuits and 2D photonic crystal (PhC) slabs. We first reviewed the state of the art of UV photonic circuits and III-nitride PhCs. Then, we described the design and fabrication of our III-nitride photonic circuits with a  $180^\circ$  bent waveguide. For this MOCVD grown sample, we observed Q factors of 3500 at 420 nm and lasing modes from 374 to 399 nm with low threshold energies of  $0.14 \text{ mJ} \cdot \text{cm}^{-2}$  per pulse or threshold peak powers of  $35 \text{ kW} \cdot \text{cm}^{-2}$ , as well as a large peak to background dynamic of 200 at the out-coupling grating for a 50 nm gap device. These devices operate at the wavelength limit for GaN as the waveguiding layer, due to the proximity to its band gap. This was the first report of an active photonic circuit in the UV spectral range. We then discussed L3 and H2 PhC cavities operating at 340 nm with Q factors as high as 1085 at 337 nm. We proposed an explanation of the reduction in Q factor with decreasing wavelength in the blue-UV spectral range based on the residual absorption of thin AlN layers on Si through spectroscopic ellipsometry.

In chapter 5, we discussed thin (1-2  $\mu\text{m}$  thick) electrically injected microdisks and microrings using III-nitrides on Si. First, we reviewed the state of the art of electrically injected "sandwich"-type microdisk lasers as well as photonic circuits. Then, we discussed two different approaches for vertical current injection into III-nitride microdisks and microrings on Si. The first one was based on the assumption that the entire heterostructure was conductive, which turned out not to be the case. The second approach bypassed the insulating buffer layers by etching the center of the ring to the silicon substrate and connecting the n-GaN to the Si with the n-contact. This approach allowed us to observe electroluminescence from 40  $\mu\text{m}$  diameter rings with a maximum current density of  $4.2 \text{ kA} \cdot \text{cm}^{-2}$ . We obtained an output power density of  $440 \text{ mW} \cdot \text{cm}^{-2}$  at  $I = 20 \text{ mA}$  from such microrings with diameters of 30 to 50  $\mu\text{m}$ . We did not

observe lasing and perhaps thicker structures with cladding layers are required to do so.

In chapter 6, we discussed passive III-nitride photonic circuits in the near-infrared (NIR) spectral range. First, we reviewed the state of the art of such photonic circuits with a focus on non-linear optics effects, such as frequency combs and optical parametric oscillators (OPOs) and described the prior results of our collaboration using III-nitride photonic circuits in the NIR. We then discussed the design and fabrication of microdisk and microring photonic circuits operating at 780 nm using III-nitrides bonded on SiO<sub>2</sub> and suspended on Si (100). Our devices are expected to operate in the over- and near-critical coupling regime with theoretical loaded Q factors in the 100k-200k range. As of June 2020, we have not been able to characterize these samples optically due to the Covid-19 pandemic. We also investigated a design for double-resonant parametric down-conversion in microrings bonded on SiO<sub>2</sub>.

## Conclusion and perspectives

The results discussed in this thesis exemplify the versatility of the III-nitride on silicon platform through the large wavelength range of active and passive integrated photonic devices. III-nitrides are a very good candidate for next generation integrated photonic circuits because of the large transparency window, band gap tunability, relatively large second and third order optical non-linearities, and large exciton binding energy at room temperature. While this work focused on the first two aspects, non-linear and quantum optics are promising fields for future research.

The work described in this thesis was performed in the framework of two ANR projects, Milagan and Opoint. Milagan continues for another year and Opoint only just started this year.

In the framework of Milagan, the main goal is to achieve lasing under electrical injection. One option is to go towards thicker heterostructures, as do Wang et al. [43–45], using waveguiding and cladding layers. This allows to achieve a lower threading dislocation density, a better overlap of the mode with the active region, and a reduced overlap with the doped regions. This would allow to extend the p-contact all the way to the edge of the disk which could help with current spreading. Devices could be smaller as the n-contact could be taken from the side instead of a central via connecting to the backside. However, it would be more difficult to make photonic circuits under electrical injection, which is another interesting perspective. Using thin suspended III-nitride layers, we could combine electrical injection with integrated photonic circuits. However, this is a very long and complicated process, which we have tried without success at numerous occasions. Implementing tunnel junctions as the top contact could also help with current spreading and could also be used in thin structures.

In the Opoint project, one important goal is to achieve OPOs using microrings in the III-nitride on SiO<sub>2</sub> platform that we introduced in chapter 6. To achieve this goal, the first step is to achieve high Q factor resonators operating near critical coupling at around 1560 nm and 780 nm. Q factors in the range of 10<sup>5</sup> to 10<sup>6</sup> will be necessary. To achieve such high Q fac-

tors, a well thought-through design and very good quality processing is essential. Secondly, double-resonant parametric frequency conversion needs to be demonstrated in carefully designed microring photonic circuits. Once we have high Q resonators operating at 1550 nm, frequency combs should also be achievable. Certainly, the future work of our consortium will put a strong focus on microrings.

Based on the active photonic circuits that we discussed in chapters 3 and 4, the next logical step would be to try to further decrease the wavelength to the UVB and UVC. While achieving critical coupling at these wavelengths is difficult to realize due to fabrication limitations, these devices should be able to lase in the under-coupled regime.

Another interesting new platform is III-nitrides on Si (100). We fabricated photonic circuits on a 330 nm AlN layer. In future work, we could grown GaN on the AlN buffer to make photonic circuits in the NIR. As a next step, we could grow InGaN QWs and try to make microdisk resonators and lasers in the blue. Then, we could make active photonic circuits in the blue, like we have demonstrated on Si (111).

# List of Publications and Contributions

## Peer-Reviewed Journal Articles

✦ F. TABATABA-VAKILI, C. BRIMONT, B. ALLOING, B. DAMILANO, L. DOYENNETTE, T. GUILLET, M. EL KURDI, S. CHENOT, V. BRÄNDLI, E. FRAYSSINET, J.-Y. DUBOZ, F. SEMOND, B. GAYRAL, and P. BOUCAUD, “Analysis of low-threshold optically pumped III-nitride microdisk lasers” , *Appl. Phys. Lett.*, vol. 117, p. 121103, 2020. [doi:10.1063/5.0015252](https://doi.org/10.1063/5.0015252)

✦ F. TABATABA-VAKILI, B. ALLOING, B. DAMILANO, H. SOUISSI, C. BRIMONT, L. DOYENNETTE, T. GUILLET, X. CHECOURY, M. EL KURDI, S. CHENOT, E. FRAYSSINET, J.-Y. DUBOZ, F. SEMOND, B. GAYRAL, and P. BOUCAUD, “Monolithic integration of ultraviolet microdisk lasers into photonic circuits in a III-nitride on silicon platform” , *Opt. Lett.*, vol. 45, p. 4276-4279, 2020. [doi:10.1364/OL.395371](https://doi.org/10.1364/OL.395371)

✦ F. TABATABA-VAKILI, L. DOYENNETTE, C. BRIMONT, T. GUILLET, S. RENNESSON, B. DAMILANO, E. FRAYSSINET, J.-Y. DUBOZ, X. CHECOURY, S. SAUVAGE, M. EL KURDI, F. SEMOND, B. GAYRAL, and P. BOUCAUD, “Demonstration of critical coupling in an active III-nitride microdisk photonic circuit on silicon” , *Sci. Rep.*, vol. 9, p. 18095, 2019. [doi:10.1038/s41598-019-54416-3](https://doi.org/10.1038/s41598-019-54416-3)

✦ F. TABATABA-VAKILI, S. RENNESSON, B. DAMILANO, E. FRAYSSINET, J.-Y. DUBOZ, F. SEMOND, I. ROLAND, B. PAULILLO, R. COLOMBELLI, M. EL KURDI, X. CHECOURY, S. SAUVAGE, L. DOYENNETTE, C. BRIMONT, T. GUILLET, B. GAYRAL, and P. BOUCAUD, “III-nitride on silicon electrically injected microrings for nanophotonic circuits” , *Opt. Express*, vol. 27, p. 11800-11808, 2019. [doi:10.1364/OE.27.011800](https://doi.org/10.1364/OE.27.011800)

✦ F. TABATABA-VAKILI, L. DOYENNETTE, C. BRIMONT, T. GUILLET, S. RENNESSON, E. FRAYSSINET, B. DAMILANO, J.-Y. DUBOZ, F. SEMOND, I. ROLAND, M. EL KURDI, X. CHECOURY, S. SAUVAGE, B. GAYRAL, and P. BOUCAUD, “Blue Microlasers Integrated on a Photonic Platform on Silicon” , *ACS Photonics*, vol. 5, p. 3643-3648, 2018. [doi:10.1021/acsphotonics.8b00542](https://doi.org/10.1021/acsphotonics.8b00542)

✦ F. TABATABA-VAKILI, I. ROLAND, T.-M. TRAN, X. CHECOURY, M. EL KURDI, S. SAUVAGE, C. BRIMONT, T. GUILLET, S. RENNESSON, J.-Y. DUBOZ, F. SEMOND, B. GAYRAL, and P. BOUCAUD, “Q factor limitation at short wavelength (around 300 nm) in III-nitride-on-silicon photonic crystal cavities” , *Appl. Phys. Lett.*, vol. 111, p. 131103, 2017. [doi:10.1063/1.4997124](https://doi.org/10.1063/1.4997124)

## International Conference Papers

✠ **F. TABATABA-VAKILI**, S. RENNESSON, B. DAMILANO, L. DOYENNETTE, C. BRIMONT, T. GUILLET, E. FRAYSSINET, J. BRAULT, J.-Y. DUBOZ, I. ROLAND, M. EL KURDI, X. CHECOURY, S. SAUVAGE, F. SEMOND, B. GAYRAL, and P. BOUCAUD, “A III-nitride on silicon nanophotonic platform: electrical injection and microlaser photonic circuits” , *ICNS 13 - 13th International Conference on Nitride Semiconductors*, Bellevue, WA, USA. 7-12 July 2019. *Oral presentation*.

✠ **F. TABATABA-VAKILI**, L. DOYENNETTE, C. BRIMONT, T. GUILLET, S. RENNESSON, E. FRAYSSINET, J. BRAULT, B. DAMILANO, J.-Y. DUBOZ, F. SEMOND, I. ROLAND, M. EL KURDI, X. CHECOURY, S. SAUVAGE, B. GAYRAL, and P. BOUCAUD, “III-Nitride on silicon microlaser photonic circuits and electrical injection” , *International Workshop on Nitride Semiconductors 2018 (IWN 2018)*, Kazanawa, Japan. 11-16 November 2018. *Oral presentation. Student Award*.

✠ **F. TABATABA-VAKILI**, L. DOYENNETTE, C. BRIMONT, T. GUILLET, S. RENNESSON, E. FRAYSSINET, B. DAMILANO, J.-Y. DUBOZ, F. SEMOND, I. ROLAND, M. EL KURDI, X. CHECOURY, S. SAUVAGE, B. GAYRAL and P. BOUCAUD, “Blue Microlaser Integrated on a Photonic Platform on Silicon” , *ICPS 2018 - 34th International conference on the physics of semiconductors*, Montpellier, France. 29 July - 3 August, 2018. *Poster presentation. Best Student Poster Award*.

✠ **F. TABATABA-VAKILI**, I. ROLAND, S. RENNESSON, E. FRAYSSINET, J. BRAULT, M. EL KURDI, X. CHECOURY, B. PAULILLO, R. COLOMBELLI, L. DOYENNETTE, T. GUILLET, C. BRIMONT, B. DAMILANO, F. SEMOND, B. GAYRAL and P. BOUCAUD, “III-Nitride on Silicon Microdisks - Electrical injection and bus waveguide side-coupling” , *Photonics West 2018*, San Francisco, CA, USA. 27 January - 1 February, 2018. *Oral presentation*.

✠ **F. TABATABA-VAKILI**, I. ROLAND, S. RENNESSON, E. FRAYSSINET, J. BRAULT, M. EL KURDI, X. CHECOURY, B. PAULILLO, R. COLOMBELLI, T. GUILLET, C. BRIMONT, B. DAMILANO, F. SEMOND, B. GAYRAL and P. BOUCAUD, “Electrically Injected III-Nitride Microdisk lasers for a Nanophotonic Platform on Silicon” , *ICNS 12 - 12th International Conference on Nitride Semiconductors*, Strasbourg, France. 24 July - 28 July, 2017. *Poster presentation*.

## National Conference Papers and Workshops

✠ **F. TABATABA-VAKILI**, B. DAMILANO, L. DOYENNETTE, C. BRIMONT, T. GUILLET, S. RENNESSON, E. FRAYSSINET, J.-Y. DUBOZ, X. CHECOURY, S. SAUVAGE, M. EL KURDI, F. SEMOND, B. GAYRAL, and P. BOUCAUD, “Demonstration of critical coupling and lasing in an active III-nitride on silicon photonic circuit” , *Micro- and Nanophotonics Days 2019*, Palaiseau, France. 20-21 November 2019. *Poster presentation*.

✠ **F. TABATABA-VAKILI**, L. DOYENNETTE, C. BRIMONT, T. GUILLET, S. RENNESSON, B. DAMILANO, E. FRAYSSINET, J.-Y. DUBOZ, X. CHECOURY, S. SAUVAGE, M. EL KURDI, F. SEMOND, B.

GAYRAL, and P. BOUCAUD, “Microlasers bleus intégrés sur silicium” , *39<sup>èmes</sup> Journées Nationales d’Optique Guidée (JNOG) 2019*, Palaiseau, France. 2-4 July 2019. *Invited oral presentation.*

✠ **F. TABATABA-VAKILI**, L. DOYENNETTE, C. BRIMONT, T. GUILLET, S. RENNESSON, E. FRAYSSINET, J. BRAULT, B. DAMILANO, J.-Y. DUBOZ, F. SEMOND, I. ROLAND, M. EL KURDI, X. CHECOURY, S. SAUVAGE, B. GAYRAL, and P. BOUCAUD, “III-Nitride Microlasers for a Nanophotonic Platform on Silicon” , *32nd Heimbach Workshop*, Mansfeld, Germany. 17-21 September 2018. *Invited oral presentation.*

✠ **F. TABATABA-VAKILI**, I. ROLAND, T.-M. TRAN, X. CHECOURY, M. EL KURDI, S. SAUVAGE, C. BRIMONT, T. GUILLET, S. RENNESSON, J.-Y. DUBOZ, F. SEMOND, B. GAYRAL, and P. BOUCAUD, “Q Factor Limitation in the UVA in III-Nitride-on-Silicon Photonic Crystal Cavities” , *DPG Spring Meeting 2018*, Berlin, Germany. 11 March - 16 March 2018. *Oral presentation.*

## International Conference Papers presented by a co-author

✠ **F. TABATABA-VAKILI**, S. RENNESSON, B. DAMILANO, L. DOYENNETTE, C. BRIMONT, T. GUILLET, E. FRAYSSINET, J. BRAULT, J.-Y. DUBOZ, I. ROLAND, M. EL KURDI, X. CHECOURY, S. SAUVAGE, F. SEMOND, P. BOUCAUD, and B. GAYRAL, “Towards III-nitride on silicon active photonic circuits” , *Frontiers in Optics + Laser Science APS/DLS*, Washington, DC, USA 13-17 September 2019. *Poster presentation.*

✠ H. ZI, K. H. LI, H. W. CHOI, **F. TABATABA-VAKILI**, S. RENNESSON, B. DAMILANO, E. FRAYSSINET, J.-Y. DUBOZ, F. SEMOND, L. DOYENNETTE, C. BRIMONT, T. GUILLET, B. GAYRAL and P. BOUCAUD, “Whispering-Gallery Mode Optically-Pumped Lasing from InGaN/GaN Microdisks on GaN Substrate” , *ICNS 13 - 13th International Conference on Nitride Semiconductors*, Bellevue, WA, USA. 7-12 July 2019. *Oral presentation.*

✠ C. BRIMONT, F. CHIARUTTINI, L. DOYENNETTE, **F. TABATABA-VAKILI**, I. ROLAND, M. EL KURDI, X. CHECOURY, S. SAUVAGE, S. RENNESSON, E. FRAYSSINET, J. BRAULT, B. DAMILANO, J.-Y. DUBOZ, F. SEMOND, B. GAYRAL, P. BOUCAUD and T. GUILLET, “Gain Modeling in InGaN/GaN Microdisk Lasers” , *ICNS 13 - 13th International Conference on Nitride Semiconductors*, Bellevue, WA, USA. 7-12 July 2019. *Poster presentation.*

✠ C. BRIMONT, L. DOYENNETTE, **F. TABATABA-VAKILI**, I. ROLAND, S. RENNESSON, E. FRAYSSINET, J. BRAULT, B. DAMILANO, J.-Y. DUBOZ, F. SEMOND, S. SAUVAGE, M. EL KURDI, X. CHECOURY, R. COLOMBELLI, B. PAULILLO, B. GAYRAL, P. BOUCAUD, and T. GUILLET, “Gain studies in InGaN microdisks” , *International Workshop on Nitride Semiconductors 2018 (IWN)*

2018), Kazanawa, Japan. 11-16 November 2018. *Oral presentation.*

✠ C. BRIMONT, J. SELLÉS, T. GUILLET, B. GAYRAL, B. DAMILANO, M. LEROUX, M. MEXIS, S. RENNESSON, F. SEMOND, I. ROLAND, **F. TABATABA-VAKILI**, X. CHECOURY, and P. BOUCAUD, “Nitride on silicon microdisk laser for UV and blue integrated photonic” , *ICPS 2018 - 34th International conference on the physics of semiconductors*, Montpellier, France. 29 July - 3 August 2018. *Poster presentation.*

✠ P. BOUCAUD, **F. TABATABA-VAKILI**, M. EL KURDI, S. SAUVAGE, X. CHECOURY, S. RENNESSON, F. SEMOND, B. DAMILANO, J. Y. DUBOZ, C. BRIMONT, L. DOYENETTE, T. GUILLET, and B. GAYRAL, “III-nitride microlasers on silicon integrated on a 2D photonic platform” , *Compound Semiconductor Week*, Boston, USA. 28 May - 2 June 2018. *Invited oral presentation.*

✠ **F. TABATABA-VAKILI**, I. ROLAND, T.-M. TRAN, X. CHECOURY, M. EL KURDI, S. SAUVAGE, C. BRIMONT, T. GUILLET, S. RENNESSON, J.-Y. DUBOZ, F. SEMOND, B. GAYRAL, and P. BOUCAUD, “Quality factor limitation for below 350 nm AlN-on-Si photonic crystal microcavities” , *IWUMD, International Workshop on UV Materials and Devices 2017*, 14-18 November 2017, Fukuoka, Japan. *Oral presentation.*

✠ J. SELLÉS, T. GUILLET, V. CREPEL, B. GAYRAL, B. DAMILANO, M. LEROUX, M. MEXIS, S. RENNESSON, F. SEMOND, I. ROLAND, **F. TABATABA-VAKILI**, X. CHECOURY, P. BOUCAUD, and C. BRIMONT, “Nitride-on-silicon platform for UV-visible photonics with integrated microlaser sources” , *META'17, the 8th International Conference on Metamaterials, Photonic Crystals and Plasmonics*, Incheon, Seoul, South Korea. 25-28 July 2017. *Oral presentation.*

✠ P. BOUCAUD, I. ROLAND, Y. ZENG, **F. TABATABA-VAKILI**, X. CHECOURY, M. EL KURDI, S. SAUVAGE, B. GAYRAL, C. BRIMONT, T. GUILLET, M. DE MICHELI, M. GROMOVYI, J. Y. DUBOZ, and F. SEMOND, “GaN-on-silicon integrated photonics for IR to visible light frequency conversion” , *ICNS 12 - 12th International Conference on Nitride Semiconductors*, Strasbourg, France. 24-28 July 2017. *Invited oral presentation.*

✠ J. SELLÉS, T. GUILLET, V. CREPEL, B. GAYRAL, B. DAMILANO, M. LEROUX, M. MEXIS, S. RENNESSON, F. SEMOND, I. ROLAND, **F. TABATABA-VAKILI**, X. CHECOURY, P. BOUCAUD, and C. BRIMONT, “Comparison of UV-C and blue emitting nitride-on-silicon microdisk lasers” , *ICNS 12 - 12th International Conference on Nitride Semiconductors*, Strasbourg, France. 24-28 July 2017. *Oral presentation.*

✠ P. BOUCAUD, I. ROLAND, Y. ZENG, **F. TABATABA-VAKILI**, X. CHECOURY, M. EL KURDI, S. SAUVAGE, B. GAYRAL, C. BRIMONT, T. GUILLET, M. DE MICHELI, M. GROMOVYI, J. Y. DUBOZ, and F. SEMOND, “GaN-on-silicon integrated photonics for IR to visible light frequency conversion” , *2017 IEEE Summer Topical Meeting Conference*, Puerto Rico. 10-12 July 2017. *Invited oral presentation.*

✠ P. BOUCAUD, I. ROLAND, Y. ZENG, **F. TABATABA-VAKILI**, X. CHECOURY, M. EL KURDI, S. SAUVAGE, B. GAYRAL, C. BRIMONT, T. GUILLET, M. DE MICHELI, M. GROMOVYI, J. Y. DUBOZ,

and F. SEMOND, “III-nitride on Silicon Photonic Circuits” , *Emerging Technologies Communications Microsystems Optoelectronics Sensors 2017 conference (ETCMOS)*, Warsaw, Poland. 28-30 May 2017. *Invited oral presentation.*

## National Conference Papers and Workshops presented by a co-author

✠ P. BOUCAUD, **F. TABATABA-VAKILI**, L. DOYENETTE, C. BRIMONT, T. GUILLET, M. EL KURDI, S. SAUVAGE, X. CHECOURY, B. GAYRAL, S. RENNESSON, E. FRAYSSINET, J. Y. DUBOZ, B. ALLOING, B. DAMILANO, and F. SEMOND, “III-nitrides photonic integrated circuits on silicon” , *Workshop on Optical Microsources*, CRHEA, Valbonne, 28th-29th November, 2019. *Invited oral presentation.*

✠ P. BOUCAUD, **F. TABATABA-VAKILI**, M. EL KURDI, S. SAUVAGE, X. CHECOURY, S. RENNESSON, F. SEMOND, B. DAMILANO, E. FRAYSSINET, J. Y. DUBOZ, C. BRIMONT, L. DOYENETTE, T. GUILLET, and B. GAYRAL, “Photonique III-N sur silicium” , *C’Nano PACA*, Porquerolles, France. 10-12 September 2018. *Invited oral presentation.*

✠ P. BOUCAUD, **F. TABATABA-VAKILI**, I. ROLAND, Y. ZENG, M. EL KURDI, S. SAUVAGE, X. CHECOURY, M. GROMOVYI, S. RENNESSON, F. SEMOND, J. Y. DUBOZ, M. DE MICHELI, J. SELLÉS, C. BRIMONT, L. DOYENETTE, T. GUILLET, and B. GAYRAL, “Integrated photonics with III-Nitrides on silicon” , *UK nitride photonics*, Manchester, UK. 10-12 January 2018. *Invited oral presentation.*

## Invited Seminar Talks

✠ **F. TABATABA-VAKILI**, B. DAMILANO, B. ALLOING, L. DOYENETTE, C. BRIMONT, T. GUILLET, E. FRAYSSINET, S. RENNESSON, J.-Y. DUBOZ, I. ROLAND, X. CHECOURY, S. SAUVAGE, M. EL KURDI, F. SEMOND, B. GAYRAL, and P. BOUCAUD, “III-nitrides on silicon: a platform for integrated photonics from the ultraviolet to the near-infrared” , CNRS-CRHEA, Valbonne, France. 30 September 2020.

✠ **F. TABATABA-VAKILI**, B. DAMILANO, B. ALLOING, L. DOYENETTE, C. BRIMONT, T. GUILLET, E. FRAYSSINET, S. RENNESSON, J.-Y. DUBOZ, I. ROLAND, X. CHECOURY, S. SAUVAGE, M. EL KURDI, F. SEMOND, B. GAYRAL, and P. BOUCAUD, “III-nitrides on silicon: a platform for integrated photonics from the ultraviolet to the near-infrared” , Nanophotonics Group, LMU, Munich, Germany. 7 September 2020.

✠ **F. TABATABA-VAKILI**, L. DOYENETTE, C. BRIMONT, T. GUILLET, S. RENNESSON, E. FRAYSSINET, J. BRAULT, B. DAMILANO, J.-Y. DUBOZ, F. SEMOND, I. ROLAND, M. EL KURDI, X.

CHECOURY, S. SAUVAGE, B. GAYRAL, and P. BOUCAUD, “III-Nitride Microdisk Photonic Circuits on Silicon: Lasing, Critical Coupling, and Electrical Injection” , Electronic Materials and Devices Laboratory, PARC, a Xerox Company, Palo Alto, CA, USA. 9 May 2019.

✠ **F. TABATABA-VAKILI**, L. DOYENNETTE, C. BRIMONT, T. GUILLET, S. RENNESSON, E. FRAYSSINET, J. BRAULT, B. DAMILANO, J.-Y. DUBOZ, F. SEMOND, I. ROLAND, M. EL KURDI, X. CHECOURY, S. SAUVAGE, B. GAYRAL, and P. BOUCAUD, “III-Nitride Microdisk Photonic Circuits on Silicon: Lasing, Critical Coupling, and Electrical Injection” , University of California, Santa Barbara, CA, USA. 30 April 2019.

✠ **F. TABATABA-VAKILI**, L. DOYENNETTE, C. BRIMONT, T. GUILLET, S. RENNESSON, E. FRAYSSINET, J. BRAULT, B. DAMILANO, J.-Y. DUBOZ, F. SEMOND, I. ROLAND, M. EL KURDI, X. CHECOURY, S. SAUVAGE, B. GAYRAL, and P. BOUCAUD, “III-Nitride Microcavities Integrated on a Photonic Platform on Silicon” , University of Hong Kong, Hong Kong. 21 November 2018.

✠ **F. TABATABA-VAKILI**, L. DOYENNETTE, C. BRIMONT, T. GUILLET, S. RENNESSON, E. FRAYSSINET, J. BRAULT, B. DAMILANO, J.-Y. DUBOZ, F. SEMOND, I. ROLAND, M. EL KURDI, X. CHECOURY, S. SAUVAGE, B. GAYRAL, and P. BOUCAUD, “III-Nitride Microlasers for a Nanophotonic Platform on Silicon” , CNRS-CRHEA, Valbonne, France. 11 October 2018.

# Synthèse en Français

## Introduction

Il y a trois décennies Isamu Akasaki, Hiroshi Amano et Shuji Nakamura ont publié leurs travaux fondateurs sur la croissance et le dopage p du nitrure de gallium (GaN) ce qui a permis le développement des diodes électroluminescentes (LEDs) bleues et blanches et a créé une révolution pour l'éclairage à semi-conducteurs. Ils ont eu le prix Nobel pour ces travaux en 2014.

Les semi-conducteurs nitrures d'éléments III sont fortement polyvalents. Ils donnent accès à des émetteurs actifs à base de puits et boîtes quantiques de l'ultraviolet (UV) profond jusqu'au visible, grâce à leur grande bande interdite directe et accordable. Les nitrures d'éléments III peuvent être dopés type n et p ce qui ouvre la voie à de multiples applications électroniques et optoélectroniques. Des LEDs bleues, vertes et blanches sont disponibles dans le commerce pour l'éclairage et pour des écrans. Des diodes lasers bleues sont utilisées dans les lecteurs de disques blu-ray. Des transistors efficaces à base de nitrures d'éléments III sont utilisés pour l'électronique de puissance et hyperfréquence, que ce soit pour des applications automobiles, télécom (5G), informatiques (chargeurs) et grand public.

Pendant les quinze dernières années, le domaine des micro- et nano-cavités photoniques à base de nitrures d'éléments III s'est développé et s'est ouvert à une gamme large d'applications potentielles. Le nitrure d'aluminium (AlN) et le GaN sont transparents de l'UV jusqu'au proche infrarouge (IR), ce qui permet d'avoir des guides d'onde avec des pertes faibles, une composante essentielle pour des circuits photoniques. Les nitrures d'éléments III ont une grande énergie de liaison d'exciton ce qui permet d'obtenir des émetteurs de photons uniques sur puce à température ambiante, ouvrant le domaine vers l'optique quantique. La détection quantique et la manipulation optique des qubits UV piégés par des ions sont aussi possibles. Des applications sur puce dans le domaine de l'optique non-linéaire sont également réalisables grâce aux non-linéarités optiques d'ordre deux et trois élevées. L'émission de paires des photons intriqués dans le proche IR par conversion paramétrique ainsi que des peignes de fréquence et des oscillateurs paramétriques optiques (OPOs) ont déjà été réalisés. La communication en lumière visible, la communication Li-Fi, ou les télécommunications avec des circuits photoniques intégrés sont également possibles. En plus, les nitrures d'éléments III sont biocompatibles, ce qui permet des applications biophotoniques et des biocapteurs sur puce.

Cette thèse a pour objectif de démontrer la viabilité de la plateforme des nitrures d'éléments III sur silicium pour la prochaine génération des circuits photoniques intégrés fonctionnant dans la gamme spectrale de l'UV jusqu'au proche IR avec des composants actifs et passifs sous pompage optique ou injection électrique. Nous visons à combiner des microlasers actifs avec des circuits photoniques passifs et à étendre les circuits photoniques passifs à des plateformes nouvelles, i.e. des nitrures d'éléments III collés sur SiO<sub>2</sub>. De plus, nous visons l'injection électrique dans des dispositifs actifs, en travaillant sur des circuits photoniques utilisant des microlasers à injection électrique.

Parmi les plateformes photoniques intégrées conventionnelles figurent le silicium sur isolant (SOI), le niobate de lithium sur isolant (LNOI), et le phosphore d'indium (InP). Ces plateformes ont des désavantages comparés avec les nitrures d'éléments III. SOI, et LNOI ne permettent pas d'avoir des émetteurs actifs (efficaces) à base de lasers. InP a des lasers natifs mais est limité à la gamme spectrale proche IR. Dans le proche IR, SOI et InP ont le désavantage de présenter de l'absorption à deux photons à cause de leurs petites bandes interdites, ce qui n'est pas observé dans les nitrures d'élément III. Les circuits photoniques des nitrures d'éléments III ont l'avantage supplémentaire d'une possible co-intégration avec l'électronique à base de nitrures d'éléments III, offrant ainsi une boîte à outils complète aux designers. Les nitrures d'éléments III sur Si offrent également un chemin pour l'intégration dans un environnement CMOS.

Des couches de nitrures d'éléments III avec une haute qualité cristalline peuvent être épitaxiées par épitaxie par jets moléculaires (MBE) ou par dépôt chimique en phase vapeur à partir de composés organométalliques (MOCVD) sur des substrats différents comprenant les substrats massifs AlN et GaN, ainsi que du saphir, du carbure de silicium, et du silicium. Pour des cavités photoniques et des circuits photoniques, l'hétéroépitaxie sur un substrat à bas indice optique ou avec une forte sélectivité de gravure est préférable pour confiner la lumière dans la direction verticale. Le matériau peut aussi être collé sur une plaque support, comme par exemple SiO<sub>2</sub> sur silicium, pour ensuite procéder au retrait de substrat. Cette approche est particulièrement fonctionnelle sur saphir ou sur silicium en utilisant soit un procédé de lift-off laser ou de la gravure sèche. L'AlN peut aussi être déposé par pulvérisation sur un isolant pour être utilisé dans des dispositifs passifs. Pour fabriquer des dispositifs actifs, le matériau doit être épitaxié pour avoir une intégration monolithique des puits quantiques ou des boîtes quantiques, qui confinent des porteurs dans une ou trois dimensions, permettant une émission efficace de la lumière.

Des micro- et nano-résonateurs actifs et des microlasers avec des nitrures d'éléments III ont été rapportés dans la littérature par différentes équipes. L'équipe de N. Grandjean à l'EPFL a démontré dans le bleu un facteur de qualité de  $1 \times 10^4$  par passivation à l'oxygène, montrant l'importance de contrôler les états de surface actifs optiquement pour avoir des microcavités avec des facteurs de qualité importants. Des circuits photoniques passifs vers 1.55 μm ont été démontrés par l'équipe de Tang à Yale en utilisant des microanneaux couplés avec des guides d'onde avec des facteurs de qualité totale ( $Q_{load}$ ) de  $6 \times 10^5$ . Des circuits photoniques dans la

gamme spectrale de l'UVA jusqu'au visible ont été démontrés avec des  $Q_{load}$  de  $1 \times 10^5$  également par l'équipe de Tang. De plus, l'effet laser avec injection électrique dans le bleu et l'UVA a été rapporté dans des microdisques épais type « sandwich » avec un seuil de  $9 \text{ kA/cm}^2$  par l'équipe de Yang de l'Académie des Sciences Chinoise.

Le consortium dans lequel j'ai travaillé rassemble des chercheurs de quatre laboratoires français (C2N, CRHEA, IRIG, L2C). Nous nous concentrons sur la plateforme de nitrures d'éléments III sur silicium. Un avantage de cette plateforme est la très grande sélectivité de gravure entre le silicium et les nitrures d'éléments III, qui donne un fort contraste d'indice optique avec l'air. Avant le début de cette thèse, ce consortium a travaillé notamment sur des micro- et nano-résonateurs et lasers individuels dans la gamme spectrale de l'UV jusqu'au visible, ainsi que sur des circuits photoniques passifs dans le proche IR, où ils ont également démontré des effets non-linéaires comme la génération de seconde et troisième harmoniques. Ils ont rapporté des lasers à microdisques de l'UVC jusqu'au vert. Dans le proche IR, ils ont démontré des circuits photoniques à base d'un microdisque et d'un guide d'onde avec un facteur de qualité totale de  $8 \times 10^4$ . Les thèses précédentes de notre consortium ont discuté la croissance et l'étude des cavités photoniques à base de boîtes quantiques crues en MBE (S. Sargent 2010), l'étude optique des microcavités des nitrures d'éléments III, incluant des résonateurs et lasers à microdisques et des guides d'onde à cristaux photonique (D. Sam-Giao 2012, J. Sellés 2015), ainsi que le design, la fabrication, et la spectroscopie dans le proche IR des circuits photoniques de nitrures d'éléments III, incluant la génération des seconde et troisième harmoniques (Y. Zeng 2017). Cette thèse est basée sur les travaux précédents de ce consortium.

Dans cette thèse, nous concevons, fabriquons, et caractérisons des cavités photoniques actives et passives opérant dans l'UVA, le bleu et le proche IR en utilisant des couches minces de nitrures d'éléments III épitaxiées sur silicium. Nous assemblons des différents éléments nécessaires pour des circuits photoniques intégrés plus complexes dans cette plateforme photonique jeune et versatile. Nous commençons avec des lasers à microdisques individuels dans le bleu et l'UVA et ensuite nous les intégrons monolithiquement dans des circuits photoniques, d'abord dans le bleu et puis dans l'UVA. Dans l'UVA, nous étudions également des cavités à cristaux photoniques 2D planaires. Ensuite, nous étudions l'injection électrique dans des microdisques et microanneaux minces avec pour but d'atteindre des circuits photoniques à microlasers injectés électriquement. Enfin, nous étudions des dispositifs passifs avec un focus sur des nitrures d'éléments III collés sur  $\text{SiO}_2$  dans le proche IR. Tous nos dispositifs fonctionnent à température ambiante. Ces travaux fournissent les briques de base pour des circuits photoniques intégrés plus avancés utilisant des nitrures d'éléments III sur silicium et sur  $\text{SiO}_2$  pour atteindre des circuits photoniques actifs injectés électriquement, ainsi que des effets non-linéaires dans le proche IR, comme des OPOs ou des peignes de fréquence.

Cette thèse a été financée par GaNeX, un Labex français sur les nitrures d'éléments III dirigé par J.-Y. Duboz. Ces travaux ont été faits dans le cadre du projet ANR Milagan (2018-2021), ainsi que des travaux préliminaires pour le projet Opoint (2020-2024). Milagan a pour but de

démontrer des lasers à microdisque injectés électriquement dans le bleu à base de nitrures d'éléments III sur silicium. Dans Opoint, nous cherchons à réaliser des OPOs en utilisant des circuits photoniques à base des microanneaux en nitrure d'éléments III sur  $\text{SiO}_2$ . Ces deux sujets très différents illustrent très bien la versatilité des nitrures d'éléments III. Ces projets impliquent des collaborations entre le C2N à Palaiseau, le CRHEA à Valbonne, le CEA-IRIG à Grenoble, le L2C à Montpellier, Inphyni à Nice et l'Université de Hong Kong. J'ai passé un peu de temps dans chaque laboratoire et j'ai été impliquée fortement dans toutes les étapes sauf la croissance et la caractérisation du matériau.

Tous les échantillons ont été épitaxiés au CRHEA par B. Damilano, F. Semond, S. Renneson, B. Alloing et E. Frayssinet. Les caractérisations des échantillons après croissance, comme la microscopie à force atomique et la photoluminescence à faible et forte excitation ont été faites au CRHEA par B. Damilano, B. Alloing, A. Courville, et S. Renneson. Tous les process en salle blanche ont été faits par moi-même au C2N, à l'IRIG, à l'Institut Néel, et au CRHEA. La spectroscopie dans le bleu et l'UV sur les dispositifs fabriqués a été faite à l'IRIG et au L2C, pour la plupart par moi-même et en interaction proche avec B. Gayral, L. Doyennette, C. Brimont, et T. Guillet. Les simulations par méthode des différences finies dans le domaine temporel (FDTD) et le design des dispositifs ont été faites par moi-même et ont été basées sur des designs précédents de I. Roland et X. Checoury. P. Boucaud a dirigé tout le projet et a donné des contributions importantes à chaque étape.

## Résumé du chapitre 1

Dans ce chapitre, nous avons présenté les informations importantes pour une compréhension de base des dispositifs photoniques dans la plateforme des nitrures d'éléments III sur silicium. Nous avons commencé en décrivant les propriétés pertinentes du matériau nitrure d'éléments III. Nous avons expliqué la structure cristalline wurtzite et les polarisations spontanée et piézo-électrique observées dans les nitrures plan c, en mentionnant brièvement des orientations semi- et non-polaires comme alternatifs. Nous avons discuté la structure de bande et l'ingénierie de la bande interdite des alliages des nitrures d'éléments III, ainsi que les efficacités quantiques externes rapportées dans la littérature pour donner une idée des gammes spectrales qui peuvent facilement être atteintes, notamment le bleu, le vert, et l'UV. Nous avons présenté les indices optiques ordinaire et extraordinaire, qui sont des paramètres très importants pour le design de nos dispositifs, parce qu'ils définissent la vitesse de la lumière dans le matériau. Puis, nous avons expliqué le choix du substrat et détaillé la croissance des nitrures d'éléments III sur silicium, soulignant les difficultés liées au décalage entre les paramètres de maille et la différence de coefficients de dilatation thermique. Ensuite, nous avons discuté théoriquement les différents composants photoniques qui constituent nos circuits photoniques intégrés, incluant les guides d'onde planaires et ridges, les cavités à microdisque, le couplage entre microdisque et guide d'onde, les lasers à semi-conducteurs, le cristaux pho-

toniques planaires 2D, et les réseaux de couplage. Nous avons expliqué la méthode FDTD et la simulation des dispositifs mentionnés avant. Nous avons également discuté la fabrication en salle blanche des dispositifs photoniques de nitrides d'éléments III sur silicium. Nous avons souligné les quatre étapes du process : la lithographie, le masque de gravure, la gravure, et la sous-gravure. Ensuite, nous avons discuté les process détaillés des dispositifs photoniques investigués dans cette thèse, incluant les microdisques type « champignon », des circuits photoniques actifs et passifs, et des cavités à cristaux photoniques 2D planaires. Nous avons souligné quelques problèmes qui peuvent se produire pendant la fabrication, comme la rugosité des flancs, des poutrelles cassés, des zones de couplage pas ouvertes, des réseaux de couplages cassés ou irréguliers, et des trous non-circulaires. À la fin, nous avons discuté les montages spectroscopiques que nous avons utilisé pour les gammes spectrales UV et bleu.

## Résumé du chapitre 2

Dans ce chapitre, nous avons étudié des lasers à microdisque de nitrides d'éléments III sur silicium. Nous avons discuté l'état de l'art des lasers à microdisque de nitrides d'éléments III sur des substrats de silicium et saphir. Puis, nous avons parlé des résultats de notre consortium d'avant le début de cette thèse. Nous avons décrit les neuf échantillons investigués dans ce chapitre et nous avons discuté quelques mesures structurales et optiques qui ont été faites sur ces échantillons après la croissance, ainsi que des simulations du confinement optique et de la structure de bande. Nous avons fabriqué des microdisques type « champignon » sur ces échantillons et nous les avons caractérisé en pompage optique pulsé à température ambiante. Nous avons discuté les caractéristiques lasers, calculé la puissance au seuil pour le meilleur échantillon, qui était en accord avec les résultats expérimentaux, et investigué l'influence du laser de pompe. La plus basse densité de puissance seuil que nous avons observée de  $18 \text{ kW/cm}^2$  est à l'état de l'art pour des lasers à microdisque en nitrides d'éléments III sur silicium pompés optiquement en pulsé. Nous avons étudié l'impact sur le seuil laser de la méthode de croissance, de la densité de dislocation et d'un traitement chimique. Des échantillons crus en MOCVD ont des seuils plus bas que ceux crus en MBE. Une densité de dislocations plus basse semble avoir pour conséquence un seuil laser plus bas, mais nos échantillons ne sont pas faciles à comparer et il faut aussi constater que nous avons réussi à avoir des seuils bas avec un matériau fin avec une densité de dislocations élevée. Le traitement chimique AZ400K n'a pas eu d'effets clairs sur le seuil laser. Cependant, nous avons observé qu'un process non optimisé peut avoir pour conséquence qu'aucun effet laser ne soit observé, en raison par exemple des dommages à l'endroit où les puits quantiques et le mode laser se situent. En outre, nous avons constaté que le seuil laser augmente avec une augmentation de la profondeur de sous-gravure à cause d'une mauvaise dissipation thermique. Nous avons également comparé des échantillons lasant dans le bleu et l'UVA, discuté la relation entre le seuil et la photoluminescence à forte excitation sur l'échantillon après croissance, ainsi qu'avec le recouvrement du mode. Les échantillons las-

ant dans le bleu montrent des seuils significativement plus bas que les échantillons UVA. Nous avons brièvement discuté le seuil plutôt élevé d'un échantillon cru sur du massif GaN qui contient une jonction pn en comparaison avec nos échantillons sur silicium. Enfin, nous avons estimé si nos échantillons pouvaient laser en continu et nous avons conclu que pour des disques de petits diamètres et des petites tailles de spot du laser de pompe, ça devrait être possible avec le laser en continu disponible.

### Résumé du chapitre 3

Dans ce chapitre, nous avons investigué des circuits photoniques actifs intégrés monolithiquement à base des nitrures d'éléments III sur silicium dans le bleu, composé d'un laser à microdisque, d'un guide d'onde et des réseaux de couplage. Nous avons discuté des approches différentes de l'intégration monolithique trouvée dans la littérature, ainsi que l'état de l'art de l'intégration hétérogène et du couplage critique dans des circuits photoniques de nitrures d'éléments III. Nous avons parlé du design et du process de fabrication des circuits photoniques dans des nitrures d'éléments III sur silicium, spécifiques à deux échantillons qui ont été crus en MBE et qui contiennent 10 puits quantiques InGaN avec une émission vers 420 nm. Le premier échantillon a des microdisques couplés avec des guides d'onde avec des distances de séparation élevées entre les deux correspondant à un régime de sous-couplage. Le deuxième échantillon a des distances de séparation plus petites, ce qui permet d'observer le couplage critique dans le régime d'émission spontané. Nous avons montré des résultats en pompage optique continu et pulsé pour ces deux échantillons. Nous avons discuté la micro-photoluminescence continue obtenue avec le premier échantillon, démontrant un circuit photonique actif dans le bleu. Des  $Q_{load}$  plus grands que 2000 ont été observés au niveau des réseaux de couplage pour des dispositifs avec de faibles gaps et grands angles du guide autour du disque. Nous avons démontré le premier microlaser bleu intégré dans un circuit photonique en utilisant des nitrures d'éléments III sur silicium. L'effet laser a été observé en pompage optique pulsé pour des dispositifs avec des gaps importants et des guides d'onde droits avec un seuil de 15 mJ/cm<sup>2</sup> par pulse (38 MW/cm<sup>2</sup> puissance pic). En utilisant le deuxième échantillon, nous avons démontré le couplage critique et l'effet laser dans un circuit photonique actif en nitrures d'éléments III sur silicium avec des microdisques et des guides d'onde courbés à 90° dans la gamme spectrale bleue. Cette étude a eu pour but d'identifier les caractéristiques principales associées avec le couplage critique et l'effet laser dans le bleu. Des seuils laser bas de 1.7 mJ/cm<sup>2</sup> par pulse (425 kW/cm<sup>2</sup> puissance pic) au couplage critique et 1.2 mJ/cm<sup>2</sup> par pulse (300 kW/cm<sup>2</sup> puissance pic) dans le régime de couplage sous-critique ont été observés. Des facteurs de qualité intrinsèques,  $Q_{int}$ , de 4700 ont été mesurés dans le régime de couplage sous-critique, et une réduction de  $Q_{load}$  d'un facteur 2 a été observée au couplage critique pour un écart de 45 nm. Une forte dépendance du seuil sur  $Q_{load}$  a été observée qui était parfaitement en accord avec la théorie. La puissance de sortie,  $P_{out}$ , a été étudiée en fonction de  $Q_c$ , et nous avons analysé

la dépendance avec la puissance de pompe,  $P_{\text{pump}}$ , trouvant un bon accord entre les données expérimentales et une formule analytique. Un effet de proximité du guide d'onde sur le disque est responsable d'un changement de la position du mode, ce qui souligne l'impact d'un design et d'une fabrication optimisés sur les paramètres intrinsèques du micro-résonateur.

## Résumé du chapitre 4

Dans ce chapitre, nous avons étudié deux dispositifs photoniques fonctionnant dans l'UV : des circuits photoniques intégrés monolithiquement et des cristaux photoniques 2D planaires. En premier, nous avons discuté l'état de l'art des circuits photoniques UV et des cavités à cristaux photonique planaires à base de nitrures d'éléments III. Nous avons conçu et fabriqué des circuits photoniques suspendus avec des microdisques qui fonctionnent dans l'UVA vers 380 nm avec un angle du guide autour du disque de  $180^\circ$ . Nous avons observé des  $Q_{\text{load}}$  de 3500 à 420 nm en excitation continue et l'effet laser des modes entre 374 et 399 nm en pompage optique pulsé. Nous avons estimé des pertes de propagation autour de  $0.08 \text{ dB} \cdot \mu\text{m}^{-1}$  et nous avons comparé cette valeur avec la littérature. L'écart en longueur d'onde entre des mesures en continu et en pulsé est lié aux niveaux excités des puits quantiques qui lasent. Les modes lasers ont des seuils très bas de  $0.14 \text{ mJ/cm}^2$  par pulse ou  $35 \text{ kW/cm}^2$  puissance pic pour un écart entre disque et guide de 80 nm et nous avons observé une dynamique très large entre pic et fond de 200 au réseau de couplage pour un dispositif avec un gap de 50 nm. Les dispositifs ont montré la réduction du seuil attendu en augmentant l'écart entre disque et guide. Les dispositifs fonctionnent à la limite de longueur d'onde pour du GaN. Pour descendre plus bas en longueur d'onde vers l'UVC, il faut utiliser de l'AlN pour la couche du guide d'onde avec des puits quantiques à base d'AlGaIn. De plus, nous avons étudié des cavités à cristaux photonique L3 et H2 dans des membranes de nitrures d'éléments III suspendus sur silicium avec des puits quantiques GaN/AlN. Nous avons observé des résonances avec des facteurs de qualité de 1085 à 337 nm. Nous avons étudié la réduction du facteur de qualité avec la décroissance de la longueur d'onde. À part l'absorption des puits quantiques en dessous de 340 nm, une contribution importante est attribuée à l'absorption résiduelle présente dans des couches fines AlN épitaxiées sur silicium, comme mesuré par ellipsométrie spectroscopique. Cette absorption résiduelle peut limiter le facteur de qualité à environ 2000 vers 300 nm quand il n'y a pas une couche active. Ces dispositifs pourraient potentiellement laser, mais ils n'ont pas été étudiés en pompage optique pulsé.

## Résumé du chapitre 5

Dans ce chapitre, nous avons étudié l'injection électrique dans des microdisques et microanneaux verticaux en nitrures d'éléments III sur silicium. Nous avons discuté l'état de l'art des lasers à microdisque type « sandwich » et l'injection électrique dans des circuits photoniques

à base des nitrures d'éléments III. Nous avons démontré deux schémas pour l'injection électrique vertical dans des microdisques et microanneaux fins en nitrure d'éléments III sur silicium. Dans notre approche initiale, nous avons supposé que la conductivité des couches tampons étaient suffisante, parce qu'une conductivité verticale a été constatée pour des aires larges. Toutefois, une électroluminescence très faible a été observée dans ces dispositifs. Le chemin du courant passait par des défauts et la conductivité disparaît pour des mesas de taille inférieure à 100  $\mu\text{m}$ . En conséquence, nous avons développé un process complexe de microanneaux avec un contact n enterré qui contourne les couches tampons isolantes. Cette approche est compatible avec des couches fines de nitrures d'éléments III épitaxiés sur silicium et avec des diodes à microlasers couplés avec des circuits photoniques intégrés, parce qu'elle autorise la sous-gravure des dispositifs et la possibilité de fabriquer des guides d'onde avec des petits écarts de moins de 100 nm entre l'anneau et le guide, nécessaire pour un couplage efficace dans la gamme spectrale bleue-UV. Nous avons démontré de l'électroluminescence avec ces microanneaux contactés avec des micro-ponts métalliques avec une densité de puissance de sortie de 440  $\text{mW}/\text{cm}^2$  à 20 mA et nous avons également démontré des LEDs blanches à base de microanneaux. L'effet laser n'a pas encore été observé, ce qui peut être dû au recouvrement important entre le mode optique et la zone dopée p et le recouvrement faible avec les puits quantiques, ou lié à la mauvaise distribution du courant dans du GaN dopé p et la distance importante entre le contact p et le mode optique au bord du disque. Des travaux futurs vont essayer de faire laser soit des structures fines type « champignon », soit des structures épaisses type « sandwich », ainsi que d'intégrer ces lasers dans des circuits photoniques.

## Résumé du chapitre 6

Dans ce chapitre, nous avons discuté des circuits photoniques passifs dans le proche IR avec des nitrures d'éléments III épitaxiés sur silicium et collés sur  $\text{SiO}_2$  et suspendus dans l'air. Nous avons discuté l'état de l'art des circuits photoniques passifs dans l'IR à base de nitrures d'éléments III avec un focus sur des effets optiques non-linéaires comme l'OPO et les peignes de fréquence. Ensuite, nous avons examiné le design et la fabrication des circuits photoniques sur deux échantillons de 330 nm de l'épaisseur totale, un collé sur  $\text{SiO}_2$  et l'autre suspendu sur silicium (100). Ces deux échantillons ne sont pas assez épais pour bien confiner la lumière vers 1560 nm et nous avons donc fait le design pour 780 nm. Nous avons utilisé des simulations FDTD pour déterminer les spectres de transmission pour obtenir une estimation de l'intervalle spectral libre et du  $Q_{load}$  pour les différents dispositifs. Les dispositifs fabriqués devraient fonctionner dans un régime de couplage critique ou sur-critique. Le couplage critique est anticipé pour des distances disque-guide autour de 200 nm pour un anneau de 20  $\mu\text{m}$  de diamètre et dans une gamme de 160 à 200 nm pour des microdisques de 8  $\mu\text{m}$  sur ces deux échantillons. Des  $Q_{load}$  très élevés d'autour de  $1 \times 10^5$  ont été obtenus en simulation dans les régimes critique et sur-critique, ce qui est du même ordre de grandeur que ce qui a été obtenu

en expérience dans la littérature. Des mesures de transmission de ces échantillons n'ont pas encore été faites à cause du confinement lié au Covid-19. En attendant, nous avons commencé le design d'un microanneau en double résonance et avec la condition d'accord de phase pour la conversion paramétrique dégénérée à 1560 nm et 780 nm avec un échantillon d'une épaisseur de 640 nm de nitrures d'éléments III sur SiO<sub>2</sub>. Les prochaines étapes vont inclure de finir ce design, de fabriquer ces circuits photoniques et de mesurer des facteurs de qualité à ces deux longueurs d'onde, ainsi que le signal converti.

## Conclusion et perspectives

Les résultats discutés dans cette thèse illustrent bien la versatilité de la plateforme de nitrures d'éléments III sur silicium à partir de la grande gamme spectrale des dispositifs photoniques intégrés actifs et passifs. Les nitrures d'éléments III sont de très bons candidats pour la prochaine génération des circuits photoniques intégrés à cause de leur grande gamme de transparence, l'accordabilité de la bande interdite, les grands non-linéarités optique d'ordre deux et trois, et la grande énergie de liaison d'exciton à température ambiante. Alors que ces travaux ont eu pour focus les deux premiers aspects, l'optique non-linéaire et quantique sont également des domaines prometteurs des futures recherches. Les travaux décrits dans cette thèse ont été faits dans le cadre de deux projets ANR, Milagan et Opoint. Milagan continue encore pour un an et Opoint vient de commencer cette année. Dans le cadre de Milagan, le but principal est de faire laser en injection électrique. Une option est d'aller vers des structures épaisses comme l'a fait l'équipe de Yang à l'Académie des Sciences Chinoise en utilisant des couches optiquement guidantes entourées d'une gaine. Cela permettrait d'avoir une densité de dislocation basse, un meilleur recouvrement du mode avec la zone active, et une réduction du recouvrement avec la zone dopée p. Cela permettrait également d'étendre le contact p jusqu'au bord du disque ce qui aiderait avec la distribution du courant. Les dispositifs pourraient être plus petits parce que le contact n pourrait être pris latéralement au lieu d'un trou central qui connecte à la face arrière. Cependant il sera plus difficile de faire des circuits photoniques en injection électrique, ce qui est une autre perspective intéressante. En utilisant des couches fines et suspendues de nitrures d'éléments III, nous pourrions combiner l'injection électrique avec des circuits photoniques intégrés. Néanmoins, cela correspond à un process très long et compliqué que nous avons essayé plusieurs fois sans succès. Implémenter des jonctions tunnels comme contact du haut pourrait également aider avec la distribution du courant dans des structures fines. Dans le projet Opoint un but important est de faire des OPOs en utilisant des microanneaux dans une plateforme de nitrures d'éléments III sur SiO<sub>2</sub> comme nous l'avons introduit dans le chapitre 6. Pour atteindre ce but, le premier pas est de réaliser des résonateurs à facteur de qualité élevé proche du couplage critique fonctionnant autour de 1560 nm et 780 nm. Ensuite, la conversion paramétrique dégénérée et non-dégénérée avec un accord de phase et en double résonance doit être démontrée dans des circuits photoniques à base de microanneaux soigneusement

conçus. Une fois que nous aurons des résonateurs à facteur de qualité élevé vers 1550 nm, il devrait également être possible de démontrer des peignes de fréquence.

Enfin, basé sur des circuits photoniques actifs discutés dans les chapitres 3 et 4, la prochaine étape logique serait de continuer à baisser la longueur d'onde pour aller vers l'UVB et C. Bien qu'il sera difficile de faire du couplage critique à cause des limitations de fabrication, ces dispositifs devraient pouvoir laser dans le régime de couplage sous-critique.

Une autre nouvelle plateforme intéressante est constituée par les nitrures d'éléments III sur Si (100). Nous avons fabriqué des circuits photoniques sur un échantillon de 330 nm AlN. Dans des prochains travaux, nous pourrions épitaxier du GaN sur la couche tampon AlN pour faire des circuits photoniques dans le proche IR. Ensuite, nous pourrions croquer des puits quantiques InGaN pour faire des résonateurs et lasers à microdisque dans le bleu. Enfin, nous pourrions faire des circuits photoniques actifs dans le bleu comme nous l'avons démontré sur Si (111).

# Bibliography

- [1] H. Amano, N. Sawaki, I. Akasaki, and Y. Toyoda. Metalorganic vapor phase epitaxial growth of a high quality GaN film using an AlN buffer layer. *Appl. Phys. Lett.*, 48(5):353–355, 1986.
- [2] H. Amano, M. Kito, K. Hiramatsu, and I. Akasaki. P-type conduction in Mg-doped GaN treated with low-energy electron beam irradiation (LEEBI). *Jpn. J. Appl. Phys.*, 28(12A):L2112, 1989.
- [3] S. Nakamura, T. Mukai, and M. Senoh. High-power GaN pn junction blue-light-emitting diodes. *Jpn. J. Appl. Phys.*, 30(12A):L1998, 1991.
- [4] S. Nakamura, T. Mukai, M. Senoh, and N. Iwasa. Thermal annealing effects on p-type Mg-doped GaN films. *Jpn. J. Appl. Phys.*, 31(2B):L139, 1992.
- [5] S. Nakamura, M. Senoh, and T. Mukai. P-GaN/N-InGaN/N-GaN double-heterostructure blue-light-emitting diodes. *Jpn. J. Appl. Phys.*, 32(1A):L8, 1993.
- [6] R. Butté and N. Grandjean. III-nitride photonic cavities. *Nanophotonics*, 9(3):569–598, 2020.
- [7] D. J. Blumenthal. Photonic integration for UV to IR applications. *APL Photonics*, 5(2):020903, 2020.
- [8] C. Xiong, W. H. P. Pernice, and H. X. Tang. Low-loss, silicon integrated, aluminum nitride photonic circuits and their use for electro-optic signal processing. *Nano Lett.*, 12:3562–3568, 2012.
- [9] W. H. P. Pernice, C. Xiong, C. Schuck, and H. X. Tang. Second harmonic generation in phase matched aluminum nitride waveguides and micro-ring resonators. *Appl. Phys. Lett.*, 100:223501, 2012.
- [10] M. Stegmaier, J. Ebert, J. M. Meckbach, K. Ilin, M. Siegel, and W. H. P. Pernice. Aluminum nitride nanophotonic circuits operating at ultraviolet wavelengths. *Appl. Phys. Lett.*, 104:091108, 2014.

- 
- [11] M. J. Holmes, K. Choi, S. Kako, M. Arita, and Y. Arakawa. Room-temperature triggered single photon emission from a III-nitride site-controlled nanowire quantum dot. *Nano Lett.*, 14(2):982–986, 2013.
- [12] G. Grosso, B. Lienhard, H. Moon, D. Scarabell, T. Schroeder, K. Jeong, T. Lu, A. M. Berhane, S. Wind, I. Aharanovich, and D. Englund. Quantum emission from atomic defects in wide-bandgap semiconductors. In *2017 IEEE Photonics Society Summer Topical Meeting Series (SUM)*, pages 103–104, 2017.
- [13] A. M. Berhane, K.-Y. Jeong, Z. Bodrog, S. Fiedler, T. Schröder, N. Vico Triviño, T. Palacios, A. Gali, M. Toth, D. Englund, and I. Aharanovich. Bright room-temperature single-photon emission from defects in gallium nitride. *Adv. Mater.*, 29(12):1605092, 2017.
- [14] F. De Leonardis, R. A. Soref, M. Soltani, and V. M. N. Passaro. Broadband biphoton generation and statistics of quantum light in the UV-visible range in an AlGaIn microring resonator. *Sci. Rep.*, 7:11387, 2017.
- [15] X. Guo, C. I. Zou, C. Schuck, H. Jung, R. Cheng, and H. X. Tang. Parametric down-conversion photon-pair source on a nanophotonic chip. *Light Sci. Appl.*, 6:e16249, 2017.
- [16] X. Liu, C. Sun, B. Xiong, L. Wang, J. Wang, Y. Han, Z. Hao, H. Li, Y. Luo, J. Yan, T. Wei, Y. Zhang, and J. Wang. Integrated high-Q crystalline AlN microresonators for broadband Kerr and Raman frequency combs. *ACS Photonics*, 5(5):1943–1950, 2018.
- [17] X. Liu, A. W. Bruch, J. Lu, Z. Gong, J. B. Surya, L. Zhang, J. Wang, J. Yan, and H. X. Tang. Beyond 100 THz-spanning ultraviolet frequency combs in a non-centrosymmetric crystalline waveguide. *Nat. Commun.*, 10(1):1–8, 2019.
- [18] A. W. Bruch, X. Liu, J. B. Surya, C.-L. Zou, and H. X. Tang. On-chip  $\chi(2)$  microring optical parametric oscillator. *Optica*, 6(10):1361–1366, 2019.
- [19] Y. Tang, Z. Gong, X. Liu, and H. X. Tang. Widely separated optical Kerr parametric oscillation in AlN microrings. *Opt. Lett.*, 45(5):1124–1127, 2020.
- [20] Y.-C. Chi, D.-H. Hsieh, C.-Y. Lin, H.-Y. Chen, C.-Y. Huang, J.-H. He, B. Ooi, S. P. DenBaars, S. Nakamura, H.-C. Kuo, and G.-R. Lin. Phosphorous diffuser diverged blue laser diode for indoor lighting and communication. *Sci. Rep.*, 5:18690, 2015.
- [21] E. Xie, X. He, M. S. Islam, A. A. Purwita, J. J. D. McKendry, E. Gu, H. Haas, and M. D. Dawson. High-speed visible light communication based on a III-nitride series-biased micro-LED array. *J. Light. Technol.*, 37:1180–1186, 2019.
- [22] S. A. Jewett, M. S. Makowski, B. Andrews, M. J. Manfra, and A. Ivanisevic. Gallium nitride is biocompatible and non-toxic before and after functionalization with peptides. *Acta Biomaterialia*, 8(2):728–733, 2012.

- 
- [23] M. Hofstetter, J. Howgate, M. Schmid, S. Schoell, M. Sachsenhauser, D. Adigüzel, M. Stutzmann, I. D. Sharp, and S. Thalhammer. In vitro bio-functionality of gallium nitride sensors for radiation biophysics. *Biochem. Biophys. Res. Commun.*, 424:348–353, 2012.
- [24] X. Lia and X. Liu. Group III nitride nanomaterials for biosensing. *Nanoscale*, 9:7320, 2017.
- [25] C. R. Doerr. Silicon photonic integration in telecommunications. *Front. Phys.*, 3:37, 2015.
- [26] M. Smit, X. Leijtens, H. Ambrosius, E. Bente, J. van der Tol, B. Smalbrugge, T. de Vries, E.-J. Geluk, J. Bolk, R. van Veldhoven, L. Augustin, P. Thijs, D. D’Agostino, H. Rabbani, K. Lawniczuk, S. Stopinski, S. Tahvili, A. Corradi, E. Kleijn, D. Dzibrou, M. Felicetti, E. Bitincka, V. Moskalenko, J. Zhao, R. Santos, G. Gilardi, W. Yao, K. Williams, P. Stabile, P. Kuindersma, J. Pello, S. Bhat, Y. Jiao, D. Heiss, G. Roelkens, M. Wale, P. Firth, F. Soares, N. Grote, M. Schell, H. Debregeas, M. Achouche, J.-L. Gentner, A. Bakker, T. Korthorst, D. Gallagher, A. Dabbs, A. Melloni, F. Morichetti, D. Melati, A. Wonfor, R. Penty, R. Broeke, B. Musk, and D. Robbins. An introduction to InP-based generic integration technology. *Semicond. Sci. Technol.*, 29:083001, 2014.
- [27] A. D. Bristow, N. Rotenberg, and H. M. Van Driel. Two-photon absorption and Kerr coefficients of silicon for 850–2200 nm. *Appl. Phys. Lett.*, 90(19):191104, 2007.
- [28] D. Vignaud, J.F. Lampin, and F. Mollot. Two-photon absorption in InP substrates in the 1.55  $\mu\text{m}$  range. *Appl. Phys. Lett.*, 85(2):239–241, 2004.
- [29] W. H. P. Pernice, C. Xiong, and H. X. Tang. High Q micro-ring resonators fabricated from polycrystalline aluminum nitride films for near infrared and visible photonics. *Opt. Express*, 20(11):12261–12269, 2012.
- [30] E. D. Haberer, R. Sharma, C. Meier, A. R. Stonas, S. Nakamura, S. P. DenBaars, and E. L. Hu. Free-standing, optically pumped, GaN/InGaN microdisk lasers fabricated by photoelectrochemical etching. *Appl. Phys. Lett.*, 84(22):5179–5181, 2004.
- [31] A. C. Tamboli, E. D. Haberer, R. Sharma, K. H. Lee, S. Nakamura, and E. L. Hu. Room-temperature continuous-wave lasing in GaN/InGaN microdisks. *Nat. Photonics*, 1:61–64, 2007.
- [32] X. Zhang, Y. F. Cheung, Y. Zhang, and H. W. Choi. Whispering-gallery mode lasing from optically free-standing InGaN microdisks. *Opt. Lett.*, 39(19):5614–5617, 2014.
- [33] M. Athanasiou, R. Smith, B. Liu, and T. Wang. Room temperature continuous-wave green lasing from an InGaN microdisk on silicon. *Sci. Rep.*, 4:7250, 2014.
- [34] N. Vico Triviño, R. Butté, J.-F. Carlin, and N. Grandjean. Continuous wave blue lasing in III-nitride nanobeam cavity on silicon. *Nano Lett.*, 15:1259–1263, 2015.

- 
- [35] I. Rousseau, I. Sanchez-Arribas, K. Shojiki, J.-F. Carlin, R. Butté, and N. Grandjean. Quantification of scattering loss of III-nitride photonic crystal cavities in the blue spectral range. *Phys. Rev. B*, 95:125313, 2017.
- [36] I. Rousseau, G. Callsen, G. Jacopin, J.-F. Carlin, R. Butté, and N. Grandjean. Optical absorption and oxygen passivation of surface states in III-nitride photonic devices. *J. Appl. Phys.*, 123:113103, 2018.
- [37] S. T. Jagsch, N. Vico Triviño, F. Lohof, G. Callsen, S. Kalinowski, I. M. Rousseau, R. Barzel, J.-F. Carlin, F. Jahnke, R. Butté, C. Gies, A. Hoffmann, N. Grandjean, and S. Reitzenstein. A quantum optical study of thresholdless lasing features in high- $\beta$  nitride nanobeam cavities. *Nat. Commun.*, 9:564, 2018.
- [38] H. Jung, C. Xiong, K. Y. Fong, X. Zhang, and H. X. Tang. Optical frequency comb generation from aluminum nitride microring resonator. *Opt. Lett.*, 38:2810–2813, 2013.
- [39] A. W. Bruch, C. Xiong, B. Leung, M. Poot, J. Han, and H. X. Tang. Broadband nanophotonic waveguides and resonators based on epitaxial GaN thin films. *Appl. Phys. Lett.*, 107:141113, 2015.
- [40] C. Xiong, W. H. P. Pernice, X. Sun, C. Schuck, K. Y. Fong, and H. X. Tang. Aluminum nitride as a new material for chip-scale optomechanics and nonlinear optics. *New J. Phys.*, 14:095014, 2012.
- [41] T.-J. Lu, M. Fanto, H. Choi, P. Thomas, J. Steidle, S. Mouradian, W. Kong, D. Zhu, H. Moon, K. Berggren, J. Kim, M. Soltani, S. Preble, and D. Englund. Aluminum nitride integrated photonics platform for the ultraviolet to visible spectrum. *Opt. Express*, 26:11147–11160, 2018.
- [42] X. Liu, A. W. Bruch, Z. Gong, J. Lu, J. B. Surya, L. Zhang, J. Wang, J. Yan, and H. X. Tang. Ultra-high-Q UV microring resonators based on single-crystalline AlN platform. *Optica*, 5:1279–1282, 2018.
- [43] M. Feng, J. He, Q. Sun, H. Gao, Z. Li, Y. Zhou, J. Liu, S. Zhang, D. Li, L. Zhang, X. Sun, D. Li, H. Wang, M. Ikeda, R. Wang, and H. Yang. Room-temperature electrically pumped InGaN based microdisk laser grown on Si. *Opt. Express*, 26(4):5043–5051, 2018.
- [44] J. Wang, M. Feng, R. Zhou, Q. Sun, J. Liu, Y. Huang, Y. Zhou, H. Gao, X. Zheng, M. Ikeda, and H. Yang. GaN-based ultraviolet microdisk laser diode grown on Si. *Photonics Res.*, 7(6):B32–B35, 2019.
- [45] J. Wang, M. Feng, R. Zhou, Q. Sun, J. Liu, X. Sun, X. Zheng, M. Ikeda, X. Sheng, and H. Yang. Continuous-wave electrically injected GaN-on-Si microdisk laser diodes. *Opt. Express*, 28(8):12201–12208, 2020.

- 
- [46] M. Mexis, S. Sergent, T. Guillet, C. Brimont, T. Bretagnon, B. Gil, F. Semond, M. Leroux, D. Néel, S. David, X. Checoury, and P. Boucaud. High quality factor nitride-based optical cavities: microdisks with embedded GaN/Al(Ga)N quantum dots. *Opt. Lett.*, 36(12):2203–2205, 2011.
- [47] D. Sam-Giao, D. Néel, S. Sergent, B. Gayral, M. J. Rashid, F. Semond, J.-Y. Duboz, M. Mexis, T. Guillet, C. Brimont, S. David, X. Checoury, and P. Boucaud. High quality factor AlN nanocavities embedded in a photonic crystal waveguide. *Appl. Phys. Lett.*, 100:191104, 2012.
- [48] D. Néel, I. Roland, X. Checoury, M. El Kurdi, S. Sauvage, C. Brimont, T. Guillet, B. Gayral, F. Semond, and P. Boucaud. Aluminum nitride photonic crystals and microdiscs for ultra-violet nanophotonics. *Adv. Nat. Sci.: Nanosci. Nanotechnol.*, 5:023001, 2014.
- [49] J. Sellés, C. Brimont, G. Cassaboïs, P. Valvin, T. Guillet, I. Roland, Y. Zeng, X. Checoury, P. Boucaud, M. Mexis, F. Semond, and B. Gayral. Deep-UV nitride-on-silicon microdisk lasers. *Sci. Rep.*, 6:21650, 2016.
- [50] J. Sellés, V. Crepel, I. Roland, M. El Kurdi, X. Checoury, P. Boucaud, M. Mexis, M. Leroux, B. Damilano, S. Rennesson, F. Semond, B. Gayral, C. Brimont, and T. Guillet. III-nitride-on-silicon microdisk lasers from the blue to the deep ultra-violet. *Appl. Phys. Lett.*, 109:231101, 2016.
- [51] I. Roland, Y. Zeng, Z. Han, X. Checoury, C. Blin, M. El Kurdi, A. Ghrib, S. Sauvage, B. Gayral, C. Brimont, T. Guillet, F. Semond, and P. Boucaud. Near-infrared gallium nitride two-dimensional photonic crystal platform on silicon. *Appl. Phys. Lett.*, 105:011104, 2014.
- [52] I. Roland, Y. Zeng, X. Checoury, M. El Kurdi, S. Sauvage, C. Brimont, T. Guillet, B. Gayral, M. Gromovyi, J.-Y. Duboz, F. Semond, M. P. de Micheli, and P. Boucaud. Near-infrared III-nitride-on-silicon nanophotonic platform with microdisk resonators. *Opt. Express*, 24(9):9602–9610, 2016.
- [53] Y. Zeng, I. Roland, X. Checoury, Z. Han, M. El Kurdi, S. Sauvage, B. Gayral, C. Brimont, T. Guillet, M. Mexis, F. Semond, and P. Boucaud. Resonant second harmonic generation in a gallium nitride two-dimensional photonic crystal on silicon. *Appl. Phys. Lett.*, 106(8):081105, 2015.
- [54] Y. Zeng, I. Roland, X. Checoury, Z. Han, M. El Kurdi, S. Sauvage, B. Gayral, C. Brimont, T. Guillet, F. Semond, and P. Boucaud. Imaging of photonic crystal localized modes through third-harmonic generation. *ACS Photonics*, 3(7):1240–1247, 2016.

- 
- [55] I. Roland, M. Gromovyi, Y. Zeng, M. El Kurdi, S. Sauvage, C. Brimont, T. Guillet, B. Gayral, F. Semond, J.-Y. Duboz, M. de Micheli, X. Checoury, and P. Boucaud. Phase-matched second harmonic generation with on-chip GaN-on-Si microdisks. *Sci. Rep.*, 6:34191, 2016.
- [56] S. Sergent. *Fabrication and study of nitride-based photonic nanocavities containing GaN quantum dots for UV emitters integrated on silicon*. PhD thesis, Université de Nice-Sophia Antipolis, 2010.
- [57] D. Sam-Giao. *Optical study of GaN nanowires and GaN/AlN microcavities*. PhD thesis, Université de Grenoble, 2012.
- [58] J. Sélles. *Spectroscopie optique de nanostructures GaN/AlN en microcavités planaires et en microdisques*. PhD thesis, Université de Montpellier, 2015.
- [59] Y. Zeng. *Circuits photoniques III-nitrure avec des cristaux photoniques et des microdisques*. PhD thesis, Université Paris-Saclay, 2017.
- [60] P. Rinke, M. Scheffler, A. Qteish, M. Winkelnkemper, D. Bimberg, and J. Neugebauer. Band gap and band parameters of InN and GaN from quasiparticle energy calculations based on exact-exchange density-functional theory. *Appl. Phys. Lett.*, 89:161919, 2006.
- [61] M. Feneberg, R. A. R. Leute, B. Neuschl, K. Thonke, and M. Bickermann. High-excitation and high-resolution photoluminescence spectra of bulk AlN. *Phys. Rev. B*, 82:075208, 2010.
- [62] F. Tabataba-Vakili. Morphological properties of GaN nanostructures grown on AlN by MOVPE. Bachelor's thesis, Technische Universität Berlin, 2013.
- [63] F. Bernardini, V. Fiorentini, and D. Vanderbilt. Spontaneous polarization and piezoelectric constants of III-V nitrides. *Phys. Rev. B*, 56(16):R10024, 1997.
- [64] D. A. B. Miller. Optical physics of quantum wells. In G.-L. Oppo, S.M. Barnett, E. Riis, and M. Wilkinson, editors, *Quantum Dynamics of Simple Systems*, pages 239–266. SUSSP Publications and Institute of Physics Publishing, Edinburgh and London, 1996.
- [65] Y. Zhao, H. Fu, G. T. Wang, and S. Nakamura. Toward ultimate efficiency: Progress and prospects on planar and 3D nanostructured nonpolar and semipolar InGaN light-emitting diodes. *Adv. Opt. Photonics*, 10(1):246–308, 2018.
- [66] Y. Zhao, R. M. Farrell, Y.-R. Wu, and J. S. Speck. Valence band states and polarized optical emission from nonpolar and semipolar III-nitride quantum well optoelectronic devices. *Jpn. J. Appl. Phys.*, 53(10):100206, 2014.
- [67] A.E. Romanov, T.J. Baker, S. Nakamura, J.S. Speck, and ERATO/JST UCSB Group. Strain-induced polarization in wurtzite III-nitride semipolar layers. *J. Appl. Phys.*, 100(2):023522, 2006.

- [68] I. Vurgaftman and J.R. Meyer. Band parameters for nitrogen-containing semiconductors. *J. Appl. Phys.*, 94(6):3675–3696, 2003.
- [69] C. Reich, M. Guttman, M. Feneberg, T. Wernicke, F. Mehnke, C. Kuhn, J. Rass, M. Lapeyrade, S. Einfeldt, A. Knauer, V. Kueller, M. Weyers, R. Goldhahn, and M. Kneissl. Strongly transverse-electric-polarized emission from deep ultraviolet AlGa<sub>N</sub> quantum well light emitting diodes. *Appl. Phys. Lett.*, 107(14):142101, 2015.
- [70] L. Cláudio de Carvalho, A. Schleife, F. Fuchs, and F. Bechstedt. Valence-band splittings in cubic and hexagonal AlN, GaN, and InN. *Appl. Phys. Lett.*, 97(23):232101, 2010.
- [71] M.-H. Kim, M. F. Schubert, Q. Dai, J. K. Kim, E. F. Schubert, J. Piprek, and Y. Park. Origin of efficiency droop in GaN-based light-emitting diodes. *Appl. Phys. Lett.*, 91(18):183507, 2007.
- [72] A. Laubsch, M. Sabathil, W. Bergbauer, M. Strassburg, H. Lugauer, M. Peter, S. Lutgen, N. Linder, K. Streubel, J. Hader, J. V. Moloney, B. Pasenow, and S. W. Koch. On the origin of IQE-‘droop’ in InGa<sub>N</sub> LEDs. *Phys. Status Solidi C*, 6(S2 2):S913–S916, 2009.
- [73] Y. Lin, Y. Zhang, Z. Liu, L. Su, J. Zhang, T. Wei, and Z. Chen. Interplay of point defects, extended defects, and carrier localization in the efficiency droop of InGa<sub>N</sub> quantum wells light-emitting diodes investigated using spatially resolved electroluminescence and photoluminescence. *J. Appl. Phys.*, 115(2):023103, 2014.
- [74] M. Auf Der Maur, A. Pecchia, G. Penazzi, W. Rodrigues, and A. Di Carlo. Efficiency drop in green InGa<sub>N</sub>/Ga<sub>N</sub> light emitting diodes: The role of random alloy fluctuations. *Phys. Rev. Lett.*, 116(2):027401, 2016.
- [75] M. Kneissl and J. Rass. *III-Nitride Ultraviolet Emitters*. Springer Science & Business Media, 2016.
- [76] Ü. Özgür, G. Webb-Wood, H. O. Everitt, F. Yun, and H. Morkoç. Systematic measurement of Al<sub>x</sub>Ga<sub>1-x</sub>N refractive indices. *Appl. Phys. Lett.*, 79(25):4103–4105, 2001.
- [77] S. Pezzagna, J. Brault, M. Leroux, J. Massies, and M. De Micheli. Refractive indices and elasto-optic coefficients of Ga<sub>N</sub> studied by optical waveguiding. *J. Appl. Phys.*, 103(12):123112, 2008.
- [78] T. Mattila and R. M. Nieminen. Point-defect complexes and broadband luminescence in Ga<sub>N</sub> and AlN. *Phys. Rev. B*, 55(15):9571, 1997.
- [79] G. Li, S.J. Chua, S.J. Xu, W. Wang, P. Li, B. Beaumont, and P. Gibart. Nature and elimination of yellow-band luminescence and donor–acceptor emission of undoped Ga<sub>N</sub>. *Appl. Phys. Lett.*, 74(19):2821–2823, 1999.

- 
- [80] M. A. Reshchikov and H. Morkoç. Luminescence properties of defects in GaN. *J. Appl. Phys.*, 97(6):5–19, 2005.
- [81] A. Dadgar, A. Krost, J. Christen, B. Bastek, F. Bertram, A. Krtschil, T. Hempel, J. Bläsing, U. Haboeck, and A. Hoffmann. MOVPE growth of high-quality AlN. *J. Cryst. Growth*, 297(2):306–310, 2006.
- [82] R. Collazo, J. Xie, B. E. Gaddy, Z. Bryan, R. Kirste, M. Hoffmann, R. Dalmau, B. Moody, Y. Kumagai, T. Nagashima, Y. Kubota, T. Kinoshita, A. Koukitu, D. L. Irving, and Z. Sitar. On the origin of the 265 nm absorption band in AlN bulk crystals. *Appl. Phys. Lett.*, 100(19):191914, 2012.
- [83] B. Gil. *III-Nitride Semiconductors and their modern devices*, volume 18. 2013.
- [84] D. A. Neumayer and J. G. Ekerdt. Growth of group III nitrides. A review of precursors and techniques. *Chem. Mater.*, 8:9–25, 1996.
- [85] O. Ambacher. Growth and applications of group III-nitrides. *J. Phys. D: Appl. Phys.*, 31:2653, 1998.
- [86] K. S. Jeon, S.-W. Kim, D.-H. Ko, and H. Y. Ryu. Relationship between threading dislocations and the optical properties in GaN-based LEDs on Si substrates. *J. Korean Phys. Soc.*, 67(7):1085–1088, 2015.
- [87] Y. Sun, K. Zhou, Q. Sun, J. Liu, M. Feng, Z. Li, Y. Zhou, L. Zhang, D. Li, S. Zhang, M. Ikeda, S. Liu, and H. Yang. Room-temperature continuous-wave electrically injected InGaN-based laser directly grown on Si. *Nat. Photon.*, 10:595–599, 2016.
- [88] T. Hossain, J. Wang, E. Frayssinet, S. Chenot, M. Leroux, B. Damilano, F. Demangeot, L. Durand, A. Ponchet, M.J. Rashid, F. Semond, and Y. Cordier. Stress distribution of 12  $\mu\text{m}$  thick crack free continuous GaN on patterned Si (110) substrate. *Phys. Status Solidi C*, 10:425–428, 2012.
- [89] A. Tanaka, W. Choi, R. Chen, and S. A. Dayeh. Si complies with GaN to overcome thermal mismatches for the heteroepitaxy of thick GaN on Si. *Adv. Mater.*, 29:1702557, 2017.
- [90] E. Frayssinet, Y. Cordier, H.P.D. Schenk, and A. Bavard. Growth of thick GaN layers on 4-in. and 6-in. silicon (111) by metal-organic vapor phase epitaxy. *Phys. Status Solidi C*, 8(5):1479–1482, 2011.
- [91] A. Le Louarn, S. Vézian, F. Semond, and J. Massies. AlN buffer layer growth for GaN epitaxy on (1 1 1) Si: Al or N first? *J. Cryst. Growth*, 311(12):3278–3284, 2009.
- [92] F. Semond. Epitaxial challenges of GaN on silicon. *MRS Bull.*, 40(5):412–417, 2015.

- 
- [93] A. V. Kavokin, J. J. Baumberg, G. Malpuech, and F. P. Laussy. *Microcavities*. Oxford University Press, 2017.
- [94] Lord Rayleigh O.M. F.R.S. The problem of the whispering gallery. *London, Edinburgh Dublin Philos. Mag. J. Sci.*, 20(120):1001–1004, 1910.
- [95] L. He, S. Kaya Özdemir, and L. Yang. Whispering gallery microcavity lasers. *Laser Photonics Rev.*, 7:60–82, 2013.
- [96] E. Rosencher and B. Vinter. *Optoelectronics*. Cambridge University Press, 2004.
- [97] OMS: 1-D mode solver for dielectric multilayer slab waveguides. <https://www.computational-photonics.eu/oms.html>. Accessed: 2020-02-28.
- [98] EIMS: 2-D multilayer waveguide mode solver, variational effective index approximation. <https://www.computational-photonics.eu/eims.html>. Accessed: 2020-02-28.
- [99] A. Ivanova, R. Stoffer, and M. Hammer. A variational mode solver for optical waveguides based on quasi-analytical vectorial slab mode expansion. *arXiv preprint arXiv:1307.1315*, 2013.
- [100] D. G. Rabus. *Integrated ring resonators*. Springer, 2007.
- [101] R. E. Slusher, A. F. J. Levi, U. Mohideen, S. L. McCall, S. J. Pearton, and R. A. Logan. Threshold characteristics of semiconductor microdisk lasers. *Appl. Phys. Lett.*, 63:1310, 1993.
- [102] G. C. Righini, Y. Dumeige, P. Féron, M. Ferrari, G. Nunzi Conti, D. Ristic, and S. Soria. Whispering gallery mode microresonators: Fundamentals and applications. *Riv. del Nuovo Cim.*, 34(7):435–488, 2011.
- [103] C. Baker. *On-chip nano-optomechanical whispering gallery resonators*. PhD thesis, Université Paris Diderot, 2013.
- [104] A. Gray, E. Gray, G. B. Mathews, and E. Meissel. *A treatise on Bessel functions and their applications to physics*. Macmillan and Company, 1895.
- [105] Meep documentation. <https://meep.readthedocs.io/en/latest/>. Accessed: 2020-03-13.
- [106] F. Toor, D. L. Sivco, H. E. Liu, and C. F. Gmachl. Effect of waveguide sidewall roughness on the threshold current density and slope efficiency of quantum cascade lasers. *Appl. Phys. Lett.*, 93(3):031104, 2008.
- [107] H. A. Haus. *Waves and Fields in Optoelectronics*. Prentice-Hall, Inc., 1984.
- [108] L. A. Coldren, S. W. Corzine, and M. L. Mashanovitch. *Diode lasers and photonic integrated circuits*. John Wiley & Sons, 2012.

- 
- [109] J. D. Joannopoulos, S. G. Johnson, J. N. Winn, and R. D. Meade. *Molding the flow of light*. Princeton Univ. Press, 2008.
- [110] Lord Rayleigh. XVII. On the maintenance of vibrations by forces of double frequency, and on the propagation of waves through a medium endowed with a periodic structure. *London, Edinburgh Dublin Philos. Mag. J. Sci.*, 24(147):145–159, 1887.
- [111] E. Yablonovitch. Inhibited spontaneous emission in solid-state physics and electronics. *Phys. Rev. Lett.*, 58(20):2059, 1987.
- [112] S. John. Strong localization of photons in certain disordered dielectric superlattices. *Phys. Rev. Lett.*, 58(23):2486, 1987.
- [113] E. Yablonovitch, T.J. Gmitter, and K.-M. Leung. Photonic band structure: The face-centered-cubic case employing nonspherical atoms. *Phys. Rev. Lett.*, 67(17):2295, 1991.
- [114] T. F. Krauss, M. Richard, and S. Brand. Two-dimensional photonic-bandgap structures operating at near-infrared wavelengths. *Nature*, 383(6602):699–702, 1996.
- [115] K. Sakoda. *Optical properties of photonic crystals*. Springer Science & Business Media, 2004.
- [116] J. D. Joannopoulos, S. G. Johnson, J. N. Winn, and R. D. Meade. *Photonic Crystals: Molding the Flow of Light*. Princeton University Press, 2008.
- [117] S. V. Gaponenko. *Introduction to Nanophotonics*. Cambridge University Press, 2010.
- [118] MPB documentation. <https://mpb.readthedocs.io/en/latest/>. Accessed: 2020-03-17.
- [119] Y. Akahane, T. Asano, B.-S. Song, and S. Noda. High-Q photonic nanocavity in a two-dimensional photonic crystal. *Nature*, 425:944, 2003.
- [120] E. Kuramochi, E. Grossman, K. Nozaki, K. Takeda, A. Shinya, H. Taniyama, and M. Notomi. Systematic hole-shifting of L-type nanocavity with an ultrahigh Q factor. *Opt. Lett.*, 39(19):5780, 2014.
- [121] D. M. Sullivan. *Electromagnetic simulation using the FDTD method*. John Wiley & Sons, 2013.
- [122] Lumerical: Mode. <https://www.lumerical.com/products/mode/>. Accessed: 2020-03-13.
- [123] I. Aharonovich, A. Woolf, K. J. Russell, T. Zhu, N. Niu, M. J. Kappers, R. A. Oliver, and E. L. Hu. Low threshold, room-temperature microdisk lasers in the blue spectral range. *Appl. Phys. Lett.*, 103:021112, 2013.

- [124] C. H. To, W. Y. Fu, K. H. Li, Y. Cheung, and H.W. Choi. GaN microdisk with direct coupled waveguide for unidirectional whispering gallery mode emission. *Opt. Lett.*, 45(4):791–794, 2020.
- [125] D. Zhuang and J.H. Edgar. Wet etching of GaN, AlN, and SiC: a review. *Mater. Sci. Eng. R Rep.*, 48(1):1–46, 2005.
- [126] I. Adesida, C. Youtsey, A.T. Ping, F. Khan, L.T. Romano, and G. Bulman. Dry and wet etching for group III–nitrides. *MRS Internet J. Nitride Semiconductor Res.*, 4(S1):38–48, 1999.
- [127] S.J. Pearton, R.J. Shul, and F. Ren. A review of dry etching of GaN and related materials. *MRS Internet J. Nitride Semiconductor Res.*, 5(1), 2000.
- [128] R. Debnath, J.-Y. Ha, B. Wen, D. Paramanik, A. Motayed, M. R. King, and A. V. Davydov. Top-down fabrication of large-area GaN micro-and nanopillars. *J. Vac. Sci. Technol. B*, 32(2):021204, 2014.
- [129] R.J. Shul, C.G. Willison, M.M. Bridges, J. Han, J.W. Lee, S.J. Pearton, C.R. Abernathy, J.D. MacKenzie, S.M. Donovan, L. Zhang, and L. F. Lester. Selective inductively coupled plasma etching of group-III nitrides in Cl<sub>2</sub>- and BCl<sub>3</sub>-based plasmas. *J. Vac. Sci. Technol. A*, 16(3):1621–1626, 1998.
- [130] Tanner L-Edit. <https://www.mentor.com/tanneredit/>. Accessed: 2020-03-18.
- [131] F. Tabataba-Vakili, C. Brimont, B. Alloing, B. Damilano, L. Doyennette, T. Guillet, M. El Kurdi, S. Chenot, V. Brändli, E. Frayssinet, J.-Y. Duboz, F. Semond, B. Gayral, and P. Boucaud. Analysis of low-threshold optically pumped III-nitride microdisk lasers. *submitted*, page 121103, 2020.
- [132] S. L. McCall, A. F. J. Levi, R. E. Slusher, S. J. Pearton, and R. A. Logan. Whispering-gallery mode microdisk lasers. *Appl. Phys. Lett.*, 60(3):289–291, 1992.
- [133] H. W. Choi, K. N. Hui, , P. T. Lai, P. Chen, X. H. Zhang, S. Tripathy, J. H. Teng, and S. J. Chua. Lasing in GaN microdisks pivoted on Si. *Appl. Phys. Lett.*, 89:211101, 2006.
- [134] D. Simeonov, E. Feltin, H.-J. Bühlmann, T. Zhu, A. Castiglia, M. Mosca, J.-F. Carlin, R. Butté, and N. Grandjean. Blue lasing at room temperature in high quality factor GaN/AlInN microdisks with InGaN quantum wells. *Appl. Phys. Lett.*, 90:061106, 2007.
- [135] D. Simeonov, E. Feltin, A. Altoukhov, A. Castiglia, J.-F. Carlin, R. Butté, and N. Grandjean. High quality nitride based microdisks obtained via selective wet etching of AlInN sacrificial layers. *Appl. Phys. Lett.*, 92:171102, 2008.

- 
- [136] G. Zhu, J. Li, N. Zhang, X. Li, J. Dai, Q. Cui, Q. Song, C. Xu, and Y. Wang. Whispering-gallery mode lasing in a floating GaN microdisk with a vertical slit. *Sci. Rep.*, 10(1):1–7, 2020.
- [137] M. Athanasiou, R. M. Smith, J. Pugh, Y. Gong, M. J. Cryan, and T. Wang. Monolithically multi-color lasing from an InGaN microdisk on a Si substrate. *Sci. Rep.*, 7:10086, 2017.
- [138] S. Sergent, J. C. Moreno, E. Frayssinet, Y. Laaroussi, S. Chenot, J. Renard, D. Sam-Giao, B. Gayral, D. Néel, S. David, P. Boucaud, M. Leroux, and F. Semond. GaN quantum dots in (Al,Ga)N-based microdisks. *J. Phys.: Conf. Ser.*, 210:012005, 2010.
- [139] B. Damilano, K. Lekhal, H. Kim-Chauveau, S. Hussain, E. Frayssinet, J. Brault, S. Chenot, P. Vennéguès, P. De Mierry, and J. Massies. Monolithic white light emitting diodes using a (Ga,In)N-based light converter. *Proc. of SPIE*, 8986:89861G, 2014.
- [140] E.C. Young, N. Grandjean, T.E. Mates, and J.S. Speck. Calcium impurity as a source of non-radiative recombination in (In, Ga)N layers grown by molecular beam epitaxy. *Appl. Phys. Lett.*, 109(21):212103, 2016.
- [141] C.J. Chang-Hasnain, E. Kapon, and R. Bhat. Spatial mode structure of broad-area semiconductor quantum well lasers. *Appl. Phys. Lett.*, 54(3):205–207, 1989.
- [142] D.P. Bour, M. Kneissl, L.T. Romano, R.M. Donaldson, C.J. Dunnrowicz, N.M. Johnson, and G.A. Evans. Stripe-width dependence of threshold current for gain-guided AlGaInN laser diodes. *Appl. Phys. Lett.*, 74(3):404–406, 1999.
- [143] Nextnano. <https://www.nextnano.de/>. Accessed: 2020-03-30.
- [144] T. Baba and D. Sano. Low-threshold lasing and Purcell effect in microdisk lasers at room temperature. *IEEE J. Sel. Top. Quantum Electron.*, 9:1340–1346, 2003.
- [145] F. Tabataba-Vakili, L. Doyennette, C. Brimont, T. Guillet, S. Rennesson, B. Damilano, E. Frayssinet, J.-Y. Duboz, X. Checoury, S. Sauvage, M. El Kurdi, F. Semond, B. Gayral, and P. Boucaud. Demonstration of critical coupling in an active III-nitride microdisk photonic circuit on silicon. *Sci. Rep.*, 9:18095, 2019.
- [146] W.W. Chow, A.F. Wright, and J.S. Nelson. Theoretical study of room temperature optical gain in GaN strained quantum wells. *Appl. Phys. Lett.*, 68(3):296–298, 1996.
- [147] A. Hangleiter, G. Frankowsky, V. Härle, and F. Scholz. Optical gain in the nitrides: are there differences to other III–V semiconductors? *Mat. Sci. Eng. B-Adv.*, 43(1-3):201–206, 1997.
- [148] T. Baba. Photonic crystals and microdisk cavities based on GaInAsP-InP system. *IEEE J. Sel. Top. Quantum Electron.*, 3(3):808–830, 1997.

- 
- [149] M.P. Van Exter, G. Nienhuis, and J.P. Woerdman. Two simple expressions for the spontaneous emission factor  $\beta$ . *Phys. Rev. A*, 54(4):3553, 1996.
- [150] H. Morkoç. *Handbook of Nitride Semiconductors and Devices: GaN-based optical and electronic devices*. Wiley-VCH, 2009.
- [151] T. Kawashima, H. Yoshikawa, S. Adachi, S. Fuke, and K. Ohtsuka. Optical properties of hexagonal GaN. *J. Appl. Phys.*, 82(7):3528–3535, 1997.
- [152] W.G. Scheibenzuber, U.T. Schwarz, L. Sulmoni, J. Dorsaz, J.-F. Carlin, and N. Grandjean. Recombination coefficients of GaN-based laser diodes. *J. Appl. Phys.*, 109(9):093106, 2011.
- [153] J. Piprek. Efficiency droop in nitride-based light-emitting diodes. *Phys. Status Solidi A*, 207(10):2217–2225, 2010.
- [154] S. Karpov. ABC-model for interpretation of internal quantum efficiency and its droop in III-nitride LEDs: a review. *Opt Quantum Electron*, 47(6):1293–1303, 2015.
- [155] Y. Arakawa and H. Sakaki. Multidimensional quantum well laser and temperature dependence of its threshold current. *Appl. Phys. Lett.*, 40(11):939–941, 1982.
- [156] J.-Y. Duboz, F. Binet, D. Dolfi, N. Laurent, F. Scholz, J. Off, A. Sohmer, O. Briot, and B. Gil. Diffusion length of photoexcited carriers in GaN. *Mat. Sci. Eng. B-Adv.*, 50(1-3):289–295, 1997.
- [157] K. Kumakura, T. Makimoto, N. Kobayashi, T. Hashizume, T. Fukui, and H. Hasegawa. Minority carrier diffusion length in GaN: Dislocation density and doping concentration dependence. *Appl. Phys. Lett.*, 86(5):052105, 2005.
- [158] M. Martens. *Optical gain and modal loss in AlGaIn based deep UV lasers*. PhD thesis, Technische Universität Berlin, 2018.
- [159] J. Holst, A. Kaschner, U. Gfug, A. Hoffmann, C. Thomsen, F. Bertram, T. Riemann, D. Rudloff, P. Fischer, J. Christen, R. Averbek, H. Riechert, M. Heuken, M. Schwambara, and O. Schön. Comparison of the mechanism of optical amplification in InGaIn/GaN heterostructures grown by molecular beam epitaxy and MOCVD. *Phys. Status Solidi A*, 180(1):327–332, 2000.
- [160] J. Heffernan, M. Kauer, S.E. Hooper, V. Bousquet, and K. Johnson. InGaIn violet laser diodes grown by molecular beam epitaxy. *Phys. Status Solidi A*, 201(12):2668–2671, 2004.
- [161] M. Kneissl, T. Kolbe, C. Chua, V. Kueller, N. Lobo, J. Stellmach, A. Knauer, H. Rodriguez, S. Einfeldt, Z. Yang, N. M. Johnson, and M. Weyers. Advances in group III-nitride-based deep UV light-emitting diode technology. *Semicond Sci. Technol.*, 26(1):014036, 2010.

- 
- [162] R.J. Shul, C.G. Willison, M.M. Bridges, J. Han, J.W. Lee, S.J. Pearton, C.R. Abernathy, J.D. Mackenzie, and S.M. Donovan. High-density plasma etch selectivity for the III–V nitrides. *Solid State Electron.*, 42(12):2269–2276, 1998.
- [163] Y. B. Hahn, R. J. Choi, J. H. Hong, H. J. Park, C. S. Choi, and H. J. Lee. High-density plasma-induced etch damage of InGaN/GaN multiple quantum well light-emitting diodes. *J. Appl. Phys.*, 92(3):1189–1194, 2002.
- [164] R. J. Shul, L. Zhang, A. G. Baca, C.G. Willison, J. Han, S.J. Pearton, and F. Ren. Inductively coupled plasma-induced etch damage of GaN pn junctions. *J. Vac. Sci. Technol. A*, 18(4):1139–1143, 2000.
- [165] H. Kim-Chauveau, E. Frayssinet, B. Damilano, P. De Mierry, L. Bodiou, L. Nguyen, P. Venéguès, J.-M. Chauveau, Y. Cordier, J.-Y. Duboz, R. Charash, A. Vajpeyi, J.-M. Lamy, M. Akhter, P. P. Maaskant, B. Corbett, A. Hangleiter, and A. Wieck. Growth optimization and characterization of lattice-matched Al<sub>0.82</sub>In<sub>0.18</sub>N optical confinement layer for edge emitting nitride laser diodes. *J. Cryst. Growth*, 338(1):20–29, 2012.
- [166] F. Tabataba-Vakili, L. Doyennette, C. Brimont, T. Guillet, S. Rennesson, E. Frayssinet, B. Damilano, J.-Y. Duboz, F. Semond, I. Roland, M. El Kurdi, X. Checoury, S. Sauvage, B. Gayral, and P. Boucaud. Blue microlasers integrated on a photonic platform on silicon. *ACS Photonics*, 5:3643–3648, 2018.
- [167] S. Koseki, B. Zhang, K. De Greve, and Y. Yamamoto. Monolithic integration of quantum dot containing microdisk microcavities coupled to air-suspended waveguides. *Appl. Phys. Lett.*, 94:051110, 2009.
- [168] X. Gao, J. Yuan, Y. Yang, Y. Li, W. Yuan, G. Zhu, H. Zhu, M. Feng, Q. Sun, Y. Liu, and Y. Wang. A 30Mbps in-plane full-duplex light communication using a monolithic GaN photonic circuit. *Semicond. Sci. Technol.*, 32:075002, 2017.
- [169] E. J. Skogen, J. W. Raring, G. B. Morrison, C. S. Wang, V. Lal, M. L. Masanovic, and L. A. Coldren. Monolithically integrated active components: a quantum-well intermixing approach. *IEEE J. Sel. Top. Quantum Electron.*, 11(2):343–355, 2005.
- [170] J. J. Coleman, R. M. Lammert, M. L. Osowski, and A. M. Jones. Progress in InGaAs-GaAs selective-area MOCVD toward photonic integrated circuits. *IEEE J. Sel. Top. Quantum Electron.*, 3(3):874–884, 1997.
- [171] S. Matsuo, A. Shinya, T. Kakitsuka, K. Nozaki, T. Segawa, T. Sato, Y. Kawaguchi, and M. Notomi. High-speed ultracompact buried heterostructure photonic-crystal laser with 13 fJ of energy consumed per bit transmitted. *Nat. Photonics*, 4:648–654, 2010.

- 
- [172] D. Remiens, B. Rose, M. Carre, and V. Hornung. GaInAsP/InP integrated ridge laser with a butt-jointed transparent optical waveguide fabricated by single-step metalorganic vapor-phase epitaxy. *J. Appl. Phys.*, 68(5):2450–2453, 1990.
- [173] Y. Honda, Y. Kawaguchi, Y. Ohtake, S. Tanaka, M. Yamaguchi, and N. Sawaki. Selective area growth of GaN microstructures on patterned (111) and (001) Si substrates. *J. Cryst. Growth*, 230(3-4):346–350, 2001.
- [174] B. Beaumont, P. Vennéguès, and P. Gibart. Epitaxial lateral overgrowth of GaN. *Phys. Status Solidi B*, 227(1):1–43, 2001.
- [175] G. Yang, P. Chen, S. Gao, G. Chen, R. Zhang, and Y. Zheng. White-light emission from InGaN/GaN quantum well microrings grown by selective area epitaxy. *Photonics Res.*, 4(1):17–20, 2016.
- [176] D. Hofstetter, B. Maisenholder, and H. P. Zappe. Quantum-well intermixing for fabrication of lasers and photonic integrated circuits. *IEEE J. Sel. Top. Quantum Electron.*, 4(4):794–802, 1998.
- [177] K. Lorenz, A. Redondo-Cubero, M.B. Lourenço, M.C. Sequeira, M. Peres, A. Freitas, L.C. Alves, E. Alves, M.P. Leitão, J. Rodrigues, N. Ben Sedrinec, M. R. Correiac, and T. Monteiro. Quantum well intermixing and radiation effects in InGaN/GaN multi quantum wells. In *Gallium Nitride Materials and Devices XI*, volume 9748, page 97480L. International Society for Optics and Photonics, 2016.
- [178] C. Shen, T. K. Ng, and B. S. Ooi. Enabling area-selective potential-energy engineering in InGaN/GaN quantum wells by post-growth intermixing. *Opt. Express*, 23(6):7991–7998, 2015.
- [179] B. Mason, G. A. Fish, S. P. DenBaars, and L. A. Coldren. Ridge waveguide sampled grating DBR lasers with 22-nm quasi-continuous tuning range. *IEEE Photon. Technol. Lett.*, 10(9):1211–1213, 1998.
- [180] Z. Shi, X. Gao, J. Yuan, S. Zhang, Y. Jiang, F. Zhang, Y. Jiang, H. Zhu, and Y. Wang. Transferrable monolithic III-nitride photonic circuit for multifunctional optoelectronics. *Appl. Phys. Lett.*, 111:241104, 2017.
- [181] R. Floyd, K. Hussain, A. Mamun, M. Gaevski, G. Simin, MVS Chandrashekhar, and A. Khan. Photonics integrated circuits using  $\text{Al}_x\text{Ga}_{1-x}\text{N}$  based UVC light-emitting diodes, photodetectors and waveguides. *Appl. Phys. Express*, 13(2):022003, 2020.
- [182] R. Floyd, K. Hussain, A. Mamun, M. Gaevski, G. Simin, M.V.S. Chandrashekhar, and A. Khan. An initial study of ultraviolet C optical losses for monolithically integrated Al-GaN heterojunction optoelectronic devices. *Phys. Status Solidi A*, 2020.

- 
- [183] T. Kamei, T. Kamikawa, M. Araki, S. P. DenBaars, S. Nakamura, and J. E. Bowers. Research toward a heterogeneously integrated InGaN laser on silicon. *Phys. Status Solidi A*, 217(7):1900770, 2020.
- [184] R. Arefin, S. H. Ramachandra, H. Jung, W. You, S. M. N. Hasan, H. Turski, S. Dwivedi, and S. Arafin. III-N/Si<sub>3</sub>N<sub>4</sub> integrated photonics platform for blue wavelengths. *IEEE J. Quantum Electron.*, pages 1–1, 2020.
- [185] B. Corbett, R. Loi, W. Zhou, D. Liu, and Z. Ma. Transfer print techniques for heterogeneous integration of photonic components. *Prog. Quantum. Electron.*, 52:1–17, 2017.
- [186] M. Cai, O. Painter, and K. J. Vahala. Observation of critical coupling in a fiber taper to a silica-microsphere whispering-gallery mode system. *Phys. Rev. Lett.*, 85:74–77, 2000.
- [187] S. M. Spillane, T. J. Kippenberg, and K. J. Vahala. Ultralow-threshold Raman laser using a spherical dielectric microcavity. *Nature*, 415:621–623, 2002.
- [188] W. Bogaerts, P. De Heyn, T. Van Vaerenbergh, K. DeVos, S. K. Selvaraja, T. Claes, P. Dumon, P. Bienstman, D. Van Thourhout, and R. Baets. Silicon microring resonators. *Laser Photonics Rev.*, 6:47–73, 2012.
- [189] E. Kioupakis, P. Rinke, A. Schleife, F. Bechstedt, and C. G. Van de Walle. Free-carrier absorption in nitrides from first principles. *Phys. Rev. B*, 81:241201(R), 2010.
- [190] M. Soltani. *Novel integrated silicon nanophotonic structures using ultra-high Q resonators*. PhD thesis, Georgia Institute of Technology, 2009.
- [191] A. Yariv. Universal relations for coupling of optical power between microresonators and dielectric waveguides. *Electron. Lett.*, 36(4):321–322, 2000.
- [192] F. Tabataba-Vakili, I. Roland, T.-M. Tran, X. Checoury, M. El Kurdi, S. Sauvage, C. Brimont, T. Guillet, S. Rennesson, J.-Y. Duboz, F. Semond, B. Gayral, and P. Boucaud. Q factor limitation at short wavelength (around 300 nm) in III-nitride-on-silicon photonic crystal cavities. *Appl. Phys. Lett.*, 111:131103, 2017.
- [193] J. Hu, N. Carlie, N.-N. Feng, L. Petit, A. Agarwal, K. Richardson, and L. Kimerling. Planar waveguide-coupled, high-index-contrast, high-Q resonators in chalcogenide glass for sensing. *Opt. Lett.*, 33(21):2500–2502, 2008.
- [194] D. J. Gargas, M. C. Moore, A. Ni, S.-W. Chang, Z. Zhang, S.-L. Chuang, and P. Yang. Whispering gallery mode lasing from zinc oxide hexagonal nanodisks. *ACS Nano*, 4:3270–3276, 2009.
- [195] B. Min, T. J. Kippenberg, L. Yang, K. J. Vahala, J. Kalkman, and A. Polman. Erbium-implanted high-Q silica toroidal microcavity laser on a silicon chip. *Phys. Rev. A*, 70:033803, 2004.

- 
- [196] A. Rasoloniaina, V. Huet, T. K.N. Nguyễn, E. Le Cren, M. Mortier, L. Michely, Y. Dumeige, and P. Féron. Controlling the coupling properties of active ultrahigh-Q WGM microcavities from undercoupling to selective amplification. *Sci. Rep.*, 4:4023, 2014.
- [197] A. E. Siegman. *Lasers*. University Science Books, 1986.
- [198] A. Yariv. *Quantum Electronics*. John Wiley & Sons, Inc., 1989.
- [199] M. S. Islam, R. X. Ferreira, X. He, E. Xie, S. Videv, S. Viola, S. Watson, N. Bamiedakis, R. V. Penty, I. H. White, A. E. Kelly, E. Gu, H. Haas, and M. D. Dawson. Towards 10 Gb/s orthogonal frequency division multiplexing-based visible light communication using a GaN violet micro-LED. *Photonics Res.*, 5:A35–A43, 2017.
- [200] M.-C. Estevez, M. Alvarez, and L. M. Lechuga. Integrated optical devices for lab-on-a-chip biosensing applications. *Laser Photonics Rev.*, 6:463–487, 2012.
- [201] F. Tabataba-Vakili, B. Alloing, B. Damilano, H. Souissi, C. Brimont, L. Doyennette, T. Guillet, X. Checoury, M. El Kurdi, S. Chenot, E. Frayssinet, J.-Y. Duboz, F. Semond, B. Gayral, and P. Boucaud. Monolithic integration of ultraviolet microdisk lasers into photonic circuits in a III-nitride on silicon platform. *Opt. Lett.*, (15):4276–4279, 2020.
- [202] S. Nakamura. The roles of structural imperfections in InGaN-based blue light-emitting diodes and laser diodes. *Science*, 281(5379):956–961, 1998.
- [203] M. Soltani, R. Soref, T. Palacios, and D. Englund. AlGaN/AlN integrated photonics platform for the ultraviolet and visible spectral range. *Opt. Express*, 24(22):25415, 2016.
- [204] G. N. West, W. Loh, D. Kharas, C. Sorace-Agaskar, K. K. Mehta, J. Sage, J. Chiaverini, and R. J. Ram. Low-loss integrated photonics for the blue and ultraviolet regime. *APL Photonics*, 4(2):026101, 2019.
- [205] S. Sergent, M. Arita, S. Kako, S. Iwamoto, and Y. Arakawa. High-Q (>5000) AlN nanobeam photonic crystal cavity embedding GaN quantum dots. *Appl. Phys. Lett.*, 100:121103, 2012.
- [206] W.H.P. Pernice, C. Xiong, C. Schuck, and H.X. Tang. High-Q aluminum nitride photonic crystal nanobeam cavities. *Appl. Phys. Lett.*, 100(9):091105, 2012.
- [207] N. Vico Triviño, M. Minkov, G. Urbinati, M. Galli, J.-F. Carlin, R. Butté, V. Savona, and N. Grandjean. Gallium nitride L3 photonic crystal cavities with an average quality factor of 16 900 in the near infrared. *Appl. Phys. Lett.*, 105:231119, 2014.
- [208] M. S. Mohamed, A. Simbula, J.-F. Carlin, M. Minkov, D. Gerace, V. Savona, N. Grandjean, M. Galli, and R. Houdré. Efficient continuous-wave nonlinear frequency conversion in high-Q gallium nitride photonic crystal cavities on silicon. *APL Photonics*, 2:031301, 2017.

- 
- [209] M. Arita, S. Ishida, S. Kako, S. Iwamoto, and Y. Arakawa. AlN air-bridge photonic crystal nanocavities demonstrating high quality factor. *Appl. Phys. Lett.*, 91:051106, 2007.
- [210] D. Néel, S. Sergent, M. Mexis, D. Sam-Giao, T. Guillet, C. Brimont, T. Bretagnon, F. Semond, B. Gayral, S. David, X. Checoury, and P. Boucaud. AlN photonic crystal nanocavities realized by epitaxial conformal growth on nanopatterned silicon substrate. *Appl. Phys. Lett.*, 98:261106, 2011.
- [211] C.-H. Lin, J.-Y. Wang, C.-Y. Chen, K.-C. Shen, D.-M. Yeh, Y.-W. Kiang, and C. C. Yang. A GaN photonic crystal membrane laser. *Nanotechnology*, 22:025201, 2011.
- [212] S. Sergent, M. Arita, S. Kako, K. Tanabe, S. Iwamoto, and Y. Arakawa. High-Q AlN photonic crystal nanobeam cavities fabricated by layer transfer. *Appl. Phys. Lett.*, 101:101106, 2012.
- [213] N. Vico Triviño, G. Rossbach, U. Dharanipathy, J. Levrat, A. Castiglia, J.-F. Carlin, K. A. Atlasov, R. Butté, R. Houdré, and N. Grandjean. High quality factor two dimensional GaN photonic crystal cavity membranes grown on silicon substrate. *Appl. Phys. Lett.*, 100:071103, 2012.
- [214] T.-T. Wu, S.-Y. Lo, H.-M. Huang, C.-W. Tsao, T.-C. Lu, and S.-C. Wang. High quality factor nonpolar GaN photonic crystal nanocavities. *Appl. Phys. Lett.*, 102:191116, 2013.
- [215] L.-W. Luo, G. S. Wiederhecker, J. Cardenas, C. Poitras, and M. Lipson. High quality factor etchless silicon photonic ring resonators. *Opt. Express*, 19(7):6284–6289, 2011.
- [216] H. A. Haus, M. A. Popović, M. R. Watts, C. Manolatou, B. E. Little, and S. T. Chu. Optical resonators and filters. In *Optical microcavities*, pages 1–37. World Scientific, 2004.
- [217] M. Gromovyi, J. Brault, A. Courville, S. Rennesson, F. Semond, G. Feuillet, P. Baldi, P. Boucaud, J.-Y. Duboz, and M. P. De Micheli. Efficient second harmonic generation in low-loss planar GaN waveguides. *Opt. Express*, 25(19):23035–23044, 2017.
- [218] L. Wang, J. Jin, C. Mi, Z. Hao, Y. Luo, C. Sun, Y. Han, B. Xiong, J. Wang, and H. Li. A review on experimental measurements for understanding efficiency droop in InGaN-based light-emitting diodes. *Materials*, 10(11):1233, 2017.
- [219] G. Yu, G. Wang, H. Ishikawa, M. Umeno, T. Soga, T. Egawa, J. Watanabe, and T. Jimbo. Optical properties of wurtzite structure GaN on sapphire around fundamental absorption edge (0.78–4.77 eV) by spectroscopic ellipsometry and the optical transmission method. *Appl. Phys. Lett.*, 70(24):3209–3211, 1997.
- [220] Y. Lai, S. Pirotta, G. Urbinati, D. Gerace, M. Minkov, V. Savona, A. Badolato, and M. Galli. Genetically designed L3 photonic crystal nanocavities with measured quality factor exceeding one million. *Appl. Phys. Lett.*, 104:241101, 2014.

- 
- [221] A. R. A. Chalcraft, S. Lam, D. O'Brien, T. F. Krauss, M. Sahin, D. Szymanski, D. Sanvitto, R. Oulton, M. S. Skolnick, A. M. Fox, D. M. Whittaker, H.-Y. Liu, and M. Hopkinson. Mode structure of the L3 photonic crystal cavity. *Appl. Phys. Lett.*, 90:241117, 2007.
- [222] M. Bickermann, B. M. Epelbaum, O. Filip, P. Heimann, S. Nagata, and A. Winnacker. UV transparent single-crystalline bulk AlN substrates. *Phys. Status Solidi C*, 7(1):21, 2010.
- [223] P. Lu, R. Collazo, R. F. Dalmau, G. Durkaya, N. Dietz, and Z. Sitar. Different optical absorption edges in AlN bulk crystals grown in m- and c-orientations. *Appl. Phys. Lett.*, 93:131922, 2008.
- [224] H. Fujiwara. *Spectroscopic Ellipsometry: Principles and Applications*. John Wiley & Sons, Ltd, Chichester, UK, 2007.
- [225] J. M. Khoshman and M. E. Kordesch. Optical characterization of sputtered amorphous aluminum nitride thin films by spectroscopic ellipsometry. *J. Non-Cryst. Solids*, 351:3334, 2005.
- [226] J. H. Davies. *The Physics of Low-Dimensional Semiconductors*. Cambridge Univ. Press, Cambridge, UK, 1998.
- [227] F. Tabataba-Vakili, S. Rennesson, B. Damilano, E. Frayssinet, J.-Y. Duboz, F. Semond, I. Roland, B. Paulillo, R. Colombelli, M. El Kurdi, X. Checoury, S. Sauvage, L. Doyennette, C. Brimont, T. Guillet, B. Gayral, and P. Boucaud. III-nitride on silicon electrically injected microrings for nanophotonic circuits. *Opt. Express*, 27:11800–11808, 2019.
- [228] S. Nakamura, M. Senoh, S.-i. Nagahama, N. Iwasa, T. Yamada, T. Matsushita, H. Kiyoku, and Y. Sugimoto. InGaN-based multi-quantum-well-structure laser diodes. *Jpn. J. Appl. Phys.*, 35(1B):L74, 1996.
- [229] Z. Zhang, M. Kushimoto, T. Sakai, N. Sugiyama, L. J. Schowalter, C. Sasaoka, and H. Amano. A 271.8 nm deep-ultraviolet laser diode for room temperature operation. *Appl. Phys. Express*, 12(12):124003, 2019.
- [230] S. Nakamura, M. Senoh, S. i. Nagahama, N. Iwasa, T. Yamada, T. Matsushita, H. Kiyoku, Y. Sugimoto, T. Kozaki, H. Umemoto, M. Sano, and K. Chocho. Present status of InGaN/GaN/AlGaN-based laser diodes. *J. Cryst. Growth*, 189-190:820–825, 1998.
- [231] M. Kneissl, M. Teepe, N. Miyashita, N. M. Johnson, G. D. Chern, and R. K. Chang. Current-injection spiral-shaped microcavity disk laser diodes with unidirectional emission. *Appl. Phys. Lett.*, 84(14):2485, 2004.
- [232] M. Hikita, M. Yanagihara, K. Nakazawa, H. Ueno, Y. Hirose, T. Ueda, Y. Uemoto, T. Tanaka, D. Ueda, and T. Egawa. AlGaN/GaN power HFET on silicon substrate with source-via grounding (SVG) structure. *IEEE Trans. Electron Devices*, 52(9):1963–1968, 2005.

- 
- [233] M. Hikita, H. Ueno, Y. Hirose, M. Yanagihara, Y. Uemoto, and T. Tanaka. Semiconductor device and method for fabricating the same, 2007. US Patent 7291872B2.
- [234] Y. Zhang, M. Yuan, N. Chowdhury, K. Cheng, and T. Palacios. 720 V/0.35 m $\Omega$  · cm<sup>2</sup> fully-vertical GaN-on-Si power diodes by selective removal of Si substrates and buffer layers. *IEEE Electron. Device Lett.*, 9(5):715–718, 2018.
- [235] D. Sizov, R. Bhat, and C.-e. Zah. Optical absorption of Mg-doped layers and InGaN quantum wells on c-plane and semipolar GaN structures. *J. Appl. Phys.*, 113(20):203108, 2013.
- [236] A. David, M. J. Grundmann, J. F. Kaeding, N. F. Gardner, T. G. Mihopoulos, and M. R. Krames. Carrier distribution in 0001 InGaN/GaN multiple quantum well light-emitting diodes. *Appl. Phys. Lett.*, 92:053502, 2008.
- [237] G. Frankowsky, F. Steuber, V. Härle, F. Scholz, and A. Hangleiter. Optical gain in GaInN/GaN heterostructures. *Appl. Phys. Lett.*, 68:3746, 1996.
- [238] R. X.G. Ferreira, E. Xie, J. J.D. McKendry, S. Rajbhandari, H. Chun, G. Faulkner, S. Watson, A. E. Kelly, E. Gu, R. V. Penty, I. H. White, D. C. O'Brien, and M. D. Dawson. High bandwidth GaN-based micro-LEDs for multi-Gb/s visible light communications. *IEEE Photon. Technol. Lett.*, 28(19):2023–2026, 2016.
- [239] H. K. Tsang, C.S. Wong, T.K. Liang, I.E. Day, S.W. Roberts, A. Harpin, J. Drake, and M. Asghari. Optical dispersion, two-photon absorption and self-phase modulation in silicon waveguides at 1.5  $\mu$ m wavelength. *Appl. Phys. Lett.*, 80(3):416–418, 2002.
- [240] D. J. Blumenthal, R. Heideman, D. Geuzebroek, A. Leinse, and C. Roeloffzen. Silicon nitride in silicon photonics. *Proc. IEEE*, 106(12):2209–2231, 2018.
- [241] X. Liu, C. Sun, B. Xiong, L. Wang, J. Wang, Y. Han, Z. Hao, H. Li, Y. Luo, J. Yan, T. Wei, Y. Zhang, and J. Wang. Aluminum nitride-on-sapphire platform for integrated high-Q microresonators. *Opt. Express*, 25(2):587–594, 2017.
- [242] A. W. Bruch, X. Liu, X. Guo, J. B. Surya, Z. Gong, L. Zhang, J. Wang, J. Yan, and H. X. Tang. 17 000%/W second-harmonic conversion efficiency in single-crystalline aluminum nitride microresonators. *Appl. Phys. Lett.*, 113:131102, 2018.
- [243] J. Wang, M. Clementi, M. Minkov, A. Barone, J.-F. Carlin, N. Grandjean, D. Gerace, S. Fan, M. Galli, and R. Houdré. Doubly resonant second-harmonic generation of a vortex beam from a bound state in the continuum. *Opt. Lett.*, 7(9):1126–1132, 2020.
- [244] X. Liu, C. Sun, B. Xiong, L. Wang, J. Wang, Y. Han, Z. Hao, H. Li, Y. Luo, J. Yan, T. Wei, Y. Zhang, and J. Wang. Generation of multiple near-visible comb lines in an AlN micro-ring via  $\chi(2)$  and  $\chi(3)$  optical nonlinearities. *Appl. Phys. Lett.*, 113(17):171106, 2018.

- 
- [245] S. Joblot. *Croissance d'hétérostructures à bases GaN sur substrat de silicium orienté (001) : application aux transistors à haute mobilité d'électrons*. PhD thesis, Université de Nice-Sophia Antipolis, 2007.





**Titre :** Nitrures d'éléments III sur silicium : une plateforme de photonique intégrée de l'ultraviolet jusqu'au proche infrarouge

**Mots clés :** microlaser, microcavité, photonique intégrée, circuit photonique, nitrures d'éléments III

**Résumé :** Les semi-conducteurs nitrures d'éléments III (AlN, GaN, InN et leurs alliages) sont devenus très importants dans notre vie quotidienne, car ils sont utilisés dans les diodes électroluminescentes blanches, bleues, vertes, et ultraviolettes, ainsi que pour des diodes lasers et l'électronique de puissance et hyperfréquence. Les matériaux nitrures sont fortement polyvalents grâce à leur grande bande interdite directe et accordable de l'ultraviolet jusqu'au visible. Ils donnent accès à une très large gamme d'applications électroniques, optoélectroniques, et photoniques. En photonique, un domaine très prometteur s'appuie sur la plateforme des nitrures d'éléments III sur silicium pour la prochaine génération de circuits photoniques intégrés grâce à sa grande fenêtre de transparence de l'ultraviolet jusqu'au proche infrarouge et la

possibilité d'intégration monolithique d'émetteurs actifs comme des puits et boîtes quantiques. Dans cette thèse, nous étudions différents dispositifs photoniques à base de nitrures et leur intégration dans des circuits photoniques actifs et passifs à des longueurs d'onde allant de l'ultraviolet jusqu'au proche infrarouge. Nous démontrons des seuils lasers bas en pompage optique pulsé et les premiers circuits photoniques actifs à microlaser dans les gammes spectrales bleue et ultraviolette. Nous proposons également une approche pour l'injection électrique dans des micro-anneaux qui est compatible avec des circuits photoniques et nous étudions des nitrures d'éléments III collés sur SiO<sub>2</sub> comme plateforme pour des circuits photoniques passifs dans le proche infrarouge.

**Title :** III-nitrides on silicon: a platform for integrated photonics from the ultraviolet to the near-infrared

**Keywords :** microlaser, microcavity, integrated photonics, photonic circuits, III-nitrides

**Abstract :** III-nitride semiconductors (AlN, GaN, InN and their alloys) have become an integral part of our daily lives as they are used in white, blue, green, and ultraviolet light emitting diodes, as well as laser diodes and power and high frequency electronics. This material is highly versatile due to its tuneable large direct band gap from the ultraviolet to the visible. III-nitrides give access to a very wide range of electronic, optoelectronic, and photonic applications. In photonics, a promising field relies on the III-nitride on silicon platform for next generation photonic integrated circuits due to its large transparency window from the ultraviolet to the near-infrared and the possibility of monolithic integration of active

emitters such as quantum wells and quantum dots. In this thesis, we study different photonic devices and their integration into active and passive photonic circuits at wavelengths going from the ultraviolet to the near-infrared. We demonstrate low threshold pulsed optically pumped lasing and the first active microlaser photonic circuits in the blue and ultraviolet spectral ranges. We also propose a scheme for electrical injection in microrings that is compatible with photonic circuits and investigate III-nitrides bonded on SiO<sub>2</sub> as a platform for passive photonic circuits in the near-infrared.